

Advances in Optical Technologies

Correlation Optics

Guest Editors: Oleg V. Angelsky, Alexander G. Ushenko,
Peter V. Polyanskii, and Igor I. Mokhun





Correlation Optics

Advances in Optical Technologies

Correlation Optics

Guest Editors: Oleg V. Angelsky, Alexander G. Ushenko,
Peter V. Polyanskii, and Igor I. Mokhun



Copyright © 2010 Hindawi Publishing Corporation. All rights reserved.

This is a special issue published in volume 2010 of "Advances in Optical Technologies." All articles are open access articles distributed under the Creative Commons Attribution License, which permits unrestricted use, distribution, and reproduction in any medium, provided the original work is properly cited.

Editorial Board

Mustafa A. G. Abushagur, USA
Partha P. Banerjee, USA
Ralph Barry Johnson, USA
Augusto Beléndez, Spain
Steve Blair, USA
Maria Luisa Calvo, Spain
H. John Caulfield, USA
Pierre Chavel, France
Zhongping Chen, USA
Fu-Pen Chiang, USA
Petr Eliseev, USA
Michael A. Fiddy, USA
Patti Gillespie, USA

Richard B. Hoover, USA
Zoran Ikonc, UK
Saulius Juodkazis, Australia
Mark A. Kahan, USA
Alexander A. Kaminskii, Russia
Qiang Lin, China
Liren Liu, China
Qing Ming Luo, China
Daniel Malacara, Mexico
Mikhail Noginov, USA
Richard Notzel, The Netherlands
Ci-Ling Pan, Taiwan
Markus Pessa, Finland

Martin Richardson, USA
Giancarlo C. Righini, Italy
Joseph Rosen, Israel
José Luís Santos, Portugal
Colin J. R. Sheppard, Singapore
Kiyoshi Shimamura, Japan
Jagdish P. Singh, USA
Yinglin L. Song, China
Theo Tschudi, Germany
Leonid P. Yaroslavsky, Israel
Jianping Yin, China
Yong Zhao, China

Contents

Correlation Optics, Oleg V. Angelsky, Alexander G. Ushenko, Peter V. Polyanskii, and Igor I. Mokhun
Volume 2010, Article ID 835340, 2 pages

Optical Computing: A 60-Year Adventure, Pierre Ambs
Volume 2010, Article ID 372652, 15 pages

Conservation Laws in Quantum-Correlation-Function Dynamics, Wei Wang and Mitsuo Takeda
Volume 2010, Article ID 171254, 8 pages

Asymptotic Principal Values and Regularization Methods for Correlation Functions with Reflective Boundary Conditions, Masafumi Seriu
Volume 2010, Article ID 798983, 7 pages

Spectral Modification by Diffraction and Scattering, M. Taghi Tavassoly, Masoomeh Dashtdar, and Mohammad Amiri
Volume 2010, Article ID 613728, 7 pages

Optical Sensing of Attached Fibrinogen on Carbon Doped Titanium Surfaces, Raimo Silvennoinen, Vladimír Vetterl, Stanislav Hasoň, Martti Silvennoinen, Kari Myller, Jiří Vaněk, and Ladislav Cvrček
Volume 2010, Article ID 942349, 7 pages

Detection and Localization of Defects in Monocrystalline Silicon Solar Cell, P. Tománek, P. Škarvada, R. Macků, and L. Grmela
Volume 2010, Article ID 805325, 5 pages

The Degree of Mutual Anisotropy of Biological Liquid Crystals Net during the Diagnostics of Human Tissues Birefringence, Oleg V. Angelsky and Yuriy A. Ushenko
Volume 2010, Article ID 321275, 9 pages

The Interconnection between the Coordinate Distribution of Mueller-Matrixes Images Characteristic Values of Biological Liquid Crystals Net and the Pathological Changes of Human Tissues, Oleg V. Angelsky, Yuriy A. Ushenko, Alexander V. Dubolazov, and Olha Yu. Telenha
Volume 2010, Article ID 130659, 10 pages

A New Method of Mueller-Matrix Diagnostics and Differentiation of Early Oncological Changes of the Skin Derma, Yu. A. Ushenko, A. P. Peresunko, and Bozan Adel Baku
Volume 2010, Article ID 952423, 9 pages

Evolution of Statistic Moments of 2D-Distributions of Biological Liquid Crystal Net Mueller Matrix Elements in the Process of Their Birefringent Structure Changes, A. G. Ushenko, I. Z. Misevich, V. Istratiy, I. Bachyns'ka, A. P. Peresunko, Omar Kamal Numan, and T. G. Moiyusuk
Volume 2010, Article ID 423145, 8 pages

On the Feasibilities of Using the Wavelet Analysis of Mueller Matrix Images of Biological Crystals, O. V. Dubolazov, A. G. Ushenko, V. T. Bachynsky, A. P. Peresunko, and O. Ya. Vanchulyak
Volume 2010, Article ID 162832, 9 pages

Editorial

Correlation Optics

Oleg V. Angelsky,¹ Alexander G. Ushenko,² Peter V. Polyanskii,¹ and Igor I. Mokhun¹

¹ *Correlation Optics Department, Chernivtsi National University, 58012 Chernivtsi, Ukraine*

² *Optics and Spectroscopy Department, Chernivtsi National University, 2 Kotsyubinsky Str., 58012 Chernivtsi, Ukraine*

Correspondence should be addressed to Oleg V. Angelsky, oleg_angelsky@ukr.net

Received 23 May 2010; Accepted 23 May 2010

Copyright © 2010 Oleg V. Angelsky et al. This is an open access article distributed under the Creative Commons Attribution License, which permits unrestricted use, distribution, and reproduction in any medium, provided the original work is properly cited.

The papers presented in this special issue are the selected reflecting the topics of the Ninth International Conference “Correlation Optics,” which became traditional being held biannually under the auspices of SPIE, ICO, OSA, and EOS in Chernivtsi (Ukraine). Distribution of the papers over the conference topics reflects current tendencies in correlation optics, when, to say, the use of well-established approaches, methods, and techniques of optical correlation data processing [1–4], singular optical [5–8], and fractal optics [9, 10] approaches provides successful solving of the problem of looking for important diagnostic information in biology and medicine [11–15], as it is seen from several papers in this issue. It is worthy to note that interconnection between spatially inhomogeneously distributed “unconventional polarization states of light” and measured correlation characteristics of optical fields are put in the base of diagnostics of states of biological tissue tomes in these papers. Timeliness and topicality of this papers approach are confirmed in Special Issue Unconventional Polarization States of Light in the journal “Optics Express” from May 12, 2010.

*Oleg V. Angelsky
Alexander G. Ushenko
Peter V. Polyanskii
Igor I. Mokhun*

References

- [1] S. M. Rytov, Yu. A. Kravtsov, and V. I. Tatarsky, *Principles of Statistical Radiophysics*, Springer, Berlin, Germany, 1989.
- [2] O. V. Angelsky, P. P. Maksimyak, and S. Hanson, *The Use of Optical—Correlation Techniques for Characterizing Scattering Object and Media*, SPIE Press PM71, Bellingham, Wash, USA, 1999.
- [3] O. V. Angelsky and P. P. Maksimyak, “Optical diagnostics of random phase objects,” *Applied Optics*, vol. 29, no. 19, pp. 2894–2898, 1990.
- [4] O. V. Angelsky, P. P. Maksimyak, V. V. Ryukhtin, and S. G. Hanson, “New feasibilities for characterizing rough surfaces by optical-correlation techniques,” *Applied Optics*, vol. 40, no. 31, pp. 5693–5707, 2001.
- [5] J. F. Nye, *Natural Focusing and Fine Structure of Light: Caustics and Wave Dislocations*, Institute of Physics, Bristol, UK, 1999.
- [6] M. S. Soskin and M. V. Vasnetsov, “Singular Optics,” *Progress in Optics*, vol. 42, pp. 219–276, 2001.
- [7] O. V. Angelsky, I. I. Mokhun, A. I. Mokhun, and M. S. Soskin, “Interferometric methods in diagnostics of polarization singularities,” *Physical Review E*, vol. 65, no. 3, Article ID 036602, 5 pages, 2002.
- [8] O. Angelsky, Ed., *Optical Correlation Applications and Techniques, PM168*, SPIE Press, Bellingham, Wash, USA, 2007.
- [9] O. V. Angelsky, D. N. Burkovets, A. V. Kovalchuk, and S. G. Hanson, “On the fractal description of rough surfaces,” *Applied Optics*, vol. 41, no. 22, pp. 4620–4629, 2002.
- [10] O. V. Angelsky, D. N. Burkovets, P. P. Maksimyak, and S. G. Hanson, “Applicability of the singular-optics concept for diagnostics of random and fractal rough surfaces,” *Applied Optics*, vol. 42, no. 22, pp. 4529–4540, 2003.
- [11] M. V. Berry, “Exploring the colours of dark light,” *New Journal of Physics*, vol. 4, no. 74, pp. 1–14, 2002.
- [12] G. V. Bogatyryova, C. V. Fel'de, P. V. Polyanskii, S. A. Ponomarenko, M. S. Soskin, and E. Wolf, “Partially coherent vortex beams with a separable phase,” *Optics Letters*, vol. 28, no. 11, pp. 878–880, 2003.
- [13] M. S. Soskin, P. V. Polyanskii, and O. O. Arkhelyuk, “Computer-synthesized hologram-based rainbow optical vortices,” *New Journal of Physics*, vol. 6, no. 196, pp. 1–8, 2004.

- [14] O. V. Angelsky, S. G. Hanson, A. P. Maksimyak, and P. P. Maksimyak, "On the feasibility for determining the amplitude zeroes in polychromatic fields," *Optics Express*, vol. 13, no. 12, pp. 4396–4405, 2005.
- [15] O. V. Angelsky, P. V. Polyanskii, and S. G. Hanson, "Singular-optical coloring of regularly scattered white light," *Optics Express*, vol. 14, no. 17, pp. 7579–7586, 2006.

Research Article

Optical Computing: A 60-Year Adventure

Pierre Ambs

Laboratoire Modélisation Intelligence Processus Systèmes, Ecole Nationale Supérieure d'Ingénieurs Sud Alsace, Université de Haute Alsace, 12 rue des Frères Lumière, 68093 Mulhouse Cedex, France

Correspondence should be addressed to Pierre Ambs, pierre.ambs@uha.fr

Received 15 December 2009; Accepted 19 February 2010

Academic Editor: Peter V. Polyanskii

Copyright © 2010 Pierre Ambs. This is an open access article distributed under the Creative Commons Attribution License, which permits unrestricted use, distribution, and reproduction in any medium, provided the original work is properly cited.

Optical computing is a very interesting 60-year old field of research. This paper gives a brief historical review of the life of optical computing from the early days until today. Optical computing generated a lot of enthusiasm in the sixties with major breakthroughs opening a large number of perspectives. The period between 1980 and 2000 could be called the golden age with numerous new technologies and innovating optical processors designed and constructed for real applications. Today the field of optical computing is not ready to die, it has evolved and its results benefit to new research topics such as nanooptics, biophotonics, or communication systems.

1. Introduction

The knowledge of some history of sciences is useful for understanding the evolution of a research domain, its successes and failures. Optical computing is an interesting candidate for a historical review. This research field is also named optical information processing, and now the terms of information optics or information photonics are frequently used, reflecting the evolution of the domain. Optical computing is approximately 60 years old and it is a well-defined domain with its own specialized conferences, sections in the scientific journals and its own research programs and funding. It was also very active worldwide and therefore it is impossible in the frame of a paper to describe all the research results. Numerous books were written on the subject, for example, the following books describe the state of the art of optical computing at the time of their publication in 1972 [1], in 1981-82 [2, 3], in 1989 [4], and in 1998-99 [5, 6].

Since optical computing is such a well defined field over such a long period of time, it is interesting to study its evolution and this study can be helpful to understand why some research domains were very successful during only a limited period of time while other have generated numerous applications that are still in use. From the beginning there was a lot of questioning about the potential of optics for computing whereas there was no doubt about the potential

and the future of electronics. Caulfield wrote in 1998 an interesting and enlightening paper on the perspectives in optical computing [7] where he discusses this competition between optics and electronics and shows that there were three phases, first “*ignorance and underestimation*” of electronics then “*awakening and fear inferiority*” and now “*realistic acceptance that optical computing and electronics are eternal partners*”.

The purpose of this paper is to show a short history of optical computing from the origin until today. This historical overview will show that the first years generated a lot of enthusiasm regarding the potential of optics for information processing, this period was followed by a small slowdown before the golden age that started around 1980 until the beginning of the new century.

Section 2 presents the basic principles of optical information processing, Section 3 gives a historical review of the research from the first years until 1980 and Section 4 describes the research activity from 1980 to 2004. Section 5 shows the evolution of the domain until today.

2. Fundamentals of Optical Information Processing

Optical information processing is based on the idea of using all the properties of speed and parallelism of the light in

order to process the information at high-data rate. The information is in the form of an optical signal or image. The inherent parallel processing was often highlighted as one of the key advantage of optical processing compared to electronic processing using computers that are mostly serial. Therefore, optics has an important potential for processing large amount of data in real time.

The Fourier transform property of a lens is the basis of optical computing. When using coherent light, a lens performs in its back focal plane the Fourier transform of a 2D transparency located in its front focal plane. The exact Fourier transform with the amplitude and the phase is computed in an analog way by the lens. All the demonstrations can be found in a book published in 1968 by Goodman [8] and this book is still a reference in the field. The well-known generic architecture of optical processors and the architectures of the optical correlators will be presented successively.

2.1. Optical Processor Architecture. The architecture of a generic optical processor for information processing is given in Figure 1.

The processor is composed by three planes: the input plane, the processing plane, and the output plane.

The data to be processed are displayed in the input plane, most of the time this plane will implement an electrical to optical conversion. A Spatial Light Modulator (SLM) performs this conversion. The input signal can be 1D or 2D. An acousto-optic cell is often used in the case of a 1D input signal and 2D SLMs for 2D signals. The different types of 2D SLMs will be described later. In the early years, due to the absence of SLMs, the input plane consisted of a fixed slide. Therefore the principles and the potential of optical processors could be demonstrated but no real-time applications were possible, making the processor most of the time useless for real life applications.

The processing plane can be composed of lenses, holograms (optically recorded or computer generated) or nonlinear components. This is the heart of the processing, and in most optical processors, this part can be performed at the speed of the light.

A photodetector, a photodetector array or a camera composes the output plane where the results of the processing are detected.

Figure 1 shows clearly that the speed of the whole process is limited by the speed of its slowest component that is most of the time the input plane SLM, since the majority of them are operating at the video rate. The SLM is a key component for the development of practical optical processors, but unfortunately also one of their weakest components. Indeed, the poor performance and high cost of SLMs have delayed the fabrication of an optical processor for real-time applications.

2.2. Optical Processors Classical Architectures. At the beginning, real-time pattern recognition was seen as one of the

most promising application of optical processors and therefore the following two architectures of optical correlators were proposed.

Figure 2(a) shows the basic correlator called 4-f since the distance between the input plane and the output plane is four times the focal length of the lenses. This very simple architecture is based on the work of Maréchal and Croce [9] in 1953 on spatial filtering and was developed during the following years by several authors [10, 11].

The input scene is displayed in the input plane which Fourier transform is performed by Lens 1. The complex conjugated of the Fourier transform of the reference is placed in the Fourier plane and therefore multiplied by the Fourier transform of the input scene. Lens 2 performs a second Fourier transform that gives in the output plane the correlation between the input scene and the reference. Implementing a complex filter with the Fourier transform of the reference was the main challenge of this set-up, and Vander Lugt proposed in 1964 to use a Fourier hologram of the reference as a filter [12]. Figures 2(b) and 2(c) show respectively, the output correlation peak for an autocorrelation when the correlation filter is a matched filter and when it is a phase only filter [13].

In 1966, Weaver and Goodman [14] presented another optical correlator architecture, the joint transform correlator (JTC) that is represented by Figure 3(a). The two images, the reference $r(x, y)$ and the scene $s(x, y)$ are placed side by side in the input plane that is Fourier transformed by the first lens. The intensity of the joint spectrum is detected and then its Fourier transform is performed. This second Fourier transform is composed by several terms including the crosscorrelations between the scene and the reference. Using a SLM this Fourier transform can be implemented optically as shown on Figure 3(a). Figure 3(b) shows the output plane of the JTC when the reference and the scene are identical [13]. Only the two crosscorrelation peaks are of interest. To have a purely optical processor, the CCD camera can be replaced by an optical component such as an optically addressed SLM or a photorefractive crystal. One of the advantages of the JTC is that no correlation filter has to be computed, therefore the JTC is the ideal architecture for real-time applications such as target tracking where the reference has to be updated at a high-data rate.

Figures 2 and 3 represent coherent optical processors. Incoherent optical processors were also proposed: the information is not carried by complex wave amplitudes but by wave intensities. Incoherent processors are not sensitive to the phase variations in the input plane and they exhibit no coherent noise. However, the nonnegative real value of the information imposes to use various tricks for the implementation of some signal processing applications [15, 16].

Linear optical processing can be decomposed into space-invariant operations such as correlation and convolution or space-variant operations such as coordinates transforms [17] and Hough transform [18]. Nonlinear processing can also be implemented optically such as logarithm transformation, thresholding or analog to digital conversion [19].

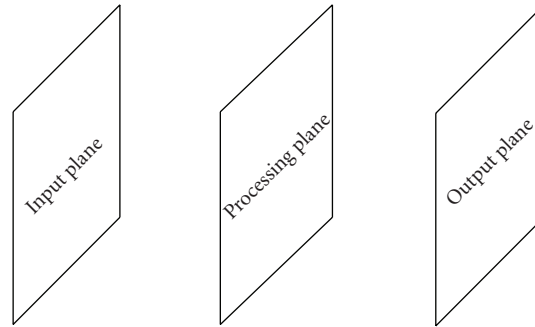


FIGURE 1: Architecture of an optical processor.

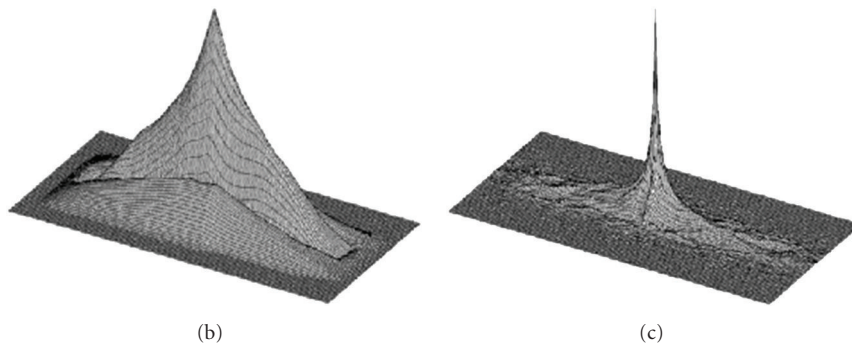
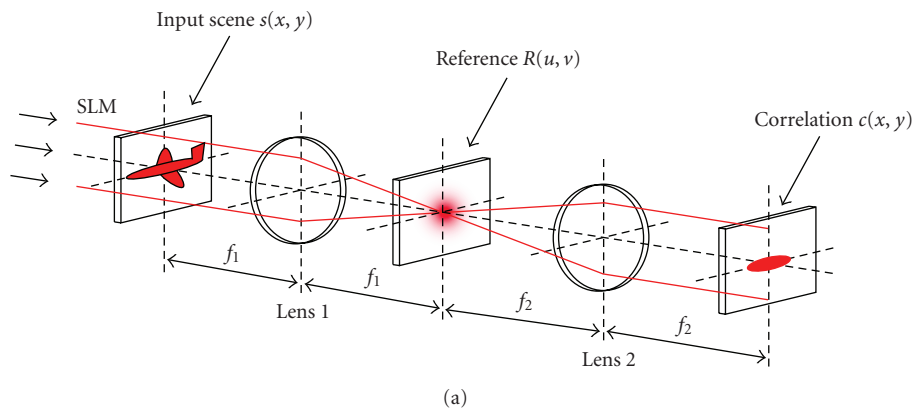


FIGURE 2: Basic 4-f correlator: (a) Optical setup. (b) Autocorrelation peak for a matched filter. (c) Autocorrelation peak for a phase only filter.

3. A New Start for Optics; the Rise of Optical Computing (1945–1980)

Information optics is a recognized branch of optics since the fifties. However, historically, the knife-edge test by Foucault in 1859 [20] can originate the optical information processing. Other contributors can be noted such as Abbe in 1873 who developed the theory of image formation in the microscope [21], or Zernike who presented in 1934 the phase contrast filter [22]. In 1946, Duffieux made a major contribution with the publication of a book on the use of the Fourier methods in optics [23]. This book was written in French and translated in English by Arsenault [24]. The work by Maréchal is another major contribution; in 1953, he demonstrated the spatial frequency filtering under a coherent illumination [9].

Optical computing is based on a new way of analyzing the optical problems; indeed, the concepts of communications and information theory constitute the basis of optical information processing. In 1952, Elias proposed to analyze the optical systems with the tools of the communication theory [25, 26]. In an historical paper [27], Lohmann, the inventor of the computer-generated holography, wrote “*In my view, Gabor’s papers were examples of physical optics, and the tools he used in his unsuccessful attempt to kill the twin image were physical tools, such as beam splitters. By contrast, Emmett (Leith) and I considered holography to be an enterprise in optical information processing. ...In our work, we considered images as information, and we applied notions about carriers from communications and information theory to separate the twin image from the desired one. In other words, our approach represented a*

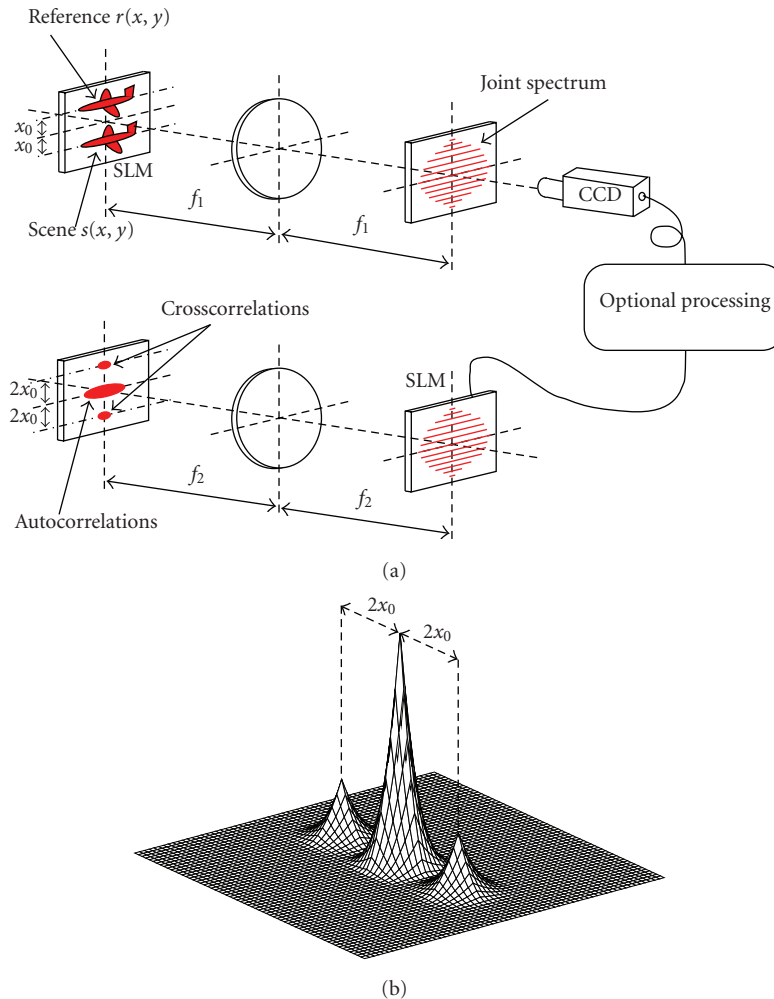


FIGURE 3: Joint transform correlator (JTC): (a) Optical setup. (b) Output plane of the JTC.

paradigm shift from physical optics to optical information processing."

Holography can be included into the domain of information optics since both fields are closely related and progressed together. As for holography invented by Gabor in 1948 [28], the development of optical image processing was limited until the invention of a coherent source of light, the laser, in 1960 [29, 30].

The history of the early years of optical computing was published by major actors of the field; for example, in 1974 by Vander Lugt [31] and in 2000 by Leith [32]. Vander Lugt presents in his paper a complete state-of-the-art for coherent optical processing with 151 references. Several books give also a good overview of the state of the art at the time of their publication [1–3, 33].

It is possible to distinguish two periods of time. First until the early seventies, there was a lot of enthusiasm for this new field of optics and information processing, all the basic inventions were made during this period and the potential of optics was very promising for real-time data processing. However real life optical processors were rare due to technological problems particularly with the

SLMs. During the seventies, the research was more realistic with several attempts to build optical processors for real applications [2, 3], and the competition with the computers was also much harder due to their progress [32].

3.1. The Funding Inventions. As soon as the laser was invented in 1960, optical information processing was in rapid expansion and all the major inventions of the field were made before 1970. In the Gabor hologram the different terms of the reconstruction were all on the same axis and this was a major drawback for the display. In 1962, Leith and Upatnieks introduced the off axis hologram that allowed the separation of the different terms of the reconstruction giving remarkable 3D reconstructions [34, 35]. This was the start of the adventure of practical holography.

In 1963, Vander Lugt proposed and demonstrated a technique for synthesizing the complex filter of a coherent optical processor using a Fourier hologram technique [12]. This invention gave to the 4-f correlator, with the matched filter or other types of filter, all its power and generated all the research in the domain. In 1966, Weawer and Goodman presented the Joint Transform Correlator (JTC) architecture

that will be widely used [14] as an alternative to the 4-f correlator for pattern recognition.

In 1966, Lohmann revolutionized holography by introducing the first computer generated hologram (CGH) [36, 37] using a cell oriented encoding adapted to the limited power of the computers available at this time. This is the start of a new field and different cell oriented encodings were developed in the seventies. In 1969, a pure phase encoded CGH, the kinoform was also proposed [38] opening the way to the modern diffractive optical elements with a high diffraction efficiency. A review of the state of the art of CGHs in 1978 was written by Lee [39]. Until 1980, the CGHs encoding methods were limited by the power of the computers.

Character recognition by incoherent spatial filtering was introduced in 1965 by Armitage and Lohmann [40] and Lohmann [41]. A review of incoherent optical processing was made by Rhodes and Sawchuk in 1982 [15].

3.2. The Early Spatial Light Modulators. As already emphasized, a practical real-time optical processor can be constructed only if it is possible to control with the SLM, the amplitude and the phase modulation of the input plane or of the filter plane (in the case of a 4-f correlator). A very large number of SLMs have been investigated over the years, using almost all possible physical properties of matter to modulate light, but only few of them have survived and are now industrial products. A review of the SLMs in 1974 can be found in chapter 5 of the book written by Preston [1].

From the beginning, SLMs have primarily been developed for large screen display. Some of the early SLMs were based on the Pockels effect and two devices were very promising: the Phototitus optical converter with a DKDP crystal was used for large screen color display and also for optical pattern recognition, however the crystal had to work at the Curie point (-50°C) [42, 43]; the Pockels Readout Optical Modulator (PROM) was used for optical processing [44, 45], but it was limited as it required blue light for writing and red light for readout. All these devices have disappeared, killed by their limitations.

The liquid crystal technology has survived and is today the mostly used technology for SLMs. The first Liquid Crystal SLMs were developed in the late sixties, for example, an electrically addressed liquid crystal matrix of 2×18 elements [46]. Then the matrix size increased and in 1975, a 128×128 matrix addressed SLM was constructed by LETI in France [47]. This device was using a nematic liquid crystal and had a pixel pitch of $300 \mu\text{m}$, of cell thickness of $8 \mu\text{m}$, and the addressing signals were 120 V root mean square (RMS) and 10 V RMS (Figure 4). In 1978, Hughes Corp. developed a very successful optically addressed liquid crystal SLM or valve that was used in optical processors for more than 10 years [48–50]. However this SLM was very expensive, it has a 40 line pairs per millimeter resolution, its speed was limited to the video rate, and since it was optically addressed it had to be coupled to a cathode ray tube (CRT) making it particularly bulky if the input signal was electrical (Figure 5).



FIGURE 4: 128×128 electrically addressed liquid crystal SLM constructed by LETI (France) in 1975.



FIGURE 5: Optically addressed liquid crystal light valve manufactured by Hughes Corp in 1978. The photo shows the light valve coupled to a CRT.

Other types of SLMs were developed in the seventies, such as deformable membrane SLMs which were presented by Knight [51] in a critical review of the SLMs existing in 1980. He pointed out that, due to their limitations in 1980, they had only a limited use in coherent optical processing applications. However, this SLM technology is still used today for adaptive optics.

In conclusion, at the end of the seventies, despite all the research effort, no SLM really suited for real-time optical information processing was available.

3.3. A Successful Application: Radar Signal Optical Processing. The first coherent optical processor was dedicated to the processing of synthetic aperture radar (SAR) data. This first major research effort in coherent optical processing was initiated in 1953 at the University of Michigan under

contracts with the US Army and the US Air Force [10, 11]. The processor has evolved successfully with different improved versions until the beginning of the seventies. The book by Preston [1] as well as the reference paper by Leith will give to the reader an overview on the subject [32]. Since the first processor was designed before the invention of the laser, it was powered by light generated by a mercury lamp. The system was not operating in real time, the input consisted of an input film transport which carried a photographic recording of incoming radar signals, the processing was carried out by a conical lens and the output was a film. At the beginning of the seventies, the digital computers were able to compete successfully with the coherent optical computers for SAR applications and finally they won and this was sadly the end of radar signal optical processing.

3.4. The Future of Optical Information Processing as Seen in 1962. In order to understand the evolution of optical computing, it is enlightening to see the topics of discussions in the early sixties. For example, in October 1962, a “Symposium on Optical Processing of Information” was held in Washington DC, cosponsored by the Information System Branch of the Office of Naval Research and the American Optical Company. About 425 scientists attended this meeting and Proceedings were published [52]. The preface of the proceedings shows that the purpose of this symposium was to bring together researchers from the fields of optics and information processing. The authors of the preface recognize that optics can be used for special-purpose optical processors in the fields of pattern recognition, character recognition, and information retrieval, since optical systems offer in these cases the ability to process many items in parallel. The authors continue with the question of a general-purpose computer. They write: “*Until recently, however, serious consideration has not been given to the possibility of developing a general-purpose optical computer. With the discovery and application of new optical effects and phenomena such as laser research and fiber optics, it became apparent that optics might contribute significantly to the development of a new class of high-speed general-purpose digital computers*”. It is interesting to list the topics of the symposium: optical effects (spatial filtering, laser, fiber optics, modulation and control, detection, electroluminescent, and photoconductive) and data processing (needs, biological systems, bionic systems, photographic, logical systems, optical storage systems, and pattern recognition). It can be noted, that one of the speakers, Teager [53] from MIT, pointed out that for him the development of an optical general-purpose computer was highly premature because the optical technology was not ready in order to compete with the electronic computers. For him, the optical computers will have a different form than the electronic computers; they will be more parallel. It is interesting to see that this debate is now almost closed, and today, 47 years after this meeting, it is widely accepted that a general-purpose pure optical processor will not exist but that the solution is to associate electronics and optics and to use

optics only if it can bring something that electronic cannot do.

3.5. Optical Memory and the Memory of the Electronic Computers. It is useful to replace the research on optical memories in the context of the memories available in the sixties. At this time the central memory of the computers was a core memory and compact memory cells were available using this technology. However, the possible evolution of this technology was limited. The memory capacity was low, for example, the Apollo Guidance Computer (AGC), introduced in 1966, and used in the lunar module that landed on the moon, had a memory of 2048 words RAM (magnetic core memory), 36864 words ROM (core rope memory), with 16-bit words. In October 1970, Intel launched the first DRAM (Dynamic Random Access Memory) the Intel 1103 circuit. This chip had a capacity of one Kbit using P-channel silicon gate MOS technology with a maximum access time of 300 ns and a minimum write time of 580 ns. This chip killed the core memory.

Compared to the memories that were available, optical memories had two attractive features: a potential high density and the possibility of parallel access. Already in 1963, van Heerden developed the theory of the optical storage in 3D materials [54]. In 1968 the Bell Labs constructed the first holographic memory [55] with a holographic matrix of 32 by 32 pages of 64 by 64 bits each. In 1974, d’Auria et al. from Thomson-CSF [56] constructed the first complete 3D optical memory system storing the information into a photorefractive crystal with angular multiplexing and achieving the storage of 10 pages of 10^4 bits. Holographic memories using films were also developed in the US. Synthetic holography has been applied to recording and storage of digital data in the Human Read/Machine Read (HRMR) system developed by Harris Corporation in 1973 for Rome Air Development Center [57].

3.6. Optical Fourier Transform Processors, Optical Pattern Recognition. Optical pattern recognition was from the beginning a prime choice for optical processing since it was using fully the parallelism of optics and the Fourier transform properties. The book edited by Stark [3] in 1982 gives a complete overview of the state of the art of the applications of optical Fourier transforms. It can be seen that coherent, incoherent; space-invariant, space-variant; linear, nonlinear architectures were used for different applications. Hybrid processors, optical/digital emerged as a solution for practical implementation and for solving real problems of data processing and pattern recognition. For example, Casasent, who was very active in this field, wrote a detailed book chapter [58] with a complete review of hybrid processors at the beginning of the eighties. All these processors gave very promising results. Almost all the proposed processors remained laboratory prototypes and never had a chance to replace electronic processors, even if at that time, electronics and computers were much less powerful. There are many reasons for this; the number of applications that could benefit from the speed of optical

processors was perhaps not large enough, but the main reason was the absence of powerful, high speed, high quality, and also affordable SLMs, for the input plane of the processor as well as for the filter plane. Optical processors are also less flexible than digital computers that allow a larger number of data manipulations very easily.

4. Optical Computing Golden Age (1980–2004)

This period of time could be called the optical computing golden age. There was a lot of enthusiasm in the field, the future looked very bright, there was funding for the programs on the topic and the research effort was very intensive worldwide. Every year, several international conferences were organized by different international societies on subjects related to optical computing. The journals had frequently a special issue on the topics and *Applied Optics* had every 10th of month an issue entitled “Information Processing”. The research was very fruitful in all the domains of optical information processing including theoretical work on algorithms, analog and digital computing, linear and non-linear computing. Optical correlators for real applications were even commercialized. However, around 2000, we could feel that the interest for the subject started to decline. The reasons are multiple, but the evolution of digital computers in term of performance, power and also flexibility can be pointed out. They are also very easy to use even for a non-specialist.

It is impossible to list here all the work carried out in the domain from 1980 to 2004. Several books give the state of the art of the domain at the time of their publication [4, 6, 59].

In the following, we will describe only some aspects of the research during this period, and we apologize for some important results that may be missing. The purpose is to give to reader an idea of the evolution of the domain during this quarter century.

4.1. From Computer Generated Holograms to Diffractive Optical Elements. CGHs are important components for optical processing since they can process the information. The first CGHs were mostly cell-oriented since these methods were well adapted to the power of the computers with a small memory capacity and to the technology of the printers of this time. In the eighties, the technological landscape has changed, more powerful computers with a larger memory capacity were available, e-beam writers were more commonly used. Therefore new encoding methods, the point-oriented methods, were developed in order to achieve high quality and high diffraction efficiency optical reconstructions of the CGHs. First, the error diffusion algorithm, used for printing applications, was adapted to encode CGHs where it was possible to separate the noise from the desired pattern in the reconstruction plane [60]. Then, iterative algorithms were proposed and the best known are the Direct Binary Search (DBS) algorithm proposed by Seldowitz et al. in 1987 [61] and the Iterative Fourier Transform Algorithm (IFTA) proposed by Wyrowski and Bryngdahl in 1988 [62]. The CGHs encoded with these algorithms produce

a reconstruction with a high Signal to Noise Ratio and a high diffraction efficiency, especially in the case of pure phase CGHs. Later some refinements were proposed, for example the introduction of an optimal multicriteria approach [63, 64]. It should be noted that these iterative methods are still used.

In the nineties, the main progress concerns the fabrication methods with the use of lithographic techniques allowing the fabrication of high precision phase only components etched into quartz. The name Diffractive Optical Elements (DOEs) that includes the CGHs is now used and reflects this evolution.

Thank to the progress in lithography, submicron DOEs can be fabricated such as a polarization-selective CGH [65], artificial dielectrics [66], a spot generator [67]. The state of the art of digital nano-optics can be found in Chapter 10 of the book written by Kress and Meyrueis [68]. The nano structures fabrication required new studies of the diffraction based on the rigorous theory of diffraction instead of the scalar theory of diffraction [69].

Several books give a complete overview of the field of DOEs and their applications [68, 70] and a very complete paper on the evolution of diffractive optics was published in 2001 by Mait [71].

4.2. The Maturity of Spatial Light Modulators. Since the availability of SLMs was an important issue for the success of optical information processing, a lot of effort has been invested after 1980 into the development of SLMs fulfilling the optical processors requirements in terms of speed, resolution, and size and modulation capability. A paper written by Fisher and Lee gives the status of the 2D SLM technology in 1987 [72] and shows that, at this time, the best feasible SLM performance values are found to include: about 100×100 resolution elements, 10-Hz framing rates, 1-s storage, less than $50 \mu\text{J}/\text{cm}^2$ sensitivity, five-level dynamic range, and 10-percent spatial uniformity. Updated reviews of the state of the art of SLMs is given in a book edited by Efron [73] in 1995 and in several special issues of “*Applied Optics*” [74–77].

More than 50 types of SLM have been introduced in the eighties and nineties [78]. Many different SLMs have been proposed and many prototypes fabricated—for example, besides liquid crystal SLMs, magneto-optic SLMs [79, 80], multiple quantum wells devices (MQW) [81], Si PLZT SLMs [82] and Deformable Mirror Devices [83, 84]. However very few of these SLMs have survived. Therefore, today, among the SLMs commercially available, mostly for display purpose, two technologies prevail: liquid crystal technology and Digital Micromirrors Devices DMD (MEMS based technology).

There are different types of liquid crystal SLMs. Twisted nematic liquid crystal SLMs are commonly used and their theory and experimental characterization show an amplitude and phase coupled modulation [85] as well as an operating speed limited to the video rate. Ferroelectric liquid crystal SLMs can reach a speed of several kilohertz, but most of the devices on the market are binary bistable devices

that consequently limit the applications. Although it is not so commonly known, analog amplitude only modulation is possible with specific ferroelectric SLMs [86]. Nematic liquid crystal or Parallel Aligned liquid (PAL) crystal SLMs produce a pure phase modulation that can exceed 2π . They are particularly attractive for applications requiring a high light efficiency such as dynamic diffractive optical elements. Their speed can reach 500 Hz [86]. The matrix electrically addressed SLMs using twisted nematic liquid crystal have progressed considerably. Around 1985, the small LC TV screens were extensively evaluated [87, 88], but their poor performance (phase nonuniformity, limited resolution, etc.) limited their use for optical computing; then VGA, SVGA, and XGA resolution SLMs were introduced in video projectors and these SLMs extracted from the video projectors were widely characterized [89] and integrated into optical processors. During the same period, high performance optically addressed SLMs were fabricated, for example, the PAL SLM from Hamamatsu [90]. Now high resolution Liquid Crystal on Silicon (LCoS) SLMs are commercially available, for example an pure phase LCoS SLM with 1920×1080 pixel resolution is commercialized [91]. All these SLMs must be characterized very precisely and numerous papers were published on the subject [92–95].

In conclusion, today, for the first time since the origin of the optical processors, commercially available SLMs are fulfilling the requirements in terms of speed, modulation capability, and resolution. The applications of SLMs are numerous, for example, recent papers have reported different applications of LCoS SLMs, such as pulse shaping [96], quantum key distribution [97], hologram reconstruction [98], computer generated holograms [99], DOEs [100], optical tweezers [101], optical metrology [102].

4.3. Optical Memories. In a parallel optical computer, a parallel access optical memory is required in order to avoid the bottleneck between the parallel processor and the memory. Therefore the research for developing a 3D parallel access optical memory was very active in the last two decades of the last century. Different architectures using different technologies were proposed. For example, Marchand et al. constructed in 1992 a motionless-head parallel readout optical-disk system [103] achieving a maximum data rate of 1.2 Gbyte/s. Psaltis from Caltech developed a complete program of research on 3D optical holographic memories using different materials such as photorefractive crystals. In the frame of this program, Mok et al. achieved to store 10000 holograms of 440 by 480 pixels [104] into a photorefractive crystal of 3 cm^3 . IBM was also very active into the field of holographic memory [105] and two important programs of the Darpa were carried out in the nineties: project PRISM (Photorefractive Information Storage Material), and project HDSS (Holographic Data Storage Systems). All the information on these holographic memories can be found in a book [106]. Several start-up companies were created for developing holographic memories and most of them disappeared. However one of them, In Phase Technologies, is now commercializing a holographic WORM disk memory

system using a photopolymer material [107]. Other types of optical memories were investigated such as a two-photon memory [108], spectral hole burning [109].

Today the holographic memory is still seen as a candidate for the memory of the future, however the problem of the recording material is not yet solved; particularly there is no easy to use and cheap rewritable material. The photopolymers can only be written once and despite all the research effort photorefractive crystals are still very difficult to use and expensive.

4.4. Optical Information Processing, Optical Pattern Recognition. The last two decades of the last century were a very intensive period for the research in optical processing and optical pattern recognition. All the aspects of these processors were investigated and the research progressed remarkably.

One key element in an optical correlator is the reference filter, and important part of the research concentrated on it. The correlation is shift-invariant but is scale-variant and orientation-variant. Therefore several solutions, using for example, Synthetic Discriminant Function (SDF) were proposed to overcome this drawback [110–112]. Beside the classical matched filter, several other improvements have been presented [113–117]. A large amount of work has been carried out to enhance the discrimination of the target in a complex scene [118].

The architecture of the JTC was also studied extensively, particularly by Javidi who proposed several improvements such as the nonlinear JTC [119–122].

A very large number of processors were constructed taking advantage of the progress of SLMs and of the theoretical work on the filters and on the architectures. Some of these processors stayed in the laboratories while some others were tested for real applications. Regarding the large number of optical processors that were constructed during this period of time, it is impossible to list them all in the frame of this paper. A book, written in French, by Tribillon gives a very complete state of the art of the optical pattern recognition in 1998 [5]. The book edited in 1999 by Yu and Yin give also a complete overview on the topic [123]. Therefore, you will find here only, some examples of the optical processors developed between 1980 and 2004.

In 1982, Cleland et al. constructed an optical processor for detecting tracks in a high-energy physics experiment. This incoherent processor was using a matrix of LEDs as input plane and a matrix of kinoforms as processing plane. It was used successfully in a real high-energy physics experiment in Brookhaven [124, 125].

The Hough transform is a space-variant operation for detecting the parameters of curves [126]. This transform can take fully advantage of the parallelism of the optical implementation. In 1986, Ambs et al. constructed an optical processor based on a matrix of 256×256 optically recorded holograms [18, 50]. This implementation was improved ten years later with the use of a large scale DOE composed of a matrix of 64 by 64 CGHs with 4 phase levels fabricated by lithographic techniques [127].

Several other optical implementations of the Hough transform were published. Casasent proposed several different optical implementations for example one using an acousto-optics cell [128]. A coherent optical implementation of Hough transform has been discussed by Eichmann and Dong [129], where the 2D space-variant transfer function is implemented by successively performing 1D space-invariant transforms by rotating the input image around its center point and translating a film plane for recording. Another implementation for coherent or incoherent light was proposed by Steier and Shori [130] where they use a rotating Dove prism to rotate the input image, and the detection is achieved by a linear detector array. Today the Hough transform is widely used in image processing for detecting parametrical curves, but the implementation is electronic.

Yu et al. proposed several optical processors for pattern recognition using different types of input SLMs [131]. For example an adaptive joint transform correlator for autonomous real-time object tracking [132], an optical disk based JTC [133].

Pu et al. constructed a robot that achieved real-time navigation using an optoelectronic processor based on a holographic memory [134].

Thomson-CSF in France, in the frame of a European project, constructed and tested successfully a compact photorefractive correlator for robotic applications. The size of the demonstrator was 600 mm × 300 mm, it was composed of a mini-YAG laser, a liquid crystal SLM and an updatable holographic BSO crystal [135]. This correlator was also used for finger print identification [136].

Guibert et al. constructed an onboard optical JTC for real-time road sign recognition that was using a nonlinear optically addressed ferroelectric liquid crystal SLM in the Fourier plane [137].

A miniature Vander Lugt optical correlator has been built around 1990 by OCA (formerly Perkin-Elmer). This correlator was composed of a Hughes liquid crystal valve, a set of cemented Porro prisms and a holographic filter. The purpose of this processor was to demonstrate this technology for autonomous missile guidance and navigation. The system was correlating on aerial imagery and guided the missile to its preselected ground target. The processor was remarkable by its rugged assembly; it was 105 mm in diameter, 90 mm long, and weighted 2.3 kg [138].

In 1995, OCA constructed a prototype of an optical correlator that was fitting in the PCI slot of a personal computer and was able to process up to 65 Mbyte of image data per second [139]. This processor was intended to be commercialized.

The Darpa in the USA launched in 1992 a project named TOPS (Transitioning of Optical Processing into Systems) associating some universities and about ten important companies potential users and developers of the technology.

BNS presented in 2004 an optical correlator using four kilohertz analog spatial light modulators. The processor was limited to 979 frames per second by the detection camera. However, the rest of the correlator was capable of 4,000 frames per second [140].

The Jet Propulsion Laboratory (JPL) developed several optical processors for real time automatic target recognition [141]. The University of Sussex constructed also an all-optical correlator and a hybrid digital-optical correlator [142].

It should also be noted that several optical correlators were available commercially but it is not sure that it was a commercial success since most of them are no longer commercialized. For example, in 2000, optical correlators were commercialized by INO [143] and BNS [86]. In 2001, Parrein listed in her PhD thesis 10 optical correlators that were available [144].

Optical processors were also designed for many other operations such as matrix operations [145], or for systolic array processing [146] and neural network processors [147].

4.5. Digital Optical Computing. The optical processors described in the previous sections were analogue. However, in order to compete more efficiently with the digital electronic computers, a very important research effort was directed toward digital optical computing. Again, the field of digital optical computing is extremely broad, and the results obtained are too numerous to be described in the frame of this paper. The interested reader will find several books on the subject, for example, [148, 149]. The proceedings of the numerous conferences dedicated on optical computing are also very instructive. For example, the proceedings of the ICO conference "Optical Computing" held in Edinburgh in 1994 show very well the situation of digital and analog optical computing [150]. Novel optical components such as vertical-cavity surface-emitting lasers (VCSELs) or symmetric self-electro-optic-effect devices (SEED) [151] were studied and constructed. Several digital optical computers were proposed, for example, Guilfoyle and Stone constructed a 32-bit, fully programmable digital optical computer (DOC II) designed to operate in a UNIX environment running RISC microcode [152].

4.6. Optical Interconnects. Optical interconnects is a field where optics has a great potential, these interconnects can be guided but also in free space. All the aspects of optical interconnections were studied: components (switches, sources, detectors, etc.), architectures, routing algorithms, and so forth. In 1989, Goodman wrote a complete analysis on optics as an interconnect technology [153] and a brief historical summary of the development of the field of optical interconnect to silicon integrated circuits can be found in a paper written by Miller in 2000 [154]. A very large number of papers were published in the nineties on the subject, for example, on optical perfect shuffle [155], on hypercube-based optical interconnects [156], on crossbar networks [157, 158], on the use of liquid crystal SLMs for optical interconnects [159], on diffractive optics for optical interconnects [160], on holographic interconnection networks and their limitations [161], on board-level interconnects [162].

Today, optics has no challenger in the domain of telecommunications with the optical fibers and optical

cables, the Wavelength-division multiplexing (WDM), the optical amplifiers and the switches based on MEMs.

In 2009, Intel is still studying the possibility of replacing electrical interconnects between chips by optical interconnects with its terahertz bandwidth, low loss, and low cross-talk [163]. Miller published also in 2009 a paper on the device requirements for optical interconnects to silicon chips where he pointed out the need of very-low-energy optoelectronic devices and novel compact optics [164].

5. Optical Computing Today

The traditional field of optical computing is no longer so active, it is not dead but it has evolved. Today, numerous research topics benefit from the results of the research in optical computing and therefore the field is perhaps no longer so well defined. Several signs show that the activity has changed. Applied Optics has no longer an issue per month on the subject, but in each issue there is a section "Information processing" with an average of only 4 papers per issue. There are no longer specialized large international conferences named "Optical Computing". However, it should be noted that there are still two conferences organized by the SPIE on the subject: "Optical Pattern Recognition" since 20 years in Orlando in the frame of the SPIE conference "Defense, Security, Sensing", and "Optics and Photonics for Information Processing" in San Diego in the frame of the SPIE conference "Optics and Photonics". In August 2009, a special section on "Optical High-Performance Computing" was published in Applied Optics and JOSA A [165].

The research on optical correlators is continued by fewer research teams, however it should be noted that the Jet Propulsion Laboratory (JPL) is still working on optical correlators for real time automatic target recognition [141].

Some of the algorithms developed for pattern recognition initially for optical processing are now used successfully in digital computers. DOEs are now mature and are part of numerous industrial products. All the research on the fabrication of DOEs made possible the fabrication of nano structures and very exciting new fields of research such as nanophotonics [166, 167], nanofluidics [168] and optofluidics [169]. The list of the papers presented in 2009 at the SPIE conference "Optics and Photonics" reflects the growing interest in all the research related to nanoscience and nanooptics.

Biophotonics is an exponentially growing field that is largely benefiting from the past research in optical processing. Typical examples are the optical tweezers and the optical trapping [170, 171].

Thanks to the digital holography, where the holographic plate is replaced by a camera, holography is again finding industrial applications particularly for the quality control of manufactured products [172–174], for digital holographic microscopy [175] opening completely new fields of applications for optical microscopy.

For information processing, optics is also finding a place where it has a unique feature such as the polarimetric imaging [176–178], or multispectral imaging [179]. Security

applications is also a promising field for optical information processing [180]. It is well known that optics is used commonly for the communication systems.

This list is too short to reflect all the optical processing evolution and its implications in the research of the future.

6. Conclusions

The history of the development of the research in the field of optical computing reveals an extraordinary scientific adventure. It started with the processing power of coherent light and particularly its Fourier transform capability. The history shows that considerable efforts were dedicated to the construction of optical processors that could process in real time a large amount of data. Today, we see that optics is very successful in information systems such as communications and memories compared to its relative failure in computing. This could have changed, if, in the seventies when the electronic computers were slow and with a limited power, today components such as efficient SLMs, laser diodes or high speed and high resolution detectors would have been available. However, all the research results in optical computing contribute strongly to the development of new research topics such as biophotonics, nanophotonics, optofluidics, and femtosecond nonlinear optics. But, the dream of an all optical computer overcoming the digital computer never became reality, and optical correlators for pattern recognition have almost disappeared. The reasons are multiple. The speed of the optical processor was always limited by the speed of the input and output devices. Digital computer have progressed very rapidly, the Moore's law is still valid, multi-core processors are more powerful, and it is clear that digital computer are easier to use and offers more flexibility. Digital computers have progressed faster than optical processors. Optical computing is mostly analogue when electronic computing is digital. The digital optical computers were not able to compete with the electronic due to the lack of appropriate optical components. It appears clearly that the solution is to associate optics and electronics and to use optics only when it can bring something that electronics cannot do. Optical processing is useful when the information is optical and that no electronics to optics transducers are needed.

The potential of optics for parallel real time processing remains and the future will tell if optical computing will be back, for example, by using nanotechnologies.

References

- [1] K. Preston, *Coherent Optical Computers*, McGraw-Hill, New York, NY, USA, 1972.
- [2] S. H. Lee, *Optical Information Processing Fundamentals*, Springer, Berlin, Germany, 1981.
- [3] H. Stark, *Application of Optical Fourier Transform*, Academic Press, Orlando, Fla, USA, 1982.
- [4] H. H. Arsenault, T. Szoplik, and B. Macukow, *Optical Processing and Computing*, Academic Pres, San Diego, Calif, USA, 1989.

- [5] J.-L. Tribillon, *Traitement Optique de l'Information & Reconnaissance des Formes par Voie Optique*, Teknea, Toulouse, France, 1998.
- [6] J. Shamir, *Optical Systems and Processes*, SPIE Press, Bellingham, Wash, USA, 1999.
- [7] H. J. Caulfield, "Perspectives in optical computing," *Computer*, vol. 31, no. 2, pp. 22–25, 1998.
- [8] J. W. Goodman, *Introduction to Fourier Optics*, McGraw-Hill, San Francisco, Calif, USA, 1968.
- [9] A. Maréchal and P. Croce, "Un filtre de fréquences spatiales pour l'amélioration du contraste des images optiques," *Comptes Rendus de l'Académie des Sciences*, vol. 237, no. 12, pp. 607–609, 1953.
- [10] L. J. Cutrona, E. N. Leith, C. J. Palermo, et al., "Optical data processing and filtering systems," *IRE Transactions on Information Theory*, vol. 6, no. 3, pp. 386–400, 1960.
- [11] E. O'Neill, "Spatial filtering in optics," *IRE Transactions on Information Theory*, vol. 2, no. 2, pp. 56–65, 1956.
- [12] A. Vander Lugt, "Signal detection by complex filtering," *IEEE Transactions on Information Theory*, vol. 10, no. 2, pp. 139–145, 1964.
- [13] L. Bigué, *Reconnaissance des formes en temps réel par voie optique: étude comparative d'implantations optiques de filtres de corrélation. Application au corrélateur optique à transformée de Fourier conjointe*, Ph.D. thesis, Université de Haute Alsace, 1996.
- [14] C. S. Weaver and J. W. Goodman, "A technique for optically convolving two functions," *Applied Optics*, vol. 5, no. 7, pp. 1248–1249, 1966.
- [15] W. T. Rhodes and A. A. Sawchuk, "Incoherent optical processing," in *Optical Information Processing Fundamentals*, S. H. Lee, Ed., pp. 69–110, Springer, Heidelberg, Germany, 1981.
- [16] E. Leith, "Incoherent optical processing and holography," in *Optical Processing and Computing*, H. H. Arsenault, T. Szoplik, and B. Macukow, Eds., pp. 421–440, Academic Press, San Diego, Calif, USA, 1989.
- [17] J. W. Goodman, "Linear space-variant optical data processing," in *Optical Information Processing Fundamentals*, S. H. Lee, Ed., pp. 235–260, Springer, Berlin, Germany, 1981.
- [18] P. Ambs, S. H. Lee, Q. Tian, et al., "Optical implementation of the Hough transform by a matrix of holograms," *Applied Optics*, vol. 25, no. 22, pp. 4039–4045, 1986.
- [19] S. H. Lee, "Nonlinear optical processing," in *Optical Information Processing Fundamentals*, S. H. Lee, Ed., pp. 261–303, Springer, Berlin, Germany, 1981.
- [20] L. Foucault, "Mémoire sur la construction des télescopes en verre argenté," *Annales de l'Observatoire Imperial de Paris*, vol. 5, pp. 197–237, 1859.
- [21] E. Abbe, "Beiträge zur Theorie des Mikroskops und der mikroskopischen Wahrnehmung," *Archiv für Mikroskopische Anatomie*, vol. 9, pp. 413–468, 1873.
- [22] F. Zernike, "Diffraction theory of the knife-edge test and its improved form, the phase-contrast method," *Monthly Notices of the Royal Astronomical Society*, vol. 94, pp. 377–384, 1934.
- [23] P.-M. Duffieux, *L'Intégrale de Fourier et ses Applications à l'Optique*, Faculté des Sciences Besançon, Chez l'Auteur, France, 1946.
- [24] P.-M. Duffieux, *The Fourier Transform and Its Applications to Optics*, John Wiley & Sons, New York, NY, USA, 1983.
- [25] P. Elias, "Optics and communication theory," *Journal of Optical Society of America*, vol. 43, no. 4, pp. 229–232, 1953.
- [26] P. Elias, D. S. Grey, and D. Z. Robinson, "Fourier treatment of optical processes," *Journal of Optical Society of America*, vol. 42, no. 2, pp. 127–132, 1952.
- [27] A. W. Lohmann, "A pre-history of computer-generated holography," *Optics & Photonics News*, vol. 19, no. 2, pp. 36–47, 2008.
- [28] D. Gabor, "A new microscopic principle," *Nature*, vol. 161, no. 4098, pp. 777–778, 1948.
- [29] T. H. Maiman, "Stimulated optical radiation in ruby," *Nature*, vol. 187, no. 4736, pp. 493–494, 1960.
- [30] T. H. Maiman, "Optical and microwave-optical experiments in ruby," *Physical Review Letters*, vol. 4, no. 11, pp. 564–566, 1960.
- [31] A. Vander Lugt, "Coherent optical processing," *Proceedings of the IEEE*, vol. 62, no. 10, pp. 1300–1319, 1974.
- [32] E. N. Leith, "The evolution of information optics," *IEEE Journal on Selected Topics in Quantum Electronics*, vol. 6, no. 6, pp. 1297–1304, 2000.
- [33] Y. E. Nesterkhin, G. W. Stroke, and W. E. Kock, *Optical Information Processing*, Plenum Press, New York, NY, USA, 1976.
- [34] E. N. Leith and J. Upatnieks, "Wavefront reconstruction with continuous-tone objects," *Journal of Optical Society of America*, vol. 53, no. 12, pp. 1377–1381, 1963.
- [35] E. N. Leith and J. Upatnieks, "Wavefront reconstruction with diffused illumination and three-dimensional objects," *Journal of Optical Society of America*, vol. 54, no. 11, pp. 1295–1301, 1964.
- [36] B. R. Brown and A. W. Lohmann, "Complex spatial filtering with binary masks," *Applied Optics*, vol. 5, no. 6, pp. 967–969, 1966.
- [37] W. Lohmann and D. P. Paris, "Binary Fraunhofer holograms, generated by computer," *Applied Optics*, vol. 6, no. 10, pp. 1739–1748, 1967.
- [38] L. B. Lesem, P. M. Hirsch, and J. A. Jordan Jr., "The kinoform: a new wavefront reconstruction device," *IBM Journal of Research and Development*, vol. 13, no. 2, pp. 150–155, 1969.
- [39] W. H. Lee, "Computer-generated holograms: techniques and applications," in *Progress in Optics XVI*, E. Wolf, Ed., pp. 118–232, North-Holland, Amsterdam, The Netherlands, 1978.
- [40] J. D. Armitage and A. W. Lohmann, "Character recognition by incoherent spatial filtering," *Applied Optics*, vol. 4, no. 4, pp. 461–467, 1965.
- [41] A. W. Lohmann, "Incoherent optical processing of complex data," *Applied Optics*, vol. 16, no. 2, pp. 261–263, 1977.
- [42] D. Casasent and T. K. Luu, "Photo-DKDP light valve in optical data processing," *Applied Optics*, vol. 18, no. 19, pp. 3307–3314, 1979.
- [43] F. Dumont, J. P. Hazan, and D. Rossier, "The phototitus optical converter," *Philips Technical Review*, vol. 34, no. 10, pp. 274–287, 1974.
- [44] S. Iwasa, "Optical processing: near real-time coherent systems using two Itek PROM devices," *Applied Optics*, vol. 15, no. 6, pp. 1418–1424, 1976.
- [45] D. S. Oliver, "Real time spatial light modulators for optical/digital processing systems," *Optical Engineering*, vol. 17, no. 3, pp. 288–294, 1978.
- [46] B. J. Lechner, F. J. Marlowe, M. E. Nester, and J. Tufts, "Liquid crystal matrix displays," *Proceedings of the IEEE*, vol. 59, no. 11, pp. 1566–1579, 1971.
- [47] G. Labrunie, J. Robert, and J. Borel, "A 128 × 128 electro-optical interface for real time data processing," *Revue de Physique Appliquée*, vol. 10, pp. 143–146, 1975.

- [48] W. P. Bleha, L. T. Lipton, E. Wiener-Avnear, et al., "Application of the liquid crystal light valve to real-time optical data processing," *Optical Engineering*, vol. 17, no. 4, pp. 371–384, 1978.
- [49] D. Casasent, "Performance evaluation of spatial light modulators," *Applied Optics*, vol. 18, no. 14, pp. 2445–2453, 1979.
- [50] P. Ambs, Y. Fainman, S. H. Lee, et al., "Computerized design and generation of space-variant holographic filters. 1: system design considerations and applications of space-variant filters to image processing," *Applied Optics*, vol. 27, no. 22, pp. 4753–4760, 1988.
- [51] G. R. Knight, "Interface devices and memory materials," in *Optical Information Processing Fundamentals*, S. H. Lee, Ed., pp. 111–179, Springer, Berlin, Germany, 1981.
- [52] D. K. Pollock, C. J. Koester, and J. T. Tippett, *Optical Processing of Information*, Spartan Books, Baltimore, Md, USA, 1963.
- [53] H. M. Teager, "Parallel organized optical computers," in *Optical Processing of Information*, D. K. Pollock, C. J. Koester, and J. T. Tippett, Eds., pp. 13–19, Spartan Books, Washington, DC, USA, 1963.
- [54] P. J. van Heerden, "Theory of optical information storage in solids," *Applied Optics*, vol. 2, no. 4, pp. 393–400, 1963.
- [55] L. K. Anderson, "Holographic optical memory for bulk data storage," *Bell Laboratories Records*, vol. 46, pp. 318–325, 1968.
- [56] L. d'Auria, J. P. Huignard, C. Slezak, and E. Spitz, "Experimental holographic read-write memory using 3-D storage," *Applied Optics*, vol. 13, no. 4, pp. 808–818, 1974.
- [57] A. Vander Lugt, "Holographic memories," in *Optical Information Processing*, Y. E. Nesterkhin, G. W. Stroke, and W. E. Kock, Eds., pp. 347–368, Plenum Press, New York, NY, USA, 1976.
- [58] D. Casasent, "Hybrid processors," in *Optical Information Processing Fundamentals*, S. H. Lee, Ed., pp. 181–233, Springer, Berlin, Germany, 1981.
- [59] J. Jahns and S. H. Lee, *Optical Computing Hardware*, Academic Press, Boston, Mass, USA, 1994.
- [60] R. Hauck and O. Bryngdahl, "Computer-generated holograms with pulse-density modulation," *Journal of the Optical Society of America A*, vol. 1, no. 1, pp. 5–10, 1984.
- [61] M. A. Seldowitz, J. P. Allebach, and D. W. Sweeney, "Synthesis of digital holograms by direct binary search," *Applied Optics*, vol. 26, no. 14, pp. 2788–2798, 1987.
- [62] F. Wyrowski and O. Bryngdahl, "Iterative Fourier-transform algorithm applied to computer holography," *Journal of Optical Society of America A*, vol. 5, no. 7, pp. 1058–1065, 1988.
- [63] L. Legeard, P. Réfrégier, and P. Ambs, "Multicriteria optimality for iterative encoding of computer-generated holograms," *Applied Optics*, vol. 36, no. 29, pp. 7444–7449, 1997.
- [64] L. Bigué and P. Ambs, "Optimal multicriteria approach to the iterative Fourier transform algorithm," *Applied Optics*, vol. 40, no. 32, pp. 5886–5893, 2001.
- [65] F. Xu, R. C. Tyan, P. C. Sun, Y. Fainman, C. C. Cheng, and A. Scherer, "Form-birefringent computer-generated holograms," *Optics Letters*, vol. 21, no. 18, pp. 1513–1515, 1996.
- [66] C. Ribot, P. Lalanne, M. S. L. Lee, B. Loiseaux, and J. P. Huignard, "Analysis of blazed diffractive optical elements formed with artificial dielectrics," *Journal of the Optical Society of America A*, vol. 24, no. 12, pp. 3819–3826, 2007.
- [67] U. Levy, C. H. Tsai, H. Y. O. C. Kim, and Y. Fainman, "Design, fabrication and characterization of subwavelength computer-generated holograms for spot array generation," *Optics Express*, vol. 12, no. 22, pp. 5345–5355, 2004.
- [68] B. Kress and P. Meyrueis, *Applied Digital Optics: From Micro-Optics to Nanophotonics*, John Wiley & Sons, Chichester, UK, 2009.
- [69] M. Born and E. Wolf, *Principles of Optics*, Pergamon Press, Oxford, UK, 1980.
- [70] J. Turunen and F. Wyrowski, *Diffractive Optics for Industrial and Commercial Applications*, Akademie, Berlin, Germany, 1997.
- [71] J. N. Mait, "From ink bottles to e-beams: a historical perspective of diffractive optic technology," in *Optical Processing and Computing: A Tribute to Adolf Lohmann*, vol. 4392 of *Proceedings of SPIE*, pp. 75–86, Orlando, Fla, USA, 2001.
- [72] A. D. Fisher and J. N. Lee, "The current status of two-dimensional spatial light modulator technology," in *Optical and Hybrid Computing*, vol. 634 of *Proceedings of SPIE*, pp. 352–371, Leesburg, Va, USA, March 1986.
- [73] U. Efron, *Spatial Light Modulator Technology. Materials, Devices, and Applications*, Marcel Dekker, New York, NY, USA, 1995.
- [74] "Applied optics special issue on spatial light modulators," *Applied Optics*, vol. 28, no. 22, pp. 4739–4908, 1989.
- [75] "Applied optics special issue on spatial light modulators," *Applied Optics*, vol. 31, no. 20, pp. 3876–4041, 1992.
- [76] "Applied optics special issue on spatial light modulators," *Applied Optics*, vol. 33, no. 14, pp. 2767–2860, 1994.
- [77] "Applied optics special issue on spatial light modulators," *Applied Optics*, vol. 37, no. 32, pp. 7471–7552, 1998.
- [78] T.-C. Poon, R. Juday, and T. Hara, "Spatial light modulators—research, development and applications: introduction to the feature issue," *Applied Optics*, vol. 37, no. 32, p. 7471, 1998.
- [79] W. E. Ross and J. A. Davis, "The magneto-optic spatial light modulator," in *Spatial Light Modulator Technology: Materials, Devices, and Applications*, U. Efron, Ed., pp. 361–390, Marcel Dekker, New York, NY, USA, 1995.
- [80] W. E. Ross, K. M. Snapp, and R. H. Anderson, "Fundamental characteristics of the Litton iron garnet magneto-optic spatial light modulator," in *Advances in Optical Information Processing I*, vol. 388 of *Proceedings of SPIE*, p. 55, Bellingham, Wash, USA, January 1983.
- [81] A. L. Lentine, "Self-electro-optic effect devices for optical information processing," in *Optical Computing Hardware*, J. Jahns and S. H. Lee, Eds., pp. 45–72, Academic Press, San Diego, Calif, USA, 1994.
- [82] T.-H. Lin, A. Ersen, J. H. Wang, et al., "Two-dimensional spatial light modulators fabricated in Si/PLZT," *Applied Optics*, vol. 29, no. 11, pp. 1595–1603, 1990.
- [83] T. G. McDonald and L. A. Yoder, "Digital micromirror devices make projection displays," *Laser Focus World*, vol. 33, no. 8, pp. S5–S8, 1997.
- [84] D. R. Pape and L. J. Hornbeck, "Characteristics of the deformable mirror device for optical information processing," *Optical Engineering*, vol. 22, no. 6, pp. 675–681, 1983.
- [85] V. Laude, S. Mazé, P. Chavel, and P. H. Réfrégier, "Amplitude and phase coding measurements of a liquid crystal television," *Optics Communications*, vol. 103, no. 1-2, pp. 33–38, 1993.
- [86] BNS, "Boulder Nonlinear Systems, Inc; Products," 2009, <http://www.bnnonlinear.com/>.
- [87] F. T. S. Yu, S. Jutamulia, T. W. Lin, et al., "Adaptive real-time pattern recognition using a liquid crystal TV based joint transform correlator," *Applied Optics*, vol. 26, no. 8, pp. 1370–1372, 1987.

- [88] F. Mok, J. Diep, H.-K. Liu, et al., "Real-time computer generated hologram by means of liquid-crystal television spatial light modulator," *Optics Letters*, vol. 11, no. 11, pp. 748–750, 1986.
- [89] C. Soutar, J. S. E. Monroe, and J. Knopp, "Measurement of the complex transmittance of the Epson liquid crystal television," *Optical Engineering*, vol. 33, no. 4, pp. 1061–1068, 1994.
- [90] N. Mukohzaka, N. Yoshida, H. Toyoda, Y. Kobayashi, and T. Hara, "Diffraction efficiency analysis of a parallel-aligned nematic-liquid-crystal spatial light modulator," *Applied Optics*, vol. 33, no. 14, pp. 2804–2811, 1994.
- [91] Holoeve, "HOLOEYE Photonics AG & HOLOEYE Corporation," 2009, <http://www.holoeye.com/>.
- [92] C. Soutar and K. Lu, "Determination of the physical properties of an arbitrary twisted-nematic liquid crystal cell," *Optical Engineering*, vol. 33, no. 8, pp. 2704–2712, 1994.
- [93] J. A. Davis, M. J. Yzuel, J. Campos, I. Moreno, A. Márquez, and J. Nicolás, "Review of operating modes for twisted nematic liquid crystal displays for applications in optical image processing," in *Wave Optics and Photonic Devices for Optical Information Processing II*, vol. 5181 of *Proceedings of SPIE*, pp. 120–131, San Diego, Calif, USA, 2003.
- [94] J. Otón, P. Ambs, M. S. Millán, and E. Pérez-Cabré, "Multipoint phase calibration for improved compensation of inherent wavefront distortion in parallel aligned liquid crystal on silicon displays," *Applied Optics*, vol. 46, no. 23, pp. 5667–5679, 2007.
- [95] A. Lizana, A. Marquez, I. Moreno, et al., "Wavelength dependence of polarimetric and phase-shift characterization of a liquid crystal on silicon display," *Journal of the European Optical Society—Rapid Publication*, vol. 3, Article ID 08012, 2008.
- [96] E. Frumker and Y. Silberberg, "Phase and amplitude pulse shaping with two-dimensional phase-only spatial light modulators," *Journal of the Optical Society of America B*, vol. 24, no. 12, pp. 2940–2947, 2007.
- [97] M. T. Gruneisen, W. A. Miller, R. C. Dymale, and A. M. Sweiti, "Holographic generation of complex fields with spatial light modulators: application to quantum key distribution," *Applied Optics*, vol. 47, no. 4, pp. A32–A42, 2008.
- [98] A. Jesacher, C. Maurer, A. Schwaighofer, S. Bernet, and M. Ritsch-Marte, "Near-perfect hologram reconstruction with a spatial light modulator," *Optics Express*, vol. 16, no. 4, pp. 2597–2603, 2008.
- [99] A. V. Kuzmenko and P. V. Yezhov, "Iterative algorithms for off-axis double-phase computer-generated holograms implemented with phase-only spatial light modulators," *Applied Optics*, vol. 46, no. 30, pp. 7392–7400, 2007.
- [100] G. Milewski, D. Engström, and J. Bengtsson, "Diffractive optical elements designed for highly precise far-field generation in the presence of artifacts typical for pixelated spatial light modulators," *Applied Optics*, vol. 46, no. 1, pp. 95–105, 2007.
- [101] A. Jesacher, S. Fürhapter, S. Bernet, and M. Ritsch-Marte, "Diffractive optical tweezers in the fresnel regime," *Optics Express*, vol. 12, no. 10, pp. 2243–2250, 2004.
- [102] W. Osten, C. Kohler, and J. Liesener, "Evaluation and application of spatial light modulators for optical metrology," *Optica Pura y Aplicada*, vol. 38, no. 3, pp. 71–81, 2005.
- [103] P. J. Marchand, A. V. Krishnamoorthy, K. S. Urquhart, et al., "Motionless-head parallel readout optical-disk system," *Applied Optics*, vol. 32, no. 2, pp. 190–203, 1993.
- [104] F. H. Mok, G. W. Burr, and D. Psaltis, "Angle and space multiplexed holographic random access memory (HRAM)," *Optical Memory and Neural Networks*, vol. 3, no. 2, pp. 119–127, 1994.
- [105] J. Ashley, M. P. Bernal, G. W. Burr, et al., "Holographic data storage," *IBM Journal of Research and Development*, vol. 44, no. 3, pp. 341–368, 2000.
- [106] H. J. Coufal, D. Psaltis, and G. T. Sincerbox, *Holographic Data Storage*, Springer, Berlin, Germany, 2000.
- [107] "In Phase Technologies Products," 2009, <http://www.inphasetechnologies.com/>.
- [108] S. Hunter, F. Kiamilev, S. Esener, et al., "Potentials of two-photon based 3-D optical memories for high performance computing," *Applied Optics*, vol. 29, no. 14, pp. 2058–2066, 1990.
- [109] B. Kohler, S. Bernet, A. Renn, et al., "Storage of 2000 holograms in a photochemical hole burning system," *Optics Letters*, vol. 18, no. 24, pp. 2144–2146, 1993.
- [110] D. Casasent and W.-T. Chang, "Correlation synthetic discriminant functions," *Applied Optics*, vol. 25, no. 14, pp. 2343–2350, 1986.
- [111] L. Bigué, M. Fracès, and P. Ambs, "Experimental implementation of a joint transform correlator using synthetic discriminant functions," *Optics and Lasers in Engineering*, vol. 23, no. 2-3, pp. 93–111, 1995.
- [112] J. Campos, A. Márquez, M. J. Yzuel, J. A. Davis, D. M. Cottrell, and I. Moreno, "Fully complex synthetic discriminant functions written onto phase-only modulators," *Applied Optics*, vol. 39, no. 32, pp. 5964–5970, 2000.
- [113] A. Mahalanobis, B. V. K. Vijaya Kumar, and D. Casasent, "Minimum average correlation energy filters," *Applied Optics*, vol. 26, no. 17, pp. 3633–3640, 1987.
- [114] B. V. K. Vijaya Kumar, "Tutorial survey of composite filter designs for optical correlators," *Applied Optics*, vol. 31, no. 23, pp. 4773–4801, 1992.
- [115] B. V. K. Vijaya Kumar and L. Hassebrook, "Performance measures for correlation filters," *Applied Optics*, vol. 29, no. 20, pp. 2997–3006, 1990.
- [116] P. Réfrégier, "Optimal trade-off filters for noise robustness, sharpness of the correlation peak, and Horner efficiency," *Optics Letters*, vol. 16, pp. 829–831, 1991.
- [117] R. D. Juday, B. V. K. Vijaya Kumar, and P. K. Rajan, "Optimal real correlation filters," *Applied Optics*, vol. 30, no. 5, pp. 520–522, 1991.
- [118] D. Lefebvre, H. H. Arsenault, and S. Roy, "Nonlinear filter for pattern recognition invariant to illumination and to out-of-plane rotations," *Applied Optics*, vol. 42, no. 23, pp. 4658–4662, 2003.
- [119] B. Javidi, "Nonlinear joint power spectrum based optical correlation," *Applied Optics*, vol. 28, no. 12, pp. 2358–2367, 1989.
- [120] B. Javidi, "Synthetic discriminant function-based binary nonlinear optical correlator," *Applied Optics*, vol. 28, no. 13, pp. 2490–2493, 1989.
- [121] B. Javidi, "Comparison of the nonlinear joint transform correlator and the nonlinearly transformed matched filter based correlator for noisy input scenes," *Optical Engineering*, vol. 29, no. 9, pp. 1013–1020, 1990.
- [122] P. Refregier, V. Laude, and B. Javidi, "Nonlinear joint-transform correlation: an optimal solution for adaptive image discrimination and input noise robustness," *Optics Letters*, vol. 19, no. 6, pp. 405–407, 1994.
- [123] F. T. S. Yu and S. Yin, *Selected Papers on Optical Pattern Recognition*, SPIE Press, Bellingham, Wash, USA, 1999.

- [124] P. Ambs, W. E. Cleland, D. E. Kraus, P. Suni, J. A. Thompson, and J. Turek, "Kinoform filter for an incoherent optical processor," *Applied Optics*, vol. 22, no. 6, pp. 796–803, 1983.
- [125] W. E. Cleland, D. E. Kraus, J. A. Thompson, and P. Ambs, "Optical trigger processor for high energy physics," *Nuclear Instruments & Methods in Physics Research*, vol. 216, no. 3, pp. 405–414, 1983.
- [126] P. Hough, "Methods and means for recognizing patterns," US patent no. 3,069,654, 1962.
- [127] S. Laut, F. Xu, P. Ambs, and Y. Fainman, "Matrix of 64×64 computer-generated holograms for an optical Hough transform processor," in *Optical Information Science and Technology (OIST97): Optical Memory and Neural Networks*, vol. 3402 of *Proceedings of SPIE*, pp. 22–31, Moscow, Russia, August 1998.
- [128] D. P. Casasent and J. Richards, "High-speed acousto-optic mapping modulator for the generalized Hough transform," *Applied Optics*, vol. 32, no. 35, pp. 7217–7224, 1993.
- [129] G. Eichmann and B. Z. Dong, "Coherent optical production of the Hough transform," *Applied Optics*, vol. 22, no. 6, pp. 830–834, 1983.
- [130] W. H. Steier and R. K. Shori, "Optical Hough transform," *Applied Optics*, vol. 25, no. 16, pp. 2734–2738, 1986.
- [131] D. A. Gregory, J. A. Loudin, J. C. Kirsch, et al., "Using the hybrid modulating properties of liquid crystal television," *Applied Optics*, vol. 30, no. 11, pp. 1374–1378, 1991.
- [132] E. C. Tam, F. T. S. Yu, D. A. Gregory, and R. D. Juday, "Autonomous real-time object tracking with an adaptive joint transform correlator," *Optical Engineering*, vol. 29, no. 4, pp. 314–320, 1990.
- [133] F. T. S. Yu, T. Lu, E. C. Tam, et al., "Optical disk based joint transform correlator," *Applied Optics*, vol. 30, no. 8, pp. 915–916, 1991.
- [134] A. Pu, R. Denkwalter, and D. Psaltis, "Real-time vehicle navigation using a holographic memory," *Optical Engineering*, vol. 36, no. 10, pp. 2737–2746, 1997.
- [135] H. Rajbenbach, S. Bann, P. Réfrégier, et al., "A compact photorefractive correlator for robotic applications," *Applied Optics*, vol. 31, no. 26, pp. 5666–5674, 1992.
- [136] J. F. Rodolfo, H. J. Rajbenbach, and J. P. Huignard, "Performance of a photorefractive joint transform correlator identification," *Optical Engineering*, vol. 34, no. 4, pp. 1166–1171, 1995.
- [137] L. Guibert, G. Keryer, A. Serval, et al., "On-board optical joint transform correlator for real-time road sign recognition," *Optical Engineering*, vol. 34, no. 1, pp. 135–143, 1995.
- [138] J. A. Sloan and D. W. Small, "Design and fabrication of a miniaturized optical correlator," *Optical Engineering*, vol. 32, no. 12, pp. 3307–3315, 1993.
- [139] S. Bains, "Miniature optical correlator fits inside a PC," *Laser Focus World*, vol. 31, no. 12, pp. 17–18, 1995.
- [140] T. Ewing, S. Serati, and K. Bauchert, "Optical correlator using four kilohertz analog spatial light modulators," in *Optical Pattern Recognition XV*, vol. 5437 of *Proceedings of SPIE*, pp. 123–133, Orlando, Fla, USA, April 2004.
- [141] T.-H. Chao and T. Lu, "Automatic target recognition (ATR) performance improvement using integrated grayscale optical correlator and neural network," in *Optical Pattern Recognition XX*, vol. 7340 of *Proceedings of SPIE*, Orlando, Fla, USA, 2009.
- [142] P. Birch, R. Young, F. Claret-Tournier, et al., "Fully complex filter implementation in all-optical and hybrid digital/optical correlators," in *Optical Pattern Recognition XII*, vol. 4387 of *Proceedings of SPIE*, pp. 16–26, Orlando, Fla, USA, April 2001.
- [143] INO, "INO Optical correlator OC-VGA-6000," 2001.
- [144] P. Parrein, *Corrélation d'images de profondeur. Application à l'inspection automatique d'objets*, Ph.D. thesis, Université Paris Sud, Orsay, France, 2001.
- [145] H. Rajbenbach, Y. Fainman, and S. H. Lee, "Optical implementation of an iterative algorithm for matrix inversion," *Applied Optics*, vol. 26, no. 6, pp. 1024–1031, 1987.
- [146] H. J. Caulfield, W. T. Rhodes, M. J. Foster, et al., "Optical implementation of systolic array processing," *Optics Communications*, vol. 40, no. 2, pp. 86–90, 1981.
- [147] D. Psaltis, D. Brady, and K. Wagner, "Adaptive optical networks using photorefractive crystals," *Applied Optics*, vol. 27, no. 9, pp. 1752–1759, 1988.
- [148] R. A. Athale, *Digital Optical Computing*, SPIE Press, Bellingham, Wash, USA, 1990.
- [149] H. J. Caulfield and G. O. Gheen, *Selected Papers on Optical Computing*, SPIE Press, Bellingham, Wash, USA, 1989.
- [150] B. S. Wherrett and P. Chavel, *Optical Computing*, Institute of Physics, Bristol, UK, 1995.
- [151] F. B. McCormick, F. A. P. Tooley, T. J. Cloonan, et al., "Experimental investigation of a free-space optical switching network by using symmetric self-electro-optic-effect devices," *Applied Optics*, vol. 31, no. 26, pp. 5431–5446, 1992.
- [152] P. S. Guilfoyle and R. V. Stone, "Digital optical computer II," in *Optical Enhancements to Computing Technology*, vol. 1563 of *Proceedings of SPIE*, pp. 214–222, 1991.
- [153] J. W. Goodman, "Optics as an interconnect technology," in *Optical Processing and Computing*, H. H. Arsenault, T. Szoplik, and B. Macukow, Eds., pp. 1–32, Academic Press, San Diego, Calif, USA, 1989.
- [154] D. Miller, "Optical interconnects to silicon," *IEEE Journal of Selected Topics in Quantum Electronics*, vol. 6, no. 6, pp. 1312–1317, 2000.
- [155] A. W. Lohmann, W. Stork, and G. Stucke, "Optical perfect shuffle," *Applied Optics*, vol. 25, no. 10, pp. 1530–1531, 1986.
- [156] A. Louri and H. Sung, "Efficient implementation methodology for three-dimensional space-invariant hypercube-based optical interconnection networks," *Applied Optics*, vol. 32, no. 35, pp. 7200–7209, 1993.
- [157] T. J. Cloonan and A. L. Lentine, "Self-routing crossbar packet switch employing free-space optics for chip-to-chip interconnections," *Applied Optics*, vol. 30, no. 26, pp. 3721–3733, 1991.
- [158] K. H. Brenner and T. M. Merklein, "Implementation of an optical crossbar network based on directional switches," *Applied Optics*, vol. 31, no. 14, pp. 2446–2451, 1992.
- [159] H. Ichikawa, T. H. Barnes, M. R. Taghizadeh, et al., "Dynamic space-variant optical interconnections using liquid crystal spatial light modulators," *Optics Communications*, vol. 93, no. 3-4, pp. 145–150, 1992.
- [160] K. S. Urquhart, P. Marchand, Y. Fainman, and S. H. Lee, "Diffractive optics applied to free-space optical interconnects," *Applied Optics*, vol. 33, no. 17, pp. 3670–3682, 1994.
- [161] J. Shamir, H. J. Caulfield, and R. B. Johnson, "Massive holographic interconnection networks and their limitations," *Applied Optics*, vol. 28, no. 2, pp. 311–324, 1989.
- [162] R. K. Kostuk, J. H. U. N. Yeh, and M. Fink, "Distributed optical data bus for board-level interconnects," *Applied Optics*, vol. 32, no. 26, pp. 5010–5021, 1993.

- [163] I. Young, E. Mohammed, J. Liao, et al., "Optical I/O technology for tera-scale computing," in *Proceedings of IEEE International Solid-State Circuits Conference (ISSCC '09)*, pp. 468–469, San Francisco, Calif, USA, February 2009.
- [164] D. A. B. Miller, "Device requirements for optical interconnects to silicon chips," *Proceedings of the IEEE*, vol. 97, no. 7, pp. 1166–1185, 2009.
- [165] H. J. Caulfield, S. Dolev, and W. M. J. Green, "Optical high-performance computing: introduction to the JOSA A and applied optics feature," *Applied Optics*, vol. 48, no. 22, pp. OHPC1–OHPC3, 2009.
- [166] Y. Fainman, K. Tetz, R. Rokitski, and L. I. N. Pang, "Surface plasmonic fields in nanophotonics," *Optics & Photonics News*, vol. 17, no. 7-8, pp. 24–29, 2006.
- [167] Y. Fainman, "Ultrafast and nanoscale optics," in *Proceedings of Conference on Lasers and Electro-Optics, and Conference on Quantum Electronics and Laser Science (CLEO/QELS '09)*, pp. 1–2, Baltimore, Md, USA, June 2009.
- [168] D. Erickson, T. Rockwood, T. Emery, A. Scherer, and D. Psaltis, "Nanofluidic tuning of photonic crystal circuits," *Optics Letters*, vol. 31, no. 1, pp. 59–61, 2006.
- [169] A. Groisman, S. Zamek, K. Campbell, L. I. N. Pang, U. Levy, and Y. Fainman, "Optofluidic 1×4 switch," *Optics Express*, vol. 16, no. 18, pp. 13499–13508, 2008.
- [170] P. J. Rodrigo, L. Kelemen, D. Palima, C. A. Alonzo, P. Ormos, and J. Glückstad, "Optical microassembly platform for constructing reconfigurable microenvironments for biomedical studies," *Optics Express*, vol. 17, no. 8, pp. 6578–6583, 2009.
- [171] P. J. Rodrigo, V. R. Daria, and J. Glückstad, "Real-time interactive optical micromanipulation of a mixture of high- and low-index particles," *Optics Express*, vol. 12, no. 7, pp. 1417–1425, 2004.
- [172] U. Schnars and W. Jueptner, *Digital Holography*, Springer, Berlin, Germany, 2005.
- [173] U. Schnars and W. Jueptner, "Direct recording of holograms by a CCD target and numerical reconstruction," *Applied Optics*, vol. 33, no. 2, pp. 179–181, 1994.
- [174] U. Schnars and W. Jueptner, "Digital recording and reconstruction of holograms in hologram interferometry and shearography," *Applied Optics*, vol. 33, no. 20, pp. 4373–4377, 1994.
- [175] J. Kühn, F. Montfort, T. Colomb, et al., "Submicrometer tomography of cells by multiple-wavelength digital holographic microscopy in reflection," *Optics Letters*, vol. 34, no. 5, pp. 653–655, 2009.
- [176] A. Jaulin and L. Bigué, "High speed partial Stokes imaging using a ferroelectric liquid crystal modulator," *Journal of the European Optical Society—Rapid Publication*, vol. 3, Article ID 08019, 2008.
- [177] B. J. DeBoo, J. M. Sasian, and R. A. Chipman, "Depolarization of diffusely reflecting man-made objects," *Applied Optics*, vol. 44, no. 26, pp. 5434–5445, 2005.
- [178] P. Réfrégier, F. Goudail, and N. Roux, "Estimation of the degree of polarization in active coherent imagery by using the natural representation," *Journal of the Optical Society of America A*, vol. 21, no. 12, pp. 2292–2300, 2004.
- [179] M. Alouini, F. Goudail, A. Grisard, et al., "Near-infrared active polarimetric and multispectral laboratory demonstrator for target detection," *Applied Optics*, vol. 48, no. 8, pp. 1610–1618, 2009.
- [180] B. Javidi, *Optical and Digital Techniques for Information Security*, Springer, New York, NY, USA, 2005.

Research Article

Conservation Laws in Quantum-Correlation-Function Dynamics

Wei Wang¹ and Mitsuo Takeda²

¹ Department of Mechanical Engineering, School of Engineering and Physical Sciences, Heriot-Watt University, Edinburgh EH14 4AS, UK

² Department of Engineering Science, Graduate School of Informatics and Engineering, The University of Electro-Communications, 1-5-1, Chofugaoka, Chofu, Tokyo 182-8585, Japan

Correspondence should be addressed to Wei Wang, w.wang@hw.ac.uk

Received 22 November 2009; Accepted 31 March 2010

Academic Editor: Oleg V. Angelsky

Copyright © 2010 W. Wang and M. Takeda. This is an open access article distributed under the Creative Commons Attribution License, which permits unrestricted use, distribution, and reproduction in any medium, provided the original work is properly cited.

For a complete and lucid discussion of quantum correlation, we introduced two new first-order correlation tensors defined as linear combinations of the general coherence tensors of the quantized fields and derived the associated coherence potentials governing the propagation of quantum correlation. On the basis of these quantum optical coherence tensors, we further introduced new concepts of scalar, vector and tensor densities and presented some related properties, such as conservation laws and the wave-particle duality for quantum correlation, which provide new insights into photon statistics and quantum correlation.

1. Introduction

Fields interact with atoms in a fundamentally random or stochastic way. As a consequence, statistical interpretation of the outcome of most optical experiments becomes indispensable due to the fact that any measurement of light is accompanied by certain unavoidable fluctuations [1, 2]. Among various descriptions of the statistical properties of light, correlation between the fields at different space-time points, known as the correlation function, has long been recognized as the most fundamental physical quantity that plays a crucial role in photon correlations. The concept of optical correlation, first introduced by Wolf, has laid a foundation on which many important problems in classical statistical optics can be treated in a unified way. Also worth special mention is the quantum theory of optical coherence created by Glauber [3–5], who took a quantum electrodynamics approach to the problems of photon statistics. Because of its theoretical and practical importance, coherence theory and quantum optics have developed into a challenging multifarious field of research.

In quantum optics, detection of photons based on the absorption of photons via the photoelectric effect constitutes the basis of the measurements of the optical field. Photon statistics and quantum correlations have been studied

extensively. However, the discussions in most of papers are restricted to the correlations between the same kinds of fields (either between electric fields \mathbf{E} themselves or between magnetic fields \mathbf{H} themselves) at different space-time points, and the mixed correlation between electric field and magnetic field, introduced by Mehta and Wolf [6], seems to have received less attention in spite of its importance. Although the quantum theory for the correlations between the same kind of fields has already been established and is indeed informative, this alone cannot constitute a self-consistent theoretical framework for the full description of the coherence properties of the quantum electromagnetic fields. The need for a more self-contained quantum correlation theory involving the \mathbf{EH} -mixed correlations has motivated us to take a fully quantum electrodynamics approach to the problems of quantum correlations.

In this paper, we will introduce, for the first time, two second-order correlation tensors: $\mathbb{E}_{jk}(\mathbf{x}_1, t_1; \mathbf{x}_2, t_2)$ and $\mathbb{S}_{jk}(\mathbf{x}_1, t_1; \mathbf{x}_2, t_2)$ for the complete and lucid description of quantum correlation on the basis of the quantized field theory. In formal analogy to the energy conservation, momentum conservation, and angular momentum laws for vector fields in classical electromagnetism, some new densities derived from \mathbb{E}_{jk} and \mathbb{S}_{jk} are introduced to quantum correlation theory and are related by new continuity

equations, which indicate new conservation laws in quantum correlation theory. In terms of Fock states and coherent states, we will represent the newly introduced densities and reveal the nature of the wave-particle duality for the quantum correlation.

2. Quantum Coherence Tensors

To fully characterize the correlations involving all the components of the electromagnetic fields at any space-time points, more general coherence matrices are needed. In addition to Glauber's E-only correlation tensor [3–5], other first-order magnetic H-correlation and EH mixed-correlation tensors have been defined by Mehta and Wolf [6], namely,

$$\begin{aligned} E_{jk}(\mathbf{x}_1, t_1; \mathbf{x}_2, t_2) &= \text{Tr}\{\hat{\rho}\hat{\mathbf{E}}_j^{(-)}(\mathbf{x}_1, t_1)\hat{\mathbf{E}}_k^{(+)}(\mathbf{x}_2, t_2)\}, \\ H_{jk}(\mathbf{x}_1, t_1; \mathbf{x}_2, t_2) &= \text{Tr}\{\hat{\rho}\hat{\mathbf{H}}_j^{(-)}(\mathbf{x}_1, t_1)\hat{\mathbf{H}}_k^{(+)}(\mathbf{x}_2, t_2)\}, \\ M_{jk}(\mathbf{x}_1, t_1; \mathbf{x}_2, t_2) &= \text{Tr}\{\hat{\rho}\hat{\mathbf{E}}_j^{(-)}(\mathbf{x}_1, t_1)\hat{\mathbf{H}}_k^{(+)}(\mathbf{x}_2, t_2)\}, \\ N_{jk}(\mathbf{x}_1, t_1; \mathbf{x}_2, t_2) &= \text{Tr}\{\hat{\rho}\hat{\mathbf{H}}_j^{(-)}(\mathbf{x}_1, t_1)\hat{\mathbf{E}}_k^{(+)}(\mathbf{x}_2, t_2)\}, \end{aligned} \quad (1)$$

where $\hat{\rho}$ is the density operator describing the field, the symbol $\text{Tr}\{\cdot\cdot\cdot\}$ stands for the trace operation, the indices ($j, k = 1, 2, 3$) label Cartesian components: ($\hat{\mathbf{x}}, \hat{\mathbf{y}}, \hat{\mathbf{z}}$), and we have already separated the electromagnetic field operators into their positive-frequency parts $\hat{\mathbf{E}}^{(+)}$ and $\hat{\mathbf{H}}^{(+)}$ and their negative-frequency parts $\hat{\mathbf{E}}^{(-)}$ and $\hat{\mathbf{H}}^{(-)}$, respectively.

Since the electric and magnetic field operators are related by Maxwell's equations in free space, their corresponding negative frequency operators $\hat{\mathbf{E}}^{(-)}$ and $\hat{\mathbf{H}}^{(-)}$ can also be expressed in the tensor form as

$$\varepsilon_{jkl}\partial_k^1\hat{\mathbf{E}}_l^{(-)}(\mathbf{x}_1, t_1) + \frac{1}{c}\frac{\partial}{\partial t_1}\hat{\mathbf{H}}_j^{(-)}(\mathbf{x}_1, t_1) = 0, \quad (2)$$

$$\varepsilon_{jkl}\partial_k^1\hat{\mathbf{H}}_l^{(-)}(\mathbf{x}_1, t_1) - \frac{1}{c}\frac{\partial}{\partial t_1}\hat{\mathbf{E}}_j^{(-)}(\mathbf{x}_1, t_1) = 0, \quad (3)$$

$$\partial_j^1\hat{\mathbf{E}}_j^{(-)}(\mathbf{x}_1, t_1) = 0, \quad (4)$$

$$\partial_j^1\hat{\mathbf{H}}_j^{(-)}(\mathbf{x}_1, t_1) = 0, \quad (5)$$

where c indicates the speed of light, ε_{jkl} is the unit tensor of Levi-Civita with antisymmetry, ∂_j^1 and $\partial/\partial t_1$ are the differential operations to be performed with respect to the point \mathbf{x}_1 and t_1 , and Einstein's summation convention has been employed. One of the essential aspects in which quantum field theory differs from classical theory is that two values of the field operators taken at different space-time points do not, in general, commute with one another. After multiplying both sides of (2) by $\hat{\mathbf{E}}_m^{(+)}(\mathbf{x}_2, t_2)$ and placing it under the operator signs, we obtain the relation

$$\begin{aligned} \varepsilon_{jkl}\partial_k^1\hat{\mathbf{E}}_l^{(-)}(\mathbf{x}_1, t_1)\hat{\mathbf{E}}_m^{(+)}(\mathbf{x}_2, t_2) \\ + \frac{1}{c}\frac{\partial}{\partial t_1}\hat{\mathbf{H}}_j^{(-)}(\mathbf{x}_1, t_1)\hat{\mathbf{E}}_m^{(+)}(\mathbf{x}_2, t_2) = 0. \end{aligned} \quad (6)$$

If we take the quantum average of (6) and interchange the order of the quantum average and differential operations, from the definition of coherence tensor in (1), we have

$$\varepsilon_{jkl}\partial_k^1 E_{lm} + \frac{1}{c}\frac{\partial}{\partial t_1} N_{jm} = 0. \quad (7)$$

If we apply the same procedure, we obtain

$$\varepsilon_{jkl}\partial_k^1 M_{lm} + \frac{1}{c}\frac{\partial}{\partial t_1} H_{jm} = 0, \quad (8)$$

$$\varepsilon_{jkl}\partial_k^1 N_{lm} - \frac{1}{c}\frac{\partial}{\partial t_1} E_{jm} = 0, \quad (9)$$

$$\varepsilon_{jkl}\partial_k^1 H_{lm} - \frac{1}{c}\frac{\partial}{\partial t_1} M_{jm} = 0. \quad (10)$$

In a similar manner, the divergence condition yields the following equations:

$$\partial_j^1 E_{jk} = 0, \quad (11)$$

$$\partial_j^1 H_{jk} = 0, \quad (12)$$

$$\partial_j^1 M_{jk} = 0, \quad (13)$$

$$\partial_j^1 N_{jk} = 0. \quad (14)$$

After adding (7) to (10), and subtracting (9) from (8), we obtain two equations, respectively:

$$\varepsilon_{jkl}\partial_k^1 E_{lm} - \frac{1}{c}\frac{\partial}{\partial t_1} S_{jm} = 0, \quad (15)$$

$$\varepsilon_{jkl}\partial_k^1 S_{lm} + \frac{1}{c}\frac{\partial}{\partial t_1} E_{jm} = 0, \quad (16)$$

where

$$\begin{aligned} \mathbb{E}_{jk}(\mathbf{x}_1, t_1; \mathbf{x}_2, t_2) \\ = E_{jk}(\mathbf{x}_1, t_1; \mathbf{x}_2, t_2) + H_{jk}(\mathbf{x}_1, t_1; \mathbf{x}_2, t_2) \\ = \text{Tr}\{\hat{\rho}[\hat{\mathbf{E}}_j^{(-)}(\mathbf{x}_1, t_1)\hat{\mathbf{E}}_k^{(+)}(\mathbf{x}_2, t_2) + \hat{\mathbf{H}}_j^{(-)}(\mathbf{x}_1, t_1)\hat{\mathbf{H}}_k^{(+)}(\mathbf{x}_2, t_2)]\}, \end{aligned} \quad (17)$$

$$\begin{aligned} \mathbb{S}_{jk}(\mathbf{x}_1, t_1; \mathbf{x}_2, t_2) \\ = M_{jk}(\mathbf{x}_1, t_1; \mathbf{x}_2, t_2) - N_{jk}(\mathbf{x}_1, t_1; \mathbf{x}_2, t_2) \\ = \text{Tr}\{\hat{\rho}[\hat{\mathbf{E}}_j^{(-)}(\mathbf{x}_1, t_1)\hat{\mathbf{H}}_k^{(+)}(\mathbf{x}_2, t_2) - \hat{\mathbf{H}}_j^{(-)}(\mathbf{x}_1, t_1)\hat{\mathbf{E}}_k^{(+)}(\mathbf{x}_2, t_2)]\}. \end{aligned} \quad (18)$$

The tensor \mathbb{E}_{jk} may be called the quantum energy coherence tensor and \mathbb{S}_{jk} the quantum energy-flow coherence tensor, which have formal resemblance to those of the classical theory [7]. Moreover, from (11) and (12), or from (13) and (14), one has

$$\partial_j^1 E_{jk} = 0, \quad (19)$$

$$\partial_j^1 S_{jk} = 0. \quad (20)$$

The equations (15)-(16) and (19)-(20) are basic equations for the propagation of the energy coherence tensor and the energy-flow coherence tensor in free space. Another set of similar equations, which involve \mathbf{r}_2 and t_2 , can also be derived in a similar way.

So far we have derived the governing equations for the correlations between all the components of the quantum electromagnetic fields at any space-time points. In order to understand the importance of the newly introduced quantum energy and energy-flow coherence tensors, let us discuss the photoelectric detection of the optical field within the quantum mechanical interaction picture. In most of optical experiments, measurements of the electromagnetic field are based on the absorption of photons (energy) via the photoelectric effect. Based on a heuristic argument, Glauber has given the expression for the average counting rate of an ideal photodetection [4], which is proportional to $\text{Tr}\{\hat{\rho}\hat{\mathbf{E}}_j^{(-)}(\mathbf{x}, t)\hat{\mathbf{E}}_j^{(+)}(\mathbf{x}, t)\}$. It is important to note here that photon absorption by an ideal detector measures the average value of the Hamiltonian of the quantized radiation field: $\hat{\mathbf{E}}^{(-)} \cdot \hat{\mathbf{E}}^{(+)} + \hat{\mathbf{H}}^{(-)} \cdot \hat{\mathbf{H}}^{(+)}$, and not that of $\hat{\mathbf{E}}^{(-)} \cdot \hat{\mathbf{E}}^{(+)}$. One should note that the energies of electric field and magnetic field are indistinguishable in photon absorption process in the detector. Therefore, the probability per unit time that a photon be absorbed by an ideal detector at point \mathbf{x} at time t should be proportional to the expectation value of the normally ordered operator $\hat{\mathbf{E}}_j^{(-)}(\mathbf{x}, t)\hat{\mathbf{E}}_j^{(+)}(\mathbf{x}, t) + \hat{\mathbf{H}}_j^{(-)}(\mathbf{x}, t)\hat{\mathbf{H}}_j^{(+)}(\mathbf{x}, t)$.

Meanwhile, due to the well-known fact that electromagnetic radiation carries both energy and momentum, any interaction between photons and matters for the exchange of energy will inevitably involve the exchange of momentum. Just as Poynting vector in the classical electromagnetic field, where $\mathbf{S} \propto \mathbf{E}^* \times \mathbf{H} + \mathbf{E} \times \mathbf{H}^* = \mathbf{E}^* \times \mathbf{H} - \mathbf{H}^* \times \mathbf{E}$, it is convenient to introduce the notion of energy flow operator, defined by

$$\hat{\mathbf{S}}(\mathbf{x}, t) = \hat{\mathbf{E}}^{(-)}(\mathbf{x}, t) \times \hat{\mathbf{H}}^{(+)}(\mathbf{x}, t) - \hat{\mathbf{H}}^{(-)}(\mathbf{x}, t) \times \hat{\mathbf{E}}^{(+)}(\mathbf{x}, t). \quad (21)$$

The operator $\hat{\mathbf{S}}$ so defined is of course the energy flow associated with the photon absorption in light of the optical equivalence theorem [8, 9]. Therefore, the average value for the i component of the detected momentum should be proportional to

$$\text{Tr}\{\hat{\rho}\hat{\epsilon}_{ijk}\left[\hat{\mathbf{E}}_j^{(-)}(\mathbf{x}, t)\hat{\mathbf{H}}_k^{(+)}(\mathbf{x}, t) - \hat{\mathbf{H}}_j^{(-)}(\mathbf{x}, t)\hat{\mathbf{E}}_k^{(+)}(\mathbf{x}, t)\right]\}, \quad (22)$$

which is the expectation value of the operator $\hat{\mathbf{S}}$ with normal ordering.

Recording the energy and energy flow of photons with a single detector does not exhaust the available measurements we can make upon the field. In the more general expression, the fields $\hat{\mathbf{E}}^{(-)}$, $\hat{\mathbf{E}}^{(+)}$, $\hat{\mathbf{H}}^{(-)}$, and $\hat{\mathbf{H}}^{(+)}$ are evaluated at the different space-time points. Therefore, these tensors \mathbb{E}_{jk} and \mathbb{S}_{jk} furnish a general measure of quantum optical correlations involving all the components of the electromagnetic field at any space-time points and give the field intensity (which is proportional to the counting rate of

the detector) and energy flow vector (which is proportional to the kinetic momentum of light) as the special case for $\mathbf{x}_1 = \mathbf{x}_2$ and $t_1 = t_2$. One should be aware of the facts that energy transition is always associated with momentum changes in photon absorption process, and the energies of electric field and magnetic field are indistinguishable in the ideal photodetector. It is the indistinguishability that makes the introduction of \mathbb{E}_{jk} and \mathbb{S}_{jk} meaningful for the better definition of photon-delayed coincidences on the basis of the general first-order coherence tensors.

3. Coherence Tensor and Vector Potentials

Borrowing from the general potential theory [10], we can also introduce a new concept of the *coherence tensor potential* \mathbb{A}_{lm} from which the energy coherence tensor \mathbb{E}_{jk} can be obtained as

$$\mathbb{E}_{jm}(\mathbf{x}_1, t_1; \mathbf{x}_2, t_2) = \epsilon_{jkl}\partial_k^1\mathbb{A}_{lm}(\mathbf{x}_1, t_1; \mathbf{x}_2, t_2), \quad (23)$$

since the divergence of the curl of any tensor is zero, namely,

$$\begin{aligned} \partial_j^1(\epsilon_{jkl}\partial_k^1\mathbb{A}_{lm}) &= \epsilon_{jkl}\partial_j^1\partial_k^1\mathbb{A}_{lm} \\ &= -\epsilon_{kjl}\partial_j^1\partial_k^1\mathbb{A}_{lm} \\ &= -\epsilon_{jkl}\partial_j^1\partial_k^1\mathbb{A}_{lm} = 0. \end{aligned} \quad (24)$$

If we substitute from (24) into (16), we have

$$\epsilon_{jkl}\partial_k^1\left(\mathbb{S}_{lm} + \frac{1}{c}\frac{\partial}{\partial t_1}\mathbb{A}_{lm}\right) = 0. \quad (25)$$

Equation (25) will hold if

$$\begin{aligned} \mathbb{S}_{lm}(\mathbf{x}_1, t_1; \mathbf{x}_2, t_2) &= -\frac{1}{c}\frac{\partial}{\partial t_1}\mathbb{A}_{lm}(\mathbf{x}_1, t_1; \mathbf{x}_2, t_2) \\ &\quad - \partial_l^1\mathbf{a}_m(\mathbf{x}_1, t_1; \mathbf{x}_2, t_2), \end{aligned} \quad (26)$$

where \mathbf{a}_m is *coherence vector potential*. \mathbb{A}_{lm} and \mathbf{a}_m must now be determined in such a way as to satisfy the remaining Maxwell equations. Let us maintain the following gauge transform relation between \mathbb{A}_{lm} and \mathbf{a}_m :

$$\partial_l^1\mathbb{A}_{lm} + \frac{1}{c}\frac{\partial}{\partial t_1}\mathbf{a}_m = 0. \quad (27)$$

Substituting (26) into (20), and making use of the gauge transform in (27), we can easily find that the coherence vector potential satisfies the wave equation:

$$\nabla_1^2\mathbf{a}_m - \frac{1}{c^2}\frac{\partial^2}{\partial t_1^2}\mathbf{a}_m = 0. \quad (28)$$

Similarly, substituting (23) and (27) into (15), we have

$$\nabla_1^2\mathbb{A}_{jm} - \frac{1}{c^2}\frac{\partial^2}{\partial t_1^2}\mathbb{A}_{jm} = 0, \quad (29)$$

which indicates the wave equations governing the propagation of the coherence tensor potential. It should be noted

that the proposed coherence tensor and vector potentials have some similar mathematical behavior with the usual vector and dual potentials [11, 12], but the underlying physics is completely different. The key point of the proposed coherence potentials is to govern propagation of quantum correlation, whereas the usual vector and dual potentials are developed for the description of the electromagnetic wave in nonlinear dielectric media. The significance of the coherence tensor and vector potentials can be explained as follows. Just as the vector and scalar potentials play a more fundamental role in quantum electrodynamics than the electromagnetic fields themselves [13], the newly introduced coherence tensor potential and coherence vector potential are expected to play a more fundamental role in the descriptions of the quantum correlation and entanglement than the energy coherence tensor and the energy-flow coherence tensor.

4. Conservation Law of Quantum-Correlation-Function Energy

Noting the formal analogy to Maxwell's equations in free space, we can introduce some concepts to characterize the spatiotemporal evolution of the energy coherence tensor and the energy-flow coherence tensor. Borrowed from scalar theory in classical wavefields, an energy-flow-density-like quantity has been defined and observed experimentally when a generic coherence vortex is reported [14, 15]. Under the framework of classical scalar coherence theory, the associated conservation law has been deduced. However, with the optical equivalence theorem for normally order operators [8, 9] as a clue, it is possible to extend this concept so as to take into account the vectorial character of light to formulate much rigorous laws for quantum optics.

Let us now take the complex conjugate of (15) and multiply by \mathbb{S}_{jm} . We then obtain

$$\varepsilon_{jkl}\mathbb{S}_{jm}\partial_k^1\mathbb{E}_{lm}^* - \frac{1}{c}\mathbb{S}_{jm}\frac{\partial}{\partial t_1}\mathbb{S}_{jm}^* = 0. \quad (30)$$

If we add (30) with its complex conjugate, we have

$$\frac{1}{c}\frac{\partial}{\partial t_1}(\mathbb{S}_{jm}^*\mathbb{S}_{jm}) - \varepsilon_{jkl}(\mathbb{S}_{jm}^*\partial_k^1\mathbb{E}_{lm} + \mathbb{S}_{jm}\partial_k^1\mathbb{E}_{lm}^*) = 0. \quad (31)$$

If we make use of relation $\varepsilon_{jkl} = -\varepsilon_{lkj}$ and interchange the dummy suffices j and m , we have

$$\frac{1}{c}\frac{\partial}{\partial t_1}(\mathbb{S}_{jm}^*\mathbb{S}_{jm}) + \varepsilon_{jkl}(\mathbb{S}_{lm}^*\partial_k^1\mathbb{E}_{jm} + \mathbb{S}_{lm}\partial_k^1\mathbb{E}_{jm}^*) = 0. \quad (32)$$

In a similar way, we obtain from (16)

$$\frac{1}{c}\frac{\partial}{\partial t_1}(\mathbb{E}_{jm}^*\mathbb{E}_{jm}) + \varepsilon_{jkl}(\mathbb{E}_{jm}^*\partial_k^1\mathbb{S}_{lm} + \mathbb{E}_{jm}\partial_k^1\mathbb{S}_{lm}^*) = 0. \quad (33)$$

After adding (32) to (33), we readily obtain

$$\frac{\partial}{\partial t_1}W(\mathbf{x}_1, t_1; \mathbf{x}_2, t_2) + \partial_k^1\mathbf{T}_k(\mathbf{x}_1, t_1; \mathbf{x}_2, t_2) = 0, \quad (34)$$

where

$$W(\mathbf{x}_1, t_1; \mathbf{x}_2, t_2) = \mathbb{E}_{jm}^*\mathbb{E}_{jm} + \mathbb{S}_{jm}^*\mathbb{S}_{jm}, \quad (35)$$

$$\mathbf{T}_k(\mathbf{x}_1, t_1; \mathbf{x}_2, t_2) = c\varepsilon_{klj}(\mathbb{S}_{lm}\mathbb{E}_{jm}^* + \mathbb{S}_{lm}^*\mathbb{E}_{jm}). \quad (36)$$

Apart from a constant factor, (34) has a formal resemblance to that of the classical theory (see [7, Equation (3.5)]), while the physical meaning has received much less attention in the latter. From its formal analogy to energy conservation law in electromagnetism, we note that (34) is a continuity equation in which the scalar quantity $W(\mathbf{x}_1, t_1; \mathbf{x}_2, t_2)$ may be regarded as representing an energy-density-like quantity of quantum correlation (which we term the *quantum-correlation-function energy density*) and the vector quantity $\mathbf{T}(\mathbf{x}_1, t_1; \mathbf{x}_2, t_2)$ as representing a flow-density-like quantity of quantum correlation (which we term the *quantum-correlation-function flow density*). Just as the magnitude and the direction of the Poynting vector represent, respectively, the field intensity and the direction of light energy flow in classic optics, the magnitude and the direction of the quantum-correlation-function flow density vector $\mathbf{T}(\mathbf{x}_1, t_1; \mathbf{x}_2, t_2)$ give, respectively, a measure of the intensity of quantum correlation and the direction of the quantum correlation flow. If we integrate (34) throughout a volume V bounded by a closed surface S and apply Gauss' theorem, we have

$$\begin{aligned} \frac{d}{dt_1} \iiint_V W(\mathbf{x}_1, t_1; \mathbf{x}_2, t_2) d^3x_1 \\ + \iint_S \mathbf{T}(\mathbf{x}_1, t_1; \mathbf{x}_2, t_2) \cdot \mathbf{n} d^2x_1 = 0, \end{aligned} \quad (37)$$

where \mathbf{n} denotes the unit outward normal to S . Equation (37) may be given the following interpretation. The rate of increase (or decrease) of the quantum-correlation-function energy contained in V is equal to the rate at which the quantum-correlation-function energy enters (or leaves) V through the boundary S via the quantum-correlation-function flow. With this interpretation (34) expresses the *conservation law of quantum-correlation-function energy*, which may be regarded as natural generalizations of those obtained on the basis of classical scalar coherence theory [15].

5. Conservation Law of Quantum-Correlation-Function Momentum

Now, let us consider a new law on the conservation of a momentum-like quantity in quantum correlation theory. If we take the complex conjugate of (15) and multiply by $\varepsilon_{inj}\mathbb{E}_{nm}$ and make use of tensor identity $\varepsilon_{jkl}\varepsilon_{inj} = \varepsilon_{klj}\varepsilon_{inj} = \delta_{ki}\delta_{ln} - \delta_{kn}\delta_{li}$ (where δ_{ki} is equal to zero if $k \neq i$, and equal to unity if $k = i$), we then obtain

$$-\mathbb{E}_{nm}\partial_i^1\mathbb{E}_{nm}^* + \mathbb{E}_{nm}\partial_n^1\mathbb{E}_{im}^* + \mathbb{E}_{im}^*\partial_n^1\mathbb{E}_{nm} + \frac{1}{c}\varepsilon_{inj}\mathbb{E}_{nm}\frac{\partial}{\partial t_1}\mathbb{S}_{jm}^* = 0, \quad (38)$$

where the use has been made of the divergence-free condition in (19). Similarly, if we apply the similar operation to (16) and use the tensor identity, we have

$$-\mathbb{S}_{nm}\partial_i^1\mathbb{S}_{nm}^* + \mathbb{S}_{nm}\partial_n^1\mathbb{S}_{im}^* + \mathbb{S}_{im}^*\partial_n^1\mathbb{S}_{nm} + \frac{1}{c}\varepsilon_{inj}\mathbb{S}_{jm}\frac{\partial}{\partial t_1}\mathbb{E}_{nm}^* = 0, \quad (39)$$

where the use has also been made of the divergence-free condition in (20). Let us add (38) and its complex conjugate to (39) and its complex conjugate; we finally arrive at

$$\frac{\partial}{\partial t_1}\mathbb{T}_i(\mathbf{x}_1, t_1; \mathbf{x}_2, t_2) + \partial_k^1\mathbb{W}_{ki}(\mathbf{x}_1, t_1; \mathbf{x}_2, t_2) = 0, \quad (40)$$

where

$$\mathbb{T}_i = \frac{\mathbf{T}_i}{c^2} = \frac{1}{c}\varepsilon_{ikj}\left(\mathbb{S}_{km}\mathbb{E}_{jm}^* + \mathbb{S}_{km}^*\mathbb{E}_{jm}\right), \quad (41)$$

$$\begin{aligned} \mathbb{W}_{ki} &= \left(\mathbb{E}_{km}\mathbb{E}_{im}^* + \mathbb{E}_{km}^*\mathbb{E}_{im}\right) - \delta_{ki}\left(\mathbb{E}_{km}\mathbb{E}_{km}^*\right) \\ &+ \left(\mathbb{S}_{km}\mathbb{S}_{im}^* + \mathbb{S}_{km}^*\mathbb{S}_{im}\right) - \delta_{ki}\left(\mathbb{S}_{km}\mathbb{S}_{km}^*\right). \end{aligned} \quad (42)$$

If we integrate (40) throughout the volume V bounded by a closed surface S and apply Gauss' theorem in the tensor form, we have

$$\begin{aligned} \frac{d}{dt_1}\iiint_V\mathbb{T}_i(\mathbf{x}_1, t_1; \mathbf{x}_2, t_2)d^3x_1 \\ + \iint_S\mathbb{W}_{ki}(\mathbf{x}_1, t_1; \mathbf{x}_2, t_2)n_kd^2x_1 = 0, \end{aligned} \quad (43)$$

where n_k is the k component of unit outward normal vector \mathbf{n} . From its formal analogy to momentum conservation law in electromagnetism, we interpret the vector $\mathbb{T}(\mathbf{x}_1, t_1; \mathbf{x}_2, t_2)$ as a momentum-density-like quantity of quantum correlation (which we term the *quantum-correlation-function momentum density*). Furthermore, the symmetric tensor $\mathbb{W}_{ki}(\mathbf{x}_1, t_1; \mathbf{x}_2, t_2)$ may be regarded as a Maxwell-stress-tensor-like quantity of quantum correlation (which we term the *quantum-correlation-function stress tensor*), representing the flux of the k th component of the *quantum-correlation-function* momentum in the i th direction. Hence, the above equation states that the rate of gain (or loss) of quantum-correlation-function momentum in the closed volume is equal to the flux of quantum-correlation-function momentum flowing into (or out of) the volume across the bounding surface. With this interpretation, (40) expresses the *conservation law of quantum-correlation-function momentum*, which bears a striking resemblance to the classical one [16, 17].

6. Relation between Energy and Momentum in Quantum Correlation Function

Borrowing from the classical optics [18], we can introduce some geometrical concepts to represent the quantum-correlation-function flow. Let us consider the propagation of the quantum correlation function with a speed c through

an area S normal to the direction of propagation. During a very small interval of time Δt , only the quantum-correlation-function energy contained in the cylindrical volume, $(c\Delta tS)W$, will flow across S . We now make the reasonable assumption (for vacuum) that the quantum-correlation-function flow is in the direction of propagation of the quantum correlation. The magnitude of the corresponding quantum-correlation-function flow is then

$$|\mathbf{T}| = \frac{c\Delta tSW}{\Delta tS} = cW. \quad (44)$$

Since $\mathbb{T}c^2 = \mathbf{T}$ (in (41)), we can express the quantum-correlation-function energy in terms of the magnitude of the quantum-correlation-function momentum, namely,

$$W = c|\mathbb{T}|. \quad (45)$$

Notice, from (45), that if some amount of quantum-correlation-function energy W is transported per square meter per second, then there will be a corresponding quantum-correlation-function momentum W/c transported per square meter per second. Thus, the mathematical relation between the energy and momentum in quantum correlation function is essentially identical to the energy-momentum relation in classical electrodynamics.

7. Conservation of Quantum-Correlation-Function Angular Momentum

Finally, we remark that the quantum-correlation-function angular momentum in quantum theory of optical coherence can also be treated in a similar way. The angular momentum density associated with the correlation tensors of the quantized field is given by

$$\mathbb{L}_m(\mathbf{x}_1, t_1; \mathbf{x}_2, t_2) = \varepsilon_{mji}x_j\mathbb{T}_i(\mathbf{x}_1, t_1; \mathbf{x}_2, t_2), \quad (46)$$

where \mathbb{T}_i is the quantum-correlation-function momentum density discussed above. The flux of angular momentum density in quantum correlation function is given by

$$\mathbb{M}_{mk}(\mathbf{x}_1, t_1; \mathbf{x}_2, t_2) = \varepsilon_{mji}x_j\mathbb{W}_{ik}(\mathbf{x}_1, t_1; \mathbf{x}_2, t_2), \quad (47)$$

where \mathbb{W}_{ki} is the quantum-correlation-function stress tensor given above. Conservation of angular momentum in quantum correlation function is also expressed by

$$\frac{\partial}{\partial t_1}\mathbb{L}_m(\mathbf{x}_1, t_1; \mathbf{x}_2, t_2) + \partial_k^1\mathbb{M}_{mk}(\mathbf{x}_1, t_1; \mathbf{x}_2, t_2) = 0, \quad (48)$$

which again bears the close analogy to the classical theories of coherence [17].

8. Specific Examples and Physical Interpretations

So far, on the basis of the theory of the quantized electromagnetic field, we have introduced some vector and tensor

densities to the quantum theory of optical coherence and have developed a very close analogy between the quantum mechanical and classical theories of coherence. To offer much more penetrating insights into the role played by quantum-correlation-function conservations in the description of the coherence properties of the quantized field, we will carry out mathematical development through the use of some particular sets of quantum states. Without loss of generality, the expansion for the vector potential of the quantized multimode electromagnetic field with its linear polarization along the \hat{x} -direction takes the form

$$\begin{aligned} \hat{\mathbf{A}}_x(z, t) &= \frac{c}{L^{3/2}} \sum_m \left[\frac{\hbar}{(2\omega_m)} \right]^{1/2} \\ &\times \left\{ \hat{a}_m \exp \left[i\omega_m \left(\frac{z}{c} - t \right) \right] + h.c. \right\}, \end{aligned} \quad (49)$$

where ω_m is the angular frequency of the m th mode, L is the side length of a cubical volume, and $h.c.$ stands for the Hermitian conjugate of the preceding term. From the expansions for the vector potential $\hat{\mathbf{A}}$ of the electromagnetic field, the electric and magnetic field operators $\hat{\mathbf{E}}$ and $\hat{\mathbf{H}}$ can therefore be written as

$$\begin{aligned} \hat{\mathbf{E}}_x(z, t) &= \hat{\mathbf{H}}_y(z, t) \\ &= \frac{i}{L^{3/2}} \sum_m \left(\frac{\hbar\omega_m}{2} \right)^{1/2} \\ &\times \left\{ \hat{a}_m \exp \left[i\omega_m \left(\frac{z}{c} - t \right) \right] + h.c. \right\}. \end{aligned} \quad (50)$$

By inserting the operators of the quantized fields $\hat{\mathbf{E}}$ and $\hat{\mathbf{H}}$ into the definition for energy coherence tensor \mathbb{E}_{jk} and the energy-flow coherence tensor \mathbb{S}_{jk} , we can evaluate the proposed quantum-correlation-function energy W and quantum-correlation-function momentum \mathbb{T} at some particular set of quantum states of the field.

8.1. Quantum Correlation Function in Fock States. As a first example, consider a multimode of the electromagnetic field in an eigenstate of Fock states (photon number states). After calculating the \mathbf{E} -only correlation tensor, \mathbf{H} -only correlation tensor, and \mathbf{EH} mixed-correlation tensors from (1), we have

$$\begin{aligned} E_{xx} &= H_{yy} = M_{xy} = N_{yx} \\ &= \frac{\hbar}{2L^3} \sum_m \left\{ \omega_m \langle n_m \rangle \exp \left[i\omega_m \left(\frac{z_2}{c} - t_2 - \frac{z_1}{c} + t_1 \right) \right] \right\} \\ &= \frac{\hbar}{2L^3} \sum_m \phi_m, \end{aligned} \quad (51)$$

where $\text{Tr}\{\hat{\rho}\hat{a}_m^\dagger\hat{a}_m\} = \langle n_m \rangle$ is the average photon number of the m th mode, and we have put for short $\phi_m = \omega_m \langle n_m \rangle \exp[i\omega_m(z_2/c - t_2 - z_1/c + t_1)]$. Substituting from (51)

into (17)-(18), we obtain

$$\mathbb{E} = \begin{pmatrix} \frac{\hbar}{2L^3} \sum_m \phi_m & 0 & 0 \\ 0 & \frac{\hbar}{2L^3} \sum_m \phi_m & 0 \\ 0 & 0 & 0 \end{pmatrix}, \quad (52)$$

$$\mathbb{S} = \begin{pmatrix} 0 & \frac{\hbar}{2L^3} \sum_m \phi_m & 0 \\ -\frac{\hbar}{2L^3} \sum_m \phi_m & 0 & 0 \\ 0 & 0 & 0 \end{pmatrix}. \quad (53)$$

Apart from a constant factor, the elements of the energy and energy flow coherence tensors are represented as the sum of many elementary phasor contributions ϕ_m . Thus, the density of quantum-correlation-function energy is proportional to the square of the absolute value of this sum. After substituting (52)-(53) into (35), we have

$$W = 4 \left(\frac{\hbar}{2L^3} \sum_m \phi_m \right) \left(\frac{\hbar}{2L^3} \sum_m \phi_m \right)^* = \frac{\hbar^2}{L^6} \left| \sum_m \phi_m \right|^2. \quad (54)$$

Equation (54) evidently introduces the phenomenon of interference into the scheme of the quantum theory of optical coherence. After straightforward algebra, the quantum-correlation-function energy is readily shown to be

$$\begin{aligned} W &= \frac{\hbar^2}{L^6} \left\{ \sum_m \omega_m^2 \langle n_m \rangle^2 + 2 \sum_{m \neq l} \omega_m \omega_l \langle n_m \rangle \langle n_l \rangle \right. \\ &\quad \left. \times \cos[(\omega_m - \omega_l)(z_2/c - t_2 - z_1/c + t_1)] \right\}. \end{aligned} \quad (55)$$

It is immediately seen from (55) that the density of quantum-correlation-function energy will depend on the two spatiotemporal variables only through their difference and has both particle and wave manifestations. For the single-point correlation function, where $z_1 = z_2, t_1 = t_2$, we have

$$W = \frac{1}{L^6} \left[\sum_m (\langle n_m \rangle \hbar \omega_m) \right]^2. \quad (56)$$

Thus the quantum-correlation-function energy density is discrete with particle behavior. Meanwhile, the quantum-correlation-function energy density has uniform distribution for all the spatiotemporal position. Meanwhile, the quantum-correlation-function energy density exhibits wave-like features for the two-point correlation in photon delayed coincidence. With this interpretation, (55) expresses the simultaneous wave-particle duality of quantum-correlation-function energy density. The dynamical behavior of the quantum correlation is governed by the total quantum-correlation-function energy that takes the form

$$\begin{aligned} \mathcal{W} &= \int_V W(\mathbf{x}_1, t_1; \mathbf{x}_2, t_2) d^3x_1 \\ &= \frac{1}{L^3} \sum_m \hbar^2 \omega_m^2 \langle n_m \rangle^2. \end{aligned} \quad (57)$$

Similarly, with the use of (52)-(53) for the expressions of the quantum energy and energy flow coherence tensor, the quantum-correlation-function momentum vector density has only $\hat{\mathbf{z}}$ -direction component:

$$\begin{aligned} \mathbb{T}_z = \frac{\hbar^2}{cL^6} & \left\{ \sum_m \omega_m^2 \langle n_m \rangle^2 + 2 \sum_{m \neq l} \omega_m \omega_l \langle n_m \rangle \langle n_l \rangle \right. \\ & \left. \times \cos \left[\left(\omega_m - \omega_l \right) \left(\frac{z_2}{c} - t_2 - \frac{z_1}{c} + t_1 \right) \right] \right\}. \end{aligned} \quad (58)$$

As expected, the quantum-correlation-function momentum also exhibits the wave-particle duality. Then, the total quantum-correlation-function momentum within the cubical volume is

$$\mathcal{T}_z = \int_V \mathbb{T}_z(\mathbf{x}_1, t_1; \mathbf{x}_2, t_2) d^3x_1 = \frac{1}{cL^3} \sum_m \hbar^2 \omega_m^2 \langle n_m \rangle^2. \quad (59)$$

From the formal analogy to the concept of single photon in quantum optics, we may envision the quantum correlation of a single mode carrying a discrete quantum-correlation-function energy $\mathcal{W} = \langle n \rangle^2 \hbar^2 \omega^2 / L^3$ with a quantum-correlation-function momentum $\mathcal{T}_z = \mathcal{W}/c = \langle n \rangle^2 \hbar^2 \omega^2 / (cL^3)$.

In light of the wave-particle duality of quantum physics, it is natural for the photon to carry the properties of both waves and of particles. Owing the Wolf [19], it has been known since 1955 that the optical coherence exhibits wave properties since the coherence function obeys a couple of wave equations. Here, it is interesting to note that, besides wave properties, the quantum correlation function also has particle nature since the correlations between the discrete photons (photon correlations) play the essential role in the quantum theory of optical coherence.

8.2. Quantum Correlation in Coherent States. In quantum optics, it is also common practice to describe the state of the photon field in terms of coherent states [4, 5]. As stressed by Glauber, one of the important properties for the coherent states is that the correlation functions can be factorized if the field is in coherent state. Therefore, the first-order correlation functions reduce to the factorized forms:

$$\begin{aligned} E_{jk}(\mathbf{x}_1, t_1; \mathbf{x}_2, t_2) &= \mathcal{E}_j^*(\mathbf{x}_1, t_1) \mathcal{E}_k(\mathbf{x}_2, t_2), \\ H_{jk}(\mathbf{x}_1, t_1; \mathbf{x}_2, t_2) &= \mathcal{H}_j^*(\mathbf{x}_1, t_1) \mathcal{H}_k(\mathbf{x}_2, t_2), \\ M_{jk}(\mathbf{x}_1, t_1; \mathbf{x}_2, t_2) &= \mathcal{E}_j^*(\mathbf{x}_1, t_1) \mathcal{H}_k(\mathbf{x}_2, t_2), \\ N_{jk}(\mathbf{x}_1, t_1; \mathbf{x}_2, t_2) &= \mathcal{H}_j^*(\mathbf{x}_1, t_1) \mathcal{E}_k(\mathbf{x}_2, t_2), \end{aligned} \quad (60)$$

in which the functions $\mathcal{E}(\mathbf{x}, t)$, and $\mathcal{H}(\mathbf{x}, t)$ and their corresponding complex conjugates play the role of the eigenvalue and satisfy the Maxwell equations. According to (50), the eigenvalue functions $\mathcal{E}_j(\mathbf{x}, t)$ and $\mathcal{H}_j(\mathbf{x}, t)$ are thus given by

$$\begin{aligned} \mathcal{E}_x(z, t) &= \mathcal{H}_y(z, t) \\ &= \frac{i}{L^{3/2}} \sum_m \left(\frac{\hbar \omega_m}{2} \right)^{1/2} \alpha_m \exp \left[i \omega_m \left(\frac{z}{c} - t \right) \right], \end{aligned} \quad (61)$$

where α_m is eigenvalue of the annihilation operator \hat{a}_m , that is, $\hat{a}_m |\alpha_m\rangle = \alpha_m |\alpha_m\rangle$. As we readily see, the energy and energy flow coherence tensors of the quantized field satisfy

$$\begin{aligned} \mathbb{E} &= \begin{pmatrix} \mathcal{E}_x^*(z_1, t_1) \mathcal{E}_x(z_2, t_2) & 0 & 0 \\ 0 & \mathcal{H}_y^*(z_1, t_1) \mathcal{H}_y(z_2, t_2) & 0 \\ 0 & 0 & 0 \end{pmatrix}, \\ \mathbb{S} &= \begin{pmatrix} 0 & \mathcal{E}_x^*(z_1, t_1) \mathcal{H}_y(z_2, t_2) & 0 \\ -\mathcal{H}_y^*(z_1, t_1) \mathcal{E}_x(z_2, t_2) & 0 & 0 \\ 0 & 0 & 0 \end{pmatrix}. \end{aligned} \quad (62)$$

Using the results of (62), we find that

$$\begin{aligned} W &= \left[|\mathcal{E}_x(z_1, t_1)|^2 + |\mathcal{H}_y(z_1, t_1)|^2 \right] \\ &\quad \times \left[|\mathcal{E}_x(z_2, t_2)|^2 + |\mathcal{H}_y(z_2, t_2)|^2 \right] \\ &= 4 |\mathcal{E}_x(z_1, t_1)|^2 \cdot |\mathcal{E}_x(z_2, t_2)|^2. \end{aligned} \quad (63)$$

Similarly, the quantum-correlation-function momentum density takes the form

$$\begin{aligned} \mathbb{T}_z &= 2c^{-1} \text{Re} \left\{ \mathcal{E}_x^*(z_1, t_1) \mathcal{H}_y(z_1, t_1) \right\} \\ &\quad \times \left[|\mathcal{E}_x(z_2, t_2)|^2 + |\mathcal{H}_y(z_2, t_2)|^2 \right] \\ &= 4c^{-1} |\mathcal{E}_x(z_1, t_1)|^2 \cdot |\mathcal{E}_x(z_2, t_2)|^2 = \frac{W}{c}, \end{aligned} \quad (64)$$

where $\text{Re}\{\dots\}$ stands for the real part of the complex eigenvalue. After substituting (61) into (63)-(64), we see that the coherent state of a single mode has quantum-correlation-function energy $\mathcal{W} = (\hbar \omega)^2 |\alpha|^4 / L^3$ with quantum-correlation-function momentum $\mathcal{T}_z = c(\hbar k)^2 |\alpha|^4 / L^3$.

Up to now we have considered the conservation laws in the quantum correlation function based on the correlation tensors of first-order only. It should also be noted that the generalization to higher-order correlation tensors can also be derived in a similar way.

Meanwhile, the proposed conservation laws in quantum correlation function may also provide an insight into other correlation phenomena in quantum mechanics. For example, the Einstein-Podolsky-Rosen (EPR) paradox draws on a phenomenon predicted by quantum mechanics, known as quantum entanglement, to show that measurements performed on spatially separated parts of a quantum system can apparently have an instantaneous influence on one another [20]. Since photons are emitted from a common source, correlations between these photons have already been established once an entangled state is created [21, 22]. In an entangled two-photon state, a measurement of one chosen variable of photon one will determine the outcome of a measurement of the corresponding variable of the other photons. No matter how far apart for these two photons, the proposed conservation laws always hold for this quantum system. It is these conservation laws for quantum correlation function that add an additional condition for

the propagation of the separated photons in their entangled state when no influence resulting from one measurement can possibly propagate to the other photon in the available time. This may give the origin of the nonlocal behavior or spooky action at a distance for quantum mechanics.

9. Conclusion

In summary, we have derived the expressions for energy coherence tensor and the energy-flow coherence tensor on the basis of quantum field theory, which provides new insights into photon statistics and quantum correlation. In terms of an electromagnetic model, we have introduced new quantities to quantum theory of optical coherence based on newly defined quantum optical coherence tensors and have related them by continuity equations, giving new conservation laws in quantum correlation function. Furthermore, we have theoretically investigated the propagation of quantum correlation function, which establishes a new relationship between the photon correlation and quantum electrodynamics and reveals the wave-particle duality of quantum correlation. Further exploration in this direction may lead to a new field in quantum optics that may be referred to as *Quantum Correlation Dynamics*.

Acknowledgments

The authors are indebted to Zhengwei Zhou for his helpful discussion. Part of this work was supported by Grant-in-Aid of JSPS B no. 21360028 and by The 21st Century Center of Excellence (COE) Program on “Innovation of Coherent Optical Science” granted to The University of Electro-Communications.

References

- [1] L. Mandel and E. Wolf, *Optical Coherence and Quantum Optics*, Cambridge University Press, Cambridge, UK, 1995.
- [2] J. Perina, *Quantum Statistics of Linear and Nonlinear Optical Phenomena*, Kluwer Academic, Dordrecht, The Netherlands, 1991.
- [3] R. J. Glauber, “Photon correlations,” *Physical Review Letters*, vol. 10, pp. 84–86, 1963.
- [4] R. J. Glauber, “The quantum theory of optical coherence,” *Physical Review*, vol. 130, no. 6, pp. 2529–2539, 1963.
- [5] R. J. Glauber, “Coherent and incoherent states of the radiation field,” *Physical Review*, vol. 131, no. 6, pp. 2766–2788, 1963.
- [6] C. L. Mehta and E. Wolf, “Coherence properties of blackbody radiation. II. Correlation tensors of the quantized field,” *Physical Review*, vol. 134, no. 5A, pp. A1149–A1153, 1964.
- [7] P. Roman and E. Wolf, “Correlation theory of stationary electromagnetic fields—part II: conservation laws,” *Il Nuovo Cimento*, vol. 17, no. 4, pp. 477–490, 1960.
- [8] E. C. G. Sudarshan, “Equivalence of semiclassical and quantum mechanical descriptions of statistical light beams,” *Physical Review Letters*, vol. 10, no. 7, pp. 277–279, 1963.
- [9] J. R. Klauder, “Improved version of optical equivalence theorem,” *Physical Review Letters*, vol. 16, no. 12, pp. 534–536, 1966.
- [10] O. D. Kellogg, *Foundations of Potential Theory*, Dover, New York, NY, USA, 1954.
- [11] M. Hillery and L. D. Mlodinow, “Quantization of electrodynamics in nonlinear dielectric media,” *Physical Review A*, vol. 30, no. 4, pp. 1860–1865, 1984.
- [12] S. Serulnik and Y. Ben-Aryeh, “Space-time description of propagation in nonlinear dielectric media,” *Quantum Optics*, vol. 3, no. 1, pp. 63–74, 1991.
- [13] Y. Aharonov and D. Bohm, “Significance of electromagnetic potentials in the quantum theory,” *Physical Review*, vol. 115, no. 3, pp. 485–491, 1959.
- [14] W. Wang, Z. Duan, S. G. Hanson, Y. Miyamoto, and M. Takeda, “Experimental study of coherence vortices: local properties of phase singularities in a spatial coherence function,” *Physical Review Letters*, vol. 96, no. 7, Article ID 073902, 4 pages, 2006.
- [15] W. Wang and M. Takeda, “Coherence current, coherence vortex, and the conservation law of coherence,” *Physical Review Letters*, vol. 96, no. 22, Article ID 223904, 4 pages, 2006.
- [16] P. Roman, “Correlation theory of stationary electromagnetic fields. Part IV. Second order conservation laws,” *Il Nuovo Cimento*, vol. 22, no. 5, pp. 1005–1011, 1961.
- [17] W. Wang and M. Takeda, “Linear and angular coherence momenta in the classical second-order coherence theory of vector electromagnetic fields,” *Optics Letters*, vol. 31, no. 17, pp. 2520–2522, 2006.
- [18] E. Hecht, *Optics*, Addison Wesley, Boston, Mass, USA, 2001.
- [19] E. Wolf, “A macroscopic theory of interference and diffraction of light from finite sources. II. Fields with a spectral range of arbitrary width,” *Proceedings of the Royal Society A*, vol. 230, no. 1181, pp. 246–265, 1955.
- [20] A. Einstein, B. Podolsky, and N. Rosen, “Can quantum-mechanical description of physical reality be considered complete?” *Physical Review*, vol. 47, no. 10, pp. 777–780, 1935.
- [21] D. Bohm, “A suggested interpretation of the quantum theory in terms of “hidden” variables. I,” *Physical Review*, vol. 85, no. 2, pp. 166–179, 1952.
- [22] D. Bohm, “A suggested interpretation of the quantum theory in terms of “hidden” variables. II,” *Physical Review*, vol. 85, no. 2, pp. 180–193, 1952.

Research Article

Asymptotic Principal Values and Regularization Methods for Correlation Functions with Reflective Boundary Conditions

Masafumi Seriu

Department of Physics, Graduate School of Engineering, University of Fukui, Fukui 910-8507, Japan

Correspondence should be addressed to Masafumi Seriu, mseriu@edu00.f-edu.u-fukui.ac.jp

Received 26 November 2009; Accepted 12 March 2010

Academic Editor: Igor I. Mokhun

Copyright © 2010 Masafumi Seriu. This is an open access article distributed under the Creative Commons Attribution License, which permits unrestricted use, distribution, and reproduction in any medium, provided the original work is properly cited.

We introduce a concept of asymptotic principal values which enables us to handle rigorously singular integrals of higher-order poles encountered in the computation of various quantities based on correlation functions of a vacuum. Several theorems on asymptotic principal values are proved, and they are expected to become bases for investigating and developing some classes of regularization methods for singular integrals. We make use of these theorems for analyzing mutual relations between some regularization methods, including a method naturally derived from asymptotic principal values. It turns out that the concept of asymptotic principal values and the theorems for them are quite useful in this type of analysis, providing a suitable language to describe what is discarded and what is retained in each regularization method.

1. Introduction

Physics of quantum vacuum fluctuations is one of the intriguing research topics expected to be developed through the interplay between theories, experiments, and practical applications.

Investigations of quantum vacuum fluctuations even stimulate the border area between physics and mathematics. As a typical example of this sort, we often encounter singular integrals in computing several quantities based on correlation functions of a vacuum in question. The occurrence of singularity or divergence is often a signal of surpassing the border of validity of a model by too much extrapolation. Furthermore, it could originate from deeper physical processes for which satisfactory consistent mathematics is still unavailable. How to handle singular integrals can be then a challenging topic, requiring both mathematical analysis and physical considerations.

Faced with singular integrals, we need to resort to some regularization method to get a finite result. The aim of this paper is to give an organized mathematical basis underlying some typical regularization methods and make clear their mutual relations. We introduce below a concept of *asymptotic principal values* which can be a key tool to

analyze some classes of regularization methods. We then prove several theorems on the asymptotic principal values useful for studying regularization procedures.

There are still various uncertainties to clear up in regularization methods, reflecting our lack of mathematical basis for handling infinities. In this situation, we cannot expect any universal regularization method, but we need to customize the method by try and error depending on the problem in question. It is far from the aim of this paper to judge which method is better than the others. It just tries to present a concrete mathematical basis for further considerations and developments of better regularization methods.

The organization of the paper is as follows. In Section 2, we present one simple example where singular integrals of a higher-order pole emerge. The origin of singularities in this example is physically clear and we can get some idea on how these integrals should be regularized. In Section 3, we introduce *asymptotic principal values* which describe precisely how singular integrals behave, which can be useful for investigating and developing several regularization methods. We then prove several useful theorems on the asymptotic principal values. In Section 4, we analyze some typical regularization methods by means of theorems prepared in

the previous section. Section 5 is devoted for a summary and several discussions.

2. Typical Example of Singular Integrals

Let us consider as an example the measurement of the electromagnetic vacuum fluctuations in a half-space bounded by a perfectly reflecting infinite mirror. Recently the switching effect [1] and the smearing effect due to the quantum spread of a probe particle [2] have been analyzed by studying the measurement process of the Brownian particle released in this environment.

We thus take a model introduced in [3] and reanalyzed in [1, 2]. Suppose that a flat, infinitely spreading mirror of perfect reflectivity is placed on the xy -plane ($z = 0$). Then let us investigate the quantum vacuum fluctuations of the electromagnetic field inside the half-space $z > 0$ by releasing a classical charged probe-particle with mass m and charge e in the environment. We can estimate the quantum fluctuations of the vacuum through the velocity dispersions of the probe-particle released in the environment.

When the velocity of the probe-particle is much smaller than the light velocity c , the motion for the particle is described by

$$m \frac{d\vec{v}}{dt} = e\vec{E}(\vec{x}, t), \quad (1)$$

where $\vec{E}(\vec{x}, t)$ is the electric field.

Within the time-period when the particle does not move so much, (1) along with the initial condition $\vec{v}(0) = \vec{v}_0$ is solved approximately as

$$\vec{v}(t) \simeq \vec{v}_0 + \frac{e}{m} \int_0^t \vec{E}(\vec{x}, t') dt'. \quad (2)$$

For simplicity, let us consider only the ‘‘sudden-switching’’ case; the measurement is switched on abruptly, stably continued for τ [sec] before switched off abruptly. It is mathematically described by a step-like switching function without any switching tails. The velocity dispersions of the particle, $\langle \Delta v_i^2 \rangle$ ($i = x, y, z$), are then given by

$$\langle \Delta v_i^2(\vec{x}, \tau) \rangle = \frac{e^2}{m^2} \int_0^\tau dt' \int_0^\tau dt'' \langle E_i(\vec{x}, t') E_i(\vec{x}, t'') \rangle_R, \quad (3)$$

by noting that $\langle E_i(\vec{x}, t) \rangle_R = 0$. Here $\langle E_i(\vec{x}, t') E_i(\vec{x}, t'') \rangle_R$ ($i = x, y, z$) are the renormalized two-point correlation functions of the electric field (the suffix ‘‘R’’ is for ‘‘renormalized’’). Now $\langle E_i(\vec{x}, t') E_i(\vec{x}, t'') \rangle_R$ ($i = x, y, z$) are computed [4] as

$$\begin{aligned} \langle E_z(\vec{x}, t') E_z(\vec{x}, t'') \rangle_R &= \frac{1}{\pi^2} \frac{1}{(T^2 - (2z)^2)^2}, \\ \langle E_x(\vec{x}, t') E_x(\vec{x}, t'') \rangle_R &= \langle E_y(\vec{x}, t') E_y(\vec{x}, t'') \rangle_R \\ &= -\frac{1}{\pi^2} \frac{T^2 + 4z^2}{(T^2 - (2z)^2)^3}, \end{aligned} \quad (4)$$

where $T := t' - t''$. (We set $c = \hbar = 1$ hereafter throughout the paper.)

It is obvious that the integral in (3) is regular when $\tau < 2z$, but singular when $\tau > 2z$, reflecting the singularity at $|T| = 2z$ inherent in the correlation functions $\langle E_i(\vec{x}, t') E_i(\vec{x}, t'') \rangle_R$ given in (4).

For the present purpose, it suffices to show only the result of $\langle \Delta v_z^2 \rangle$ for $\tau > 2z$ [1]

$$\langle \Delta v_z^2 \rangle = \frac{e^2}{32\pi^2 m^2} \left\{ \frac{\tau}{z^3} \ln \left(\frac{\tau + 2z}{\tau - 2z} \right)^2 + \frac{8(1 - 2z/\tau)}{z^2 \rho} + O(\rho) \right\} \quad (5)$$

$$\sim \frac{e^2}{4\pi^2 m^2 z^2} \left(1 + \frac{1}{\rho} \right) \quad (\text{for } \tau \gg 2z), \quad (6)$$

where $\rho (> 0)$ is a dimension-free asymptotic parameter for handling the singular integral properly (see Section 3 for details). Accordingly the above expression should be understood as an asymptotic expression as $\rho \sim 0$.

This result is derived by a formula for an *asymptotic principal value*, the rigorous definition of which shall be given in the next section,

$$\wp_{(\rho)} \int_0^1 dx \frac{1-x}{(x^2 - \sigma^2)^2} = \frac{1}{8\sigma^3} \ln \left(\frac{1+\sigma}{1-\sigma} \right)^2 + \frac{1-\sigma}{2\sigma^2 \rho} + O(\rho), \quad (7)$$

for $0 < \sigma < 1$. One can derive (7) with the help of Theorem 1; a more direct derivation is also found in *Appendix C* of [1].

Leaving the rigorous treatment of singular integrals for the next section, we here focus on the physical reason why the singularity of correlation functions occurs at $|T| = 2z$. Due to the mirror reflections of signals with the light velocity, the values of the electric field at the two world-points (t', x, y, z) and (t'', x, y, z) are expected to be strongly correlated when $|t' - t''| = 2z$. When the measuring time τ is short enough (shorter than the travel-time of the signal $2z$), then it always follows $|t' - t''| < 2z$, so that these correlations are not captured by the probe. When the measuring time is long enough ($\tau > 2z$), however, these strong correlations accumulate in the velocity fluctuations of the particle at z . Therefore it is expected that the resulting singular term of the form A/ρ ($A > 0$) contains information on the reflecting boundary.

On the other hand, typical regularization procedures [5] correspond to discarding such a singular term (e.g., the $1/\rho$ term in (6)) in effect. It should be clarified when this type of regularization is valid and when not. We shall discuss on this point in more detail in Section 4.

It turns out that the model given here is too simplified and should be modified taking into account the switching effect [1] and the smearing effect due to the quantum spread of the probe-particle [2]. However, it suffices for the present purpose of giving some example of singular integrals.

3. Basic Formulas for Handling Singular Integrals

In view of the example in the previous section, it is clear that we sometimes need to estimate a singular integral whose integrand possesses a higher-order pole. In order to investigate various regularization methods later, we first need some concrete quantity corresponding to a singular integral for which all the information is retained and nothing is discarded. Then, the following asymptotic definition of a singular integral may be relevant.

Definition 1. Let $f(x)$ be an arbitrary real function defined around an interval $[a, b]$, differentiable at $x = c$ ($a < c < b$) sufficiently many times. For a positive integer n , then, let us introduce an *asymptotic principal value* of order ρ defined by

$$\begin{aligned} \wp_{(c,\rho)}(f, n) &:= \wp_{(\rho)} \int_a^b \frac{f(x)}{(x-c)^n} dx \\ &:= \left\{ \int_a^{c-\rho} + \int_{c+\rho}^b \right\} \frac{f(x)}{(x-c)^n} dx, \end{aligned} \quad (8)$$

where ρ is a sufficiently small positive parameter.

The asymptotic principal value is a generalization of the standard Cauchy principal value, corresponding to $\lim_{\rho \rightarrow 0} \wp_{(c,\rho)}(f, 1)$, in two ways. First, the order of singularity n can be greater than 1. Second, only the asymptotic behavior as $\rho \sim 0$ is concerned and the convergence for the limit $\rho \rightarrow 0$ is not necessarily required. In other words, we focus on how the integral behaves near $\rho \sim 0$ rather than the $\rho \rightarrow 0$ limit itself. In this sense, all the information is retained and no infinities are discarded in defining the asymptotic principal value.

Let us now introduce another asymptotic quantity.

Definition 2. With the same premises as in *Definition 1*, we define

$$\wp_{(\rho)} \left[\frac{f(x)}{(x-c)^n} \right]_a^b := \left[\frac{f(x)}{(x-c)^n} \right]_a^{c-\rho} + \left[\frac{f(x)}{(x-c)^n} \right]_{c+\rho}^b. \quad (9)$$

It is easily shown that

$$\wp_{(\rho)} \left[\frac{f(x)}{(x-c)^n} \right]_a^b = \left[\frac{f(x)}{(x-c)^n} \right]_a^b - \frac{1}{\rho^n} \{f\}_{(n)}^{(c,\rho)} \quad (10)$$

with

$$\{f\}_{(n)}^{(c,\rho)} := f(c+\rho) - (-)^n f(c-\rho). \quad (11)$$

By a Taylor-expansion in ρ , it is obvious that $\{f\}_{(n)}^{(c,\rho)}$ is $O(\rho)$ for an even n (when $f'(c) \neq 0$), so that the term $(1/\rho^n)\{f\}_{(n)}^{(c,\rho)}$ in (10) is $O(1/\rho^{n-1})$ and singular in the $\rho \rightarrow 0$ limit. Similarly, $\{f\}_{(n)}^{(c,\rho)}$ is $O(1)$ for an odd n (when $f(c) \neq 0$), so that $(1/\rho^n)\{f\}_{(n)}^{(c,\rho)}$ is $O(1/\rho^n)$ and singular as $\rho \rightarrow 0$.

The following definition is just for making formulas below concise.

Definition 3. We have

$$\zeta_{(c,\rho)}(f, n) := \frac{1}{n} \wp_{(\rho)} \left[\frac{f(x)}{(x-c)^n} \right]_a^b. \quad (12)$$

With these preparations, let us start with the following lemma.

Lemma 1. For any function $f(x)$ differentiable at $x = c$ and for any integer n (≥ 2), it follows that

$$\wp_{(c,\rho)}(f, n) = \frac{1}{n-1} \wp_{(c,\rho)}(f', n-1) - \zeta_{(c,\rho)}(f, n-1). \quad (13)$$

Proof. Noting that

$$\frac{1}{(x-c)^n} = -\frac{1}{n-1} \left(\frac{1}{(x-c)^{n-1}} \right)', \quad (14)$$

we have

$$\begin{aligned} \wp_{(c,\rho)}(f, n) &:= -\frac{1}{n-1} \wp_{(\rho)} \int_a^b \left(\frac{1}{(x-c)^{n-1}} \right)' f(x) dx \\ &= -\frac{1}{n-1} \left\{ \wp_{(\rho)} \left[\frac{f(x)}{(x-c)^{n-1}} \right]_a^b \right. \\ &\quad \left. - \wp_{(\rho)} \int_a^b \frac{f'(x)}{(x-c)^{n-1}} dx \right\}, \end{aligned} \quad (15)$$

where the partial-integral has been performed to get the last line. Then the equality follows. \square

We now prove a formula which relates a multipole integral with a simple-pole integral.

Theorem 1. For any function $f(x)$ differentiable sufficiently many times at $x = c$ and for any integer n (≥ 2), it follows that

$$\begin{aligned} \wp_{(c,\rho)}(f, n) &= \frac{1}{(n-1)!} \wp_{(c,\rho)}(f^{(n-1)}, 1) \\ &\quad - \sum_{k=1}^{n-1} \frac{(n-k)!}{(n-1)!} \zeta_{(c,\rho)}(f^{(k-1)}, n-k). \end{aligned} \quad (16)$$

Proof. (1°) For $n = 2$, the claimed equality reduces to

$$\wp_{(c,\rho)}(f, 2) = \wp_{(c,\rho)}(f', 1) - \zeta_{(c,\rho)}(f, 1), \quad (17)$$

which clearly holds due to Lemma 1.

(2°) Let us assume that the equality holds for a function $F(x)$ and for $n = m$ ($m \geq 2$), that is,

$$\begin{aligned} \wp_{(c,\rho)}(F, m) &= \frac{1}{(m-1)!} \wp_{(c,\rho)}(F^{(m-1)}, 1) \\ &\quad - \sum_{k=1}^{m-1} \frac{(m-k)!}{(m-1)!} \zeta_{(c,\rho)}(F^{(k-1)}, m-k). \end{aligned} \quad (18)$$

Now applying Lemma 1 for $n = m + 1$, we have

$$\begin{aligned} & \wp_{(c,\rho)}(f, m+1) \\ &= \frac{1}{m} \wp_{(c,\rho)}(f', m) - \zeta_{(c,\rho)}(f, m) \\ &= \frac{1}{m} \left\{ \frac{1}{(m-1)!} \wp_{(c,\rho)}(f^{(m)}, 1) \right. \\ &\quad \left. - \sum_{k=1}^{m-1} \frac{(m-k)!}{(m-1)!} \zeta_{(c,\rho)}(f^{(k)}, m-k) \right\} \\ &\quad - \zeta_{(c,\rho)}(f, m), \end{aligned} \quad (19)$$

where the assumed equation (18) for $F(x) = f'(x)$ has been used to get the second equality. Rearranging the summation, the last equality reduces to

$$\begin{aligned} & \wp_{(c,\rho)}(f, m+1) \\ &= \frac{1}{m!} \wp_{(c,\rho)}(f^{(m)}, 1) \\ &\quad - \sum_{k=1}^m \frac{((m+1)-k)!}{m!} \zeta_{(c,\rho)}(f^{(k-1)}, (m+1)-k). \end{aligned} \quad (20)$$

Thus the claimed equation (16) holds for $n = m + 1$.

(3°) By the mathematical induction, (16) holds for any integer n ($n \geq 2$). \square

Based on Theorem 1, it is natural to introduce a quantity $\tilde{\wp}_{(c,\rho)}(f, n)$, which is a simple-pole part plus a regular part of $\wp_{(c,\rho)}(f, n)$, putting aside singular contributions from higher-order poles.

Definition 4. We define

$$\begin{aligned} \tilde{\wp}_{(c,\rho)}(f, n) &:= \frac{1}{(n-1)!} \wp_{(c,\rho)}(f^{(n-1)}, 1) \\ &\quad - \sum_{k=1}^{n-1} \frac{(n-k-1)!}{(n-1)!} \left[\frac{f^{(k-1)}(x)}{(x-c)^{n-k}} \right]_a^b. \end{aligned} \quad (21)$$

The ‘‘mild part’’ $\tilde{\wp}_{(c,\rho)}(f, n)$ of $\wp_{(c,\rho)}(f, n)$ shall be important in the discussion of regularization methods in Section 4.

We now have a formula which enables us to separate singular contributions from a multipole integral.

Theorem 2. For any function $f(x)$ differentiable sufficiently many times at $x = c$ and for any integer n (≥ 2), it follows that

$$\begin{aligned} \wp_{(c,\rho)}(f, n) &= \tilde{\wp}_{(c,\rho)}(f, n) \\ &\quad + \sum_{k=1}^{n-1} \frac{(n-k-1)!}{(n-1)!} \frac{1}{\rho^{n-k}} \{f^{(k-1)}\}_{(n-k)}^{(c,\rho)}. \end{aligned} \quad (22)$$

Proof. It is straightforward to show this formula due to Theorem 1 along with (12) and (10). \square

Lemma 2. For any function $f(x)$ differentiable at $x = c$ and for a positive integer n , it follows that

$$\wp_{(c,\rho)}(f, n+1) = \frac{1}{n} \partial_c \wp_{(c,\rho)}(f, n) + \frac{1}{n\rho^n} \{f\}_n^{(c,\rho)}. \quad (23)$$

Proof. We compute $\partial_c \wp_{(c,\rho)}(f, n)$ directly as

$$\begin{aligned} \partial_c \wp_{(c,\rho)}(f, n) &= \partial_c \left(\left\{ \int_a^{c-\rho} + \int_{c+\rho}^b \right\} \frac{f(x)}{(x-c)^n} dx \right) \\ &= n \wp_{(c,\rho)}(f, n+1) - \frac{1}{\rho^n} \{f\}_n^{(c,\rho)}, \end{aligned} \quad (24)$$

where the second term in the last line comes from the c -derivative applied to the upper and the lower limit of the integral region. Thus the claimed equation follows. \square

Theorem 3. For any function $f(x)$ differentiable sufficiently many times at $x = c$ and for an integer n (≥ 2), it follows that

$$\tilde{\wp}_{(c,\rho)}(f, n) = \frac{1}{(n-1)!} \partial_c^{n-1} \wp_{(c,\rho)}(f, 1). \quad (25)$$

Proof. Due to Theorem 2, the claimed equation (25) is equivalent to

$$\begin{aligned} \wp_{(c,\rho)}(f, n) &= \frac{1}{(n-1)!} \partial_c^{n-1} \wp_{(c,\rho)}(f, 1) \\ &\quad + \sum_{k=1}^{n-1} \frac{(n-k-1)!}{(n-1)!} \frac{1}{\rho^{n-k}} \{f^{(k-1)}\}_{(n-k)}^{(c,\rho)}. \end{aligned} \quad (26)$$

Thus it suffices to show (26).

(1°) Let us consider the case $n = 2$, where the R.H.S. (right-hand side) of (26) becomes

$$\frac{\partial}{\partial c} \left(\left\{ \int_a^{c-\rho} + \int_{c+\rho}^b \right\} \frac{f(x)}{x-c} dx \right) + \frac{1}{\rho} \{f(c-\rho) + f(c+\rho)\}. \quad (27)$$

In this expression, the c -derivative applied to the upper and the lower limit of the integral region yields a term which exactly cancels the second term. As a result, the above expression reduces to $\wp_{(c,\rho)}(f, 2)$, that is, the L.H.S. (left-hand side) of (26). Thus (26) holds for $n = 2$.

(2°) Let us now assume that (26) holds for $n = m$ ($m \geq 2$), that is,

$$\begin{aligned} \wp_{(c,\rho)}(f, m) &= \frac{1}{(m-1)!} \partial_c^{m-1} \wp_{(c,\rho)}(f, 1) \\ &\quad + \sum_{k=1}^{m-1} \frac{(m-k-1)!}{(m-1)!} \frac{1}{\rho^{m-k}} \{f^{(k-1)}\}_{(m-k)}^{(c,\rho)}. \end{aligned} \quad (28)$$

Due to Lemma 2, then, it becomes

$$\begin{aligned} \wp_{(c,\rho)}(f, m + 1) &= \frac{1}{m} \partial_c \wp_{(c,\rho)}(f, m) + \frac{1}{m\rho^m} \{f\}_m^{(c,\rho)} \\ &= \frac{1}{m} \partial_c \left\{ \frac{1}{(m-1)!} \partial_c^{m-1} \wp_{(c,\rho)}(f, 1) \right. \\ &\quad \left. + \sum_{k=1}^{m-1} \frac{(m-k-1)!}{(m-1)!} \frac{1}{\rho^{m-k}} \{f^{(k-1)}\}_{(m-k)}^{(c,\rho)} \right\} \\ &\quad + \frac{1}{m\rho^m} \{f\}_m^{(c,\rho)}, \end{aligned} \tag{29}$$

where (28) has been used to get the last line. Noting that the relation

$$\partial_c \{f\}_m^{(c,\rho)} = \{f'\}_m^{(c,\rho)}, \tag{30}$$

which obviously holds from (11), it reduces to

$$\begin{aligned} \wp_{(c,\rho)}(f, m + 1) &= \frac{1}{m!} \partial_c^m \wp_{(c,\rho)}(f, 1) \\ &\quad + \sum_{k=1}^m \frac{(m-k)!}{m!} \frac{1}{\rho^{m-k+1}} \{f^{(k-1)}\}_{(m-k+1)}^{(c,\rho)}. \end{aligned} \tag{31}$$

Thus (26) holds for $n = m + 1$.

(3°) By the mathematical induction, (26) holds for any integer n ($n \geq 2$). Thus the claimed formula (25) has been shown. \square

4. Typical Regularization Methods and Their Mutual Relations

Based on the results in the previous section, let us now come back to the problem of regularization methods for singular integrals.

Let us consider a typical singular integral

$$I = \int_a^b \frac{f(x)}{(x-c)^n} dx \tag{32}$$

for any function $f(x)$ differentiable sufficiently many times at $x = c$ ($a < c < b$) and for a positive integer n .

4.1. Regularization Method with Partial Integrals. The first method of regularization we consider is a *method of partial integrals* which is sometimes made used of. We insert an identity

$$\frac{1}{(x-c)^n} = -\frac{1}{n-1} \left(\frac{1}{(x-c)^{n-1}} \right)', \tag{33}$$

into (32) and *formally* perform a partial integral

$$\begin{aligned} I &= -\frac{1}{n-1} \int_a^b \left(\frac{1}{(x-c)^{n-1}} \right)' f(x) dx \\ &= \frac{1}{n-1} \left\{ \int_a^b \frac{f'(x)}{(x-c)^{n-1}} dx - \left[\frac{f(x)}{(x-c)^{n-1}} \right]_a^b \right\}. \end{aligned} \tag{34}$$

In this way, the order of singularity is reduced by one. Repeating the similar procedure, the integral I is reduced to the $n = 1$ case for which the prescription of the Cauchy principal value may be applied.

Due to Theorem 2, however, it is obvious that singular terms should exist and should have been discarded by hand in the above procedure. Indeed, compared with (34) with the rigorous expression (15), it is obvious that the singularities which should reside in the second term on the R.H.S. of (34) are simply discarded by hand. Thus, in view of Theorem 2, the above method is equivalent to the simple replacement of I as

$$I \mapsto \tilde{\wp}_{(c,\rho)}(f, n). \tag{35}$$

There is still room, however, to regard the method of partial integrals as a shorthand prescription of what we here call the *method of infinitesimal imaginary part*, which is much more of theoretical grounds [5]. We shall consider this method in the next subsection.

4.2. Regularization Method with Infinitesimal Imaginary Part.

The method of infinitesimal imaginary part is based on well-known Dirac's formula [6] for an integral kernel

$$\frac{1}{(x-c) \pm i\rho} = \wp_{(c,\rho)} \frac{1}{x-c} \mp i\pi \delta(x-c), \tag{36}$$

which is most easily shown by estimating an integral $\int_a^b dx f(x)/((x-c) \pm i\rho)$ by means of an appropriate contour-integral for a suitable function $f(x)$.

By differentiating the both-sides of (36) $n - 1$ times with respect to c , and by applying Theorem 3, we get

$$\frac{1}{((x-c) \pm i\rho)^n} = \tilde{\wp}_{(\rho,c)}(\cdot, n) \mp i \frac{\pi}{(n-1)!} \delta^{(n-1)}(x-c) \tag{37}$$

in the sense of an integral kernel. Recalling *Definition 4*, however, we see that the R.H.S. is reduced to the $n = 1$ case, for which the prescription of the Cauchy principal value may be applied.

It is notable that just the introduction of some infinitesimal imaginary part results in a tamable quantity such as $\tilde{\wp}_{(\rho,c)}(\cdot, n)$ at the cost of the imaginary contribution of the second term on the R.H.S. of (37). Thus along with some causality arguments [5], it is often argued that the singular integral I should be interpreted as the real part of $\int (f(x)/((x-c) \pm i\rho)^n) dx$, that is,

$$I \mapsto \Re \int \frac{f(x)}{((x-c) \pm i\rho)^n} dx. \tag{38}$$

As far as one is evaluating *real* quantities, one may further argue that the second term on the R.H.S. of (37) shall not contribute. If so, the procedure is in effect equivalent to the replacement (35). In this sense, the method of partial integrals discussed in the previous subsection may be justified provided that it is regarded as a shorthand prescription of the method of infinitesimal imaginary part.

Another way of looking at this method is to pay attention to the L.H.S. (rather than the R.H.S.) of (37). As far as computations of real quantities are concerned, then, this method is equivalent to the replacement $1/(x-c)^n$ with $((x-c)/((x-c)^2 + \rho^2))^n$ along with taking the limit $\rho \rightarrow 0$ after evaluating the integral

$$I \mapsto \lim_{\rho \rightarrow 0} \int_a^b f(x) \left(\frac{x-c}{(x-c)^2 + \rho^2} \right)^n dx. \quad (39)$$

There is some subtle points in this method. One of them is to discard the imaginary part of the R.H.S. of (37) on the grounds that one is evaluating *real* quantities. Considering that the regularization has been achieved at the cost of introducing the imaginary part though tiny, the imaginary part should carry important information and some concern naturally arises whether one can discard it so freely.

Indeed, a simple example can be presented for which this kind of procedure fails. Let us consider an integral $I_1 = \int_{-1}^1 dx$ which is purposefully regarded as

$$I_1 = \int_{-1}^1 x \cdot \frac{1}{x} dx. \quad (40)$$

It is obvious that $I_1 = 2$. The analysis by the asymptotic principal value (see the next subsection) also results in $I_1^{(\rho)} \rightarrow 2$ in the limit $\rho \rightarrow 0$. This is because all the information is retained in the prescription of the asymptotic principal value.

On the other hand, the above-mentioned scheme makes a replacement

$$\frac{1}{x} \mapsto \frac{x}{x^2 + \rho^2} = \frac{1}{2} (\ln(x^2 + \rho^2))', \quad (41)$$

so that

$$\begin{aligned} I_1 \mapsto I_1^{(\rho)} &:= \int_{-1}^1 x \cdot \frac{1}{2} (\ln(x^2 + \rho^2))' dx \\ &= \ln(1 + \rho^2) - \int_0^1 \ln(x^2 + \rho^2) dx, \end{aligned} \quad (42)$$

where a partial integral has been performed to get the last line. However, it is clear that $I_1^{(\rho)} \rightarrow \infty$ as $\rho \rightarrow 0$, contradicting with the obvious result $I_1 = 2$.

Quite interestingly, no contradiction occurs for $I_m = \int_{-1}^1 x^m \cdot (1/x) dx$ with $m \geq 2$ since the second term in (42) becomes $-m \int_0^1 x^{m-1} \ln(x^2 + \rho^2) dx$ so that no singularity occurs around $x \sim 0$ for $m \geq 2$. More generally, the integral of the form $\int_{-1}^1 (f(x)/x) dx$, if treated by the above prescription, gives rise to the dominant contribution $-f'(0) \int_0^1 \ln(x^2 + \rho^2) dx$ which diverges as $\rho \rightarrow 0$.

With these caveats in mind, let us now move to a new regularization method based on the asymptotic principal values.

4.3. Regularization Method with Asymptotic Principal Values. Let us finally introduce a new regularization method based on the asymptotic principal values.

For the simple example in Section 2, there has been a definite physical interpretation of the singularity in the correlation function. Furthermore, the system considered there has been a combination of quantum objects with a macroscopic mirror. Therefore it might be also probable that the deepest cause of the singularity resides in the validity issue of the model originating from too much extrapolation from the quantum side to the macroscopic situation. Indeed there is an investigation showing that the quantum fluctuations of the mirror boundary drastically decrease the singular behavior near the mirror [7]. Therefore it is reasonable to take the origin of the singularity more realistically (rather than just mathematical phenomenon), expecting that some physical processes suppress the order of singularity.

Going back to the example of the integral I in (32), then, it is possible to interpret I in the sense of an asymptotic principal value,

$$I \mapsto \mathcal{P}_{(c,\rho)}(f, n) \quad (43)$$

with the dimension-free parameter ρ being provided by the ratio of some natural cut-off scale with the system-size in question. (E.g., the ratio of the plasma wave-length of the mirror with $2z$ for the example in Section 2). The advantage of this regularization scheme is that one can explicitly analyze the ρ -dependence of the integral. For instance, one may study the influence of the quantum fluctuations of the mirror by treating ρ as a fluctuation parameter. The result for $\langle \Delta v_z^2 \rangle$ given in (6) along with (7) is an example of the computation by the method of asymptotic principal values.

We see that Theorem 2 is the basis for understanding the relation between the regularization methods discussed so far. The difference between the method of asymptotic principal value ($\mathcal{P}_{(c,\rho)}(f, n)$) and the method of infinitesimal imaginary part ($\hat{\mathcal{P}}_{(c,\rho)}(f, n)$) is given by the second term on the R.H.S. of (22), which is of $O(1/\rho^{n-1})$.

5. Summary and Discussions

In this paper, we have focussed on singular integrals with a higher-order pole which frequently emerge in computing quantities based on two-point correlation functions of a vacuum.

To deal with this type of singular integrals, we have introduced the concept of *asymptotic principal values*. The asymptotic principal value of order ρ , which is a generalization of the Cauchy principal value, is defined by introducing a cut-off parameter ρ , focussing solely on the asymptotic behavior of the integral as $\rho \sim 0$. In this sense, it is a rigorous object retaining all the information on the singular integral.

We have then proved several theorems on asymptotic principal values which are expected to serve as bases for studying regularization methods for singular integrals.

To see how asymptotic principal values can be made use of, we have selected three typical regularization methods

and have analyzed their mutual relations with the help of theorems we have prepared. It has turned out that the concept of asymptotic principal values and related theorems are quite useful in this kind of analysis. Indeed, in terms of asymptotic principal values, it has been possible to describe without ambiguity what is discarded and what is retained in each regularization method.

No universal regularization method is available so far and we need to carefully select or invent a suitable method depending on the problem in question. For instance, we recall the example in Section 2, where velocity dispersion of the probe, $\langle \Delta v_z^2 \rangle$, is sensitive to the regularization method. In particular, the result expected by the method of infinitesimal imaginary part (Section 4.2) (and the method of partial integrals (Section 4.1)) is

$$\langle \Delta v_z^2 \rangle \sim \frac{e^2}{4\pi^2 m^2 z^2} \quad (\text{for } \tau \gg 2z). \quad (44)$$

On the other hand, the result expected by the method of asymptotic principal values (Section 4.3) is

$$\langle \Delta v_z^2 \rangle \sim \frac{e^2}{4\pi^2 m^2 z^2} \left(1 + \frac{1}{\rho} \right) \quad (\text{for } \tau \gg 2z), \quad (45)$$

by choosing ρ in the order of the ratio of plasma wavelength and the typical size $2z$. Strictly speaking, the model in Section 2 is a too simplified one and should be modified taking into account the quantum spread of the probe-particle itself. Then the behavior of $\langle \Delta v_z^2 \rangle$ at late time is corrected to a more reasonable one $\langle \Delta v_z^2 \rangle \sim 1/\tau^2$ rather than $\sim 1/z^2$ [2].

In any case it is significant to compare the results derived by different regularization methods in more detail for approaching to a more satisfactory mathematical theory of regularization procedures.

Acknowledgment

The author would like to thank C. H. Wu for various discussions.

References

- [1] M. Seriu and C.-H. Wu, "Switching effect on the quantum Brownian motion near a reflecting boundary," *Physical Review A*, vol. 77, no. 2, Article ID 022107, 11 pages, 2008.
- [2] M. Seriu and C.-H. Wu, "Smearing effect due to the spread of a probe particle on the Brownian motion near a perfectly reflecting boundary," *Physical Review A*, vol. 80, no. 5, Article ID 052101, 8 pages, 2009.
- [3] H. Yu and L. H. Ford, "Vacuum fluctuations and Brownian motion of a charged test particle near a reflecting boundary," *Physical Review D*, vol. 70, no. 6, Article ID 065009, 4 pages, 2004.
- [4] L. S. Brown and G. J. Maclay, "Vacuum stress between conducting plates: an image solution," *Physical Review*, vol. 184, no. 5, pp. 1272–1279, 1969.
- [5] K. T. R. Davies and R. W. Davies, "Evaluation of a class of integrals occurring in mathematical physics via a higher order generalization of the principal value," *Canadian Journal of Physics*, vol. 67, no. 8, pp. 759–765, 1989.

- [6] P. A. M. Dirac, *The Principles of Quantum Mechanics*, Oxford University Press, London, UK, 4th edition, 1958, Equation (35) in Section 50.
- [7] L. H. Ford and N. F. Svaiter, "Vacuum energy density near fluctuating boundaries," *Physical Review D*, vol. 58, no. 6, Article ID 065007, 8 pages, 1998.

Research Article

Spectral Modification by Diffraction and Scattering

M. Taghi Tavassoly,¹ Masoomeh Dashtdar,² and Mohammad Amiri³

¹ Physics Department, University of Tehran, 14395-547 Tehran, Iran

² Department of Physics, Shahid Beheshti University, Evin, 1983963113 Tehran, Iran

³ Physics Department, Bu-Ali Sina University, 65178 Hamedan, Iran

Correspondence should be addressed to M. Taghi Tavassoly, tavasoli@iasbs.ac.ir

Received 1 December 2009; Accepted 2 March 2010

Academic Editor: Oleg V. Angelsky

Copyright © 2010 M. Taghi Tavassoly et al. This is an open access article distributed under the Creative Commons Attribution License, which permits unrestricted use, distribution, and reproduction in any medium, provided the original work is properly cited.

Different effects induce spectral changes, for example, correlation of source fluctuations, propagation of light, random changes in optical properties of a medium, diffraction and scattering from objects, and rough interfaces. We review the spectral changes that occur as a result of light diffraction from phase steps, and particularly we discuss the spectral changes in the neighborhood of phase singularities. We also review the redshift and blueshift in the spectra of the lights coherently and diffusely scattered from rough interfaces. In addition, we study the effects of roughness and incident angle on the spectral profiles of scattered lights in reflection and transmission modes.

1. Introduction

After being realized in 1986 [1] that the spectrum of radiation may change on propagation, a considerable volume of works has been carried out dealing with spectral changes induced by the correlated fluctuations in sources and changes in coherence properties of radiations [2, 3]. Since the spatial coherence width of a light beam increases with the distance from the source, any light beam is coherent to some extent that depends on the source size and the distance from the source. Thus, as a coherent or partially coherent polychromatic beam of light passes through a medium that imposes different phases on different parts of the beam, the beam scatters from these parts and interference of the scattered lights leads to spectral changes. In this paper we study the spectral changes that occur as a result of light diffraction from phase steps and light scattering from rough interfaces in reflection and transmission modes.

2. Modified Spectrum of Diffracted Light

When a fully or partially coherent beam of light experiences a sharp change in amplitude or in phase, redistribution of intensity occurs in space that is called diffraction. A sharp change in amplitude occurs as the beam passage is

partly obstructed by an opaque object. A sharp change in phase happens as a beam of light is reflected from a step, Figure 1(a), or passes through a transparent plate immersed in a liquid or gas where a sharp change in refractive index is imposed at the plate edge, Figure 1(b). The lights diffracted from the neighborhood of the change-affected area interfere and lead to different spectra at different points in the diffraction field. The amount of spectral change varies from point to point, but it is remarkable and anomalous in the neighborhoods of phase singularities.

Gbur et al. [4] used the Fresnel-Kirchhoff integral and obtained the following expression:

$$M(r, \lambda) = \frac{1}{\lambda} \left| \int \int_W \frac{e^{ikR}}{R} d^2r' \right|^2 \quad (1)$$

for spectral modifying function for a fully coherent spherical wave front passing through a lens, at points in the neighborhood of the geometrical focal point. In (1), r , λ , k , d^2r' , and R stand for the distance between the focal point and observation point, wavelength, wavenumber, surface element, and the distance between a point on the aperture and observation point. The above function leads to drastic spectral changes in the neighborhoods of the phase singularities on the symmetry axis. But intensities at these

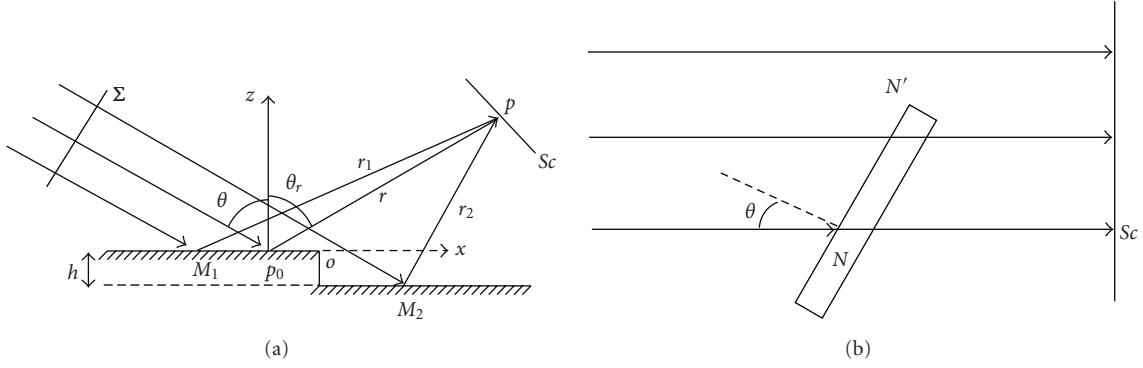


FIGURE 1: (a) The geometry of the Fresnel diffraction of light from a 1D phase step. By displacing point p_0 on the step, the point p on the screen is shifted to satisfy equation $\theta_r = \theta$. Therefore, the complex amplitude varies as a function of r . (b) A phase step in transmission is formed at the edges of a transparent plate of refractive index N that is immersed in a transparent gas or liquid of refractive index N' .

parts are so low that challenges the experimental studies [5]. However, the diffracted intensities are quite appreciable at points corresponding to the neighborhoods of the phase singularities that are formed by the phase steps. In the following we describe these singularities with more details.

In Figure 1(a), the plane wave Σ is incident to a 1D step of height h at incident angle θ . Using the Fresnel-Kirchhoff integral, the diffracted complex amplitude at point p , the intersection of the screen and the ray that is specularly reflected from the step, can be given as [6, 7]

$$U(r, \lambda) = \sqrt{\frac{-i}{\lambda}} A(\lambda) \frac{e^{ikr}}{\sqrt{r}} \left[\int_{-\infty}^{x_0} e^{ikx^2/2r} dx + e^{i2kh \cos \theta} \int_{x_0}^{\infty} e^{ikx^2/2r} dx \right], \quad (2)$$

where $A(\lambda)$ and x_0 stand for the amplitude of the incident light and the distance from p_0 to the step edge, p_0o , respectively. Using the abbreviations

$$\frac{kx^2}{r} = \pi v^2, \quad 2kh \cos \theta = \phi, \quad \frac{e^{ikr}}{\sqrt{r}} = u_0, \quad (3)$$

the complex amplitude at point p , for p_0 on the left side of the step edge, can be given by

$$U_L(r, \lambda) = K' A(\lambda) \left[\int_{-\infty}^{v_L} e^{i\pi v^2/2} dv + e^{i\phi} \int_{v_L}^{\infty} e^{i\pi v^2/2} dv \right] \quad (4)$$

and for p_0 on the right side of the step edge by

$$U_R(r, \lambda) = K' A(\lambda) \left[\int_{-\infty}^{-v_R} e^{i\pi v^2/2} dv + e^{i\phi} \int_{-v_R}^{\infty} e^{i\pi v^2/2} dv \right], \quad (5)$$

where $K' = \sqrt{-i/2}u_0$; v_R and v_L are the Fresnel variables corresponding to the distance between the step edge and

point p_0 , for p_0 on the left and right sides of the step edge. The corresponding intensities are [6, 7]

$$I_L(r, \lambda) = \frac{I_0(\lambda)}{r} \left[\cos^2\left(\frac{\phi}{2}\right) + 2(C_L^2 + S_L^2) \sin^2\left(\frac{\phi}{2}\right) - (C_L - S_L) \sin \phi \right], \quad (6)$$

$$I_R(r, \lambda) = \frac{I_0(\lambda)}{r} \left[\cos^2\left(\frac{\phi}{2}\right) + 2(C_R^2 + S_R^2) \sin^2\left(\frac{\phi}{2}\right) + (C_R - S_R) \sin \phi \right],$$

where C_L , S_L and C_R , S_R are the Fresnel cosine and sine integrals for the cases p_0 lying on the left and right sides of the step edge. These equations show that the diffracted light spectrum is modified, and the modifying functions are

$$M_L(r, \lambda) = \left[\cos^2\left(\frac{\phi}{2}\right) + 2(C_L^2 + S_L^2) \sin^2\left(\frac{\phi}{2}\right) - (C_L - S_L) \sin \phi \right], \quad (7)$$

$$M_R(r, \lambda) = \left[\cos^2\left(\frac{\phi}{2}\right) + 2(C_R^2 + S_R^2) \sin^2\left(\frac{\phi}{2}\right) + (C_R - S_R) \sin \phi \right].$$

Immersing a transparent plate of refractive index N in a transparent gas or liquid of refractive index N' , a phase step is formed in transmission. Calculating the amplitudes and intensities in the same manner that is done for a phase step in reflection leads to similar equations, but the phase change should be replaced by the following:

$$\phi = kN'h \left[\sqrt{n^2 - \sin^2 \theta} - \cos \theta \right], \quad (8)$$

where $n = N/N'$.

At the exact edge, that is, for $v_R = v_L = 0$ and

$$\phi = (2m + 1)\pi, \quad m = 0, \pm 1, \dots, \quad (9)$$

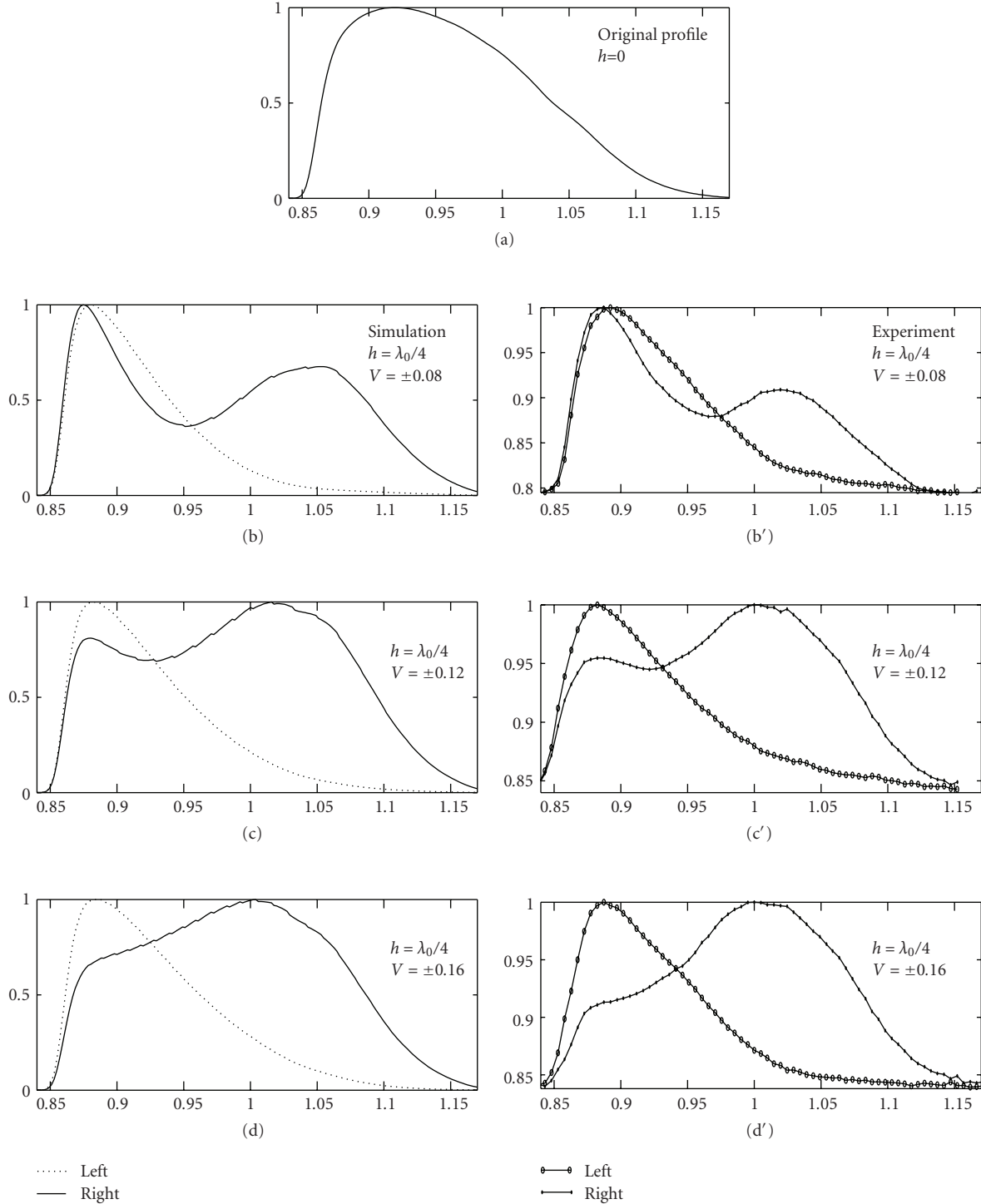


FIGURE 2: (a) The spectral profile of the light incident to a phase step formed by the Michelson interferometer versus λ/λ_0 ($\lambda_0 = 510$ nm). The plots (b'), (c'), and (d') on the right are the experimental spectral profiles of the incident lights (a) diffracted from the step at points corresponding to different distances from the step edge. The plots (b), (c) and (d) on the left are the corresponding spectral profiles obtained by simulation.

we have phase singularity. Thus, by changing the step height or the incident angle θ , one can create a phase singularity with the desired depth. For a phase singularity at λ_0 , that is, for $4\pi h \cos \theta / \lambda_0 = (2m + 1)\pi$, the modifying function for wavelengths close to λ_0 at points near the step edge can be

approximated by

$$\begin{aligned} M_L(r, \lambda) &\approx 2C_L(C_L + \alpha), \\ M_R(r, \lambda) &\approx 2C_R(C_R - \alpha), \end{aligned} \quad (10)$$

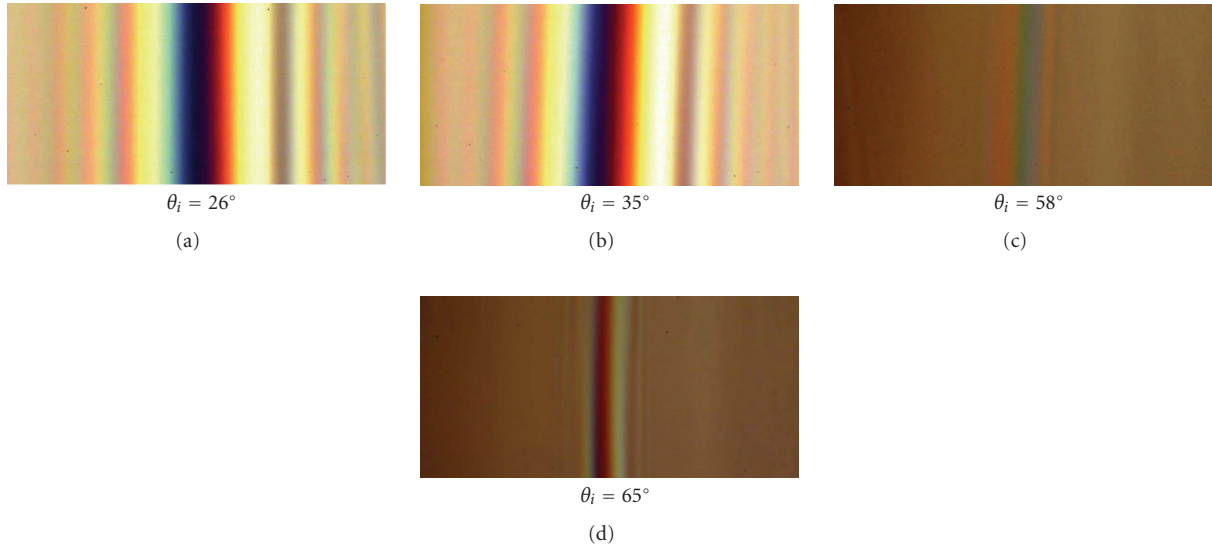


FIGURE 3: Diffraction patterns of spatially coherent white light diffracted from a 1D phase step of height $h = 440$ nm constructed by coating aluminum film on a glass substrate. The changes in colors occur by changing the light incident angle.

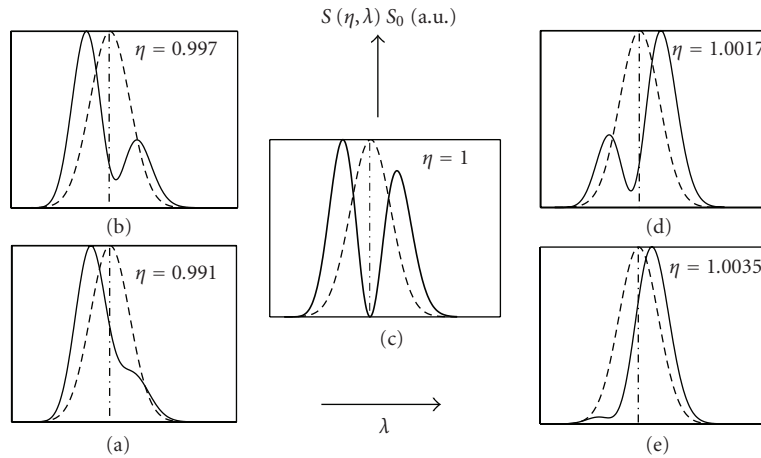


FIGURE 4: Modified spectral profiles for TM component of the incident light in the neighborhood of Brewster angle θ_B for five different incident angles, $\eta = \theta/\theta_B$.

where α denotes the phase change that is obtained for replacing λ_0 by λ . For $\lambda > \lambda_0$, we have $\alpha < 0$. That means that the spectra at points on the right side of the step edge are redshifted and at points on the left side are blueshifted, and the amount of modification increases by the distance from the step edge. However, the spectral modification becomes complicated by the further increase of the distance as a result of entering in Cornu spirals.

Phase steps can be formed in different ways. For example, if in the Michelson or Mach-Zehnder interferometer we block the alternative halves of the beams incident to the mirrors by two opaque plates, a 1D phase step is formed [8], and by displacing one of the mirrors, the height of the step is varied. Another simple way for fabricating 1D step is to coat a film on a substrate in the form of a step. In this case the phase ϕ can vary by changing the incident angle.

On the top of Figure 2 the spectrum of the light beam is plotted that was used to illuminate a 1D step formed in the Michelson interferometer. The other plots are the spectral profiles of the diffracted lights from the step at different distances from the step edge. The plots on the left side are the corresponding spectral profiles obtained by simulation. There are remarkable differences between the spectra corresponding to the same distances on the sides of the step edge.

In Figure 3 the diffraction patterns of white lights are shown, that diffracted from a step formed by coating aluminum on a substrate for different incident angles. The film thickness was 440 nm.

Another interesting phase singularity happens at Brewster angle for TM component of incident light beam illuminating the surface of a dielectric at angles close to

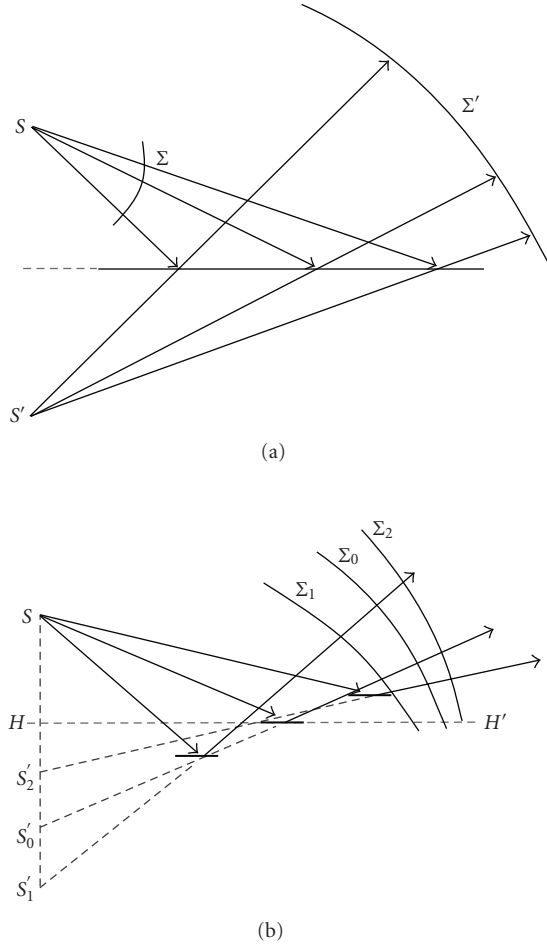


FIGURE 5: (a) The image of a point object is observed in a smooth surface because the reflected wave front is a continuous spherical surface. (b) The image is not observed in a very rough interface because the waves reflected from different parts of the rough interface do not form a continuous wave front.

the Brewster angle. For this component we have a step of height equivalent to a phase change of π at Brewster angle. Using the Fresnel-Kirchhoff integral and applying the Fresnel equations for the amplitude reflection coefficients, the following modifying function is obtained [9]:

$$M(\theta, \lambda) = \frac{K^2 R}{\lambda} [C^2(\theta, \lambda) + S^2(\theta, \lambda)], \quad (11)$$

where K is the propagation factor, R is the distance between the light incident point and observation point, $C(\theta, \lambda)$, and $S(\theta, \lambda)$ are the Fresnel sine and cosine integrals at incident angle θ that is close to the Brewster angle. In Figure 4 the modified spectral profiles in the neighborhood of the Brewster angle versus λ are plotted for an incident light of Gaussian spectral profile. As the plots shown for angles less than Brewster angle θ_B , $\eta < 1$ ($\eta = \theta/\theta_B$), the spectrum is blueshifted, and for $\eta > 1$ it is redshifted.

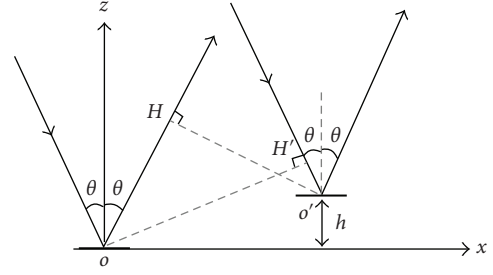


FIGURE 6: The optical path difference between the rays reflected from two parallel facets at arbitrary locations, $2h \cos \theta$, reduces as incident angle increases.

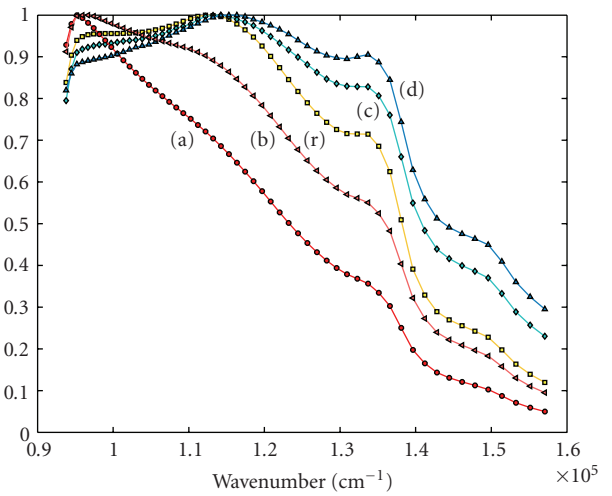


FIGURE 7: The measured spectral profiles of the incident light beam, (r), the coherently scattered lights, (a) and (b), and the diffusely scattered lights at scattering angle $\theta_s = 1^\circ$, (c) and (d), from interfaces of roughness $\sigma = 0.42 \mu\text{m}$ and $\sigma = 0.08 \mu\text{m}$, respectively.

3. Spectral Modification of the Light Scattered from Rough Interfaces

When a spherical wave that is originated from a point object strikes a flat smooth surface, the reflected wave is coherent on a sphere centered at the image of the object, Figure 5(a). However, if a spherical wave is incident to a flat rough surface, we face different sections of waves reflected from a large number of facets at different heights that are not correlated. Therefore, the image is not observed, Figure 5(b). But as the object gets closer to the rough interface, in other words, for large incident angles, the waves diffracted from different facets become correlated, and for very large incident angles the spherical wave is restored and the image reappears. Thus, at very large incident angles rough surfaces look smooth. In fact, it is easy to see from Figure 6 that the optical path difference between the lights reflected from two facets at height difference h , at two arbitrary locations, is the following:

$$\Delta = 2h \cos \theta. \quad (12)$$

Thus, we conclude that when a coherent parallel beam of light is incident to a rough interface, depending on the roughness, incident angle, and light wavelength, there may be coherently scattered light in specular direction. However, by the increase of incident angle the spatial coherence property of light improves, and beyond a threshold incident angle we have partially coherent light in specular direction. Also we have diffusely scattered light in all directions. The partially coherent scattered lights interfere and lead to spectral modification, including redshift and blueshift. There are reports on spectral modification of light scattered from rough interfaces [10, 11]. But recently rather detailed theoretical and experimental studies of the subject in reflection and transmission modes have been reported [12–15]. According to these works the amplitude of the coherently scattered monochromatic light from a randomly rough interface versus incident angle is the Fourier transform of the height distribution on the rough interface. In addition, for polychromatic incident light the coherently scattered light amplitude versus wave number is also the Fourier transform of the height distribution on the rough interface. Calculation of the coherently scattered light intensity leads to the following expression [13–15]:

$$S(k, P_n, f) = S_0(k)\beta^2 \left| \int_{-\infty}^{+\infty} P_n(h) \exp(-ikhf) dh \right|^2, \quad (13)$$

where $S_0(k)$, β , and $P_n(h)$ denote the illuminating light intensity at wavenumber k , a dimensionless constant, and the probability density function of height distribution on the rough interface. Also, we should substitute

$$f = 2 \cos \theta_i \quad (14)$$

in reflection mode and

$$f = N_1 \left(\sqrt{N^2 - \sin^2 \theta_i} - \cos \theta_i \right) \quad (15)$$

in transmission mode, where θ_i is the incident angle and $N = N_2/N_1$ where N_1 and N_2 are the refractive indices of the media surrounding the rough interface. As shown in (13) the coherently scattered light intensity depends on k , f , and $P_n(h)$. Thus, we have spectral modification with the following modifying function:

$$M(k, P_n, f) = \beta^2 \left| \int_{-\infty}^{+\infty} P_n(h) \exp(-ikhf) dh \right|^2. \quad (16)$$

For an incident light of Gaussian spectral profile

$$S_0(k) = s_0 \beta^2 \exp\left(-\frac{(k - k_0)^2}{2\sigma_k^2}\right), \quad (17)$$

the modified spectral profile becomes

$$S(k, p_n, f) = S_0 \exp(-k_0^2 \sigma^2 f^2) \times \exp\left[-\frac{\left(k - k_0 / (1 + 2\sigma_k^2 \sigma^2 f^2)\right)^2}{2\sigma_k^2 / (1 + 2\sigma_k^2 \sigma^2 f^2)}\right], \quad (18)$$

where σ is the RMS of height distribution. We see that when $s_0 \exp(-k_0^2 \sigma^2 f^2)$ is appreciable, we have the following redshift and spectral width shrinkage:

$$\delta k_0 = \frac{k_0}{1 + 1/2\sigma_k^2 \sigma^2 f^2}, \quad (19)$$

$$\sigma_M = \frac{\sigma_k}{\sqrt{1 + 2\sigma_k^2 \sigma^2 f^2}}.$$

According to (18) and (19) when $s_0 \exp(-k_0^2 \sigma^2 f^2)$ is appreciable, the coherently scattered light spectrum is always redshifted with a shrinkage in spectral width. This result implies that in this situation the diffusely scattered light is blueshifted. Theoretical predictions and experimental results show that blueshift reduces with the increase of scattering angle. In addition, the spectral modification is significant near the threshold angle, the angle at which the coherently scattered light intensity becomes nonzero. In Figure 7 the spectral profiles of the incident beam, (r), and the coherently scattered beams, (a) and (b), and the diffusely scattered lights at scattering angle $\theta_s = 1^\circ$, (c) and (d), are plotted for interfaces having roughness $\sigma = 0.42 \mu\text{m}$ and $\sigma = 0.08 \mu\text{m}$, respectively.

4. Conclusions

- (1) Spectral modification by diffraction of light from phase steps is a rich subject and can provide adequate ground for deeper studies of phase singularities.
- (2) Polychromatic light diffraction from phase steps has applications in metrology, optical switching, and in dealing with transparent nonlinear materials.
- (3) The scattering of polychromatic lights from rough interfaces gives better understanding of the optical field near the rough interfaces and it can provide valuable information about the properties of rough interfaces.
- (4) The results obtained can be applied to transparent materials that impose irregular or random phases on lights propagating through them.

References

- [1] M. Born and E. Wolf, *Principles of Optics*, 7th edition, 2002.
- [2] E. Wolf and D. F. V. James, "Correlation-induced spectral changes," *Reports on Progress in Physics*, vol. 59, no. 6, pp. 771–818, 1996.
- [3] L. Mandel and E. Wolf, *Optical Coherence and Quantum Optics*, section 5.8., Cambridge University Press, Cambridge, UK, 1995.
- [4] G. Gbur, T. D. Visser, and E. Wolf, "Anomalous behavior of spectra near phase singularities of focused waves," *Physical Review Letters*, vol. 88, no. 1, Article ID 013901, 4 pages, 2002.
- [5] G. Popescu and A. Dogariu, "Spectral anomalies at wave-front dislocations," *Physical Review Letters*, vol. 88, no. 18, Article ID 0183902, 4 pages, 2002.

- [6] M. T. Tavassoly, M. Amiri, E. Karimi, and H. R. Khalesifard, "Spectral modification by line singularity in Fresnel diffraction from 1D phase step," *Optics Communications*, vol. 255, no. 1–3, pp. 23–34, 2005.
- [7] M. Amiri and M. T. Tavassoly, "Fresnel diffraction from 1D and 2D phase steps in reflection and transmission modes," *Optics Communications*, vol. 272, no. 2, pp. 349–361, 2007.
- [8] M. T. Tavassoly, M. Amiri, A. Darudi, R. Aalipour, A. Saber, and A. R. Moradi, "Optical diffractometry," *Journal of the Optical Society of America A*, vol. 26, no. 3, pp. 540–547, 2009.
- [9] M. Amiri and M. T. Tavassoly, "Spectral anomalies near phase singularities in reflection at Brewster's angle and colored castastrophes," *Optics Letters*, vol. 33, no. 16, pp. 1863–1865, 2008.
- [10] O. V. Angelsky, P. V. Polyanskii, and S. G. Hanson, "Singular-optical coloring of regularly scattered white light," *Optics Express*, vol. 14, no. 17, pp. 7579–7586, 2006.
- [11] V. K. Polyanskii, O. V. Angelsky, and P. V. Polyanskii, "Scattering-induced spectral changes as a singular optical effect," *Optica Applicata*, vol. 32, no. 4, pp. 843–848, 2002.
- [12] M. T. Tavassoly, A. Nahal, and Z. Ebadi, "Image formation in rough surfaces," *Optics Communications*, vol. 238, no. 4–6, pp. 252–260, 2004.
- [13] M. Dashtdar and M. T. Tavassoly, "Determination of height distribution on a rough interface by measuring the coherently transmitted or reflected light intensity," *Journal of the Optical Society of America A*, vol. 25, no. 10, pp. 2509–2517, 2008.
- [14] M. Dashtdar and M. T. Tavassoly, "Redshift and blueshift in the spectra of lights coherently and diffusely scattered from random rough interfaces," *Journal of the Optical Society of America A*, vol. 26, no. 10, pp. 2134–2138, 2009.
- [15] M. T. Tavassoly and M. Dashtdar, "Height distribution on a rough plane and specularly diffracted light amplitude are Fourier transform pair," *Optics Communications*, vol. 281, no. 9, pp. 2397–2405, 2008.

Research Article

Optical Sensing of Attached Fibrinogen on Carbon Doped Titanium Surfaces

Raimo Silvennoinen,¹ Vladimír Vetterl,² Stanislav Hasoň,² Martti Silvennoinen,¹ Kari Myller,³ Jiří Vaněk,⁴ and Ladislav Cvrček⁵

¹Department of Physics and Mathematics, University of Eastern Finland, Joensuu Campus, P.O. Box 111, 80101 Joensuu, Finland

²Institute of Biophysics, v.v.i., Academy of Sciences of the Czech Republic, Královiopolská 135, 612 65 Brno, Czech Republic

³MGM-Devices Ltd., 82210 Suhmura, Finland

⁴Centre for Dental and Craniofacial Research, Faculty of Medicine, Masaryk University, Komenského nám 2, 662 43 Brno, Czech Republic

⁵HVM Plasma Ltd., Research and Development Department, Na Hutmance 2, 158 00 Prague 5, Czech Republic

Correspondence should be addressed to Raimo Silvennoinen, raimo.silvennoinen@uef.fi

Received 24 November 2009; Accepted 2 March 2010

Academic Editor: Peter V. Polyanskii

Copyright © 2010 Raimo Silvennoinen et al. This is an open access article distributed under the Creative Commons Attribution License, which permits unrestricted use, distribution, and reproduction in any medium, provided the original work is properly cited.

The adsorption/desorption of Human Plasma fibrinogen (HPF) molecules on biosurfaces was measured in spectroscopic cuvette by a diffractive optical element- (DOE-) based sensor. To characterize the surfaces, the basic parameters as surface tension was obtained by sensing of a contact angle of water droplet and dielectric constant was measured by ellipsometry in the absence of HPF molecules. It was observed a significant correlation between the adsorption ability of HPF molecules (sensed by DOE on the basis of the changes in optical roughness (R_{opt}) of studied surface in the absence and presence of HPF molecules), and dielectric constant (measured by ellipsometry) of differently treated titanium surfaces, where the permittivity and dielectric loss have the known linear relation. These findings with carbon-treated biomaterial surfaces can help us to understand mechanisms behind attachment of HPF molecules on biomaterial surfaces to realize and extend variety of implants for hard tissue replacement.

1. Introduction

Titanium is frequently used as a biomaterial for hard tissue replacement, such as dental and orthopaedic implants, and biomaterial devices made of titanium give a satisfactory performance [1–7]. The effective surface energy related to topography of surface, which can be varied by different processing methods, is assumed to influence to the final interactions of the implant with the surrounding environment. Rough surfaces promote better osseointegration than smooth surfaces [8–11]. Within a few seconds after implantation the biomaterial surface becomes coated with a film of adsorbed proteins, which mediate the interaction between the implant and the body environment. Since most implants are exposed to blood during implantation, the initial protein film is mainly composed of plasma proteins. Human plasma fibrinogen (HPF) is one of the most relevant

proteins adsorbed on biomaterial surfaces. HPF partakes in blood coagulation facilitate adhesion and aggregation of platelets [12, 13]. The structure and composition of the adsorbed protein layer determine the type and extent of the subsequent biological reactions, such as activation of coagulation and immune response and osseointegration [14]. The initially adsorbed protein layer is thus a factor for conditioning the biocompatibility [15–17]. The mechanisms and the factors, which are important for protein adsorption and desorption, are still subject of scientific research and not understood very well. Therefore it is important to investigate how different surfaces influence the formation and properties of adsorbed protein layers.

In this paper we express characteristics, which relate to the adsorption/desorption of HPF molecules on differently treated titanium surfaces. The treatments were (i) mechanical polishing and (ii) plasma-enhanced chemical

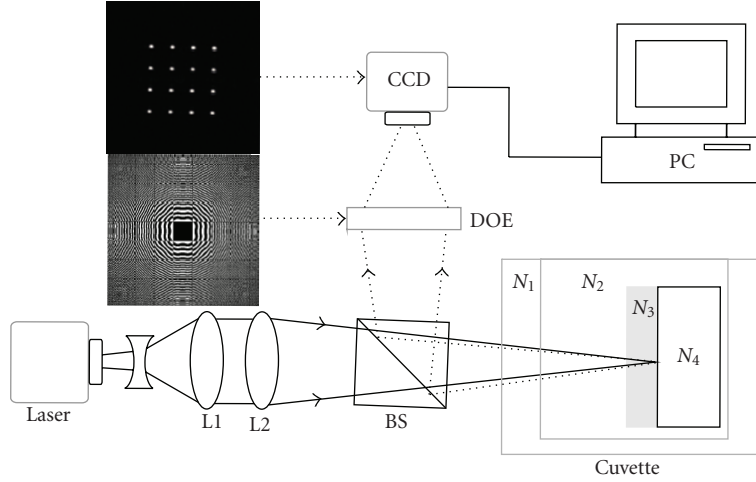


FIGURE 1: Geometric setup of DOE sensor with sample cuvette compartment for R_{opt} measurements. Lower inset denotes aperture of DOE whereas upper inset denotes reconstructed 4×4 spot matrix image of DOE by using nondistorted wavefront.

vapor deposition (PECVD) of either titanium carbide layers with different concentrations of carbon (three samples) or diamond-like carbon (DLC) coating. The surface tension and surface energy of the samples were obtained from optical measuring of the contact angle of distilled water droplet on the dry bulk sample surface. The dielectric constant of each bulk surface was measured in dry environment utilizing ellipsometry. The temporal adsorption process of HPF molecules on test surfaces was measured in vitro using one arm optical interferometer, which utilizes a diffractive optical element (DOE) [18, 19]. This optical interferometer works in coherent and in noncoherent mode, which allows sensing of optical path differences providing information on the optical roughness (R_{opt}), and reflectance of the surfaces immersed into various liquids. This method can thus be used for the study of the interactions of the molecules dissolved in the liquid with the surface to find out parameters to understand mechanisms behind adsorption/desorption of HPF molecules on biomaterial surfaces to realize implants in hard tissue replacement.

2. Materials and Methods

2.1. Ellipsometry and Water Contact Angle of Treated Titanium Surfaces. In this work were used following surfaces: (1) mechanically polished titanium, (2)–(4) plasma-enhanced chemical vapor deposited titanium carbides with three different concentrations of carbon [$\text{Ti}_{0.82} - \text{C}_{0.18}$ (2); $\text{Ti}_{0.38} - \text{C}_{0.62}$ (3); $\text{Ti}_{0.09} - \text{C}_{0.91}$ (4)], and (5) diamond-like carbon ($\text{Ti}_{0.00} - \text{C}_{1.00}$). The thickness of titanium oxide layer was measured with polished titanium surface, and its depth was about 220 nm. The thickness of $\text{Ti}_x - \text{C}_{1-x}$ coatings produced by using PECVD ranged from $2.5 \mu\text{m}$ to $3.5 \mu\text{m}$, which is thick enough in optical sense to consider it as solid bulk layer [20, 21]. The ellipsometric measurements of these differently treated surfaces were performed in dry environment to gain information about the permittivity possible related to adsorption of HPF molecules. The complex refractive index

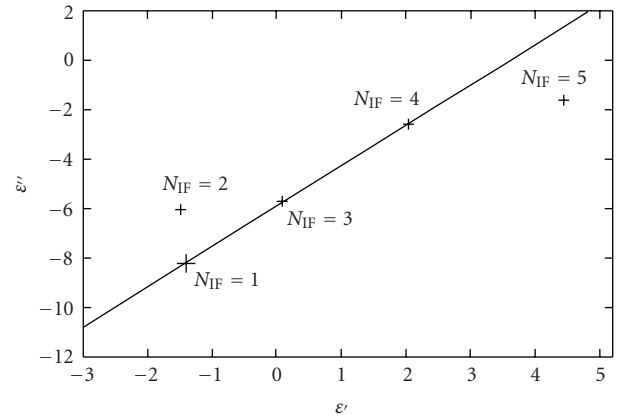


FIGURE 2: Complex effective dielectric constants (dielectric permittivity) for treated titanium surfaces at $E_\lambda = 1.959 \text{ eV}$. $N_{\text{IF}} = 1 \equiv$ polished titanium, $N_{\text{IF}} = 2 \equiv \text{Ti}_{0.82} - \text{C}_{0.18}$, $N_{\text{IF}} = 3 \equiv \text{Ti}_{0.38} - \text{C}_{0.62}$, $N_{\text{IF}} = 4 \equiv \text{Ti}_{0.09} - \text{C}_{0.91}$, and $N_{\text{IF}} = 5 \equiv \text{Ti}_{0.00} - \text{C}_{1.00}$ (diamond-like carbon). The standard deviations in permittivity ϵ' and dielectric loss ϵ'' directions are indicated on each dielectric constant by horizontal and vertical lines. Parameters for the line are as follows: $\epsilon'' = a\epsilon' + b$, where $a = 1.634$ and $b = -5.877$.

values ($N_{nk} = n - ik$), in turn, were utilized in the calculation of the effective dielectric constant $\epsilon = \epsilon' + i\epsilon'' = N_{nk}^2$, where $\epsilon' = n^2 - \kappa^2$ and $\epsilon'' = -2n\kappa$. To avoid the harmful effects caused by the possible appearance of surface roughness [22, 23], the ellipsometric measurements were performed at the incidence angle of 75° for probe beam utilizing Woollam variable angle spectroellipsometer (W-VASE), which is operating in the wavelength range from 200 nm to 1700 nm. The complex permittivity values of the all studied surfaces were calculated from the complex refractive index values, which were obtained by the spectroellipsometer (cf. Table 1). The surface energy of each of studied surfaces was estimated from optical measurements of the contact-angle of water droplet injected on the dry surface (cf. Table 1).

TABLE 1: Complex effective dielectric constants (dielectric permittivity) $\varepsilon = \varepsilon' + i\varepsilon''$ at $E_\lambda = 1.959$ eV with standard deviations and water contact angles (θ°) for the five studied surfaces. Sample number indexes N_{IF} shown in Figure 2 are listed according to severity of dielectric losses ε'' .

Sample	Treatment	ε	$\Delta\varepsilon (\times 10^{-2})$	θ°
1	Polished titanium	$-1.406 - 8.207i$	$34.1 + 128.4i$	66.5 ± 4.1
2	PECVD Ti _{0.82} -C _{0.18}	$-1.492 - 6.024i$	$17.2 + 23.1i$	81.1 ± 2.6
3	PECVD Ti _{0.38} -C _{0.62}	$0.084 - 5.681i$	$20.5 + 40.4i$	77.9 ± 3.1
4	PECVD Ti _{0.09} -C _{0.91}	$2.034 - 2.580i$	$6.7 + 3.4i$	75.0 ± 0.4
5	DLC Ti _{0.00} -C _{1.00}	$4.448 - 1.570i$	$13.5 + 14.9i$	70.7 ± 2.0

2.2. *Coherent Response of DOE Sensor.* The thicknesses of the adsorbed layers of HPF molecules on differently treated titanium surfaces were sensed utilizing the coherence response of DOE sensor as shown in Figure 1. The DOE sensor uses expanded and focused laser beam ($\lambda = 633$ nm) realized with the aid of the lens system L1-L2 to hit on studied surface N_4 through reference liquid (water) in cuvette via beam splitter BS and cuvette window N_1 . Backscattered laser beam is directed with the aid of beam splitter on DOE aperture (shown in the lower inset of Figure 1), which analyses if the wavefront is distorted after adsorption either the ions of background electrolyte or added HPF molecules (denoted as N_3) on studied surface in the aqueous environment of background electrolyte (N_2). Distorted 4×4 light spot DOE image is grabbed from two-dimensional (2D) photo array of the charge-coupled device (CCD) and analyzed using a personal computer (PC). The changes in R_{opt} , which relate to surface roughness R_a [24], are detected utilizing the coherent response of the DOE sensor. The thickness of the adsorbed layer on treated titanium surfaces is calculated from the captured DOE image data of the 4×4 light spot matrix, which is shown in the upper inset of Figure 1. The irradiance of the peaks was calculated utilizing (1) as follows:

$$I_C = \frac{1}{n_{pk}m_{pk}} \sum_{i_{pk}=1, j_{pk}=1}^{n_{pk}, m_{pk}} I_{i_{pk}, j_{pk}}, \quad (1)$$

where n_{pk} and m_{pk} are the pixel dimensions of each 16 peaks in DOE image and $I_{i_{pk}, j_{pk}}$ is the image irradiance observed by the (i_{pk}, j_{pk}) th element of the peak in DOE image captured by a CCD camera. The 16 different diffractive lenses are integrated utilizing superposition principle in the DOE aperture obeying coherent response for each pixel with complex wavefront amplitude $A_{i,j}$ as follows: $I_C = |\sum A_{i,j}|^2$, which satisfies the principle of compact and phase sensitive interferometer. The DOE element images the 4×4 light spot matrix in its focal plane. If the reconstructing wavefront does not satisfy the terms of hologram imaginary, the spot image matrix does not appear in the image plane. The same holds, for instance, in the case, where the radiant exitance from the laser resonator in TEM₀₀ mode starts to suffer from appearance of side modes, and DOE will spatially filter out those images from its original 4×4 light spot image. With the tedious numerical simulations, it is showed that the irradiance of the 4×4 spots will decrease as a function of optical path length (OPL) and disappears when the OPL exceeds $\lambda/4$. This response is published and appears

in Figure 8.21(b) of [18]. It is also observable that this response resembles the response of Beckmann-Spizzichino model [25]. To discover the thickness of the adsorbed layer N_3 we first calculated the irradiance of the peaks utilizing (1) and after that the optical path difference Δr , understood as an optical roughness (R_{opt}), is solved inversely by using this response. We have noted during our previous measurements that the accuracy of 0.2 nm can be achieved by using this one arm interferometric technique [19]. The similar accuracy limits are also reported recently for the coupling dynamics of lasers of self-mixing interferometers in vibrometer applications ranging from 0.1 nm to 100 μ m [26]; whereas the accuracy of conventional two arm interferometers used in optical diagnostics of random phase objects [27] as well as in optical diagnostics of rough surfaces [28] is estimated to be $\sim 0.005 \mu$ m.

2.3. DOE Sensor Measurements of Treated Titanium Surfaces.

First the DOE sensor images were made in water for 100 seconds in aim to perform the reference signal level from each surface, and during that time frame 1000 reference samples were grabbed. Thereafter the water was removed by syringe from cuvette and the background electrolyte was injected in the cuvette. Immediately after injection of background electrolyte, the grabbing of the DOE images was started, and the image grabbing was repeated after two minutes interval. Before HPF measurement, the cuvette was washed, and after washing the new treated titanium sample was installed in the sample holder inside the cuvette. The water was injected in the cuvette, and the DOE image references from the new sample surface were taken. Before adding the HPF solution in the cuvette, the immersion water was removed, and DOE image grabbing process was started. The image grabbing was repeated two times consecutively after two minutes interval. The diameter of the laser beam waist on the all surfaces was 1 mm. Thereafter we compared the optical roughness R_{opt} values, which were measured by DOE sensor as a function of time from the interface of the treated titanium surface-electrolyte in the absence or presence of HPF molecules. The threshold of optical roughness of the treated titanium surface was cancelled out by measuring the base line of R_{opt} in distilled water, which refractive index ($n = 1.333$) was close to background electrolyte ($n = 1.338$). The R_{opt} values for all studied surfaces in the absence and presence of HPF molecules are shown in Table 2.

TABLE 2: Optical roughness (R_{opt}) of the five studied surfaces with standard deviations at $E_{\lambda} = 1.959$ eV immersed in background electrolyte in absence or presence of HPF molecules. Sample number indexes N_{IF} resemble those appearing in Figure 2.

Sample N_{IF}	Absence of HPF molecules		Presence of HPF molecules	
	R_{opt} (nm)	ΔR_{opt} (nm)	R_{opt} (nm)	ΔR_{opt} (nm)
1	23.2	3.2	39.2	9.7
2	25.7	9.1	17.4	6.7
3	10.7	5.0	25.0	7.1
4	11.4	4.6	27.2	7.5
5	35.5	2.6	29.9	6.7

2.4. *Chemicals.* Human plasma fibrinogen (HPF), fraction I, type III were purchased from Sigma. In all experiments the HPF was dissolved in phosphate buffer solution (PBS) + 0.1362 M sodium citrate, which serve as a background electrolyte at a concentration of 500 nM. Measurements were performed at room temperature.

3. Results and Discussion

In Figure 2 are shown the effective dielectric constants (dielectric permittivity) from five studied surfaces at photon energy $E_{\lambda} = 1.959$ eV. The first sample represents mechanically polished titanium surface, which act as the reference ($N_{\text{IF}} = 1$). The three titanium carbide and diamond-like carbon samples were produced PECVD method controlling the severity of chemical vapor deposition in plasma-enhancement to satisfy the carbon concentrations and are denoted as follows: $N_{\text{IF}} = 2$ –5. The standard deviations in permittivity ϵ' and dielectric loss ϵ'' directions, which are shown in Table 1, are indicated on each dielectric constant by horizontal and vertical lines in Figure 2.

The optical roughness (R_{opt}) values for each of the studied surfaces in the absence or presence of the HPF molecules were calculated from DOE sensor measurements performing under wet environment (Table 2). The R_{opt} data reveals that the adsorption of HPF molecules is significant for the three surfaces ($N_{\text{IF}} = 1$, $N_{\text{IF}} = 3$ and $N_{\text{IF}} = 4$) compared with the other two surfaces ($N_{\text{IF}} = 2$ and $N_{\text{IF}} = 5$). Let us denote later these two set of surfaces by A and B, respectively. In the deeper evaluation it was observed that in the permittivity ϵ' and dielectric loss ϵ'' plane the (ϵ', ϵ'') -point value representing each surface in set A hit on a line, which is also shown in Figure 2; whereas the other two points with the coordinate pairs of set B (including titanium carbide surface $N_{\text{IF}} = 2$ and diamond-like carbon $N_{\text{IF}} = 5$ surface) do not coincident the line. This notation allows us to make an assumption that the adsorption of HPF molecules relates to a slope of dielectric loss and permittivity $(\partial\epsilon''/\partial\epsilon')$ as follows: $\epsilon'' = a\epsilon' + b$, where $a = 1.634$ and $b = -5.877$. Also the distance of (ϵ', ϵ'') -point from the line $\epsilon'' = 1.634\epsilon' - 5.877$ indicates that the surfaces in the set A have small distance deviation (0.017, 0.036, and 0.013), whereas in the set B the respective distances deviate more than one decade being (1.198 and 1.547). To compare furthermore permittivity values of the five test surfaces to

those surfaces, which are considered to have toxic effects on some bacteria, viruses, and other microbial organisms in vitro, as silver, mercury, and germanium [29–31], we calculated those permittivity values at photon energy $E_{\lambda} = 1.959$ eV from complex refractive index values available in the series of books of Palik [32]. It is worth to observe that the permittivity values for silver, mercury and germanium, which are $\epsilon_{\text{Ag}} = -16.174 - 1.093i$, $\epsilon_{\text{Hg}} = 29.257 - 8.916i$ and $\epsilon_{\text{Ge}} = -23.443 - 20.715i$, deviate significantly from the permittivity values of the five test surfaces. This can be concluded from the respective distance values, which are as follows: 16.255, 12.109 and 26.492 being rather huge compared with deviating distances in the surface set A. In Figure 3 is shown two SEM images. The both images are from the set A to show the different surface morphology. The polished titanium surface (set A— $N_{\text{IF}} = 1$) looks rather uniform containing some grooves, which is assumed to arise from the polishing process. The titanium carbide surface with lower content of titanium (set A— $N_{\text{IF}} = 4$) consists of nanometre scale carbide agglomerates, which in turn is assumed to be originated from the surface energy driven grain growth [33].

The water contact angles (θ) of the surfaces, those appear in Figure 3, indicate that the surfaces are hydrophilic with level ranging from 81° (~ 0.100 J/m²) to 66° (~ 0.173 J/m²), see Table 1. However estimated from water contact-angles the surface energy density (γ) of the titanium carbide surfaces covered by nanometre-scale agglomerates (θ is decreasing consecutively from $N_{\text{IF}} = 2$ to $N_{\text{IF}} = 5$) are smaller than the surface energy density of carbon black (0.257 J/m²) in comparison to that of the same carbon black after graphitization (0.189 J/m²) [34] and the carbon nanofibers surface [35]. The difference should originate from the agglomerates, which decrease the effective contact area of water droplet and titanium carbide increasing the effective area of gas-water interface under droplet. Although the surface energy density does not correlate direct, one to one, with the ability of the adhesion of HPF molecules on surfaces nevertheless it have influences to the hydrophilic interaction of background electrolyte and surface. Moreover, the measured contact angle of water droplet and electrolyte on dry surfaces did not differed significantly from each other whereas the contact angle of electrolyte droplet with HPF molecules was ca. 10 per cent lower than the respective contact angles of water and electrolyte. On the contrary, the hydrophobic behaviour may contribute appearance of

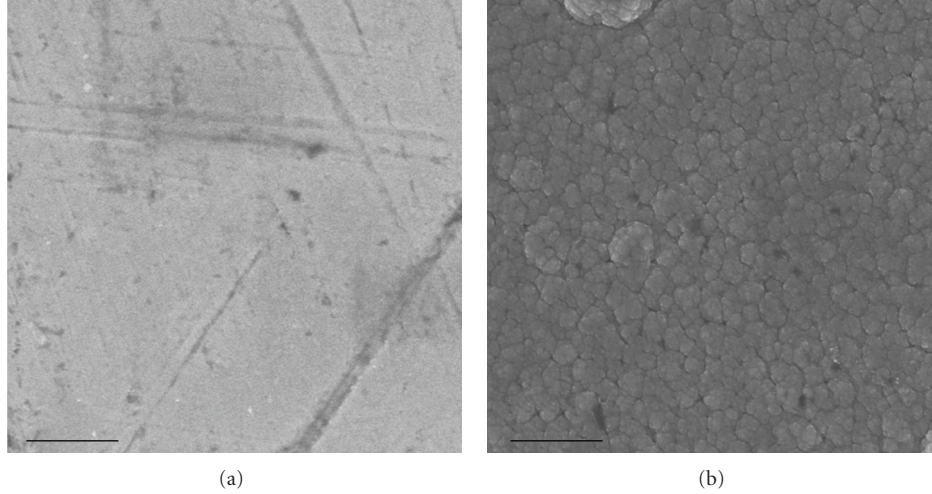


FIGURE 3: SEM image from two different treated titanium surface: (a) $N_{IF} = 1 \equiv$ polished titanium and (b) $N_{IF} = 3 \equiv \text{Ti}_{0.38}\text{C}_{0.62}$. The length of black horizontal scale bar in left lower corner of each image is $1 \mu\text{m}$.

nanobubbles at the interface between water (including background electrolyte) and hydrophobic solid surface [36].

The interaction of the probe light with the surfaces is also estimated utilizing the reflectance R , which relates to energy loss or absorption of photons. The reflectance R is calculated from the relation $R = |(1 - N_{nk})/(1 + N_{nk})|^2$. The reflectance responses of the five studied surfaces were showing decreasing evolution as a function of photon energy in the range from 1.5 eV to 3.0 eV including the energy of probe light (1.959 eV) used in the experiments. The Pearson second-moment correlation of the five measured surfaces between the absorption $(1 - R)$ and the dielectric losses ϵ'' at the probe light energy is $r^2 = 0.9313$, which do not explain one to one the ability of the adhesion of HPF molecules on surfaces. Here we point out that the energy of probe light is negligible compared with the binding energies of reported Ti/CH films being in the range from 280 eV to 535 eV [37].

For the convenience to compare dielectric constant and refractive index we have included the locus of dielectric line shown in Figure 2 in complex refractive index plane, which is now the parabola $n = -\kappa + \sqrt{\kappa^2(1 + a^2) - ab}$ as shown in Figure 4. The knowledge of the parabola shaped locus in (n, κ) -plane (or linear shaped locus in (ϵ', ϵ'') -plane) helps us now to search the valid surface candidates, which are effective to adsorb HPF molecules without complicated experiments in vitro.

4. Conclusion

In the progress of this work we have noted the relation to surface parameters, which explain the ability of adsorption/desorption of HPF molecules (fraction I, type III) on the biosurfaces with different surface treatments. Three of the surfaces were titanium carbide surfaces performed utilizing plasma-enhanced chemical vapor deposition. The polished titanium and diamond-like carbon were acting as the reference surfaces.

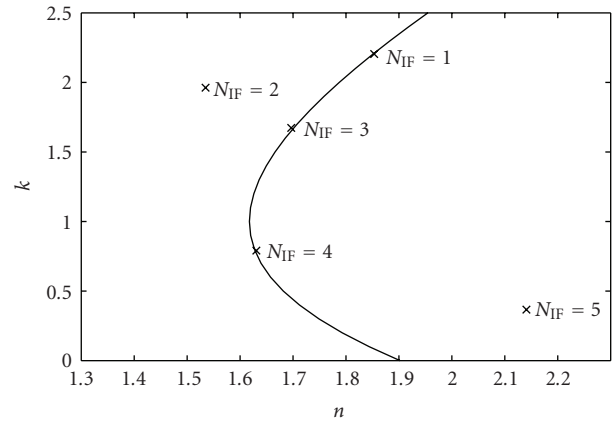


FIGURE 4: Complex effective refractive index $N_{nk} = n + i\kappa$ for the five-treated titanium surfaces shown in Figure 3 at $E_\lambda = 1.959 \text{ eV}$; whereas parabola $n = -\kappa + \sqrt{\kappa^2(1 + a^2) - ab}$ with constants $a = 1.616$ and $b = -5.848$ respects projection of dielectric line shown in Figure 2.

The significant correlation between the complex dielectric constant of dry titanium carbide surfaces and ability of adsorption of HPF molecules on these titanium carbide was observed, where permittivity ϵ' and dielectric loss ϵ'' have the known linear relation. Whereas the surface tension and surface energy of the titanium carbide samples, which was estimated from the optically measured contact angle of the droplet of distilled water (as well as the electrolyte droplet without and with HPF molecules) on the dry surface, did not give direct correlation with ability of adsorption of HPF on titanium carbide surfaces. The low correlation was also recognized from the surface capability to reflect energy back from the interface of air-titanium carbide surface. The findings in dielectric constants, which relate to interactions of the HPF molecules dissolved in the electrolyte and the titanium carbide surface, help us to understand mechanisms

behind adsorption/desorption of HPF molecules on biomaterial surfaces in hard tissue replacement.

Acknowledgments

This work was supported by the Ministry of Education and Sport of the Czech Republic (1M0528), the Academy of Sciences of the Czech Republic (KAN200040651), the Grant Agency of the Czech Republic (202/08/1688, 205/10/2378), the Ministry of Education, Youth and Sports of the Czech Republic (LC06035), and institutional research plans, AVOZ50040507, AVOZ50040702).

References

- [1] B. Walivaara, B.-O. Aronsson, M. Rodahl, J. Lausmaa, and P. Tengvall, "Titanium with different oxides: in vitro studies of protein adsorption and contact activation," *Biomaterials*, vol. 15, no. 10, pp. 827–834, 1994.
- [2] V. Ball, A. Bentaleb, J. Hemmerle, J.-C. Voegel, and P. Schaaf, "Dynamic aspects of protein adsorption onto titanium surfaces: mechanism of desorption into buffer and release in the presence of proteins in the bulk," *Langmuir*, vol. 12, no. 6, pp. 1614–1621, 1996.
- [3] M. I. Jones, I. R. McColl, D. M. Grant, K. G. Parker, and T. L. Parker, "Protein adsorption and platelet attachment and activation, on TiN, TiC, and DLC coatings on titanium for cardiovascular applications," *Journal of Biomedical Materials Research*, vol. 52, no. 2, pp. 413–421, 2000.
- [4] Y. Yang, R. Cavin, and J. L. Ong, "Protein adsorption on titanium surfaces and their effect on osteoblast attachment," *Journal of Biomedical Materials Research Part A*, vol. 67, no. 1, pp. 344–349, 2003.
- [5] N. Huang, P. Yang, Y. X. Leng, et al., "Hemocompatibility of titanium oxide films," *Biomaterials*, vol. 24, no. 13, pp. 2177–2187, 2003.
- [6] F. F. Hook, J. Voros, M. Rodahl, et al., "A comparative study of protein adsorption on titanium oxide surfaces using in situ ellipsometry, optical waveguide lightmode spectroscopy, and quartz crystal microbalance/dissipation," *Colloids and Surfaces B*, vol. 24, no. 2, pp. 155–170, 2002.
- [7] K. Imamura, M. Shimomura, S. Nagai, M. Akamatsu, and K. Nakanishi, "Adsorption characteristics of various proteins to a titanium surface," *Journal of Bioscience and Bioengineering*, vol. 106, no. 3, pp. 273–278, 2008.
- [8] D. L. Cochran, "A comparison of endosseous dental implant surfaces," *Journal of Periodontology*, vol. 70, no. 12, pp. 1523–1539, 1999.
- [9] T. J. Webster, R. W. Siegel, and R. Bizios, "Osteoblast adhesion on nanophase ceramics," *Biomaterials*, vol. 20, no. 13, pp. 1221–1227, 1999.
- [10] P. M. Brett, J. Harle, V. Salih, et al., "Roughness response genes in osteoblasts," *Bone*, vol. 35, no. 1, pp. 124–133, 2004.
- [11] E. Jansson and P. Tengvall, "Adsorption of albumin and IgG to porous and smooth titanium," *Colloids and Surfaces B*, vol. 35, no. 1, pp. 45–51, 2004.
- [12] P. Cacciafesta, A. D. L. Humphris, K. D. Jandt, and M. J. Miles, "Human plasma fibrinogen adsorption on ultraflat titanium oxide surfaces studied with atomic force microscopy," *Langmuir*, vol. 16, no. 21, pp. 8167–8175, 2000.
- [13] P. Cacciafesta, K. R. Hallam, A. C. Watkinson, G. C. Allen, M. J. Miles, and K. D. Jandt, "Visualisation of human plasma fibrinogen adsorbed on titanium implant surfaces with different roughness," *Surface Science*, vol. 491, no. 3, pp. 405–420, 2001.
- [14] H. Nygren, P. Tengvall, and I. Lundstrom, "The initial reactions of TiO₂ with blood," *Journal of Biomedical Materials Research*, vol. 34, no. 4, pp. 487–492, 1997.
- [15] S. Kidoaki and T. Matsuda, "Adhesion forces of the blood plasma proteins on self-assembled monolayer surfaces of alkanethiolates with different functional groups measured by an atomic force microscope," *Langmuir*, vol. 15, no. 22, pp. 7639–7646, 1999.
- [16] A. G. Hemmersam, M. Foss, J. Chevallier, and F. Besenbacher, "Adsorption of fibrinogen on tantalum oxide, titanium oxide and gold studied by the QCM-D technique," *Colloids and Surfaces B*, vol. 43, no. 3-4, pp. 208–215, 2005.
- [17] M. Rouahi, E. Champion, O. Gallet, A. Jada, and K. Anselme, "Physico-chemical characteristics and protein adsorption potential of hydroxyapatite particles: influence on in vitro biocompatibility of ceramics after sintering," *Colloids and Surfaces B*, vol. 47, no. 1, pp. 10–19, 2006.
- [18] R. Silvennoinen, K.-E. Peiponen, and K. Myller, *Specular Gloss*, Elsevier, Amsterdam, The Netherlands, 1st edition, 2008.
- [19] R. Silvennoinen, V. Vetterl, S. Hasoň, et al., "Sensing of human plasma fibrinogen on polished, chemically etched and carbon treated titanium surfaces by diffractive optical element based sensor," *Optics Express*, vol. 16, no. 14, pp. 10130–10140, 2008.
- [20] T. Vitu, T. Polcar, L. Cvrcek, et al., "Structure and tribology of biocompatible Ti-C:H coatings," *Surface and Coatings Technology*, vol. 202, no. 22-23, pp. 5790–5793, 2008.
- [21] T. Polcar, T. Vitu, L. Cvrcek, R. Novak, J. Vyskocil, and A. Cavaleiro, "Tribological behaviour of nanostructured Ti-C:H coatings for biomedical applications," *Solid State Sciences*, vol. 11, no. 10, pp. 1757–1761, 2009.
- [22] R. A. M. Azzam and N. M. Bashra, *Ellipsometry and Polarized Light*, North-Holland, Amsterdam, The Netherlands, 1977.
- [23] S.-M. F. Nee and T.-W. Nee, "Principal Mueller matrix of reflection and scattering measured for a one-dimensional rough surface," *Optical Engineering*, vol. 41, no. 5, pp. 994–1001, 2002.
- [24] J. T. Räsänen, M. Savolainen, R. Silvennoinen, and K.-E. Peiponen, "Optical sensing of surface roughness and waviness by a computer-generated hologram," *Optical Engineering*, vol. 34, no. 9, pp. 2574–2580, 1995.
- [25] P. Beckmann and A. Spizzichino, *The Scattering of Electromagnetic Waves from Rough Surface*, Pergamon Press, Oxford, UK, 1963.
- [26] S. Donati, "Coupling dynamics in lasers and applications in self-mixing interferometry," in *Proceedings of the 2nd International Meeting on Optical Sensing and Artificial Vision (OSAV'08)*, p. 67, 2008.
- [27] O. V. Angelsky and P. P. Maksimyak, "Optical diagnostics of random phase objects," *Applied Optics*, vol. 29, pp. 2894–2898, 1990.
- [28] O. V. Angelsky, A. P. Maksimyak, P. P. Maksimyak, and S. G. Hanson, "Optical correlation diagnostics of rough surfaces with large surface inhomogeneities," *Optics Express*, vol. 14, no. 16, pp. 7299–7311, 2006.
- [29] R. M. Slawson, M. I. Van Dyke, H. Lee, and J. T. Trevors, "Germanium and silver resistance, accumulation, and toxicity in microorganisms," *Plasmid*, vol. 27, no. 1, pp. 72–79, 1992.
- [30] I. Chopra, "The increasing use of silver-based products as antimicrobial agents: a useful development or a cause for concern?" *Journal of Antimicrobial Chemotherapy*, vol. 59, no. 4, pp. 587–590, 2007.

- [31] O. Akhavan and E. Ghaderi, "Enhancement of antibacterial properties of Ag nanorods by electric field," *Science and Technology of Advanced Materials*, vol. 10, no. 1, Article ID 015003, 2009.
- [32] E. D. Palik, Ed., *Handbook of Optical Constants of Solids, Volume I, II, and III*, Academic Press, San Diego, Calif, USA, 1998.
- [33] J.-M. Zhang, F. Ma, K.-W. Xu, and X.-T. Xin, "Anisotropy analysis of the surface energy of diamond cubic crystals," *Surface and Interface Analysis*, vol. 35, no. 10, pp. 805–809, 2003.
- [34] S. Bar-Chaput and C. Carrot, "Interactions of active carbon with low- and high-molecular weight polyethylene glycol and polyethylene oxide," *Journal of Applied Polymer Science*, vol. 100, no. 5, pp. 3490–3497, 2006.
- [35] W. Brandl, G. Marginean, V. Chirila, and W. Warschewski, "Production and characterisation of vapour grown carbon fiber/polypropylene composites," *Carbon*, vol. 42, no. 1, pp. 5–9, 2004.
- [36] X. H. Zhang, A. Quinn, and W. A. Ducker, "Nanobubbles at the interface between water and a hydrophobic solid," *Langmuir*, vol. 24, no. 9, pp. 4756–4764, 2008.
- [37] A. Grinevich, L. Bacakova, A. Choukourov, et al., "Nanocomposite Ti/hydrocarbon plasma polymer films from reactive magnetron sputtering as growth support for osteoblast-like and endothelial cells," *Journal of Biomedical Materials Research Part A*, vol. 88, no. 4, pp. 952–966, 2009.

Research Article

Detection and Localization of Defects in Monocrystalline Silicon Solar Cell

P. Tománek, P. Škarvada, R. Macků, and L. Grmela

Department of Physics, Faculty of Electrical Engineering and Communication, Brno University of Technology, Technická 8, 616 00 Brno, Czech Republic

Correspondence should be addressed to P. Tománek, tomanek@feec.vutbr.cz

Received 14 December 2009; Accepted 16 March 2010

Academic Editor: Peter V. Polyanskii

Copyright © 2010 P. Tománek et al. This is an open access article distributed under the Creative Commons Attribution License, which permits unrestricted use, distribution, and reproduction in any medium, provided the original work is properly cited.

Near-surface defects in solar cell wafer have undesirable influence upon device properties, as its efficiency and lifetime. When reverse-bias voltage is applied to the wafer, a magnitude of electric signals from defects can be measured electronically, but the localization of defects is difficult using classical optical far-field methods. Therefore, the paper introduces a novel combination of electric and optical methods showing promise of being useful in detection and localization of defects with resolution of 250 nm using near-field nondestructive characterization techniques. The results of mapped topography, local surface reflection, and local light to electric energy conversion measurement in areas with small defects strongly support the development and further evaluation of the technique.

1. Introduction

Although the concept of photovoltaic (PV) devices descends from the mid-19th century, its modern age began after 1950 [1]. Solar cells fulfill two principal functions: photo-generation of charge carriers—electrons and holes—in a light-absorbing material, and separation of the charge carriers to a conductive contact that transmits the electric current [2]. Their efficiency is limited by a number of factors, which include fundamental power losses (incomplete absorption of light or dissipation of a part of the photon energy as heat); losses caused by the reflection of light from the cell surface; and finally, a recombination of the electron-hole pairs in the substrate.

The basic methods for the characterization of silicon solar cells are generally electrical measurements [3–5]. Electrical methods represent an integral measurement on the whole cell. Unfortunately, they do not enable to localize defects occurring in the structure. Local defects in the p-n junction may be associated with structural imperfections (such as grain boundaries, dislocations, and scratches), impurities, higher concentrations of donors and acceptors, or both [6]. Therefore, it is important not only to find most

harmful defects, but also to understand their nature and identify the factors which affect adversely their formation and recombination properties. The used PV analytical tools are generally divided into two groups.

- (i) Mapping techniques which allow the access to the areas of interest (usually the areas with high probability of defects). For materials analysis, lifetime-mapping tools such as surface photo voltage (SPV) [7], microwave photo conductance decay (MW PCD) [8] are frequently applied. Other methods map spatial distribution of photocurrent induced by laser beam (LBIC) [9], or by electron beam-induced current (EB-IC) [10] over whole wafer.
- (ii) Nonmapping techniques that are applied to provide better insight into the nature of recombination centers [11, 12].

For this reason, and for more precise mapping, the use of local characterization methods seems to be very important. Owing to the diffraction, there are Rayleigh limitations of the resolution in traditional optical microscopy. A higher

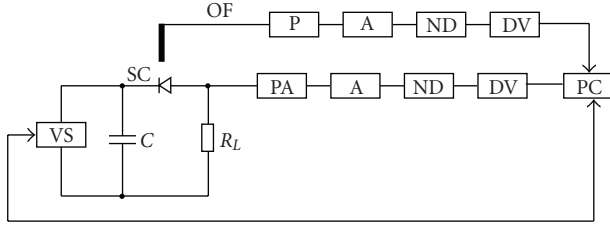


FIGURE 1: Scheme of experimental setup for the measurement of effective values of noise current versus reverse-bias voltage of electric (lower arm) and optical (upper arm) signals.

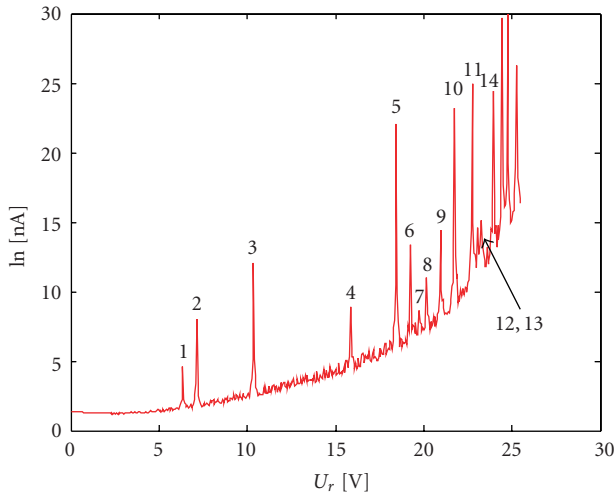
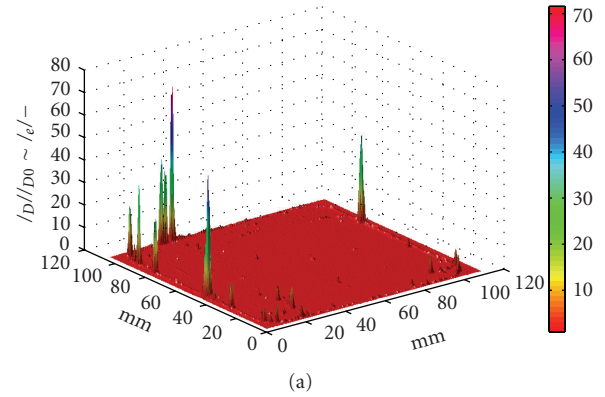


FIGURE 2: Defect noise current versus reverse voltage of the solar cell wafer. Numbers show a noise signal. By repeating a measurement, the noise current figure always appears at same bias voltages.

resolution can be achieved with confocal microscopy [13] or Scanning Near-field Microscopy (SNOM) [14].

The combination of SNOM with LBIC allows creating a strong characterization method of Near-field Optical Beam-Induced Photocurrent (NOB-IC) [15]. This method provides a measurement of the current locally induced by optical near-field. The combination of high resolution of the microscope with locally induced light by sharpened optical fiber allows obtaining a resolution below the wavelength of used light.

Due to the fact that solar cells are optoelectronic devices based on photoelectric effect, it is natural and desirable testing them by using optical and optoelectronic methods. Nevertheless, almost all scientific groups studied one kind of these characteristics only—electrical or optical ones. Our previous effort has been focused on the investigation of solar cells [16, 17], because their local properties are not well described yet. To elucidate slightly more this problem, elaborated combination of electric and localized optical measurement, which allows the detection and localization of defects in the solar cell wafer, and to compare experimental results and obtain higher resolution, is presented.



(a)



(b)

FIGURE 3: Localization of defects imperfection areas of solar cell wafer using reverse-bias light emission from different wafer sites ($U_r = 18.5\text{V}$).

2. Experimental Methods and Material

The sample of monocrystalline silicon solar cell wafer with area of $10\text{ cm} \times 10\text{ cm}$ has been tested. Most important part of the solar cell is its p-n junction. When reverse-bias voltage is applied, lower voltage breakdown of p-n junction occurs in defect sites. reversing the current shift in the homogeneous breakdown may be primarily formed by the current flux in local defects. The emission from defect could be considered as noise current. In areas of increased concentration of free charge carriers due to the small cross sections, there is a large current density which can lead to strong local heating and then to the local diffusion and heat breakdown.

2.1. Photoelectric Measurement. To set a suitable reverse voltage, which leads to emission of radiation from defects, computer-controlled voltage source (VS), filter capacitor (C), and parallel load resistance (R_L) were used (Figure 1). The circuit was connected to the reverse state monocrystalline solar cell wafer (SC) with area of $10\text{ cm} \times 10\text{ cm}$. The electrical signal was detected at the load resistor $R_L = 5.17\ \Omega$. The obtained signal was amplified by preamplifier (PA) and amplifier (A). Plastic optical fiber (OF) with aperture of $200\ \mu\text{m}$ has scanned over solar cell and collected a weak optical signal emitted from this place and sent it to the photomultiplier (P) and amplifier (A) (Figure 1).

To measure noise voltage characteristics and photoelectric signals in the sample, two noise detectors (NDS) (selective Nanovoltmeters Unipan 237) have been used. The upper arm of the setup was tuned to the frequency of 10 kHz for the optical signal, and the lower arm to 4.2 kHz

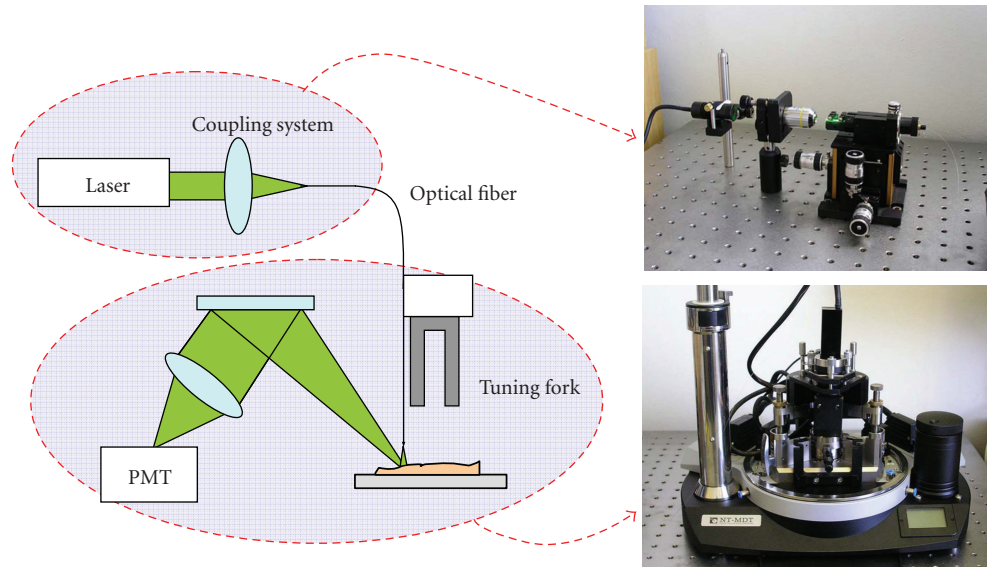


FIGURE 4: SNOM experimental setup for the measurement of effective values of electric response, optical properties—reflectance, and topography of solar cell in the near-field.

for the electric one. The voltage was measured by digital voltmeter (DV) and values were stored on PC. With this setup, the effective values of noise current versus reverse-bias voltage of electric and optical signals were measured. The bias voltage was continuously set from 0 to 25 V. Figure 2 represents the relation between defect noise current and reverse-bias voltage over whole solar cell wafer. By repeating this measurement, the noise signals appeared for the same values of bias voltages.

The corresponding optical application in upper arm provides localization of defects or imperfections. When the reverse-bias voltage was applied, any noise signal from defect site has not been observed up to first important current peak at $U_r = 6.8$ V (peak 1 in Figure 2). With further increasing of the voltage, other near-surface defects appeared in different sites on the sample. When bias voltage reached a value of $U_r = 18.5$ V, several very intensive spots, originated mainly in ill-cutting edges of solar cell, defects in p-n junction, or imperfections of structure, have been clearly localized (Figure 3), and a corresponding current signal was quite strong (peak 5 in Figure 2). For other values, the location of these sites could vary in function of defects nature. Above 23 V, the electric noise signals inside silicon wafer dominated over defect signals and interpretation of results was no more meaningful.

2.2. Near-Field Measurements. In the second method (near-field NOBIC experiment) [18, 19], a very small area of silicon solar cell surface (approx. 150 nm in diameter) has been excited by green laser diode ($\lambda = 532$ nm) light transmitted through a nanometer-sized (70 nm) aperture in the Ag-coated sharpened single mode fiber probe (Figure 4).

The excitation light was amplitude modulated by the light chopper at frequency of 300 Hz. The input power coupled into the optical fiber probe was 3 mW, and output

power from the fiber probe varied between 10 nW and 100 nW, when detected by remote detector. Consequently, the detected photo-induced current varied in the range 100–300 pA. The localized photo-induced current across the layer of solar cell was then detected as a function of the tip position above the sample surface mounted on an x-y-z piezo and was scanned (the scanning step of 50 nm) related to the probe tip. During the scan the tip-sample distance is kept constant at (5 ± 1) nm using an optical shear force feedback control. Thanks to this setup, the xy current distribution map of solar cell has been obtained. The photo-induced current signal has been detected by a lock-in nanovoltmeter while the solar cell was reverse-biased or unbiased [20].

The accuracy of this method depends primarily on the light spot size and on the scanning step of the piezo driver, which are inversely proportional. By long step the accuracy of the method is low, but whole measurement process accelerates because of reduced number of measured points. Therefore, it was very important to choose an optimal ratio scanning step/spot size.

The topography of the sample with a pyramidal texture is shown in Figure 5(a). The electrical response signals, corresponding reflectance, and topography are demonstrated by dependence on spatial coordinate in Figure 5(b). Black curve corresponds to the profile of the sample surface. Blue one corresponds to the electrical response signal and purple one represents a local surface reflectance (in one scanning line).

Relative electrical response mapped by color scale onto original topography of the sample is shown in Figure 6. The pyramidal structure form Figure 5 has been etched so to decrease the electrical response on the tops of texture, which allow obtaining higher electric efficiency of the cell. This new mesa structure of the samples is presently the object of intensive study.

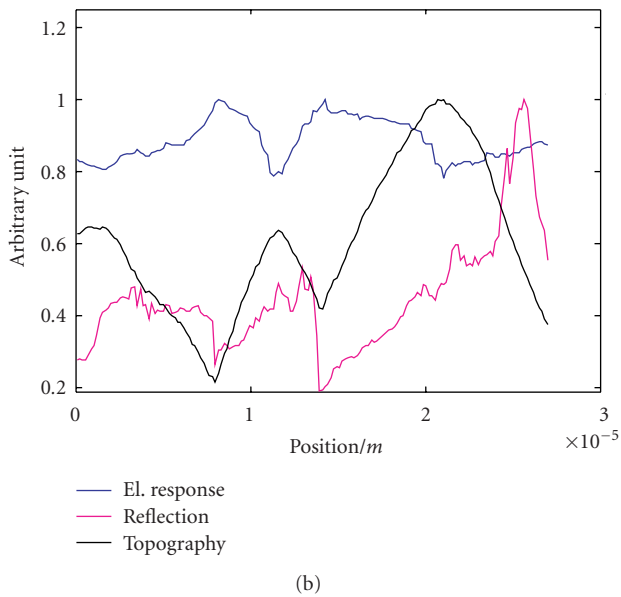
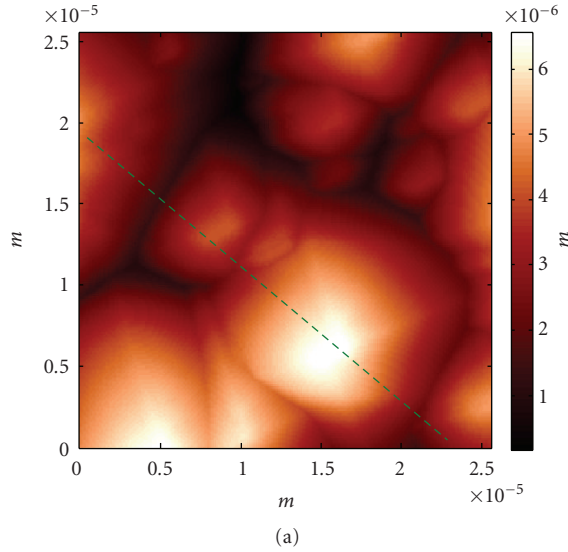


FIGURE 5: Local topography of solar cell sample with pyramidal structure (a), and corresponding scan of electrical response, reflectivity and topography (b).

3. Conclusions

The novel combination of methods for samples local electric detection and optical localization with micro- and nano-scale resolution for the study of monocrystalline silicon solar cell wafer is presented. Applying the reverse-bias voltage, several intensity spots, originated mainly in ill-cutting edges of solar cell, defects in p-n junction, or imperfections of structure, have been clearly localized (Figure 3), and noise current signal peak was quite strong (peak 5 in Figure 2). Above 23 V, the electric noise signals inside silicon wafer dominated over defect signals and interpretation of results was no more meaningful.

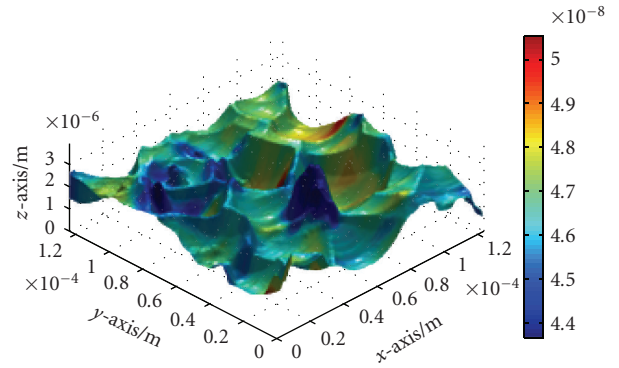


FIGURE 6: Constant local light to current conversion distribution mapped at sample surface topography. Measurement parameters: scanning velocity $v = 18.5 \mu\text{m/s}$, set point $U = 8.9 \text{ V}$, feedback gain 0.5, modulation frequency $f = 850 \text{ Hz}$, used light wavelength $\lambda = 532 \text{ nm}$, temperature $T = 298 \text{ K}$, load resistance $R = 3.3 \Omega$.

A combination of NOBIC and reflectivity measurement with the resolution of about 250 nm has also been established. After calibration of the setup, the accuracy of the combined reflection measurements is better than 5%. At short circuit condition, the NOBIC photocurrent of this cell dominates over the variation of the reflectivity. Based on correlations with aperture-SNOM, the sites corresponding to largest and smallest reflections have been assigned. The photocurrent is the smallest on top of protruding peaks which have a greater local reflectivity, and is the largest in the valleys with the smallest reflectivity. Using this correlation we have found, that the photocurrent for applying a forward voltage decreases inhomogeneously at different locations (Figures 5 and 6). The measurement has shown smaller relative fall of the photocurrent for the illumination of valleys in comparison with the peaks in the structure.

Proposed characterization method based on scanning probe microscopy technique SNOM allows nondestructive and noncontact sample study (defects in p-n junction, structure imperfections, and local photoelectric measurements). A maximum of optically excited photocurrent is indicator of local conversion efficiency due to local light constant energy excitation, and number of imperfections is a quality indicator for solar cell lifetime and only precise testing can help to determine a nature of defects. At present time, it is quite difficult to find a correlation between defect nature and its appearance. Therefore, for further improvement of monocrystalline silicon solar cells efficiency, more intensive mapping and nonmapping measurements of optical and electric properties are challenged.

Acknowledgments

This work has been supported by the Czech Ministry of Education in the frame of MSM 0021630503 Research Intention MIKROSYN “New Trends in Microelectronic System and Nanotechnologies” and by GACR Grant 102/08/1474 “Local optical and electric characterization of optoelectronic devices with nanometer resolution”.

References

- [1] D. M. Chapin, C. S. Fuller, and G. L. Pearson, "A new silicon *p-n* junction photocell for converting solar radiation into electrical power," *Journal of Applied Physics*, vol. 25, no. 5, pp. 676–677, 1954.
- [2] European Renewable Energy Council, "Renewable Energy Target for Europe—20% by 2020," January 2004, http://www.erec.org/fileadmin/erec_docs/Documents/Publications/Renewable_Energy_Technology_Roadmap.pdf.
- [3] A. G. Chynoweth and K. G. McKay, "Light emission and noise studies of individual microplasmas in silicon *p-n* junctions," *Journal of Applied Physics*, vol. 30, no. 11, pp. 1811–1813, 1959.
- [4] A. R. Haitz, "Model for the electrical behaviour of microplasma," *Journal of Applied Physics*, vol. 35, no. 5, pp. 1370–1376, 1964.
- [5] J. Nelson, *The Physics of Solar Cells*, Imperial College Press, London, UK, 2007.
- [6] P. Škarvada and P. Tománek, "Local light to electric energy conversion measurement of silicon solar cells," in *Proceedings of the Reliability and Life-Time Prediction*, pp. 101–104, Zsolt Illyefalvi-Vitéz, Bálint Balogh, Budapest Hungary, 2008.
- [7] L. Kronik and Y. Shapira, "Surface photovoltage spectroscopy of semiconductor structures: at the crossroads of physics, chemistry and electrical engineering," *Surface and Interface Analysis*, vol. 31, no. 10, pp. 954–965, 2001.
- [8] P. A. Basore and B. R. Hansen, "Microwave-detected photoconductance decay," in *Proceedings of the Conference Record of the 21st IEEE Photovoltaic Specialists Conference*, vol. 1, pp. 374–379, 1990.
- [9] C. Donolato, "Theory of beam induced current characterization of grain boundaries in polycrystalline solar cells," *Journal of Applied Physics*, vol. 54, no. 3, pp. 1314–1322, 1983.
- [10] P. Koptavy, J. Vanek, Z. Chobola, K. Kubickova, and J. Kazelle, "Solar cell noise diagnostic and LBIC comparison," in *Proceedings of the International Conference on Noise and Fluctuations*, vol. 922, pp. 306–309, 2007.
- [11] D. K. Schroder, *Semiconductor Material and Device Characterization*, Wiley-IEEE Press, 3rd edition, 2006.
- [12] S. Rein, *Lifetime Spectroscopy: A Method of Defect Characterization in Silicon for Photovoltaic Applications*, vol. 85, Springer, Berlin, Germany, 2005.
- [13] E. Esposito, F.-J. Kao, and G. McConnell, "Confocal optical beam induced current microscopy of light-emitting diodes with a white-light supercontinuum source," *Applied Physics B*, vol. 88, no. 4, pp. 551–555, 2007.
- [14] P. Tománek, J. Brüstlová, P. Dobis, and L. Grmela, "Hybrid STM/R-SNOM with novel probe," *Ultramicroscopy*, vol. 71, no. 1–4, pp. 199–203, 1998.
- [15] M. S. Unlü, B. B. Goldberg, W. D. Herzog, D. Sun, and E. Towe, "Near-field optical beam induced current measurements on heterostructures," *Applied Physics Letters*, vol. 67, no. 13, pp. 1862–1864, 1995.
- [16] P. Škarvada, P. Tománek, and R. Macků, "Study of local properties of silicon solar cells," in *Proceedings of the 23rd European Photovoltaic Solar Energy Conference*, pp. 1644–1647, WIP-Renewable Energies, Valencia, Spain, 2008.
- [17] P. Tománek, P. Škarvada, and L. Grmela, "Local optical and electron characteristics of solar cells," in *9th International Conference on Correlation Optics*, vol. 7388 of *Proceedings of SPIE*, Chernivtsi, Ukraine, September 2009.
- [18] D. C. Coffey, O. G. Reid, D. B. Rodovsky, G. P. Bartholomew, and D. S. Ginger, "Mapping local photocurrents in polymer/fullerene solar cells with photoconductive atomic force microscopy," *Nano Letters*, vol. 7, no. 3, pp. 738–744, 2007.
- [19] M. Benešová, P. Dobis, P. Tománek, and N. Uhdeová, "Local measurement of optically induced photocurrent in semiconductor structures," in *Photonics, Devices, and Systems II*, vol. 5036 of *Proceedings of SPIE*, pp. 635–639, 2002.
- [20] P. Škarvada, L. Grmela, I. F. Abuettwirat, and P. Tománek, "Nanooptics of locally induced photocurrent in monocrystalline Si solar cells," in *Photonics, Devices, and Systems IV*, vol. 7138 of *Proceedings of SPIE*, 2008.

Research Article

The Degree of Mutual Anisotropy of Biological Liquid Crystals Net during the Diagnostics of Human Tissues Birefringence

Oleg V. Angelsky and Yuriy A. Ushenko

Correlation Optics Department, Chernivtsi National University, 2 Kotsyubinsky Str., 58012 Chernivtsi, Ukraine

Correspondence should be addressed to Yuriy A. Ushenko, o.ushenko@chnu.edu.ua

Received 1 December 2009; Accepted 6 April 2010

Academic Editor: Igor I. Mokhun

Copyright © 2010 O. V. Angelsky and Y. A. Ushenko. This is an open access article distributed under the Creative Commons Attribution License, which permits unrestricted use, distribution, and reproduction in any medium, provided the original work is properly cited.

To characterize the degree of consistency of parameters of the optically uniaxial birefringent liquid crystals (protein fibrils) nets of biological tissues a new parameter-complex degree of mutual anisotropy is suggested. The technique of polarization measuring the coordinate distributions of the complex degree of mutual anisotropy of biological tissues is developed. It is shown that statistic approach to the analysis of complex degree of mutual anisotropy distributions of biological tissues of various morphological and physiological states and optical thicknesses appears to be more sensitive and efficient in differentiation of physiological state in comparison with investigations of complex degree of mutual polarization of the corresponding laser images.

1. Introduction

In [1, 2] for characterizing the consistency between the polarization states the laser object field in the points (r_1, r_2) with the intensities $I(r_1)$, $I(r_2)$ a new parameter-complex degree of mutual polarization (CDMP) in the next form

$$V(r_1, r_2) = \frac{(U_x(r_1)U_x^*(r_2) + U_y(r_1)U_y^*(r_2))^2}{I(r_1)I(r_2)}. \quad (1)$$

This “two-point” theoretical approach was extended to the analysis of polarization-inhomogeneous laser images of human BT with the aim of experimental diagnostics of optical anisotropic structure [3]. In [4] a method of direct polarization measurement of the real part of CDMP for different points (r_1, r_2) of optically thin image (attenuation coefficient $\tau \leq 0, 1$) of BT layers is proposed

$$\begin{aligned} \operatorname{Re}\{V\} &\equiv \tilde{V}(r_1, r_2) \\ &= \frac{\{U_x(r_1)U_x(r_2) - U_y(r_1)U_y(r_2) \cos[\varphi(r_1) - \varphi(r_2)]\}^2}{I(r_1)I(r_2)}, \end{aligned} \quad (2)$$

where $\varphi(r_1)$ and $\varphi(r_2)$ are the phase shifts between the orthogonal components U_x , U_y of laser amplitude in object field.

The ranges of changes of the 1st–4th distribution order statistic moments $\tilde{V}(x, y)$ of the corresponding laser images, important for diagnostics of the human connective tissue oncologic state were determined in [5, 6]. On the other hand, such analysis techniques of $\tilde{V}(x, y)$ lead to disregarding the BT extracellular matrix birefringence, which is a principal physical mechanism of their polarization-heterogeneous images formation [7–11]. That is why it appears to be important to search for new diagnostic parameters directly characterizing the degree of consistency of optical axes and birefringence orientations of various points of protein fibrils network forming the BT extracellular matrix [3].

This paper is aimed on investigation of diagnostic possibilities of optical-anisotropic structure of biological tissues extracellular matrix of different morphology and physiological state by means of statistic analysis of a new parameter-CDMA coordinate distribution.

2. Theoretical Analysis of Laser Radiation Parameters Transformation by the Network of Optically Uniaxial Birefringent Liquid Crystals

The processes of laser beam interaction with BT are discussed in the following model approximation [12–16]:

- (1) Morphologically all of variety of human tissues consists of four main types (connective, muscle, epithelial, and nervous), each of it is formed by a two-component amorphous-crystalline structure.
- (2) The crystalline component of the BT (extracellular matrix) is formed by a network of coaxial cylindrical liquid crystals (collagen, elastin, myosin, etc, fibrils).
- (3) From the optical point of view, protein fibrils possess properties of optically uniaxial crystals with the index of birefringence Δn . Parameters of anisotropy ($\rho(r)$, $\delta(r)$) of these fibrils in every point (r) are described by the operator of Jones [17]

$$\{D\} = \begin{vmatrix} d_{11}(r) & d_{12}(r) \\ d_{21}(r) & d_{22}(r) \end{vmatrix} \quad (3)$$

$$= \begin{vmatrix} \cos^2 \rho(r) + \sin^2 \mathfrak{A} & \mathfrak{B} \\ \mathfrak{B} & \sin^2 \rho(r) + \cos^2 \mathfrak{A} \end{vmatrix},$$

where \mathfrak{B} denotes $\cos \rho(r) \sin \rho(r) [1 - \exp(-i\delta(r))]$ and \mathfrak{A} denotes $\rho(r) \exp(-i\delta(r))$.

Here $\rho(r)$ —the angle (orientation) of the optical axis, which is determined by the direction of packing of birefringent (Δn) protein fibrils with a transverse size $d(r)$; $\delta(r) = (2\pi/\lambda)\Delta n d(r)$ —phase shift of laser beam with the wavelength λ at coordinate r .

It should be mentioned that further consideration of the possibilities of two-point Jones matrix description of complex anisotropy will be performed in a 2D approximation for (x, y) plane of biological crystals anisotropic layer— $r \equiv r(x, y)$.

With accordance to the approach outlined in [2], use (1)–(3) we obtain the following expression for the parameter $W(r_1, r_2)$ (complex degree of mutual anisotropy—CDMA) that characterizes the degree of coordination between the orientation ($\rho_1(r_1), \rho_2(r_2)$) and phase ($\delta_1(r_1); \delta_2(r_2)$) parameters of the anisotropy of different points (r_1, r_2) in the plane of birefringent protein crystals network of the extracellular matrix

$$W(r_1, r_2) = \frac{A(r_1, r_2) + B(r_1, r_2)}{C(r_1, r_2)}, \quad (4)$$

where

$$A = [d_{11}(r_1) + d_{12}(r_1)tg\Omega_0 \exp(-i\varphi_0)] \times [d_{11}(r_2) + d_{12}(r_2)tg\Omega_0 \exp(-i\varphi_0)]^*,$$

$$B = \{ [d_{21}(r_1) + d_{22}(r_1)tg\Omega_0 \exp(-i\varphi_0)] \times [d_{21}(r_2) + d_{22}(r_2)tg\Omega_0 \exp(-i\varphi_0)]^* \} \times \exp\{-i[\delta_2(r_2) - \delta_1(r_1)]\},$$

$$C = \{ [d_{11}(r_1) + d_{12}(r_1)tg\Omega_0 \exp(-i\varphi_0)] \times [d_{11}(r_1) + d_{12}(r_1)tg\Omega_0 \exp(-i\varphi_0)]^* \quad (5)$$

$$+ [d_{21}(r_1) + d_{22}(r_1)tg\Omega_0 \exp(-i\varphi_0)] \times [d_{21}(r_1) + d_{22}(r_1)tg\Omega_0 \exp(-i\varphi_0)]^* \}$$

$$+ \{ [d_{11}(r_2) + d_{12}(r_2)tg\Omega_0 \exp(-i\varphi_0)] \times [d_{11}(r_2) + d_{12}(r_2)tg\Omega_0 \exp(-i\varphi_0)]^*$$

$$+ [d_{21}(r_2) + d_{22}(r_2)tg\Omega_0 \exp(-i\varphi_0)] \times [d_{21}(r_2) + d_{22}(r_2)tg\Omega_0 \exp(-i\varphi_0)]^* \}.$$

Here φ_0 —(constant and crystals network anisotropic parameters independent) the phase shift between the orthogonal components U_{0x} and U_{0y} of the illuminating laser beam amplitude, $tg\Omega_0 = U_{0y}/U_{0x}$. Multipliers $\exp(-i\varphi_0)$ and $tg\Omega_0$ are defined by illuminated laser beam polarization state and birefringent biological crystals optical-geometric structure independent.

Analysis of (4) and (5) shows the dependence of $W(r_1, r_2)$ on rotation of the polarization plane of the illuminating laser wave or rotation of the BT layer to the irradiation direction. The only exception is a case of irradiation of BT by the circular polarized ($tg\Omega_0 = 1; \varphi_0 = 0, 5\pi$) laser wave U_0

$$U_0 = \begin{pmatrix} U_{0x} \\ U_{0y} \exp(-i\varphi_0) \end{pmatrix} \equiv \frac{1}{\sqrt{2}} \begin{pmatrix} 1 \\ i \end{pmatrix}. \quad (6)$$

In accordance with (6) the equations (4) and (5) become the following form:

$$W(r_1, r_2) = \frac{\{ [d_{11}(r_1) + id_{12}(r_1)][d_{11}(r_2) + id_{12}(r_2)]^* + [d_{21}(r_1) + id_{22}(r_1)][d_{21}(r_2) + id_{22}(r_2)]^* \}^2}{I(r_1)I(r_2)}. \quad (7)$$

Here $I(r_1)$ and $I(r_2)$ are determined by relations

$$I(r_1) = \left\{ [d_{11}(r_1) + id_{12}(r_1)][d_{11}(r_1) + id_{12}(r_1)]^* + [d_{21}(r_1) + id_{22}(r_1)][d_{21}(r_1) + id_{22}(r_1)]^* \right\},$$

$$I(r_2) = \left\{ [d_{11}(r_2) + id_{12}(r_2)][d_{11}(r_2) + id_{12}(r_2)]^* + [d_{21}(r_2) + id_{22}(r_2)][d_{21}(r_2) + id_{22}(r_2)]^* \right\}.$$

$$+ [d_{21}(r_2) + id_{22}(r_2)][d_{21}(r_1) + id_{22}(r_2)]^* \}. \quad (8)$$

Taking the real part ($\text{Re}\{d_{ik}(r)\} \equiv \tilde{d}_{ik}(r)$) of the Jones matrix elements (3), we obtain an expression for the real part of the CDMA ($\text{Re}\{W(r_1, r_2)\} \equiv \tilde{W}(r_1, r_2)$) of extracellular matrix of BT layer, which can be obtained by direct polarization measurements

$$\tilde{W}(r_1, r_2) = \frac{\left\{ [\tilde{d}_{11}(r_1)\tilde{d}_{11}(r_2) - \tilde{d}_{12}(r_1)\tilde{d}_{12}(r_2)] + [\tilde{d}_{21}(r_1)\tilde{d}_{21}(r_2) - \tilde{d}_{22}(r_1)\tilde{d}_{22}(r_2)] \right\}^2}{I(r_1)I(r_2)}, \quad (9)$$

where

$$\begin{aligned} \tilde{d}_{11}(r_{1,2}) &= \cos^2\rho(r_{1,2}) + \sin^2\rho(r_{1,2}) \cos\delta(r_{1,2}), \\ \tilde{d}_{12,21}(r_{1,2}) &= \cos\rho(r_{1,2}) \sin\rho(r_{1,2}) (1 - \cos\delta(r_{1,2})), \\ \tilde{d}_{22}(r_{1,2}) &= \sin^2\rho(r_{1,2}) + \cos^2\rho(r_{1,2}) \cos\delta(r_{1,2}). \end{aligned} \quad (10)$$

Let us analyze the relationship of CDMA $\tilde{W}(r_1, r_2)$ of BT layer extracellular matrix with variations orientations $\rho_1(r_1)$, $\rho_2(r_2)$ of optical axes and the phase shifts $\delta_1(r_1)$, $\delta_2(r_2)$ that introduced by the protein crystals of the extracellular matrix in the points (r_1, r_2) .

Table 1 shows the main characteristic values of CDMA $\tilde{W}(r_1, r_2)$ in two arbitrary points (r_1, r_2) of the extracellular matrix of BT layer.

From the obtained data one can see that CDMA has a wide range of value changes ($0, 0 \leq \tilde{W}(r_1, r_2) \leq 1, 0$) against to changes of orientation ($\rho(r)$) and phase ($\delta(r)$) anisotropic parameters in different points of biological crystals network. Therefore, the coordinate distribution $\tilde{W}(x, y)$ can be used in diagnostics of optical-geometric structure of biological tissues layers.

3. Optical Scheme and Experimental Measurements of Coordinate CDMA Distributions of Biological Tissue

Experimental investigations were carried out in the classical polarimeter the main parts and elements of which are presented in Figure 1 [4, 5].

It was illuminated by collimated ($\varnothing = 10^4 \mu\text{m}$) He-Ne laser beam ($\lambda = 0.6328 \mu\text{m}$) with the power of $50 \mu\text{W}$. Polarization illuminator (quarter-wavelength plates 3, 5 and polarizer 4) formed the beam with arbitrary polarization azimuth and ellipticity. Polarization images of BT by means of microobjective 7 (focal distance: 1.5 cm, aperture: 0.2, magnification: 4x) were projected into the plane of light-sensitive area of CCD camera (overall amount of pixels: 800×600 , light sensitive area size: $4000 \times 3000 \mu\text{m}$, deviation of photosensitive characteristics from linear no more than 15%), which provided the range of measuring the structural elements of BT with the resolution 2–2000 μm . Maximal

resolution verification (2 μm) where performed using the stage micrometer (linear scale), which image was projected into the light sensitive area of CCD camera with the help of microobjective 7.

Minimal resolution (2000 μm) corresponds to the situation when the light sensitive area of CCD camera is entirely filled by two equal sized structural elements (light and dark) of stage micrometer. The conditions of the experiment were chosen in such a way that it enabled to reduce the space-angular aperture filtering while forming the BT images. This was ensured by conformance of angular characteristics of indicatrices of light scattering by the BT samples ($\Delta\gamma \approx 16^\circ$) and angular aperture of microobjective ($\Delta\omega = 20^\circ$). Here $\Delta\gamma$ is the solid angle within which 98% of all the energy of light-scattered radiation is concentrated.

Initially, according to the classical technique given in [11], it was measured two-dimensional distribution

$$(m \times n) \equiv \begin{pmatrix} r_{11} & \cdots & r_{1m} \\ \cdots & \cdots & \cdots \\ r_{n1} & \cdots & r_{nm} \end{pmatrix}$$

$$\equiv (x = 1 \div m; y = 1 \div n) -$$

$$\left. \begin{array}{l} \text{coordinates of CCD camera pixels} \end{array} \right) \quad (11)$$

of the real parts of Jones matrix elements $\tilde{d}_{ik}(m \times n)$ of BT histological section.

Further rotation of the analyzer 9 transmission plane (Θ) in the limits $\Theta = 0^\circ \div 180^\circ$ it is possible to determine minimum (I_{\min}) and maximum (I_{\max}) levels of intensity for each pixel of CCD-camera 10. Thus, the arrays of the intensity extreme values $I_{\min}(m \times n)$, $I_{\max}(m \times n)$ of laser images of BT histological Section 6 and the corresponding angles of rotation $\Theta_{\min}(m \times n) \Leftrightarrow I_{\min}(m \times n)$ of the analyzer 9 can be obtained.

On the basis of the obtained data it is possible to calculate the coordinate distribution of azimuth $\alpha(m \times n)$

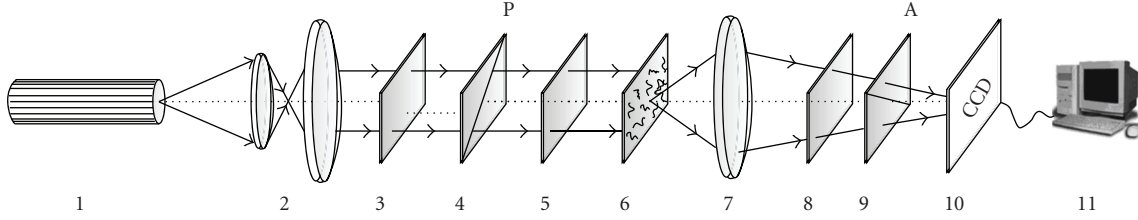


FIGURE 1: Optical scheme of polarimeter for measuring coordinate CDMA distributions of BT. Here 1—He-Ne laser ($\lambda = 0.6328 \mu\text{m}$); 2—collimator; 3, 5 and 8—quarter-wave plates; 4 and 9 polarizers; 6—BT histological section; 7—projection microscope objective; 10—CCD-camera; 11—PC.

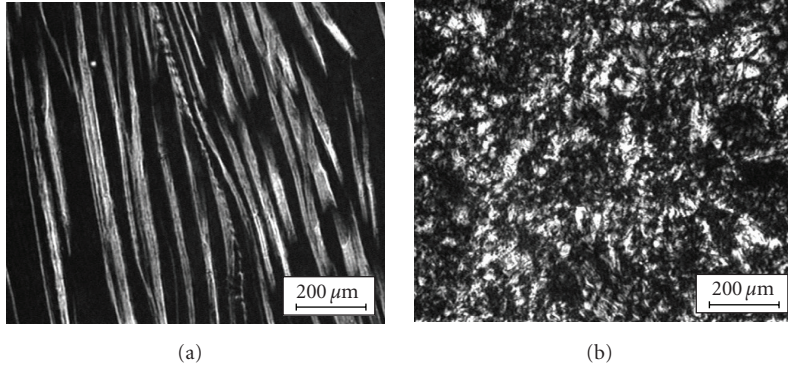


FIGURE 2: Architectonics of the muscular tissue (a) and the dermal layer (b) in crossed polarizer and analyzer.

TABLE 1: Characteristic values of CDMA $\tilde{W}(r_1, r_2)$ of BT extracellular matrix.

$\rho(r_1), \rho(r_2)$	$\delta(r_1) = \delta(r_2)$	$\tilde{W}(r_1, r_2)$
$\rho(r_1) = \rho(r_2),$ $\rho(r_2) = 0, 5\pi + \rho(r_2)$	0	1,0
	$0, 5\pi$	1,0
	π	1,0
$\rho(r_1) = \rho(r_2),$ $\rho(r_2) = 0, 5\pi + \rho(r_2)$	$\delta_2(r_1) = 0, 5\pi + \delta_1(r_2)$	$\tilde{W}(r_1, r_2)$
	$0, 5\pi$	0,5
	π	0,5
	$1, 5\pi$	0,5
$\rho(r_1) = \rho(r_2),$ $\rho(r_2) = 0, 5\pi + \rho(r_2)$	$\delta_2(r_1) = \pi + \delta_1(r_2)$	$\tilde{W}(r_1, r_2)$
	π	0
	$1, 5\pi$	0
	2π	0

and ellipticity $\beta(m \times n)$ of polarization and determine the two-dimensional distribution of phase shifts by using the following algorithms

$$\begin{aligned}
 \alpha(m \times n) &= 0, 5\pi - \Theta(m \times n), \\
 \beta(m \times n) &= \arctg \frac{I_{\min}(m \times n)}{I_{\max}(m \times n)}, \\
 \delta(m \times n) &= \arctg \left[\frac{\text{tg} 2\beta(m \times n)}{\text{tg} \alpha(m \times n)} \right].
 \end{aligned} \tag{12}$$

The value of CDMA $\tilde{W}(r_1, r_2 = r_1 + \Delta r)$ of the two points $(r_1, r_1 + \Delta r)$ shifted by the interval Δr of the network of protein crystals is calculated using the algorithm (9), (10). Coordinate distribution $\tilde{W}(x, y)$ of the BT layer extracellular matrix is determined by scanning with the $\Delta r = 1$ pix step in two mutually transverse directions ($x = 1 \div m, y = 1 \div n$).

4. Experimental Researches of Coordinate Distribution of CDMA of BT with Different Morphological and Physiological States

It should be noted that the structure of the anisotropic component of the different types of BT is rather complicated and diverse [3]. Therefore the analysis of coordinate distribution of optical parameters that are characterized the BT extracellular matrix of various types objectively requires complex statistical, correlation, fractal and topological [11] and other approaches. In our paper we will restrict by study of the relationship of statistical moments of the 1st–4th order [12], which characterize the coordinate distribution $\tilde{W}(x, y)$ of the BT extracellular matrix, with pathological changes of its orientation-phase structure.

As objects of study (Figure 2) were chosen the histological sections of myocardium muscle tissue (MT) (Figure 2(a)) and skin derma layer (SD) (Figure 2(b)). This choice objects of study due to the fact that birefringence indexes (Δn) of myosin (MT— $\Delta n = 1, 35 \cdot 10^{-2}$ [13]) and collagen (SD: $\Delta n = 1, 5 \cdot 10^{-2}$ [14]) fibrils of the extracellular matrix of these tissues are similar. Therefore we can assume that the ranges of phase shifts values ($\delta(x, y)$) are determined

TABLE 2: Statistic moments of the 1st–4th orders of CDMA $\tilde{W}(x, y)$ and CDMP $\tilde{V}(x, y)$ distributions of optically thin ($\tau = 0, 09$) layers of physiologically normal and pathological changed samples of MT and SD.

M_k	Sound ($k = 21$)		Dystrophic changed ($k = 19$)		Sound ($k = 20$)		Oncological changed ($k = 19$)	
	BT		MT		SD		SD	
	\tilde{W}	\tilde{V}	\tilde{W}	\tilde{V}	\tilde{W}	\tilde{V}	\tilde{W}	\tilde{V}
M_1	$0,8 \pm 0,09$	$0,65 \pm 0,07$	$0,58 \pm 0,06$	$0,61 \pm 0,05$	$0,38 \pm 0,04$	$0,27 \pm 0,03$	$0,33 \pm 0,04$	$0,31 \pm 0,03$
M_2	$0,03 \pm 0,004$	$0,04 \pm 0,006$	$0,045 \pm 0,006$	$0,043 \pm 0,005$	$0,1 \pm 0,02$	$0,07 \pm 0,008$	$0,085 \pm 0,009$	$0,063 \pm 0,008$
M_3	$18,1 \pm 1,92$	$11,2 \pm 1,21$	$6,54 \pm 0,87$	$5,15 \pm 0,61$	$9,4 \pm 0,87$	$14,7 \pm 1,16$	$21,7 \pm 1,96$	$19,4 \pm 1,78$
M_4	$30,6 \pm 2,98$	$41,8 \pm 3,17$	$64,7 \pm 6,08$	$61,9 \pm 5,87$	$99,5 \pm 9,63$	$76,9 \pm 6,98$	$36,9 \pm 4,08$	$42,6 \pm 4,17$

TABLE 3: Statistic moments of the 1st–4th orders of CDMA $\tilde{W}(x, y)$ and CDMP $\tilde{V}(x, y)$ distributions of optically thick ($\tau = 0, 75$) layers of physiologically normal and pathological changed samples of SD tissue.

M_k	Sound ($k = 21$)		Dystrophic changed ($k = 19$)		Sound ($k = 20$)		Oncological changed ($k = 19$)	
	BT		MT		SD		SD	
	\tilde{W}	\tilde{V}	\tilde{W}	\tilde{V}	\tilde{W}	\tilde{V}	\tilde{W}	\tilde{V}
M_1	$0,57 \pm 0,062$	$0,45 \pm 0,055$	$0,48 \pm 0,042$	$0,41 \pm 0,047$	$0,45 \pm 0,051$	$0,37 \pm 0,041$	$0,63 \pm 0,057$	$0,41 \pm 0,039$
M_2	$0,04 \pm 0,005$	$0,05 \pm 0,006$	$0,06 \pm 0,005$	$0,065 \pm 0,007$	$0,16 \pm 0,014$	$0,27 \pm 0,033$	$0,18 \pm 0,021$	$0,23 \pm 0,025$
M_3	$12,7 \pm 1,15$	$1,32 \pm 0,14$	$6,34 \pm 0,71$	$0,95 \pm 0,11$	$8,65 \pm 0,83$	$0,77 \pm 0,082$	$12,1 \pm 1,18$	$1,08 \pm 0,09$
M_4	$23,7 \pm 2,12$	$1,78 \pm 0,98$	$41,7 \pm 3,85$	$1,29 \pm 0,16$	$43,3 \pm 4,88$	$1,13 \pm 0,15$	$29,7 \pm 3,07$	$0,86 \pm 0,09$

primarily by transverse geometric dimensions $d(x, y)$ of protein crystals. Range of sizes for a network of SD collagen fibrils constitute the next interval $d = 5 \mu\text{m} \div 45 \mu\text{m}$. For a MT layer of myosin fibrils the variations of sizes is in the range $d = 25 \mu\text{m} \div 35 \mu\text{m}$.

Pathological changes of the MT morphological structure of (myocardial dystrophy) appear in the reduction of birefringence and disordering of packing direction of network myosin fibrils. The peculiarity of the extracellular matrix structure of sound SD is a random distribution of directions ($\rho(x, y)$) of the protein crystals optical axes (Figure 2). Extracellular matrix of oncological changed object of investigation is characterized by a set of ordered “the newly formed” collagen fibrils with a greater value of the birefringence parameter [16].

Therefore, comparative studies of CDMA coordinate distributions of such BT extracellular matrix will help to determine the range of statistical parameters variation of $\tilde{W}(x, y)$ and on this basis, to implement the diagnostic of their physiological state.

The series of coordinate distributions ($x = 1 \text{ pix} \div 600 \text{ pix}$; $y = 1 \text{ pix} \div 800 \text{ pix}$ —fragments (a), (d); $50 \text{ pix} \times 50 \text{ pix}$ —fragments (b), (e)) and the histograms (fragments (c), (f)) of CDMA values $\tilde{W}(x, y)$ of physiologically normal (fragments (a), (b), (c)) and pathologically changed (fragments (d), (e), (f)) histological sections of MT (Figure 3) and SD (Figure 4) histological sections.

The analysis of the obtained experimental data discovered that the coordinate distributions of CDMA (Figures 3(a), 3(d), 4(a), and 4(d)) are formed by the set of the local areas (domains $\tilde{W} \approx \text{const}$,—Figures 3(b), 3(e), and 4(b), 4(e)) with the maximum possible range of variation $0, 0 \leq \tilde{W} \leq 1, 0$ (Figures 3(c), 3(f) and 4(c), 4(f)).

Two-dimensional distribution (Figures 3(a) and 3(d)) of CDMA $\tilde{W}(x, y)$ of MT samples are formed by the domains (Figure 3(b) and 3(d)) with sizes $10 \mu\text{m} \div 30 \mu\text{m}$. Degenerative changes of myosin fibrils network appears in the process of the scale reducing (15%–30%) of the domain structure of CDMA coordinate distribution.

Coordinate structure of CDMA parameter $\tilde{W}(x, y)$ of the SD collagen network is smaller-scale (Figures 4(a), 4(d)). The range of geometric dimensions of domain changes (Figures 4(b) and 4(d)) varies in limits $5 \mu\text{m} \div 15 \mu\text{m}$. Cancer changes of SD architectonic network are revealed in some increase (up to 10%–15%) of the local domains scale.

The experimental data satisfactorily correlate with the proposed model analysis of the extracellular matrix structure with the help of CDMA. Thus, there will always be points ($r, r + \Delta r$) in the network of protein fibrils that define such relationships between the parameters of anisotropy (ρ, δ) (Table 1), which correspond to extreme values of CDMA

$$\tilde{W}(r, r + \Delta r) = \begin{cases} 0; \\ 1, 0. \end{cases} \quad (13)$$

On the other hand, the specificity of the morphological construction of BT extracellular matrix of various types is manifested in different probabilities of CDMA $\tilde{W}(x, y)$ values. It is believed that for directional ordered ($\rho(r = x, y)$) and the geometric dimensions ($d(r = x, y)$) of MT myosin fibrils network (Figure 3(a)) the dispersion of the orientations of optical axes and the phase shifts are substantially less than for the disordered network of SD collagen fibrils (Figure 4(a)). Therefore, the distribution of CDMA random values of MT layer predominantly localized in a small range ($0, 5 \leq \tilde{W} \leq 1, 0$) relatively to the main

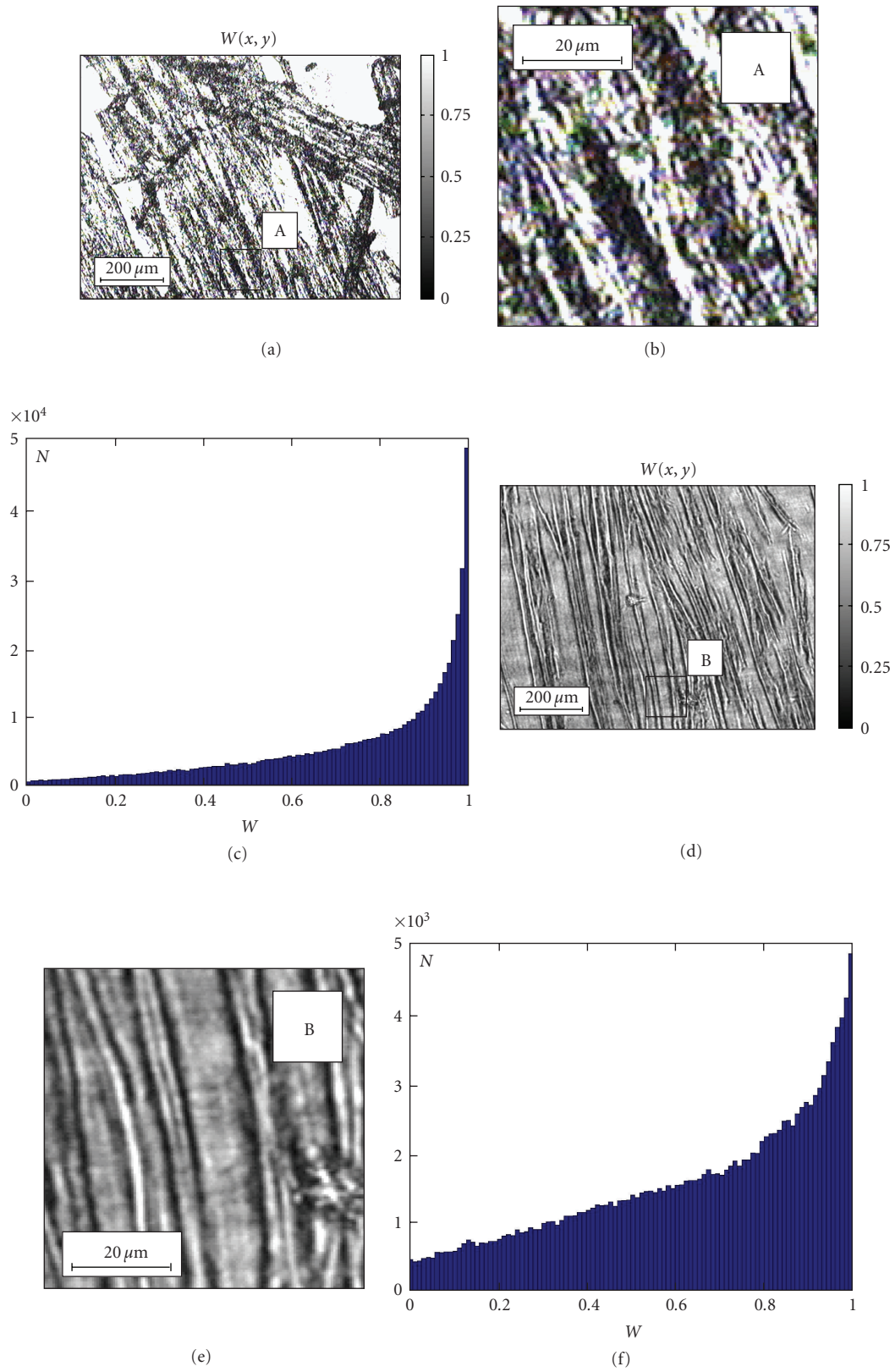


FIGURE 3: Coordinate distributions (600 pix \times 800 pix—fragments a, d; 50 pix \times 50 pix—fragments b, e) and histograms (fragments c, f) of values $\tilde{W}(x, y)$ of physiologically normal (a, b, c) and pathologically changed (d, e, f) of MT.

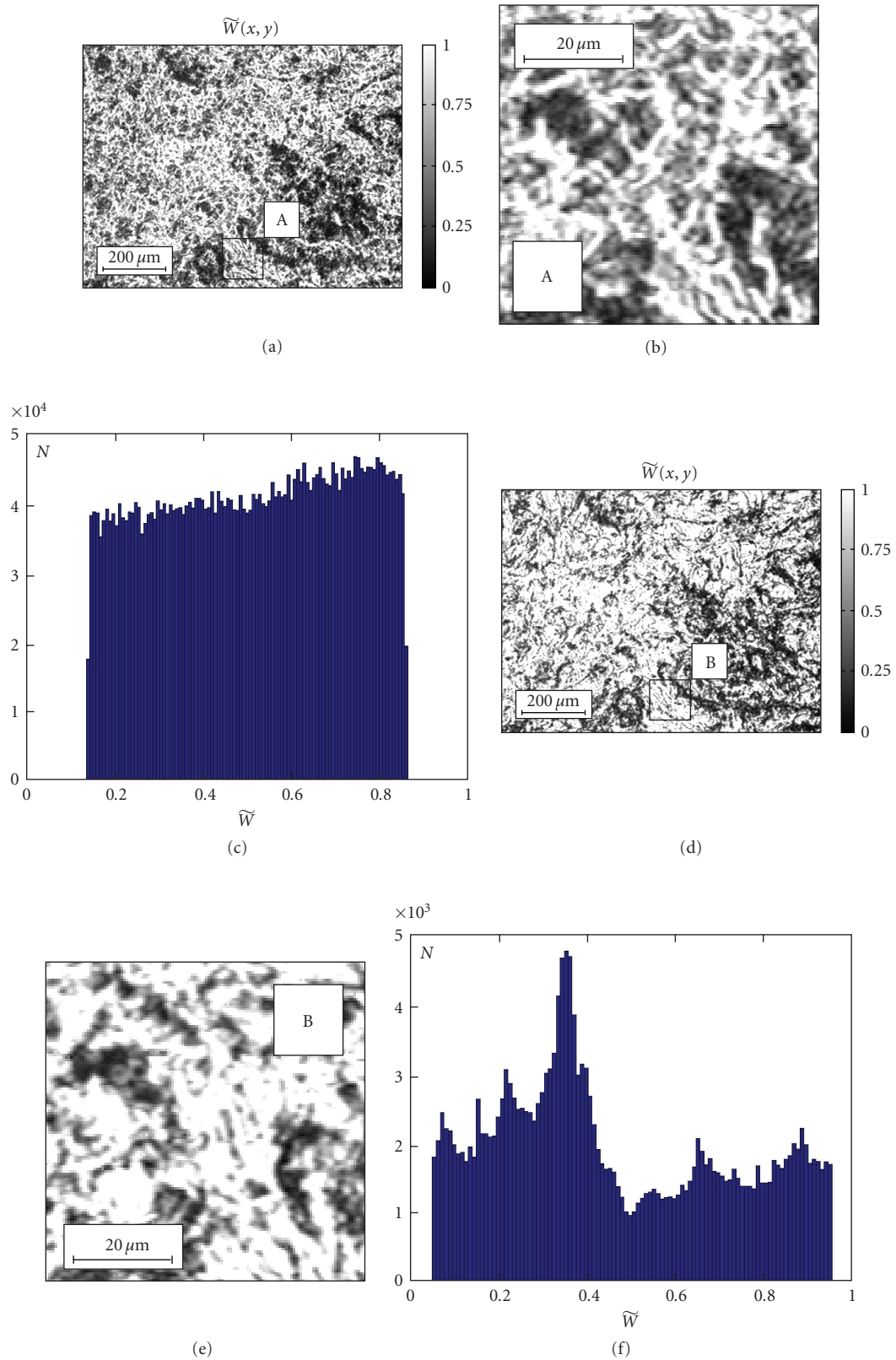


FIGURE 4: Coordinate distributions (600 pix × 800 pix—fragments a, d; 50 pix × 50 pix—fragments b, e) and histograms (fragments c, f) of values $\tilde{W}(x, y)$ of physiologically normal (a, b, c) and oncologically changed (d, e, f) of SD tissue.

extrema (Figure 3(a)). Histograms of CDMA values \tilde{W} of SD layer are fairly equiprobable distribution in the broadest possible range ($0 \leq \tilde{W} \leq 1,0$) of this parameter changing (Figure 4(a)).

Degenerative changes of MT myosin crystal network are shown (Figure 3(e)) in the distribution of extreme values CDMA ($\tilde{W} \rightarrow 1,0$) to lower values ($\tilde{W} = 0,6 \div 0,8$). For chaotically oriented network of collagen fibrils of the sound tissue extracellular matrix (Figures 4(a) and 4(b)) the values of $\tilde{W}(x, y)$ histograms represent rather equiprobable distributions (Figure 4(c)). Early oncologic changes of SD are accompanied with the formation of the collagen fibrils growth direction. It is optically shown (Figures 4(d) and 4(e)) in some localization of the CDMA random values distribution (Figure 4(f)) in the domain of $\tilde{W} = 0,4 \div 0,6$ extrema.

In order to obtain objective criteria of diagnostic efficiency, the comparative investigation of CDMP ($\tilde{V}(x, y)$) [4, 5] and CDMA $\tilde{W}(x, y)$ techniques was performed in the conditions of single and multiple scattering of laser radiation by the layers of MT and SD.

5. Comparative Statistical Analysis of Coordinate Distributions of CDMA of BT Extracellular Matrix and CDMP of Its Laser Images

With the aim of determination the ranges of statistical moments changes that characterize the coordinate distribution of $\tilde{W}(x, y)$ and $\tilde{V}(x, y)$ four groups of histological sections of MT (sound: 21 samples; dystrophic changed: 19 samples) and SD layer samples were formed (sound: 20 samples; oncological changed: 19 samples).

Statistical moments of the 1st–4th-order $M_{k=1,2,3,4}$ of

$$Q = \begin{cases} \tilde{V} \\ \tilde{W} \end{cases} \quad (14)$$

distributions were calculated with the help of Matlab software product on the basis of the following algorithms [12]

$$\begin{aligned} M_1 &= \frac{1}{N} \sum_{i=1}^N |Q_i|, & M_2 &= \sqrt{\frac{1}{N} \sum_{i=1}^N Q_i^2}, \\ M_3 &= \frac{1}{M_2^3} \frac{1}{N} \sum_{i=1}^N Q_i^3, & M_4 &= \frac{1}{M_2^4} \frac{1}{N} \sum_{i=1}^N Q_i^4, \end{aligned} \quad (15)$$

where $N = m \times n$ —quantity of pixels of CCD-camera photosensitive area.

In Tables 2 and 3 the comparative results of calculations of the average (M_1), dispersion (M_2), the skewness (M_3) and the kurtosis (M_4) coefficients of CDMA $\tilde{W}(x, y)$ distributions of four groups of MT and SD of different optical thickness (attenuation coefficient $\tau = 0,09$ and $\tau = 0,75$) and of CDMP $\tilde{V}(x, y)$ of their laser images are presented.

From the obtained data about the coordinate distributions of CDMA of optically thin ($\tau = 0,09$) layers of MT and SD tissue one can see the following.

- (i) The average and dispersion of distributions $\tilde{W}(x, y)$ of physiologically normal and pathological changed MT and SD differ insufficiently within 1.3 (M_1)–1.5 (M_2) times. For two-dimensional distributions $\tilde{V}(x, y)$ of laser images there is practically no difference between M_1 and M_2 .
- (ii) The skewness values M_3 of distributions $\tilde{W}(x, y)$ of the investigated samples differ by 2.1 times; the kurtosis values—by 3.2 times. For CDMP distributions $\tilde{V}(x, y)$ the values of the 3rd and 4th statistic moments vary for M_3 —by 1.3 times; for M_4 —by 1.8 times.

On the other hand, with increasing the light scattering the distribution of azimuths and ellipticities of polarization of the BT object field are changed [8–10, 18, 19]. As a result, the interconnection between the parameters $\tilde{W}(r_1, r_2)$ and $\tilde{V}(r_1, r_2)$ is destroyed (Table 3):

- (i) As diagnostically actual parameters of the physiological state of optically thick BT the statistical moments of higher order can be used. Thus, skewness values M_3 of coordinate distributions $\tilde{W}(x, y)$ for the sound and oncological changed SD tissue differ by 1.4 times; the kurtosis values M_4 —by 1.45 times.
- (ii) The values of the 3rd–4th order statistic moments of distributions $\tilde{V}(x, y)$ of CDMP of object field of optically thick BT layers do not depend much on their physiological state and are the an order less than the values of CDMP $\tilde{W}(x, y)$ skewness and the kurtosis.

6. Conclusions

To characterize the degree of consistency of parameters of the optically uniaxial birefringent (liquid crystals) protein fibrils nets of biological tissues a new parameter—complex degree of mutual anisotropy is suggested. The technique of polarization measuring the coordinate distributions of the complex degree of mutual anisotropy of biological tissues is developed. It is shown that statistic approach to the analysis of complex degree of mutual anisotropy distributions of biological tissues of various morphological and physiological states and optical thicknesses appears to be more sensitive and efficient in differentiation of physiological state in comparison with investigations of complex degree of mutual polarization of the corresponding laser images.

References

- [1] M. Mujat, A. Dogariu, and G. S. Agarwal, “Interferometric measurement of the degree of polarization and control of the contrast of intensity fluctuations,” *Optics Letters*, vol. 29, no. 13, pp. 1539–1541, 2004.
- [2] J. Ellis and A. Dogariu, “Complex degree of mutual polarization,” *Optics Letters*, vol. 29, no. 6, pp. 536–538, 2004.

- [3] S. C. Cowin, "How is a tissue built?" *Journal of Biomechanical Engineering*, vol. 122, no. 6, pp. 553–569, 2000.
- [4] O. V. Angelsky, A. G. Ushenko, and Y. G. Ushenko, "Complex degree of mutual polarization of biological tissue coherent images for the diagnostics of their physiological state," *Journal of Biomedical Optics*, vol. 10, no. 6, Article ID 060502, 2005.
- [5] Y. G. Ushenko, "Complex degree of mutual polarization of Biotissue's Speckle-images," *Ukrainian Journal of Physics*, vol. 6, pp. 104–113, 2005.
- [6] M. Mujat and A. Dogariu, "Polarimetric and spectral changes in random electromagnetic fields," *Optics Letters*, vol. 28, no. 22, pp. 2153–2155, 2003.
- [7] O. V. Angelsky, A. G. Ushenko, V. P. Pishak, et al., "Polarizing-correlative processing of images of statistic objects in the problem of visualization and topology reconstruction of their phase heterogeneity," in *Photonics, Devices, and Systems*, vol. 4016 of *Proceedings of SPIE*, pp. 419–424, 1999.
- [8] S. P. Morgan, M. P. Khong, and M. G. Somekh, "Effects of polarization state and scatterer concentration on optical imaging through scattering media," *Applied Optics*, vol. 36, no. 7, pp. 1560–1565, 1997.
- [9] S. G. Demos and R. R. Alfano, "Optical polarization imaging," *Applied Optics*, vol. 36, no. 1, pp. 150–155, 1997.
- [10] S. L. Jacques, J. R. Roman, and K. Lee, "Imaging superficial tissues with polarized light," *Lasers in Surgery & Medicine*, vol. 26, no. 2, pp. 119–129, 2000.
- [11] A. G. Ushenko and V. P. Pishak, *Coherent-Domain Optical Methods*, Biomedical Diagnostics, Environmental and Material Science, Kluwer Academic Publishers, Dordrecht, The Netherlands, 2004.
- [12] Y. A. Ushenko, "Statistical structure of polarization-inhomogeneous images of biotissues with different morphological structures," *Ukrainian Journal of Physics*, vol. 6, pp. 63–70, 2005.
- [13] O. V. Angelsky, D. N. Burkovets, V. P. Pishak, and Y. A. Ushenko, "Polarization-correlation investigations of biotissue multifractal structures and their pathological changes diagnostics," *Laser Physics*, vol. 10, pp. 1136–1142, 2000.
- [14] A. G. Ushenko, "The vector structure of laser biospeckle fields and polarization diagnostics of collagen skin structures," *Laser Physics*, vol. 10, no. 5, pp. 1143–1149, 2000.
- [15] O. V. Angelsky, P. P. Maksymyak, and T. O. Perun, "Optical correlation method for measuring spatial complexity in optical fields," *Optics Letters*, vol. 18, no. 2, pp. 90–92, 1993.
- [16] O. V. Angel'skiï, A. G. Ushenko, S. B. Ermolenko, et al., "Polarization-based visualization of multifractal structures for the diagnostics of pathological changes in biological tissues," *Optics and Spectroscopy*, vol. 89, no. 5, pp. 799–804, 2000.
- [17] M. Born and E. Wolf, *Principles of Optics*, Cambridge University Press, Cambridge, UK, 1999.
- [18] R. R. Alfano and J. G. Fujimoto, *Advances in Optical Imaging and Photon Migration*, vol. 2 of *Topics in Optics and Photonics Series*, Optical Society of America, Washington, DC, USA, 1996.
- [19] S. Bartel and A. H. Hielscher, "Monte Carlo simulations of the diffuse backscattering Mueller matrix for highly scattering media," *Applied Optics*, vol. 39, no. 10, pp. 1580–1588, 2000.

Research Article

The Interconnection between the Coordinate Distribution of Mueller-Matrixes Images Characteristic Values of Biological Liquid Crystals Net and the Pathological Changes of Human Tissues

Oleg V. Angelsky, Yuriy A. Ushenko, Alexander V. Dubolazov, and Olha Yu. Telenha

Correlation Optics Department, Chernivtsi National University, 2 Kotsyubynsky Street, 58012 Chernivtsi, Ukraine

Correspondence should be addressed to Oleg V. Angelsky, angelsky@itf.cv.ua

Received 1 December 2009; Revised 18 March 2010; Accepted 6 April 2010

Academic Editor: Igor I. Mokhun

Copyright © 2010 Oleg V. Angelsky et al. This is an open access article distributed under the Creative Commons Attribution License, which permits unrestricted use, distribution, and reproduction in any medium, provided the original work is properly cited.

We have theoretically grounded conceptions of characteristic points observed in coordinate distributions of Mueller matrix elements for a network of human tissue biological crystals. The interrelation between polarization singularities of laser images inherent to these biological crystals and characteristic values of above matrix elements is found. We have determined the criteria for statistical diagnostics of pathological changes in the birefringent structure of biological crystal network by using myometrium tissue as an example.

1. Introduction

In recent years, in laser diagnostics of biological tissue (BT) structures they effectively use the model approach [1] that allows considering this object as containing two components: amorphous and optically anisotropic ones. Topicality of this modeling is related with the possibility to apply the Mueller matrix analysis of changes in polarization properties caused by transformation of the optic-and-geometric structure of anisotropic components in these biological objects [2–7], optical properties of which are often described using the Mueller matrix [8].

Being based on the approximation of a single light scattering, they found interrelation between the set of statistic distribution moments of the first to fourth orders that characterizes orientation and phase structure of BT birefringent architectonics as well as the set of respective moments [9] for two-dimensional distributions of Mueller matrix elements or Mueller-matrix images (MMIs) [10–14], that is, as it was done during the investigation of random phase objects [15]. In parallel with traditional statistical investigations, formed in the recent 10 to 15 years is the new optical approach to describe a structure of polarization

inhomogeneous fields in the case of scattered coherent radiation. The main feature of this approach is the analysis of definite polarization states to determine the whole structure of coordinate distributions for azimuths and ellipticities of polarization. The so-called polarization singularities are commonly used as the following states [15–32].

- (i) States with linear polarization when the direction of rotation for the electric field vector is indefinite, the so-called *L*-points.
- (ii) Circularly-polarized states when the azimuth of polarization for the electric field vector is indefinite, the so-called *C*-points.

Investigations of polarization inhomogeneous object fields for BT with different morphology [33–35] allowed us to ascertain that they possess a developed network of *L*- and *C*-points. For example in [34], the authors found interrelations between conditions providing formation of polarization singular points and particularity of the orientation-phase structure of biological crystals present in territorial matrix of human tissue architectonic network. These interrelations served as a base to make statistical and fractal analyses of distribution densities for the number

of singular points in BT images. As a result, the authors confirmed the efficiency of this method for investigation of object fields to differentiate optical properties of BT with a different morphological structure and physiological state.

The present work is devoted to investigation of new possibilities and differentiation of such objects on the basis of statistic analysis of Mueller matrix characteristic values coordinate distributions, which correspond to polarization singular states in laser image of BT layer.

2. Characteristic Values of the Mueller-Matrix Images of Biological Tissues

In accordance with a two-component biological tissue structure its optical properties can be described by combination

$$\{F\} = \begin{vmatrix} 1 & 0 & 0 & 0 \\ 0 & f_{22} & f_{23} & f_{24} \\ 0 & f_{32} & f_{33} & f_{34} \\ 0 & f_{42} & f_{43} & f_{44} \end{vmatrix} = \begin{vmatrix} 1 & 0 & 0 & 0 \\ 0 & \cos^2 2\rho + \sin^2 2\rho \cdot \cos \delta & \cos 2\rho \sin 2\rho (1 - \cos \delta) & \sin 2\rho \sin \delta \\ 0 & \cos 2\rho \sin 2\rho (1 - \cos \delta) & \sin^2 2\rho + \cos^2 2\rho \cos \delta & \cos 2\rho \sin \delta \\ 0 & -\sin 2\rho \sin \delta & -\cos 2\rho \sin \delta & \cos \delta \end{vmatrix}. \quad (2)$$

Here, ρ is the orientation of a protein fibril in the architectonic network, the matter of which introduces the phase shift δ between orthogonal components of the laser wave amplitudes.

The analysis of (1) and (2) shows that the major role in laser beam polarization state transformation belongs to birefringent fibrils network. Among the different values of ρ and δ one can separate the particular (characteristic) values of orientation ρ^* and phase δ^* protein fibrils of BT extracellular matrix

$$\begin{aligned} \rho^* &= 0^\circ, \pm 45^\circ, 90^\circ; \\ \delta^* &= 0^\circ, \pm 90^\circ, 180^\circ. \end{aligned} \quad (3)$$

As it can be seen from relations (3) the necessary terms for forming polarization singular states of the optically birefringent crystal laser images are (L : ($\delta^* = 0^\circ, 180^\circ$) and $\pm C$: ($\delta^* = \pm 90^\circ$) points). The values of the fourth Stokes vector parameter, which correspond to above mentioned polarization singular states of the points in laser image are the following:

$$\begin{aligned} S_4(\rho^*, \delta^*) &= 0 \iff L\text{-point}, \\ S_4(\rho^*, \delta^*) &= +1, 0 \iff +C\text{-point}, \\ S_4(\rho^*, \delta^*) &= -1, 0 \iff -C\text{-point}. \end{aligned} \quad (4)$$

On the other hand, the values (3) for biological crystals network parameters are connected with particular (characteristic) values of Mueller matrix elements $f_{ik}^*(\rho^*, \delta^*)$.

Considering expressions (2)–(4) the characteristic values f_{ik}^* were defined, corresponding to the L - and C -points in laser image of the extracellular matrix of the BT layer, as follows:

of Mueller matrixes of isotropic $\{A\}$ and anisotropic $\{F\}$ structures. Each of these components is characterized by intrinsic matrix operators

$$\{A\} = \begin{vmatrix} 1 & 0 & 0 & 0 \\ 0 & 1 & 0 & 0 \\ 0 & 0 & 1 & 0 \\ 0 & 0 & 0 & 1 \end{vmatrix} \cdot e^{-\tau l}, \quad (1)$$

where τ is the extinction coefficient inherent to the layer of biological tissue with the geometric thickness l

- (i) the values $f_{44} = 0$ correspond to the complete set of $\pm C$ -points;
- (ii) the complete set of L -points of the laser image is caused by the terms $f_{22} = f_{33} = f_{44} = 1$.

Mueller-matrix analysis enables us to perform the sampling of polarization singularities of the laser image, formed by biological crystals with orthogonally oriented ($\rho = 0^\circ - 90^\circ$ and $\rho = \pm 45^\circ \equiv 45^\circ - 135^\circ$) optical axes to

- (i) “orthogonal” $\pm C$ -points

$$\begin{aligned} f_{33} &= 0, & f_{34,43} &= \pm 1 - \pm C_{0;90} - (\rho = 0^\circ - 90^\circ), \\ f_{22} &= 0, & f_{24,42} &= \pm 1 - \pm C_{45;135} - (\rho = 45^\circ - 135^\circ); \end{aligned} \quad (5)$$

- (ii) “orthogonal” $L_{0;90}$ - and $L_{45;135}$ -points

$$\begin{aligned} f_{24,42} &= 0 - L_{0;90} - (\rho = 0^\circ - 90^\circ), \\ f_{34,43} &= 0 - L_{45;135} - (\rho = 45^\circ - 135^\circ). \end{aligned} \quad (6)$$

Thus, measuring the coordinate distributions of the characteristic values ($f_{ik}^* = 0, \pm 1$) of the BT Mueller matrix elements enables us not only to foresee the scenario of forming the ensemble of polarization singularities of its image, but also to additionally realize their differentiation, conditioned by the specificity of orientation structure of biological crystals.

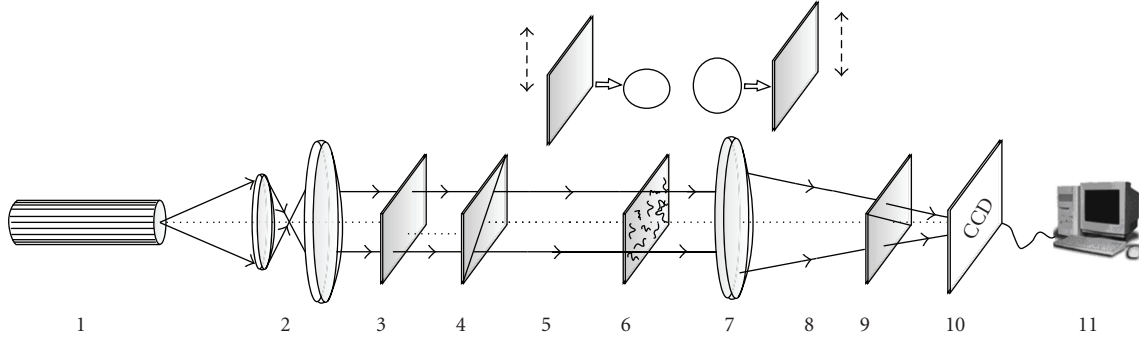


FIGURE 1: Optical scheme of a polarimeter: 1: He-Ne laser; 2: collimator; 3: stationary quarter-wave plate; 5, 8: mechanically movable quarter-wave plates; 4, 9: polarizer and analyzer, respectively; 6: studied object; 7: micro-objective; 10: CCD camera; 11: personal computer.

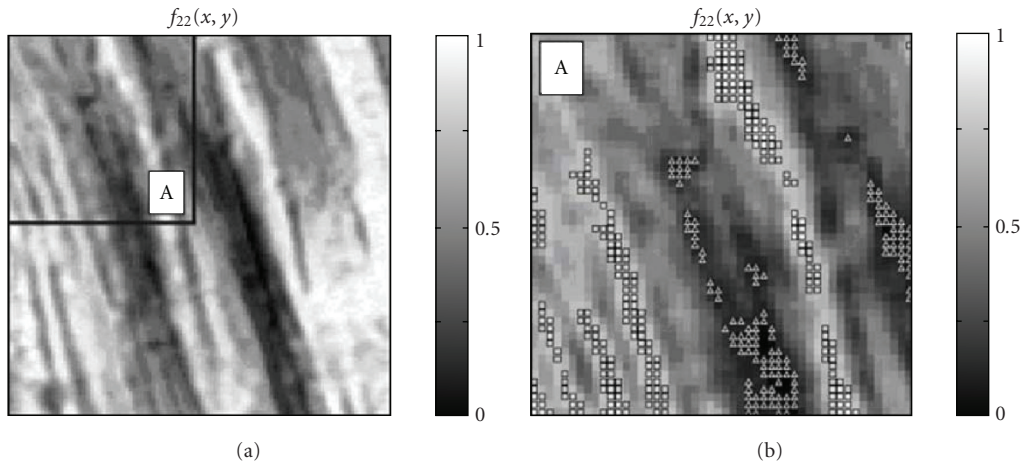


FIGURE 2: Coordinate structure of the matrix element f_{22} for myometrium (a). A: coordinate distribution of characteristic values $f_{22} = 1.0$ labeled as (\square) and $f_{22} = 0$ labeled as (Δ) .

3. The Scheme of Experimental Measuring the Coordinate Distributions of Characteristic Points in Mueller Matrix Images of Biological Tissues

Figure 1 shows the traditional optical scheme of a polarimeter to measure the sets of MMI of BT [14].

Illumination was performed with a parallel ($\varnothing = 10^4 \mu\text{m}$) beam of a He-Ne laser ($\lambda = 0.6328 \mu\text{m}$, $W = 5.0 \text{ mW}$). The polarization illuminator consists of the quarter-wave plates 3 and 5 as well as polarizer 4, which provides formation of a laser beam with an arbitrary azimuth $0^\circ \leq \alpha_0 \leq 180^\circ$ or ellipticity $0^\circ \leq \beta_0 \leq 90^\circ$ of polarization.

Polarization images of BT were projected using the micro-objective 7 into the light-sensitive plane (800×600 pixels) of CCD-camera 10 that provided measurements of BT structural elements within the range 2 to $2,000 \mu\text{m}$.

Experimental conditions were chosen in such a manner that spatial-angular filtration was practically eliminated when forming BT images. It was provided by matching the angular characteristics of light scattering indicatrices by BT samples ($\Omega \approx 16^\circ$) and angular aperture of the micro-objective ($\Delta\omega = 20^\circ$). Here, Ω is the angular cone of

an indicatrix where 98% of the total scattered radiation energy is concentrated.

Analysis of BT images was made using the polarizer 9 and quarter-wave plate 8. As a result, we determined the Stokes vectors for BT images $\{S_{j=1,2,3,4}\}$ and calculated the ensemble of Mueller matrix elements in one point illuminated with a laser beam in accord with the following algorithm:

$$\begin{aligned} f_{i1} &= 0.5[S_i^{(1)} + S_i^{(2)}], \\ f_{i2} &= 0.5[S_i^{(1)} - S_i^{(2)}], \\ f_{i3} &= S_i^{(3)} - f_{i1}, \\ f_{i4} &= S_i^{(4)} - f_{i1}, \quad i = 1, 2, 3, 4. \end{aligned} \quad (7)$$

The indexes 1 to 4 correspond to the following polarization states of the beam illuminating BT: 1: 0° ; 2: 90° ; 3: $+45^\circ$; 4: \otimes (right circulation).

The method used to measure MMI characteristic values for BT samples was as follows.

- (i) BT mount was illuminated with a laser beam, within the area of which, in accord with the algorithm (7) we

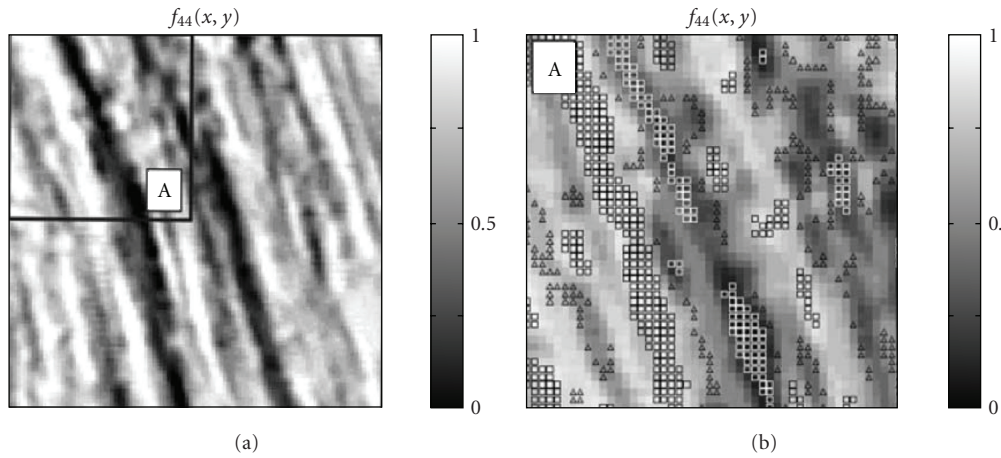


FIGURE 3: Coordinate structure of the matrix element f_{44} for myometrium (a). A: coordinate distribution of characteristic values $f_{44} = 1,0$ labeled as (\square) and $f_{44} = 0$ labeled as (Δ) .

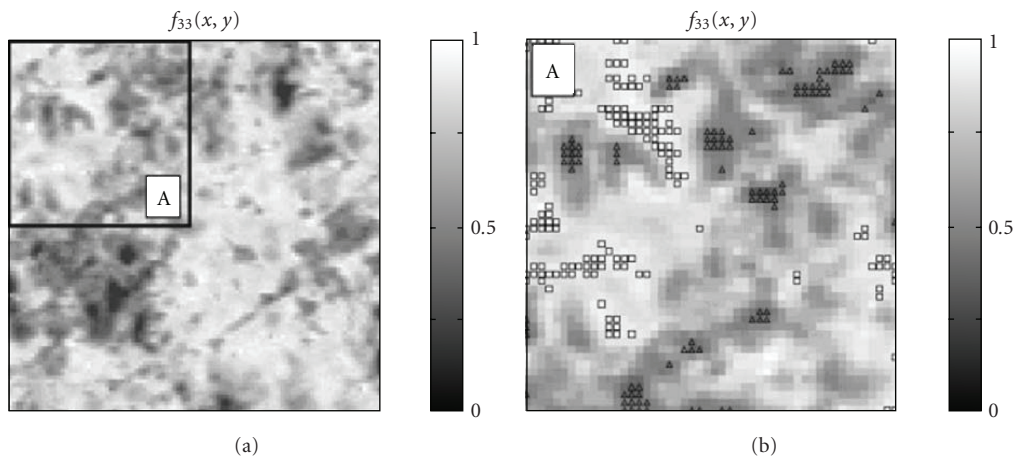


FIGURE 4: Coordinate structure of the matrix element f_{33} for myometrium (a). A: coordinate distribution of characteristic values $f_{33} = 1,0$ labeled as (\square) and $f_{33} = 0$ labeled as (Δ) .

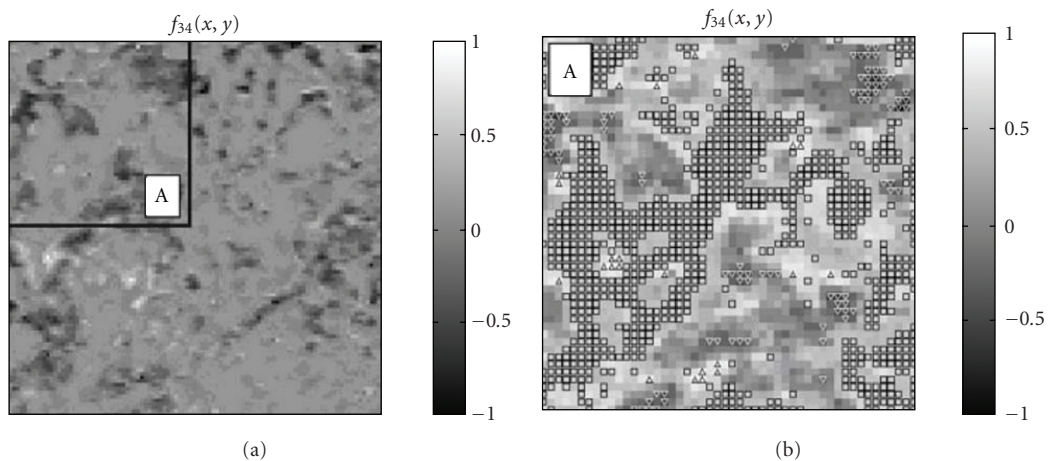


FIGURE 5: Coordinate structure of the matrix element f_{34} for myometrium (a). A: coordinate distribution of characteristic values $f_{34} = 0$ labeled as (\square) : $f_{34} = +1,0$ (Δ) and $f_{34} = -1,0$ (∇) .

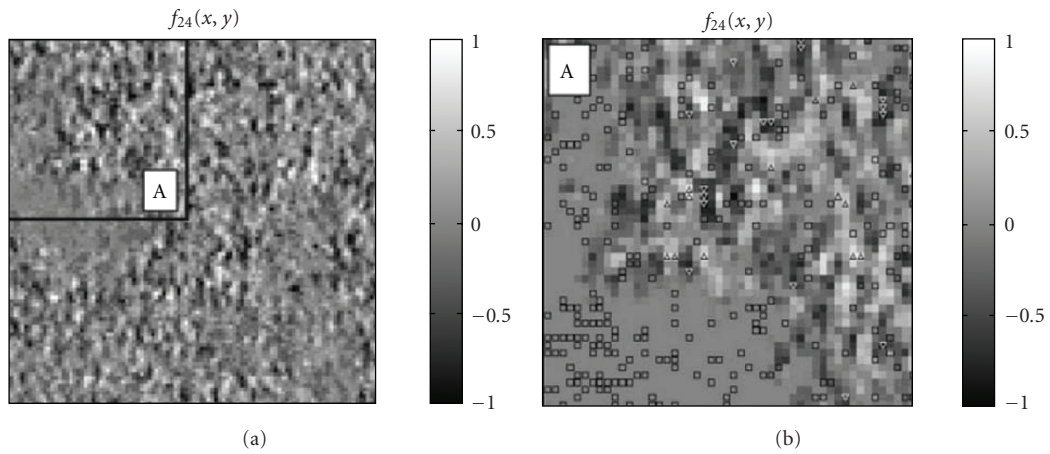


FIGURE 6: Coordinate structure of the matrix element f_{24} for myometrium (a). A: coordinate distribution of characteristic values $f_{24} = 0$ labeled as (\square), $f_{24} = +1, 0$ (Δ) and $f_{24} = -1, 0$ (∇).

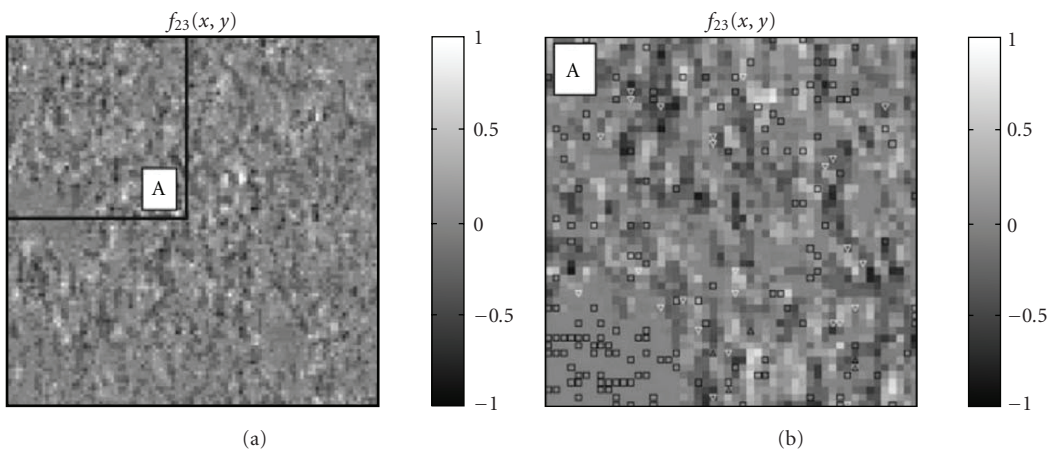


FIGURE 7: Coordinate structure of the matrix element f_{23} for myometrium (a). A: coordinate distribution of characteristic values $f_{23} = 0$ labeled as (\square), $f_{23} = +1, 0$ (Δ) and $f_{23} = -1, 0$ (∇).

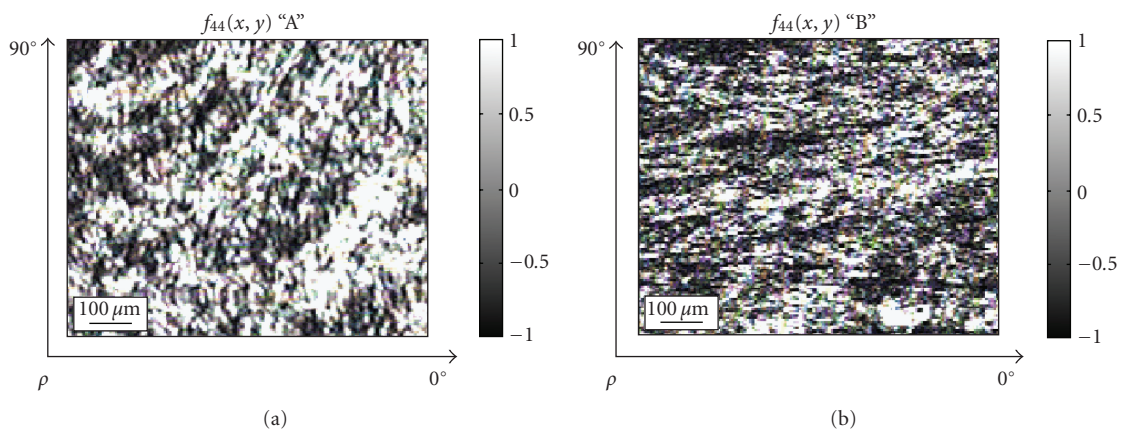


FIGURE 8: Mueller-matrixes image of the element f_{44} for myometrium tissue of A (a) and B (b) types.

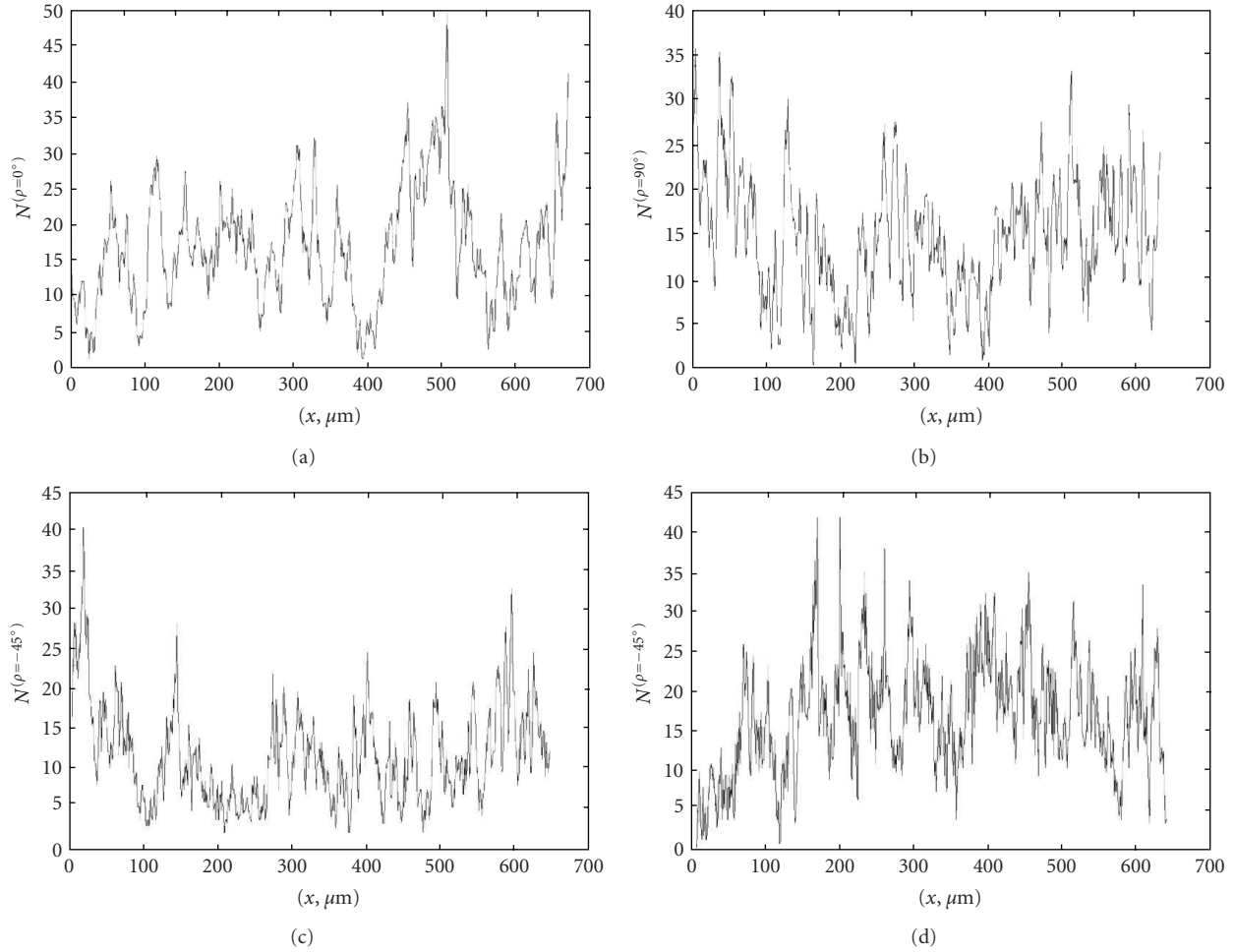


FIGURE 9: $N_\rho(X)$ -dependences for myometrium tissue of A type.

determined the array ($m \times n = 800 \times 600$) of values for each element of the Mueller matrix

$$f_{ik}(m \times n) = \begin{pmatrix} f_{ik}^{11}, \dots, f_{ik}^{1m}, \\ f_{ik}^{n1}, \dots, f_{ik}^{nm} \end{pmatrix}. \quad (8)$$

(ii) Determined for each massif $f_{ik}(m \times n)$ were coordinate distributions of its characteristic values

$$f_{ik}^*(m \times n) = \begin{pmatrix} f_{ik}^{11} = 0; \pm 1, 0; \dots; f_{ik}^{1m} = 0; \pm 1, 0; \\ f_{ik}^{n1} = 0; \pm 1, 0; \dots; f_{ik}^{nm} = 0; \pm 1, 0. \end{pmatrix}. \quad (9)$$

As an object of the experimental study, we used tissues of a woman matrix (myometrium).

4. Coordinate Distributions of the Mueller Matrixes Images Characteristic Values of Biological Tissues

Figures 2, 3, 4, 5, 6, and 7 show coordinate distributions for all the types of characteristic values f_{ik}^* inherent to the

ensemble of protein birefringence liquid crystal net Mueller-matrixes images.

As seen from these experimental data, the coordinate distributions of all the Mueller matrix elements for myometrium possess a developed network of characteristic values. Being based on this fact, we have offered Mueller-matrixes differentiation of changes in the distribution of optical axis orientations in biological crystals that form the architectonic network, by using as an example the woman matrix tissue.

5. Mueller-Matrix Diagnostics of Orientation Changes of Liquid Crystals Nets in Biological Tissues

As objects for our experimental investigations, we used mounts of myometrium tissue of two types:

- (i) biopsy of healthy tissue from a woman matrix (type A),
- (ii) biopsy of conditionally normal tissue from the vicinity of a benign hysteromyoma (type B).

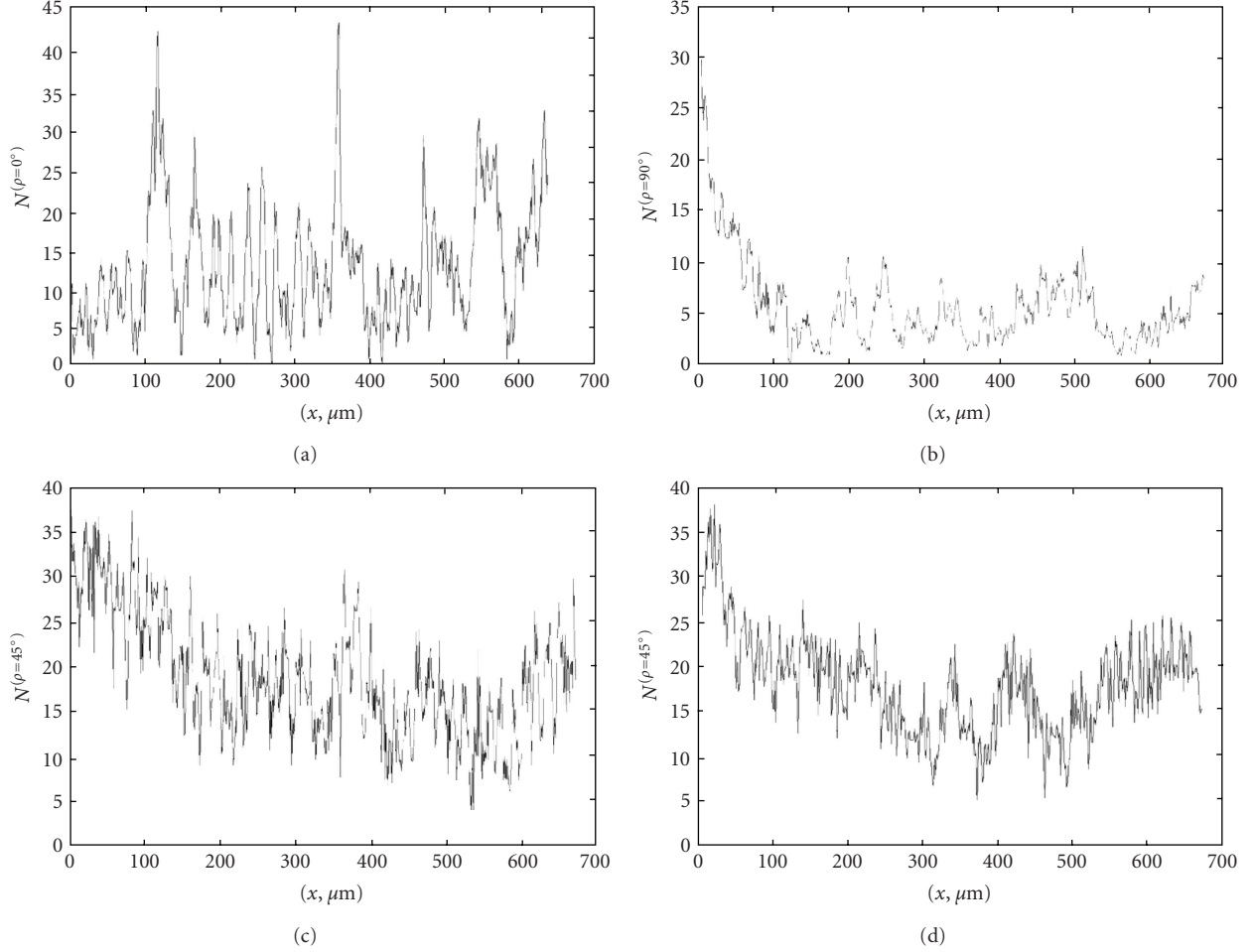
FIGURE 10: $N_\rho(X)$ -dependences for myometrium tissue of B type.

Figure 8 shows MMI of the element f_{44} for myometrium samples of A and B types.

From the optical viewpoint, the obtained two-dimensional distributions $f_{44}(x, y)$ characterize the degree of anisotropy in the matter of studied samples. Thereof, it can be easily seen that the birefringence value of the samples A and B is practically identical. It is confirmed by the close level of relative values for the matrix element $f_{44}(x, y)$ describing the tissues of A and B types ($f_{44}^B(x, y) \approx f_{44}^A(x, y)$). In parallel with it, one can observe the ordering of the directions of optical axes inherent to anisotropic structures of type B myometrium.

Thus, the main parameter allowing differentiation of optical properties for the samples of this type is the orientation structure of their birefringent networks.

To obtain objective criteria for Mueller-matrix differentiation of optical properties inherent to the myometrium samples of A and B types, we have used the following approach:

- (i) measured in sequence were the MMI elements $f_{24,42}$ and $f_{34,43}$, that are basic to determine characteristic states (± 1) formed in biological crystals with

orthogonal orientations of optical axes ($\rho = 0^\circ, 90^\circ \rightarrow f_{34,43} = \pm 1, 0; \rho = 45^\circ, 135^\circ \rightarrow f_{24,42} = \pm 1, 0$ ((5) and (6));

- (a) two-dimension array $x = 1 \div m; y = 1 \div n$ of CCD-camera pixels can be represented by the set of columns shifted along the x -direction by $\Delta x = 1$ pix

$$m \times n = \begin{pmatrix} r_{11} \\ \vdots \\ r_{1n} \end{pmatrix} \equiv X_1, \quad \begin{pmatrix} r_{11} + \Delta x \equiv r_{21} \\ \vdots \\ r_{1n} + \Delta x \equiv r_{2n} \end{pmatrix} \equiv X_2; \dots, \\ \begin{pmatrix} r_{11} + (m-1)\Delta x \equiv r_{(m-1)1} \\ \vdots \\ r_{11} + (m-1)\Delta x \equiv r_{(m-1)1} \end{pmatrix} \equiv X_{m-1}, \\ \begin{pmatrix} r_{11} + m\Delta x \equiv r_{m1} \\ \vdots \\ r_{11} + m\Delta x \equiv r_{m1} \end{pmatrix} \equiv X_m,$$

(10)

(ii) the amount $N_{j=1 \div m}$ of characteristic points $f_{34,43}(x, y) = \pm 1, 0$ within each column $X_{j=1 \div m}$ was calculated, and $f_{24,42}(x, y) = \pm 1, 0$ within Mueller matrix images obtaining the distributions of

$N_\rho(X)$ for different optical axes orientations $\rho = 0^\circ; 90^\circ, +45^\circ; 135^\circ$ of biological crystals birefringent network.

$$\begin{aligned}
 N_{\rho=0}(X) &= N_1(f_{34;43} = +1, 0); N_2(f_{34;43} = +1, 0); \dots; N_{m-1}(f_{34;43} = +1, 0); N_m(f_{34;43} = +1, 0), \\
 N_{\rho=90}(X) &= N_1(f_{34;43} = -1, 0); N_2(f_{34;43} = -1, 0); \dots; N_{m-1}(f_{34;43} = -1, 0); N_m(f_{34;43} = -1, 0), \\
 N_{\rho=45}(X) &= N_1(f_{24;42} = +1, 0); N_2(f_{24;42} = +1, 0); \dots; N_{m-1}(f_{24;42} = +1, 0); N_m(f_{24;42} = +1, 0), \\
 N_{\rho=135}(X) &= N_1(f_{24;42} = -1, 0); N_2(f_{24;42} = -1, 0); \dots; N_{m-1}(f_{24;42} = -1, 0); N_m(f_{24;42} = -1, 0).
 \end{aligned} \tag{11}$$

TABLE 1: The skewness coefficients of characteristic values distributions in Mueller-matrix images.

Z	Myometrium (normal state) (25 samples)	Myometrium (pathological state) (23 samples)
$Q_M^{f_{34,34}}$	0.03 ± 0.005	0.45 ± 0.063
$W_\sigma^{f_{34,34}}$	0.02 ± 0.004	0.12 ± 0.019
$Q_M^{f_{24,24}}$	0.025 ± 0.0036	0.28 ± 0.037
$W_\sigma^{f_{24,24}}$	0.03 ± 0.0047	0.14 ± 0.021

(iii) $N_\rho(X)$ dependences were processed using the following algorithms

$$\begin{aligned}
 Q_M^{(f_{34,43})} &= \frac{M(N_{\rho=0^\circ}) - M(N_{\rho=90^\circ})}{M(N_{\rho=0^\circ}) + M(N_{\rho=90^\circ})}, \\
 Q_M^{(f_{24,42})} &= \frac{M(N_{\rho=45^\circ}) - M(N_{\rho=135^\circ})}{M(N_{\rho=45^\circ}) + M(N_{\rho=135^\circ})}, \\
 W_\sigma^{(f_{34,43})} &= \frac{\sigma(N_{\rho=0^\circ}) - \sigma(N_{\rho=90^\circ})}{\sigma(N_{\rho=0^\circ}) + \sigma(N_{\rho=90^\circ})}, \\
 W_\sigma^{(f_{24,42})} &= \frac{\sigma(N_{\rho=45^\circ}) - \sigma(N_{\rho=135^\circ})}{\sigma(N_{\rho=45^\circ}) + \sigma(N_{\rho=135^\circ})}.
 \end{aligned} \tag{12}$$

Here, $M(N_\rho)$ and $\sigma(N_\rho)$ are the average and dispersion of $N_\rho(X)$ distributions.

Shown in Figures 9 and 10 are the distributions $N_\rho(X)$ of Mueller-matrixes images for the myometrium tissue of A and B types.

In the case of myometrium tissue with pathological changes, one can observe asymmetry between the ranges of changes in values of the dependences $N_{\rho=0}(X)$ (Figure 10(a)) and $N_{\rho=90}(X)$ (Figure 10(b)).

The above results can be explained as based on the relation found between conditions, providing formation of MMI characteristic values and orientation-phase structure of biological crystals in the myometrium tissue ((5) and (6)).

Orientation structure of MMI for the element f_{44} describing the myometrium tissue of B type (Figure 8(b)) contains characteristic points $f_{44}(x, y) = 1, 0$ asymmetrically located in the direction $\rho = 90^\circ$. Thereof, one should expect a maximal number of characteristic values for the element $f_{34}(x, y) = -1, 0$ as compared to that of characteristic values $f_{34,43}(x, y) = 1, 0$ and $f_{24,42}(x, y) = \pm 1, 0$.

Statistically found asymmetry in distributions of characteristic points for MMI describing the myometrium tissue of both types was estimated using the asymmetry coefficients (12) introduced by us. Table 1 shows statistically averaged values of the coefficients Q_M and W_σ within two groups of myometrium samples of A and B types.

Analysis of data represented in Table 1 allowed us to conclude the following:

(i) first- and second-order statistical moments for distributions of characteristic values $f_{34,43}(x, y)$ and $f_{24,42}(x, y)$ of healthy myometrium tissue do not practically differ from zero, which is indicative of their azimuthal symmetry;

(ii) values of the skewness coefficient for distributions of MMI characteristic values $f_{34,43}(x, y)$ and $f_{24,42}(x, y)$ describing the pathologically changed myometrium tissue of B type grow practically by one order, which indicates the formation of their azimuthal asymmetry related with the direction of pathological growth of birefringent protein fibrils.

6. Conclusion

Thus, the above analysis of statistical distributions describing the number of points for MMI characteristic values inherent to the set of elements f_{ik} characterizing biological tissues of different kinds seems to be efficient in differentiation of phase and orientation changes in the structure of their birefringent components, which are related with changes in their physiological state.

References

- [1] S. C. Cowin, "How is a tissue built?" *Journal of Biomechanical Engineering*, vol. 122, no. 6, pp. 553–569, 2000.
- [2] O. V. Angelsky, A. G. Ushenko, Yu. A. Ushenko, Ye. G. Ushenko, Yu. Ya. Tomka, and V. P. Pishak, "Polarization-correlation mapping of biological tissue coherent images," *Journal of Biomedical Optics*, vol. 10, no. 6, Article ID 064025, 2005.
- [3] J. F. de Boer and T. E. Milner, "Review of polarization sensitive optical coherence tomography and Stokes vector determination," *Journal of Biomedical Optics*, vol. 7, no. 3, pp. 359–371, 2002.
- [4] J. F. de Boer, T. E. Milner, and J. S. Nelson, "Two dimensional birefringence imaging in biological tissue using phase and polarization sensitive optical coherence tomography," in *Trends in Optics and Photonics (TOPS): Advances in Optical Imaging and Photon Migration*, OSA, Washington, DC, USA, 1998.
- [5] M. J. Everett, K. Schoenenberger, B. W. Colston Jr., and L. B. Da Silva, "Birefringence characterization of biological tissue by use of optical coherence tomography," *Optics Letters*, vol. 23, no. 3, pp. 228–230, 1998.
- [6] O. V. Angelsky, G. V. Demianovsky, A. G. Ushenko, D. N. Burkovets, and Y. A. Ushenko, "Wavelet analysis of two-dimensional birefringence images of architectonics in biotissues for diagnosing pathological changes," *Journal of Biomedical Optics*, vol. 9, no. 4, pp. 679–690, 2004.
- [7] O. V. Angelsky, Yu. Ya. Tomka, A. G. Ushenko, Ye. G. Ushenko, S. B. Yermolenko, and Yu. A. Ushenko, "2-D tomography of biotissues images in pre-clinic diagnostics of their pre-cancer states," in *Advanced Topics in Optoelectronics, Microelectronics, and Nanotechnologies II*, vol. 5972 of *Proceeding of SPIE*, August 2005.
- [8] O. V. Angelsky, A. G. Ushenko, D. N. Burkovets, and Yu. A. Ushenko, "Polarization visualization and selection of biotissue image two-layer scattering medium," *Journal of Biomedical Optics*, vol. 10, no. 1, 2005.
- [9] O. V. Angelsky, Yu. Ya. Tomka, A. G. Ushenko, Ye. G. Ushenko, and Yu. A. Ushenko, "Investigation of 2D Mueller matrix structure of biological tissues for pre-clinical diagnostics of their pathological states," *Journal of Physics D*, vol. 38, no. 23, pp. 4227–4235, 2005.
- [10] S. Jiao, W. Yu, G. Stoica, and L. V. Wang, "Optical-fiber-based Mueller optical coherence tomography," *Optics Letters*, vol. 28, no. 14, pp. 1206–1208, 2003.
- [11] Yu. A. Ushenko, "Statistical structure of polarization-inhomogeneous images of biotissues with different morphological structures," *Ukrainian Journal of Physical Optics*, vol. 6, pp. 63–70, 2005.
- [12] O. V. Angelsky, A. G. Ushenko, Yu. A. Ushenko, Ye. G. Ushenko, Yu. Ya. Tomka, and V. P. Pishak, "Polarization-correlation mapping of biological tissue coherent images," *Journal of Biomedical Optics*, vol. 10, no. 6, Article ID 064025, 2005.
- [13] O. V. Angelsky, A. G. Ushenko, and Yu. A. Ushenko, "Polarization reconstruction of orientation structure of biological tissues birefringent architectonic nets by using their Mueller-matrix speckle-images," *Journal of Holography and Speckle*, vol. 2, pp. 72–79, 2005.
- [14] A. G. Ushenko and V. P. Pishak, "Laser polarimetry of biological tissue. Principles and applications," in *Coherent-Domain Optical Methods. Biomedical Diagnostics, Environmental and Material Science*, V. Tuchin, Ed., pp. 67–93, Kluwer Academic Publishers, Dodrecht, The Netherlands, 2004.
- [15] O. V. Angelsky and P. P. Maksimyak, "Optical diagnostics of random phase objects," *Applied Optics*, vol. 29, pp. 2894–2898, 1990.
- [16] O. V. Angelsky, P. P. Maksimyak, V. V. Ryukhtin, and S. G. Hanson, "New feasibilities for characterizing rough surfaces by optical-correlation techniques," *Applied Optics*, vol. 40, no. 31, pp. 5693–5707, 2001.
- [17] J. F. Nye, "Polarization effects in the diffraction of electromagnetic waves: the role of disclinations," *Proceedings of the Royal Society A*, vol. 387, no. 1792, pp. 105–132, 1983.
- [18] O. V. Angelsky, I. I. Mokhun, A. I. Mokhun, and M. S. Soskin, "Interferometric methods in diagnostics of polarization singularities," *Physical Review E*, vol. 65, no. 3, Article ID 036602, 2002.
- [19] J. F. Nye and J. V. Hajnal, "The wave structure of monochromatic electromagnetic radiation," *Proceedings of the Royal Society A*, vol. 409, no. 1836, pp. 21–36, 1987.
- [20] M. V. Berry and M. R. Dennis, "Polarization singularities in isotropic random vector waves," *Proceedings of the Royal Society A*, vol. 457, no. 2005, pp. 141–155, 2001.
- [21] A. D. Dolgov, A. G. Doroshkevich, D. I. Novikov, and I. D. Novikov, "Classification of singular points in the polarization field of the cosmic microwave background and eigenvectors of the Stokes matrix," *JETP Letters*, vol. 69, no. 6, pp. 427–433, 1999.
- [22] A. I. Konukhov and L. A. Melnikov, "Optical vortices in a vector field: the general definition based on the analogy with topological solitons in a 2D ferromagnet, and examples from the polarization transverse patterns in a laser," *Journal of Optics B*, vol. 3, no. 2, pp. 139–144, 2001.
- [23] I. Freund, "Poincare vortices," *Optics Letters*, vol. 26, no. 24, pp. 1996–1998, 2001.
- [24] J. F. Nye, "Lines of circular polarization in electromagnetic wave fields," *Proceedings of the Royal Society A*, vol. 389, no. 1797, pp. 279–290, 1983.
- [25] I. Freund, "Coherency matrix description of optical polarization singularities," *Journal of Optics A*, vol. 6, no. 5, pp. 229–234, 2004.
- [26] M. Soskin, V. Denisenko, and R. Egorov, "Topological networks of paraxial ellipse speckle-fields," *Journal of Optics A*, vol. 6, no. 5, pp. 281–287, 2004.
- [27] I. Freund, M. S. Soskin, and A. I. Mokhun, "Elliptic critical points in paraxial optical fields," *Optics Communications*, vol. 208, no. 4–6, pp. 223–253, 2002.
- [28] M. S. Soskin, V. Denisenko, and I. Freund, "Optical polarization singularities and elliptic stationary points," *Optics Letters*, vol. 28, no. 16, pp. 1475–1477, 2003.
- [29] M. R. Dennis, "Polarization singularities in paraxial vector fields: morphology and statistics," *Optics Communications*, vol. 213, no. 4–6, pp. 201–221, 2002.
- [30] O. Angelsky, R. Besaha, A. Mokhun, et al., "Singularities in vectorial fields," in *Fourth International Conference on Correlation Optics*, O. V. Angelsky, Ed., vol. 3904 of *Proceeding of SPIE*, Chernivtsy, Ukraine, May 1999.
- [31] I. Freund, A. I. Mokhun, M. S. Soskin, O. V. Angelsky, and I. I. Mokhun, "Stokes singularity relations," *Optics Letters*, vol. 27, no. 7, pp. 545–547, 2002.
- [32] O. Angelsky, A. Mokhun, I. Mokhun, and M. Soskin, "The relationship between topological characteristics of component

- vortices and polarization singularities,” *Optics Communications*, vol. 207, no. 1–6, pp. 57–65, 2002.
- [33] O. V. Angelsky, A. G. Ushenko, and Ye. G. Ushenko, “2-D Stokes polarimetry of biospeckle tissues images in pre-clinic diagnostics of their pre-cancer states,” *Journal of Holography and Speckle*, vol. 2, pp. 26–33, 2005.
- [34] O. V. Angelsky, A. G. Ushenko, Yu. A. Ushenko, and Ye. G. Ushenko, “Polarization singularities of the object field of skin surface,” *Journal of Physics D*, vol. 39, no. 16, pp. 3547–3558, 2006.
- [35] O. V. Angelsky, A. G. Ushenko, Ye. G. Ushenko, and Y. Y. Tomka, “Polarization singularities of biological tissues images,” *Journal of Biomedical Optics*, vol. 11, no. 5, Article ID 054030, 2006.

Research Article

A New Method of Mueller-Matrix Diagnostics and Differentiation of Early Oncological Changes of the Skin Derma

Yu. A. Ushenko,¹ A. P. Peresunko,² and Bozan Adel Baku²

¹ Correlation Optics Department, Chernivtsi National University, 2 Kotsyubinsky Str., 58012 Chernivtsi, Ukraine

² Chernivtsi State Medical University, 2 Theatral Sq, 58002 Chernivtsi, Ukraine

Correspondence should be addressed to Yu. A. Ushenko, o.ushenko@chnu.edu.ua

Received 3 December 2009; Revised 18 March 2010; Accepted 29 March 2010

Academic Editor: Oleg V. Angelsky

Copyright © 2010 Yu. A. Ushenko et al. This is an open access article distributed under the Creative Commons Attribution License, which permits unrestricted use, distribution, and reproduction in any medium, provided the original work is properly cited.

The paper deals with investigation of the processes of laser radiation transformation by biological crystals networks using the singular optics techniques. The results obtained showed a distinct correlation between the points of “characteristic” values of coordinate distributions of Mueller matrix ($M_{ik} = 0, \pm 1$) elements and polarization singularities (L- and C-points) of laser transformation of biological crystals networks with the following possibility of Mueller-matrix selection of polarization singularity. The technique of Mueller-matrix diagnostics of pathological changes of skin derma is proposed.

1. Introduction

Laser polarimetry [1] enabling to obtain information about optical anisotropy [2–5] of biological tissues (BT) is an important direction of noninvasive diagnostics of organic phase-heterogeneous layers. For statistic analysis of such polarimetric information a model approach has been worked out based on the following conditions [1, 2, 6–12]:

- (i) all the variety of human BT can be represented by four main types—connective, muscular epithelial, and neural tissues;

- (ii) structure of any BT type is regarded as a two-component amorphous-crystalline one;
- (iii) the crystalline component or extracellular matrix is formed by the network of optically uniaxial birefringent protein (collagen, myosin, elastine, etc.) fibrils or biological crystals;
- (iv) the process of transformation of laser radiation polarization state by biological crystal is characterized by Mueller $\{M\}$ matrix operators of an optically uniaxial crystal

$$\{M\} = \begin{vmatrix} 1 & 0 & 0 & 0 \\ 0 & M_{22} & M_{23} & M_{24} \\ 0 & M_{32} & M_{33} & M_{34} \\ 0 & M_{42} & M_{43} & M_{44} \end{vmatrix} = \begin{vmatrix} 1 & 0 & 0 & 0 \\ 0 & (\cos^2 2\rho + \sin^2 2\rho \cos \delta) & \cos 2\rho \sin 2\rho(1 - \cos \delta) & (\sin 2\rho \sin \delta) \\ 0 & (\cos 2\rho \sin 2\rho(1 - \cos \delta)) & (\sin^2 2\rho + \cos^2 2\rho \cos \delta) & (\cos 2\rho \sin \delta) \\ 0 & (-\sin 2\rho \sin \delta) & (-\cos 2\rho \sin \delta) & (\cos \delta) \end{vmatrix}. \quad (1)$$

Here ρ -direction of optical axis of biological crystal with birefringence index Δn , $\delta = (2\pi/\lambda)\Delta n l$ -phase shift between

orthogonal components of the amplitude of a probing laser beam with wave length λ .

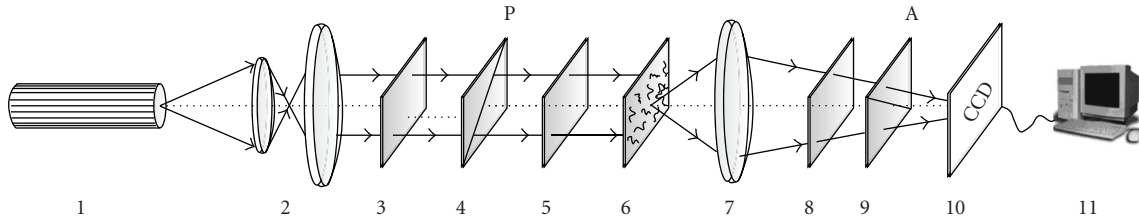


FIGURE 1: Optical scheme of polarimeter, where 1: He-Ne laser; 2: collimator; 3: stationary quarter-wave plates; 5, 8: mechanically movable quarter-wave plates; 4, 9: polarizer and analyzer correspondingly; 6: object of investigation; 7: microobjective; 10: CCD camera; 11: personal computer.

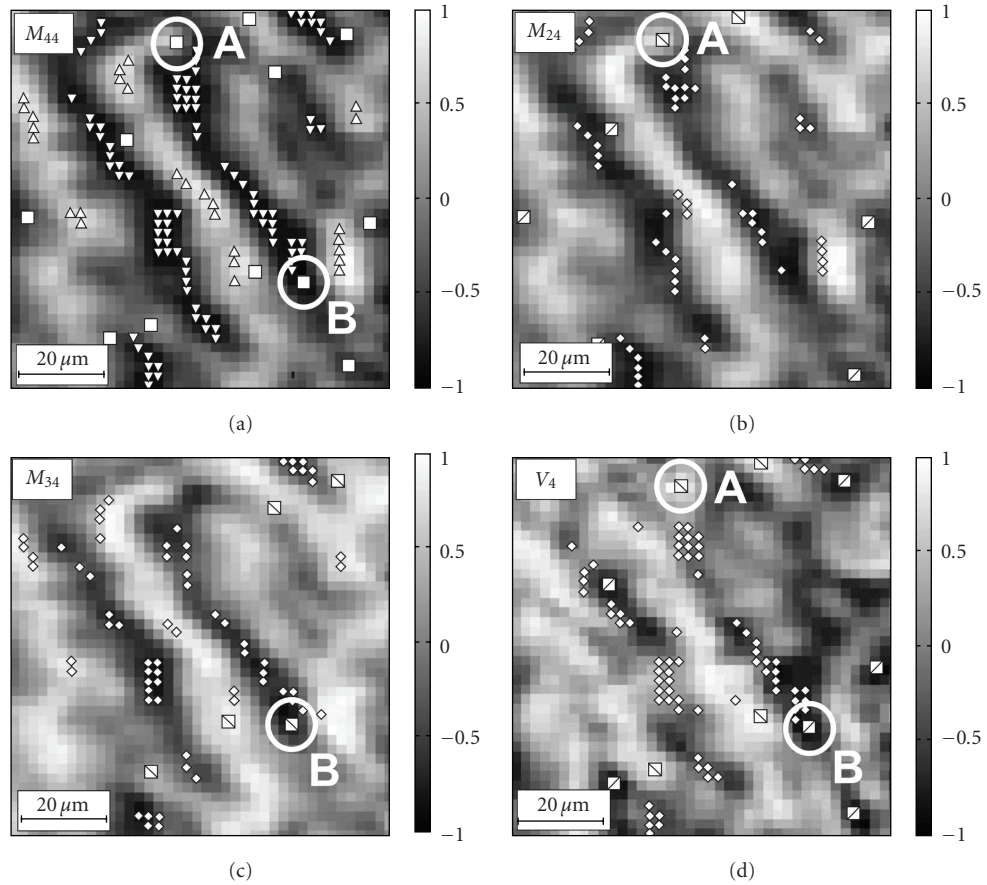


FIGURE 2: Networks of characteristic values $M_{44,24,34}^*(m \times n)$ of matrix elements $M_{44,24,34}$ (a, b, c) and singularities of polarization image of the skin derma layer histological section V_4 ("d"): "+C"-points (\boxplus) ($M_{44} = 0$); "-C"-points (\boxminus) ($M_{24,34} = +1$, $V_4 = +1$); "+L"-points (Δ) ($M_{44} = +1$); "-L"-points (∇) ($M_{44} = -1$); "±L"-points (\diamond) ($M_{24,34} = 0$, $V_4 = 0$).

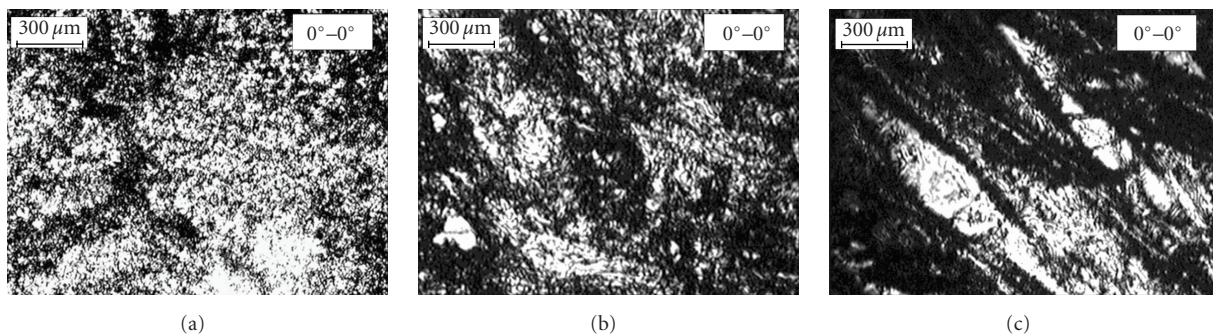


FIGURE 3: Polarization images of the skin derma "A" (a), "B" (b), and "C" (c)-types in coaxial polarizer and analyzer.

A new approach to description of the BT laser images based on the analysis of coordinate distributions of polarization singularities became developed the above-mentioned statistical [13–22]. Linearly (L-points) and circularly (C-points) polarized states of light oscillations belong to them. For L-points the direction of the electric-intensity vector's rotation is indefinite (singular). For a C-point, the polarization azimuth of the electric intensity vector is indefinite.

Investigation of laser images of the connective tissue layers revealed a developed network of polarization singularities [23–26], which was quantitatively estimated in the form of distribution of the amount of L- and C-points. By means of the analysis of the given distribution's statistical moments of the 1st–4th orders (the technique of polarization mapping) the criteria of diagnostics of oncological changes of uterus neck tissue were found.

It should be pointed out that singular approach is predominantly realized out of the analysis of the mechanisms of forming polarizationally heterogeneous laser images of BT by an extracellular matrix. Thus, development of laser polarimetry techniques based on determination of singular interconnections “object-field” in order to find new methods of diagnostics of transformation of the BT extracellular matrix orientation-phase structure connected with precancer changes of their physiological state is very important.

To solve such a problem, we should revert to the analysis of optical properties of biological crystals' nets, comprehensively described by the Mueller matrix though within a singular approach.

2. A Brief Theory of the Mueller Matrixes Approach in the Analysis of the Biological Tissue Birefringent Nets Polarization Properties

The use of the fourth parameter of the Stokes vector appears to be a suitable and widely applied means of such singularities representation

$$V_4 = \begin{cases} 0 \leftrightarrow L \\ \pm 1 \leftrightarrow C. \end{cases} \quad (2)$$

According to analysis of (1) and (2), one can see the interconnection between the polarization singular states and certain (characteristic) values of orientation ρ^* and phase δ^* parameters of the BT crystals' nets of the extracellular matrix

$$\begin{aligned} \rho^* &= 0^\circ; \pm 45^\circ 90^\circ; \\ \delta^* &= 0^\circ, 90^\circ, 180^\circ. \end{aligned} \quad (3)$$

As it can be seen, relations (3) are the necessary terms for forming polarization singular states of the laser beam (L- ($\delta = 0^\circ, 180^\circ$) and C- ($\delta = \pm 90^\circ$) points) by optically coaxial birefringent crystal.

Considering expressions (1)–(3) the characteristic values M_{ik}^* were defined that determine the L- and C-points in laser image of the extracellular matrix of the BT layer:

- (i) the values $M_{44} = 0$ and $V_4 = \pm 1$ determine the complete set of \pm C-points ($\delta = \pm 90^\circ$);
- (ii) the complete set of L-points ($\delta = 0^\circ$) of the laser image is caused by the terms $M_{22} = M_{33} = M_{44} = 1$ and $V_4 = 0$.

Mueller-matrix analysis enables to perform the sampling of polarization singularities of the laser image, formed by biological crystals with orthogonally oriented ($\delta = 0^\circ, 90^\circ$ and $\delta = 45^\circ, 135^\circ$) optical axes to

- (i) “orthogonal” \pm C-points

$$\begin{aligned} M_{33} &= 0, M_{34,43} = \pm 1 - \pm C - (\rho = 0^\circ, 90^\circ), \\ M_{22} &= 0, M_{24,42} = \pm 1 - \pm C - (\rho = 45^\circ, 135^\circ). \end{aligned} \quad (4)$$

- (ii) “orthogonal” $L_{0;90^\circ}$ - and $L_{45;135^\circ}$ - points

$$\begin{aligned} M_{24,42} &= 0 - L_{0^\circ,90^\circ} - (\rho = 0^\circ, 90^\circ), \\ M_{34,43} &= 0 - L_{45^\circ,135^\circ} - (\rho = 45^\circ, 135^\circ). \end{aligned} \quad (5)$$

Thus, measuring the coordinate distributions of the characteristic values ($M_{ik}^* = 0, \pm 1$) of the BT Mueller matrix elements enables not only to foresee the scenario ($M_{ik}^* \rightarrow V_4^*$) of forming the ensemble of polarization singularities ($V_4 = 0, \pm 1$) of its image, but also to additionally realize their differentiation, conditioned by the specificity of orientation structure of biological crystals.

3. The Scheme and Methods of Experimental Investigations

Figure 1 shows traditional optical scheme of polarimeter for measuring due to Gerrard technique [27] of Stokes parameters and elements of Mueller matrix of the BT histological sections.

The parallel ($\varnothing = 10^4 \mu\text{m}$) beam of He-Ne laser ($\lambda = 0.6328 \mu\text{m}$, $W = 5.0 \mu\text{W}$) was used as an illuminator. Polarization illuminator consists of quarter-wave plates 3, 5 and polarizer 4, and it sequentially forms a series of linearly polarized ($I_0, I_{45}, I_{90}, I_{135}$) with azimuths $0^\circ, 90^\circ, 45^\circ, 135^\circ$, and right-hand (I_\otimes) and left-hand (I_\oplus) circularly polarized probing BT laser beams. The BT images made by microobjective ($4\times$) 7 were projected into the plane of a light-sensitive plate ($m \times n = 800 \times 600$ pixels) of CCD-camera 10. Polarization analysis of the BT images was performed by means of polarizer 9 and quarter-wave plate 8.

The optical thin (the absorption coefficient $\tau < 0, 1$) BT histological sections were used as the objects of investigation. In this situation, one has a single scattering regime of laser radiation scattered by BT network and the narrow-band scattering indicatrix is formed (95% of energy is

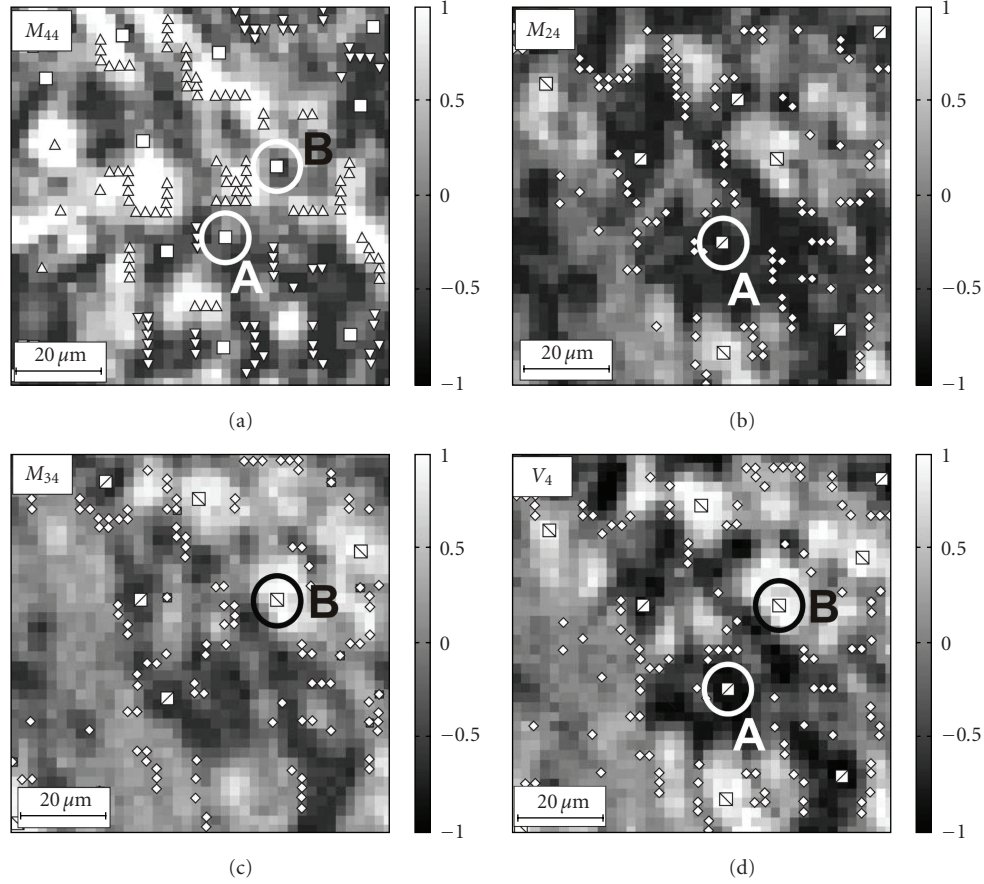


FIGURE 4: Networks of characteristic values $M_{44,24,34}^*(m \times n)$ of matrix elements $M_{44,24,34}$ (a, b, c) and singularities of polarization image of skin derma histological section of “A”-type V_4 (d): “ $\pm C$ ”-points (\square) ($M_{44} = 0$); “+C”-points (\boxplus) ($M_{24,34} = +1$, $V_4 = +1$); “-C”-points (\boxminus) ($M_{24,34} = -1$, $V_4 = -1$); “+L”-points (Δ) ($M_{44} = +1$); “-L”-points (∇) ($M_{44} = -1$); “ $\pm L$ ”-points (\diamond) ($M_{24,34} = 0$, $V_4 = 0$).

concentrated within the angle cone $\Delta\Omega \leq 15^\circ$). Therefore, the speckle background formation in the BT histological section image due to scattering on optical elements is insignificant.

At the first stage the interconnections ($M_{ik}^* \rightarrow V_4^*$) of matrix and polarization singularities were investigated on the example of histological section of healthy skin derma layer.

Figure 2 represents coordinate distributions of matrix elements $M_{44,24,34}(m \times n)$ of histological section of skin derma and the fourth parameter $V_4(m \times n)$ of its image’s Stokes vector with the characteristic values $0, \pm 1$ plotted on them (within the marked $100 \text{ pix} \times 100 \text{ pix}$ sampling plot).

It can be seen from the data obtained that there is direct correlation between the coordinate (k, g $1 \leq k \leq m, 1 \leq g \leq n$) positions of characteristic values of the matrix element M_{44}^* of skin derma and the network of L- and C-points of its laser image $\{M_{44}^*(k, g) = \begin{Bmatrix} 0 \\ \pm 1 \end{Bmatrix}\} \Leftrightarrow V_4^*(k, g) = \begin{Bmatrix} \pm 1 \\ \pm C \end{Bmatrix}$ (Figures 2(a) and 2(d)).

Coordinate distributions of characteristic values of matrix elements $M_{24,42}^*(m, n)$, $M_{34,43}^*(m, n)$ and corresponding networks of “orthogonal” $L_{0,90^-}$, $L_{45,135^-}$ and $C_{0,90^-}$, $C_{45,135^-}$ -points (relations (4) and (5)) possess individual structure. Such peculiarities of singular networks of laser

image of skin derma are obviously conditioned by the asymmetry of various directions ($\rho = 0^\circ, 90^\circ$ and $\rho = 45^\circ, 135^\circ$) of orientation of optical axes of biological crystals in the plane of the investigated sample (Figures 2(b) and 2(c)).

Analytically substantiated and experimentally proven interconnections between the matrix and polarization singularities were used as the basis for Mueller-matrix singular diagnostics of oncological changes of the tissues of women’s reproductive sphere.

4. Mueller-Matrix Diagnostics and Differentiation of Pathological Changes of the Skin Derma

Three groups of histological sections of the main tissue of skin derma—were used as the objects of investigation:

- (i) biopsy of the sound tissue of skin derma (type “A”—Figure 3(a));
- (ii) biopsy of the skin derma in precancer state (type “B”—Figure 3(b));

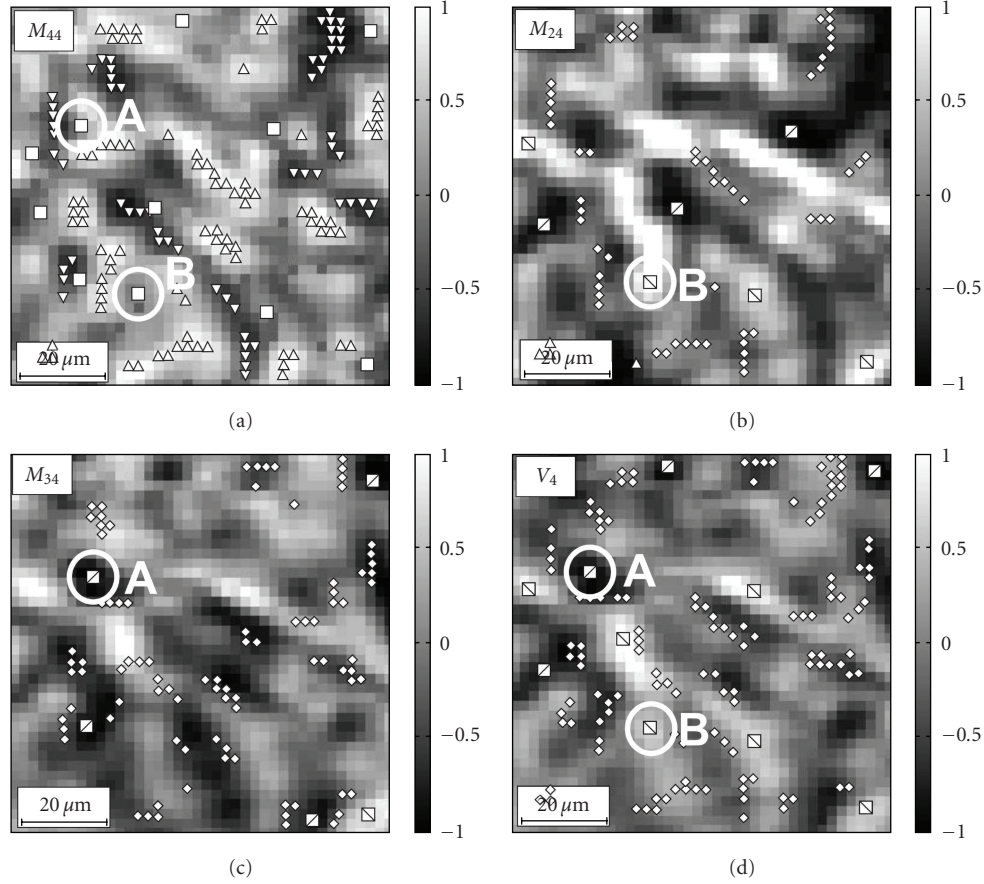


FIGURE 5: Networks of characteristic values $M_{44,24,34}^*(m \times n)$ of matrix elements $M_{44,24,34}$ (a, b, c) and singularities of polarization image of skin derma histological section of “B”-type V_4 (d): “ $\pm C$ ”-points (\square) ($M_{44} = 0$); “+C”-points (\boxplus) ($M_{24,34} = +1$, $V_4 = +1$); “-C”-points (\boxminus) ($M_{24,34} = -1$, $V_4 = -1$); “+L”-points (Δ) ($M_{44} = +1$); “-L”-points (∇) ($M_{44} = -1$); “ $\pm L$ ”-points (\diamond) ($M_{24,34} = 0$, $V_4 = 0$).

(iii) biopsy of the skin derma in cancer state (type “C”—Figure 3(c)).

To determine the criteria of Mueller-matrix diagnostics of skin derma oncological state and differentiation of its severity degree the following technique was used:

- (i) coordinate networks of characteristic values of matrix elements $M_{44,24,34}^*(m \times n) = 0, \pm 1$ were scanned in the direction $x \equiv 1, \dots, m$ with the step $\Delta x = 1$ pixel;
- (ii) within the obtained sampling $(1_{\text{pix}} \times n_{\text{pix}})^{(k=1,2,\dots,m)}$ for coordinate distribution of the element $M_{44}(m \times n)$ the total amount ($N^{(k)}$) of characteristic points ($0, \pm 1$), which set the complete ensemble of singular points was calculated and the dependencies $N(x) \equiv (N^{(1)}, N^{(2)}, \dots, N^{(m)})$ were determined;
- (iii) distributions of the number of “orthogonal” singular L- and $\pm C$ -points were determined according to the terms (4) and (5);

$$\begin{aligned} \rho = 0^\circ, 90^\circ &\Leftrightarrow N_{0,90}(x) = N_C(M_{34,43} = \pm 1) \\ &\quad + N_L(M_{24,42} = 0), \\ \rho = 45^\circ, 135^\circ &\Leftrightarrow N_{45,135}(x) = N_L(M_{34,43} = 0) \\ &\quad + N_C(M_{24,42} = \pm 1); \end{aligned} \quad (6)$$

(iv) statistical moments of the 1st–4th orders of the obtained distributions of $N(x)$ amount of singularities were calculated according to the algorithms

$$\begin{aligned} Z_1 &= \frac{1}{m \times n} \sum_{i=1}^{m \times n} |N(x)|, \\ Z_2 &= \sqrt{\frac{1}{m \times n} \sum_{i=1}^{m \times n} [N(x)]^2}, \\ Z_3 &= \frac{1}{Z_2^3} \frac{1}{m \times n} \sum_{i=1}^{m \times n} [N(x)]^3, \\ Z_4 &= \frac{1}{Z_2^4} \frac{1}{m \times n} \sum_{i=1}^{m \times n} [N(x)]^4. \end{aligned} \quad (7)$$

Figures 4, 5, and 6 show the networks of characteristic values $M_{44,24,34}^*(m \times n)$ of coordinate distributions of matrix elements $M_{44,24,34}(m \times n)$ of histological sections of skin derma of “A”, “B”, “C”-types.

Figure 7 illustrates the distributions of the number of characteristic values $N(x)$, $N_{0,90}(x)$, $N_{45,135}(x)$ of skin derma tissues of “A” (left column), “B” (central column), “C” (right column) types.

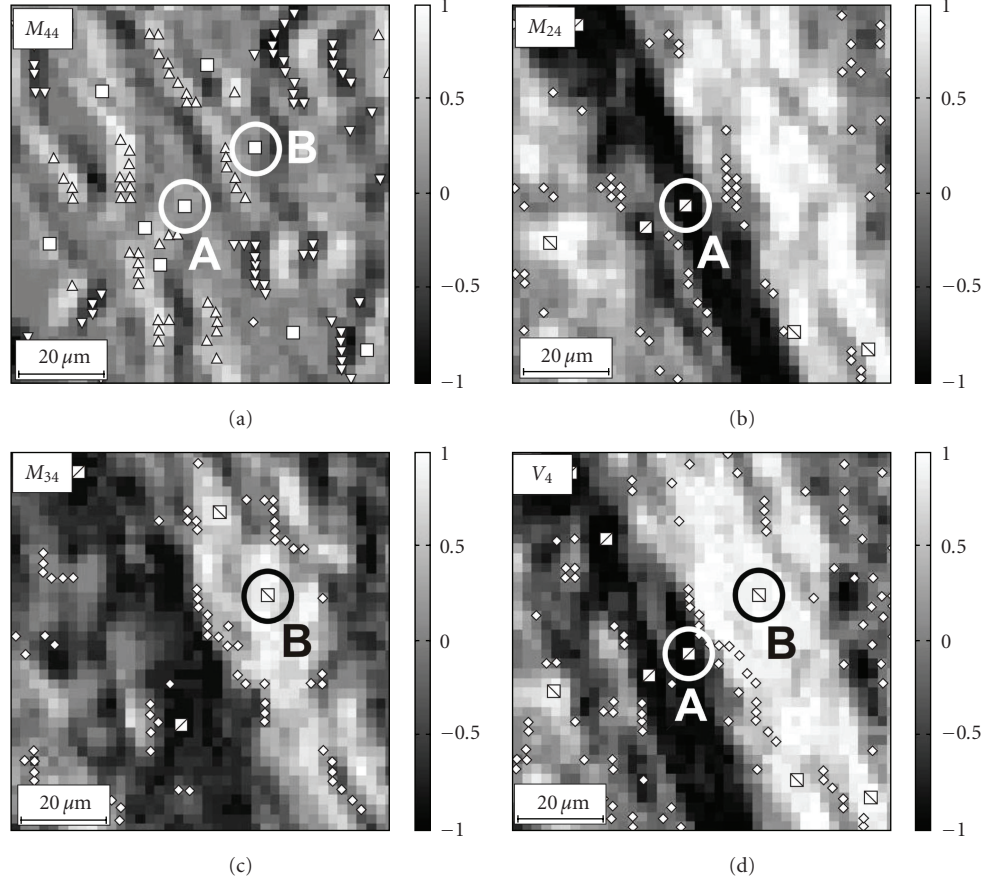


FIGURE 6: Networks of characteristic values $M_{44,24,34}^*(m \times n)$ of matrix elements $M_{44,24,34}$ (a, b, c) and singularities of polarization image of skin derma histological section of “C”-type V_4 (d): “ $\pm C$ ”-points (\square) ($M_{44} = 0$); “+C”-points (\boxplus) ($M_{24,34} = +1$, $V_4 = +1$); “-C”-points (\boxminus) ($M_{24,34} = -1$, $V_4 = -1$); “+L”-points (Δ) ($M_{44} = +1$); “-L”-points (∇) ($M_{44} = -1$); “ $\pm L$ ”-points (\diamond) ($M_{24,34} = 0$, $V_4 = 0$).

The comparative analysis of the data obtained shows that

- (i) coordinate distributions of the elements $M_{44,24,34}^*(m \times n)$ of Mueller matrix of skin derma tissue of all types is characterized by individual (according to quantitative and topological structure) networks of characteristic points (Figures 4–6);
- (ii) total amount of $\pm C$ -points ($M_{44}^*(m \times n) = 0$) sequentially increases for the samples of skin derma of “A”, “B”, “C” types (Figures 4(a)–6(a));
- (iii) dependencies $N_{0,90}(x)$ of the number of characteristic values of matrix elements (8) and (9) for the samples of skin derma tissue of all types are similar in their structure (Figures 7(d), 7(e) and 7(f));
- (iv) distributions $N_{45,135}(x)$ for the samples of skin derma tissue of “B”-type are characterized by sufficient increase (by 2-3 times) of the number of characteristic values in comparison with similar dependencies $N_{0,90}(x)$ (Figures 7(e) and 7(h)).

The obtained results can be connected with the increase of birefringence ($\Delta n \approx 1.5 \times 10^{-2}$) of collagen fibrils of pathologically changes skin derma of “B”- and “C”-types. Besides, at early stages (precancer) the directions of the

growth of newly formed fibrils are being formed. At cancer states such pathologically changed fibrils form specifically oriented network of biological crystals.

In terms of physics, such morphological processes are manifested in the increase of probability of forming the $\pm C$ -points (skin derma samples of “B” and “C”-types), as well as in appearance of asymmetry between ranges of dependences values $N_{0,90}(x)$ and $N_{45,135}(x)$, which characterize the number of orthogonal L- and C-points.

In the end, the comparative investigations of diagnostic efficiency of the potential of famous techniques of laser polarimetry ($Z_{1,2,3,4}(M_{44,34,24}(m \times n))$) [27]; polarization-correlation mapping ($Z_{1,2,3,4}(V_4(m \times n) = \begin{Bmatrix} 0 \\ \pm 1 \end{Bmatrix})$) [24, 25] and the technique of Mueller-matrix singular diagnostics $Z_{1,2,3,4}(N(x), N_{0,90}(x), N_{45,135}(x))$ were suggested.

Table 1 presents statistical averaged values within the three groups of samples of myometrium tissue ($Z_{1,2,3,4}(M_{44,34,24}(m \times n))$); ($Z_{1,2,3,4}(V_4(m \times n) = \begin{Bmatrix} 0 \\ \pm 1 \end{Bmatrix})$) and $Z_{1,2,3,4}(N(x), N_{0,90}(x), N_{45,135}(x))$).

It follows from the data presented that:

- (i) efficiency of laser polarimetry for diagnostics and differentiation of early oncological changes of skin derma tissue is insufficient—the difference

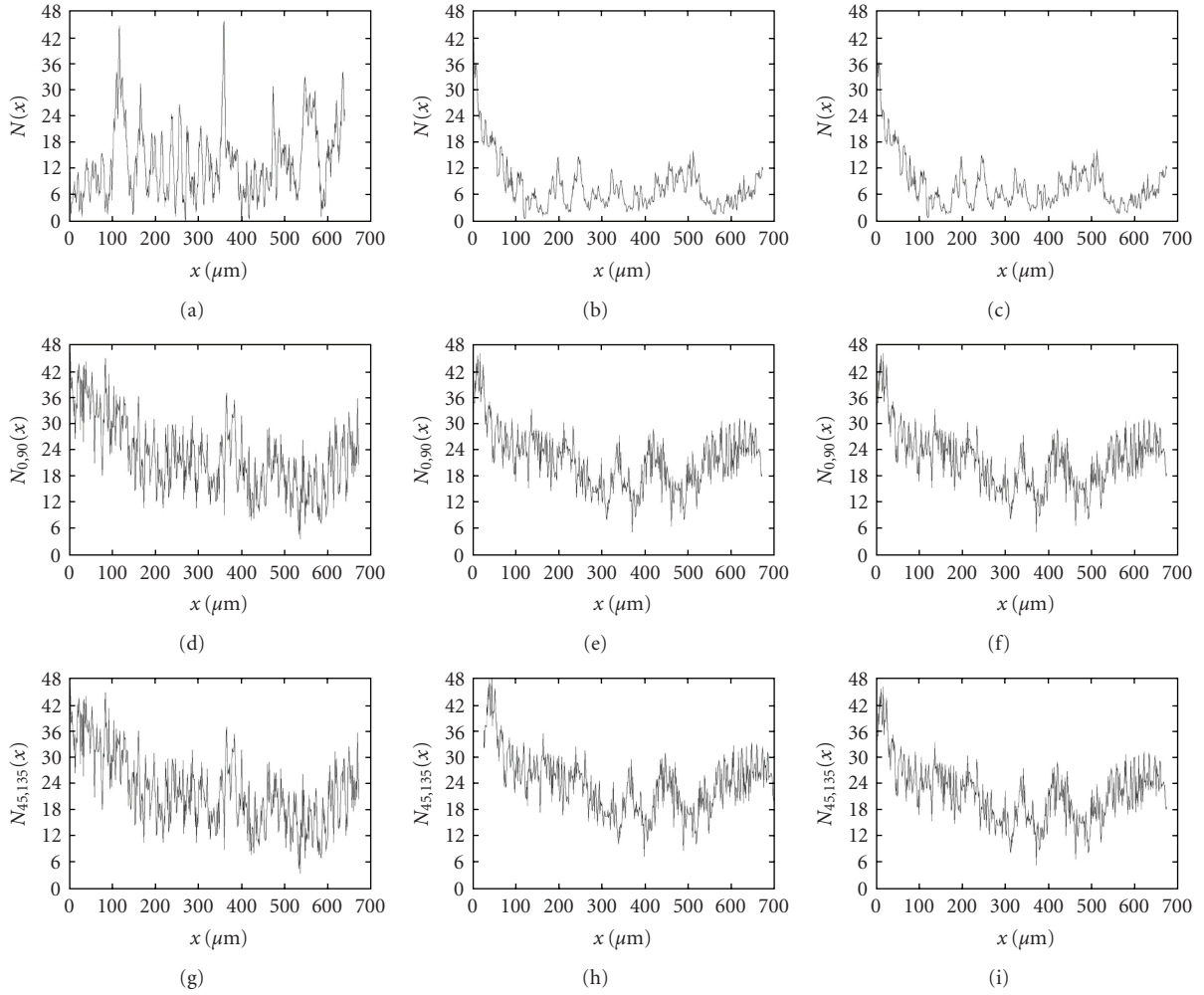


FIGURE 7: Distributions of the amount of characteristic values $N(x)$, $N_{0,90}(x)$, $N_{45,135}(x)$ of skin derma tissues of “A”-(left column), “B”-(central column), “C” (right column)-types.

TABLE 1: Values ($Z_{1,2,3,4}(M_{44,34,24}(m \times n))$), ($Z_{1,2,3,4}(V_4(m \times n) = 0, \text{ or } \pm 1)$) and $Z_{1,2,3,4}(N(x), N_{0,90}(x), N_{45,135}(x))$ statistically averaged within the three groups of skin derma samples.

$Z_{j=1,2,3,4}$	skin derma “A”-type (21 samples)			skin derma “B”-type (21 samples)			skin derma “C”-type (21 samples)		
	M_{44}	M_{34}	M_{24}	M_{44}	M_{34}	M_{24}	M_{44}	M_{34}	M_{24}
Z_1	$0,67 \pm 0,059$	$0,32 \pm 0,031$	$0,27 \pm 0,02$	$0,59 \pm 0,048$	$0,27 \pm 0,02$	$0,24 \pm 0,05$	$0,37 \pm 0,034$	$0,19 \pm 0,015$	$0,18 \pm 0,019$
Z_2	$0,51 \pm 0,046$	$0,29 \pm 0,019$	$0,26 \pm 0,021$	$0,57 \pm 0,05$	$0,23 \pm 0,013$	$0,21 \pm 0,01$	$0,28 \pm 0,023$	$0,21 \pm 0,018$	$0,17 \pm 0,015$
Z_3	$1,13 \pm 0,12$	$0,88 \pm 0,09$	$0,74 \pm 0,08$	$0,98 \pm 0,1$	$0,79 \pm 0,081$	$0,66 \pm 0,069$	$0,66 \pm 0,071$	$0,49 \pm 0,042$	$0,41 \pm 0,04$
Z_4	$3,15 \pm 0,32$	$2,11 \pm 0,29$	$2,27 \pm 0,31$	$2,84 \pm 0,24$	$1,79 \pm 0,18$	$1,87 \pm 0,17$	$1,57 \pm 0,14$	$1,07 \pm 0,1$	$1,12 \pm 0,11$
$Z_{j=1,2,3,4}$	$V_4 = 0$		$V_4 = \pm 1$	$V_4 = 0$		$V_4 = \pm 1$	$V_4 = 0$		$V_4 = \pm 1$
Z_1	$0.12 \pm 0,079$		$0.24 \pm 0,038$	$0.15 \pm 0,067$		$0.28 \pm 0,068$	$0.18 \pm 0,071$		$0.29 \pm 0,076$
Z_2	$0.16 \pm 0,074$		$0.31 \pm 0,042$	$0.19 \pm 0,031$		$0.38 \pm 0,052$	$0.23 \pm 0,019$		$0.4 \pm 0,048$
Z_3	$0.70 \pm 0,052$		$0.92 \pm 0,086$	$0.93 \pm 0,094$		$1.12 \pm 0,101$	$1.27 \pm 0,112$		$1.72 \pm 0,123$
Z_4	$1.71 \pm 0,13$		$2.19 \pm 0,18$	$2.01 \pm 0,19$		$3.13 \pm 0,27$	$3.41 \pm 0,31$		$4.01 \pm 0,31$
$Z_{j=1,2,3,4}$	$N(x)$	$N_{0,90}(x)$	$N_{45,135}(x)$	$N(x)$	$N_{0,90}(x)$	$N_{45,135}(x)$	$N(x)$	$N_{0,90}(x)$	$N_{45,135}(x)$
Z_1	$0,61 \pm 0,052$	$0,43 \pm 0,038$	$0,12 \pm 0,034$	$0,39 \pm 0,05$	$0,37 \pm 0,042$	$0,23 \pm 0,048$	$0,29 \pm 0,039$	$0,28 \pm 0,036$	$0,19 \pm 0,038$
Z_2	$0,75 \pm 0,068$	$0,82 \pm 0,076$	$0,15 \pm 0,021$	$0,36 \pm 0,042$	$0,69 \pm 0,056$	$0,46 \pm 0,02$	$0,31 \pm 0,024$	$0,55 \pm 0,049$	$0,23 \pm 0,026$
Z_3	$1,19 \pm 0,15$	$0,92 \pm 0,01$	$1,86 \pm 0,19$	$0,63 \pm 0,051$	$0,87 \pm 0,07$	$1,86 \pm 0,19$	$0,53 \pm 0,041$	$0,76 \pm 0,062$	$2,06 \pm 0,21$
Z_4	$1,99 \pm 0,17$	$2,31 \pm 0,19$	$2,32 \pm 0,21$	$1,01 \pm 0,1$	$2,07 \pm 0,17$	$8,45 \pm 0,73$	$0,8 \pm 0,07$	$1,87 \pm 0,19$	$2,91 \pm 0,32$

between the values of statistical moments ($Z_{1,2,3,4}(M_{44,34,24}(m \times n))$) of samples “A”, “B” and “C”-types is insufficient and does not exceed 20%–45%;

- (ii) the technique of polarization-correlation mapping is efficient for differentiation of optical properties of sound and oncologically changed skin derma tissue—skewness (Z_3) and kurtosis (Z_4) of distribution of the number of singular points of “A”- and “B”-types of laser images differ by 1.53 and 2.15 times;
- (iii) the technique of Mueller-matrix singular diagnostics is efficient for differentiation of optical properties of all types of samples—statistical moments of the 3rd and 4th orders of distributions $N(x)$ for the samples “A”, “B” and “C”-types differ by 1.7 and 2.5 times respectively;
- (iv) for distributions $N_{45,135}(x)$ of the amount of orthogonal singular $L_{45,135}$ - and $C_{45,135}$ -points of skin derma tissue of “A” and “B” types the maximal difference (from 2.2 to 4.1 times) is observed between all statistical $Z_{j=1,2,3,4}$.

5. Conclusions

Correlation between the coordinate locations of characteristic points of 2D elements of Mueller matrix of optically thin layer of biological tissue and the network of L- and C-points in its laser image is defined. The potentiality of Mueller-matrix sampling of polarization singularities formed by biological crystals with orthogonally oriented ($\rho = 0^\circ, 90^\circ$ and $\rho = 45^\circ, 135^\circ$) optical axes is shown. The efficiency of Mueller-matrix diagnostics not only for oncological changes of skin derma tissue but also for differentiating their severity degree is demonstrated.

References

- [1] S. C. Cowin, “How is a tissue built?” *Journal of Biomechanical Engineering*, vol. 122, no. 6, pp. 553–569, 2000.
- [2] O. V. Angelsky, A. G. Ushenko, Yu. A. Ushenko, Ye. G. Ushenko, Yu. Ya. Tomka, and V. P. Pishak, “Polarization-correlation mapping of biological tissue coherent images,” *Journal of Biomedical Optics*, vol. 10, no. 6, Article ID 064025, 2005.
- [3] J. F. de Boer and T. E. Milner, “Review of polarization sensitive optical coherence tomography and Stokes vector determination,” *Journal of Biomedical Optics*, vol. 7, no. 3, pp. 359–371, 2002.
- [4] J. F. de Boer, T. E. Milner, and J. S. Nelson, “Trends in optics and photonics (TOPS),” in *Advances in Optical Imaging and Photon Migration*, OSA, Washington, DC, USA, 1998.
- [5] M. J. Everett, K. Schoenenberger, B. W. Colston Jr., and L. B. Da Silva, “Birefringence characterization of biological tissue by use of optical coherence tomography,” *Optics Letters*, vol. 23, no. 3, pp. 228–230, 1998.
- [6] O. V. Angelsky, Yu. Ya. Tomka, A. G. Ushenko, Ye. G. Ushenko, S. B. Yermolenko, and Yu. A. Ushenko, “2-D tomography of biotissues images in pre-clinic diagnostics of their pre-cancer states,” in *Advanced Topics in Optoelectronics, Microelectronics, and Nanotechnologies II*, vol. 5972 of *Proceedings of the SPIE*, pp. 158–162, 2004.
- [7] O. V. Angelsky, A. G. Ushenko, D. N. Burkovets, and Yu. A. Ushenko, “Polarization visualization and selection of biotissue image two-layer scattering medium,” *Journal of Biomedical Optics*, vol. 10, no. 1, Article ID 014010, 2005.
- [8] O. V. Angelsky, Yu. Ya. Tomka, A. G. Ushenko, Ye. G. Ushenko, and Yu. A. Ushenko, “Investigation of 2D Mueller matrix structure of biological tissues for pre-clinical diagnostics of their pathological states,” *Journal of Physics D*, vol. 38, no. 23, pp. 4227–4235, 2005.
- [9] S. Jiao, W. Yu, G. Stoica, and L. V. Wang, “Optical-fiber-based Mueller optical coherence tomography,” *Optics Letters*, vol. 28, no. 14, pp. 1206–1208, 2003.
- [10] Yu. A. Ushenko, “Statistical structure of polarization-inhomogeneous images of biotissues with different morphological structures,” *Ukrainian Journal of Physical Optics*, vol. 6, pp. 63–70, 2005.
- [11] O. V. Angel’skii, A. G. Ushenko, A. D. Arkhelyuk, S. B. Ermolenko, D. N. Burkovets, and Yu. A. Ushenko, “Laser polarimetry of pathological changes in biotissues,” *Optics and Spectroscopy*, vol. 89, no. 6, pp. 973–978, 2000.
- [12] O. V. Angelsky, A. G. Ushenko, and Yu. A. Ushenko, “Polarization reconstruction of orientation structure of biological tissues birefringent architectonic nets by using their Mueller-matrix speckle-images,” *Journal of Holography and Speckle*, vol. 2, pp. 72–79, 2005.
- [13] J. F. Nye, *Natural Focusing and the Fine Structure of Light*, Institute of Physics, Bristol, UK, 1999.
- [14] J. F. Nye, “Polarization effects in the diffraction of electromagnetic waves: the role of disclinations,” *Proceedings of the Royal Society of London A*, vol. 387, no. 1792, pp. 105–132, 1983.
- [15] O. V. Angelsky, A. P. Maksimyak, P. P. Maksimyak, and S. G. Hanson, “Interference diagnostics of white-light vortices,” *Optics Express*, vol. 13, no. 20, pp. 8179–8183, 2005.
- [16] J. F. Nye and J. V. Hajnal, “The wave structure of monochromatic electromagnetic radiation,” *Proceedings of the Royal Society of London A*, vol. 409, no. 1836, pp. 21–36, 1987.
- [17] M. V. Berry and M. R. Dennis, “Polarization singularities in isotropic random vector waves,” *Proceedings of the Royal Society A*, vol. 457, no. 2005, pp. 141–155, 2001.
- [18] A. D. Dolgov, A. G. Doroshkevich, D. I. Novikov, and I. D. Novikov, “Classification of singular points in the polarization field of the cosmic microwave background and eigenvectors of the Stokes matrix,” *JETP Letters*, vol. 69, no. 6, pp. 427–433, 1999.
- [19] A. I. Konukhov and L. A. Melnikov, “Optical vortices in a vector field: the general definition based on the analogy with topological solitons in a 2D ferromagnet, and examples from the polarization transverse patterns in a laser,” *Journal of Optics B*, vol. 3, no. 2, pp. S139–S144, 2001.
- [20] O. V. Angelsky, I. I. Mokhun, A. I. Mokhun, and M. S. Soskin, “Interferometric methods in diagnostics of polarization singularities,” *Physical Review E*, vol. 65, no. 3, Article ID 036602, 5 pages, 2002.
- [21] J. F. Nye, “Lines of circular polarization in electromagnetic wave fields,” *Proceedings of the Royal Society of London A*, vol. 389, no. 1797, pp. 279–290, 1983.
- [22] O. V. Angelsky, D. N. Burkovets, P. P. Maksimyak, and S. G. Hanson, “Applicability of the singular-optics concept for diagnostics of random and fractal rough surfaces,” *Applied Optics*, vol. 42, no. 22, pp. 4529–4540, 2003.
- [23] O. V. Angelsky, A. G. Ushenko, and Ye. G. Ushenko, “2-D Stokes polarimetry of biospeckle tissues images in pre-clinic

- diagnostics of their pre-cancer states,” *Journal of Holography and Speckle*, vol. 2, pp. 26–33, 2005.
- [24] O. V. Angelsky, A. G. Ushenko, Yu. A. Ushenko, and Ye. G. Ushenko, “Polarization singularities of the object field of skin surface,” *Journal of Physics D*, vol. 39, no. 16, pp. 3547–3558, 2006.
- [25] O. V. Angelsky, A. G. Ushenko, Ye. G. Ushenko, and Y. Y. Tomka, “Polarization singularities of biological tissues images,” *Journal of Biomedical Optics*, vol. 11, no. 5, Article ID 054030, 2006.
- [26] O. V. Angelsky, S. G. Hanson, A. P. Maksimyak, and P. P. Maksimyak, “On the feasibility for determining the amplitude zeroes in polychromatic fields,” *Optics Express*, vol. 13, no. 12, pp. 4396–4405, 2005.
- [27] A. G. Ushenko and V. P. Pishak, *Coherent-Domain Optical Methods. Biomedical Diagnostics, Environmental and Material Science*, Kluwer Academic Publishers, Dordrecht, The Netherlands, 2004.

Research Article

Evolution of Statistic Moments of 2D-Distributions of Biological Liquid Crystal Net Mueller Matrix Elements in the Process of Their Birefringent Structure Changes

A. G. Ushenko,¹ I. Z. Misevich,¹ V. Istratiy,¹ I. Bachyn's'ka,² A. P. Peresunko,² Omar Kamal Numan,² and T. G. Moiyuk²

¹Optics and Spectroscopy Department, Chernivtsi National University, 2 Kotsyubinsky Street, Chernivtsi 58012, Ukraine

²Chernivtsi Medical University, 2 Theatral Square, Chernivtsi 58002, Ukraine

Correspondence should be addressed to A. G. Ushenko, yuriyu@gmail.com

Received 3 December 2009; Accepted 29 March 2010

Academic Editor: Oleg V. Angelsky

Copyright © 2010 A. G. Ushenko et al. This is an open access article distributed under the Creative Commons Attribution License, which permits unrestricted use, distribution, and reproduction in any medium, provided the original work is properly cited.

This research is aimed to investigate the reliability of Mueller-matrix differentiation of birefringence change of optically thick layers of biological liquid crystals at the early stages of the change in their physiological state. This is performed by measuring the set of skewness and kurtosis values of Mueller matrix image of the phase element M_{44} in various points of the object under investigation.

1. Introduction

Among many methods of optical diagnostics of organic phase-inhomogeneous object a new technique—laser polarimetry [1]—has been formulated within recent 10 years. It enables to obtain information about optical anisotropy [2–5] of biological tissues (BT) in the form of coordinate distributions of BT Mueller matrix elements, azimuths, and ellipticities of their object field polarization.

To analyze this polarimetric information the following model approach was elaborated [1, 2, 6–13]:

- (i) all the variety of human BT can be represented as four main types—connective, muscle, epithelial, and nerve tissues;
- (ii) morphological structure of any BT type is regarded as a 2-component amorphous-crystalline structure;
- (iii) the crystalline component or extracellular matrix is an architectonic net consisting of coaxial cylindrical protein (collagen, myosin, elastin, etc.) fibrils;
- (iv) optically, the protein fibrils possess the properties of uniaxial birefringent crystals;
- (v) interaction of laser radiation with the BT layer is considered in the single scattering approximation, when the attenuation factor corresponds to $\tau \leq 0, 1$.

Specifically, the above mentioned model was used for finding and substantiating the interconnections between the ensemble of statistic moments of the 1st–4th orders that characterize the orientation-phase structure (distribution of optical axes and phase shifts of protein fibrils networks directions) of birefringent BT architectonics and that of 2D distributions of the elements of the corresponding Mueller matrix [6, 10]. It was determined [8, 11] that the 3rd and the 4th statistic moments of coordinate distributions of “phase” matrix elements (z_{24} , z_{34} , z_{44}) are the most sensitive to the change (dystrophic and oncological processes) of optical anisotropy of protein crystals. These statistic moments characterize the BT extracellular matrix birefringence. On this basis the criteria of early diagnostics of muscle dystrophy, precancer states of connective tissue, collagenosis, and so forth were determined.

However, such techniques do not take into account the coordinate heterogeneity of orientation-phase structure of protein crystals nets of the BT layer as well as the order of scattering in its depth. Thus it is important to investigate the distribution of statistic moments of the 1st–4th orders that characterize the 2D elements of Mueller matrix not only in the section of the probing laser beam but also within the whole BT layer of various optical thickness and physiological state.

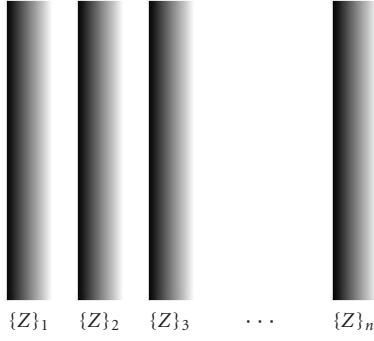


FIGURE 1: On the analysis of modeling polarization properties of anisotropic component of optically thick biological tissue.

For this we shall consider the potentiality of matrix modeling of polarization properties of optically thick BT layer.

2. Mueller Matrix Modeling of the Properties of Optically Thick Biological Tissue

Let us represent the layer of such a biological object as the set of successively located optical thin partial layers (Figure 1).

Polarization properties of birefringent nets of every other BT layer are described by the Mueller matrix $\{Z\}_j$ representing a superposition of matrix operators of optically separate coaxial protein fibrils $\{z\}_j$ [1]:

$$\{z\}_j = \begin{pmatrix} 1 & 0 & 0 & 0 \\ 0 & z_{22} & z_{23} & z_{24} \\ 0 & z_{32} & z_{33} & z_{34} \\ 0 & z_{42} & z_{43} & z_{44} \end{pmatrix}, \quad (1)$$

where

$$z_{ik}(\rho, \delta) = \begin{cases} z_{22} = \cos^2 2\rho + \sin^2 2\rho \cos \delta, \\ z_{23,32} = \cos 2\rho \sin 2\rho (1 - \cos \delta), \\ z_{33} = \sin^2 2\rho + \cos^2 2\rho \cos \delta, \\ z_{34,43} = \pm \cos 2\rho \sin \delta, \\ z_{24,42} = \pm \sin 2\rho \sin \delta, \\ z_{44} = \cos \delta. \end{cases} \quad (2)$$

Here ρ is the direction of optical axis determined by the direction of packing of the birefringent fibril, $\delta = (2\pi/\lambda)\Delta nd$ is the phase shift introduced between the orthogonal components of the amplitude of laser wave with the length λ passing through the fibril with linear size of its geometrical section d and birefringence index Δn .

Mueller matrix $(Z_{ik})_j$ elements of the net of protein fibrils of partial BT layer (j) are determined by the following algorithms:

(i) for finite number (N) of fibrils

$$Z_{ik} = \sum_{u=1}^N \sum_{v=1}^N z_{ik}(\rho_u, \delta_u), \quad (3)$$

(ii) for “infinite” ($N \rightarrow \infty$) number of fibrils

$$Z_{ik} = \int_0^\pi \int_0^{2\pi} Q_\rho W_\delta z_{ik}(\rho, \delta) d\rho d\delta. \quad (4)$$

Here Q_ρ and W_δ are the distribution function of orientation (ρ) and phase (δ) parameters of biological crystals network.

Mueller matrix of optically thick BT is determined by multiplication of partial matrix operators:

$$\{Z\} = \{Z\}_n \{Z\}_{n-1} \cdots \{Z\}_2 \{Z\}_1. \quad (5)$$

To make it simpler (without decreasing the analysis depth) further we shall consider only a 2-layered BT:

$$\{Z\} = \{Z\}_2 \{Z\}_1 \equiv \{Y\} \{X\}. \quad (6)$$

In the expanded form the matrix operator elements (6) are written as follows:

$$Z_{ik}(\rho_x, \rho_y, \delta_x, \delta_y) = \begin{cases} Z_{22} = y_{22}x_{22} + y_{23}x_{32} + y_{24}x_{42}, \\ Z_{23} = y_{22}x_{23} + y_{23}x_{33} + y_{24}x_{43}, \\ Z_{32} = y_{32}x_{22} + y_{33}x_{32} + y_{34}x_{42}, \\ Z_{33} = y_{32}x_{23} + y_{33}x_{33} + y_{34}x_{43}, \\ Z_{34} = y_{32}x_{24} + y_{33}x_{34} + y_{34}x_{44}, \\ Z_{43} = y_{42}x_{23} + y_{43}x_{33} + y_{44}x_{43}, \\ Z_{24} = y_{22}x_{24} + y_{23}x_{34} + y_{24}x_{44}, \\ Z_{42} = y_{42}x_{22} + y_{43}x_{32} + y_{44}x_{42}, \\ Z_{44} = y_{42}x_{24} + y_{43}x_{34} + y_{44}x_{44}. \end{cases} \quad (7)$$

The analysis of relations (7) shows that optical properties of anisotropic component of 2-layered BT (Z_{ik}) are described by complex superposition of orientation and phase parameters of its partial layers' biological crystals ($x_{ik}(\rho_x, \delta_x), y_{ik}(\rho_y, \delta_y)$). The concrete form of such dependences for “phase” $z_{42,43,44}$ matrix elements [10] is illustrated by the following relations:

$$\begin{aligned} z_{24} &= \sin \delta_y \left[\cos 2\rho_x \sin 2(\rho_x - \rho_y) \right. \\ &\quad \left. + \cos \delta_x \sin 2\rho_x \cos 2(\rho_x + \rho_y) \right] \\ &\quad + \sin \delta_x \cos \delta_y \sin 2\rho_x; \\ z_{34} &= \sin \delta_x \left[\sin 2\rho_y \sin 2(\rho_x - \rho_y) \right. \\ &\quad \left. + \cos \delta_y \cos 2\rho_y \cos 2(\rho_x + \rho_y) \right] \\ &\quad + \cos \delta_x \sin \delta_y \cos 2\rho_y; \\ z_{44} &= \cos(2\rho_x - 2\rho_y) \sin \delta_x \sin \delta_y + \cos \delta_x \cos \delta_y. \end{aligned} \quad (8)$$

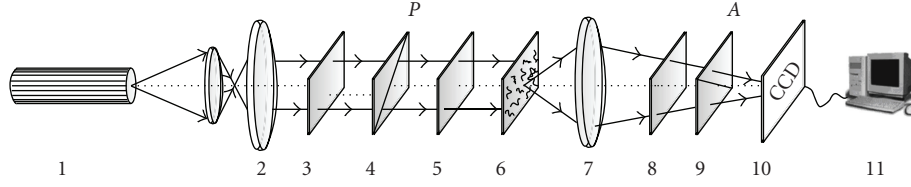


FIGURE 2: Optical scheme of polarimeter, where 1: He-Ne laser; 2: collimator; 3: stationary quarter-wave plate; 5, 8: mechanically movable quarter-wave plates; 4, 9: polarizer and analyzer correspondingly; 6: object of investigation; 7: microobjective; 10: CCD camera; 11: PC.

The analysis of relations (8) shows that a strict solution of the inverse problem $\{\rho_x = q(z_{ik}, \rho_y, \delta_y); \delta_x = g(z_{ik}, \rho_y, \delta_y)\}$, revealing the changes in the structure of biological crystals network of one of the layers on the basis of data about matrix elements z_{ik} and y_{ik} , is both mathematically incorrect and physically ambiguous.

Thus, it is important to elaborate approximated statistical methods of experimental solution of such diagnostic task.

Generally speaking, the increase of optical thickness of biological layer results in multiple scattering regime in its volume. Such process appeared in formation of integral depolarization of laser field and results in averaging within angular aperture of photodetector of azimuth and ellipticity random values of fully polarized isolated speckles [8]. In this case the direct interconnection between the scattered field polarization parameters and the orientation and phase structure of biological crystals will be lost. From the other hand, for such integrally depolarized fields the Mueller matrix approach remains adequate [1]. Therefore, the search of interconnections “object-laser field” on the level of indirect, statistic parameters, which characterizes their structure is topical.

3. Scheme of Experimental Changes of Coordinate Distributions of Biological Tissue Mueller Matrix Elements

The histological sections of different geometrical (optical) thickness were used as the objects of investigation. The technique of obtaining of such objects is convenient: biological tissue is freezing to nitrogen temperature with the following obtaining, by means of medical microtome, the histological sections (from $10 \mu\text{m}$ to $100 \mu\text{m}$). Such a technique allows preserving the optical properties of biological tissues over a period of 24 hours.

Conventional optical scheme of polarimeter for measuring 2D distributions of the BT Mueller matrix elements is presented in Figure 2 [1].

Histological sections of BT were illuminated by a parallel beam of He-Ne laser ($\lambda = 0.6328 \mu\text{m}$, $W = 5.0 \mu\text{W}$) with the radius $r = 1 \text{ mm}$. Polarization illuminator consists of quarter-wave plates 3, 5 and polarizer 4, providing the formation of laser beam with random azimuth $0^\circ \leq \alpha_0 \leq 180^\circ$ or ellipticity $0^\circ \leq \beta_0 \leq 90^\circ$ of polarization. Polarization images of BT by means of microobjective 7 were projected into the plane of sensitized plate ($m \times n = 800 \times 600$ pixels)

if with CCD-camera 10. The analysis of BT images was carried out by means of polarizer 9 and quarter-wave plate 8. As a result, the Stokes vector parameters for every pixel of the BT image $\{S_{i=1,2,3,4}\}$ were determined and the set of elements of Mueller matrix was calculated according to algorithm [10]:

$$\begin{aligned} Z_{i1} &= 0,5[S_i^{(1)} + S_i^{(1)}], \\ Z_{i2} &= 0,5[S_i^{(1)} - S_i^{(1)}], \\ Z_{i3} &= S_i^{(3)} - Z_{i1}, \\ Z_{i4} &= S_i^{(4)} - Z_{i1}, \quad i = 1, 2, 3, 4. \end{aligned} \quad (9)$$

Indices 1–4 correspond to the following polarization states of the beam probing the BT layer: 1– 0° ; 2– 90° ; 3– $+45^\circ$; 4– \otimes (right-hand circulation).

The technique of measuring the ensemble (j —the number of probing areas) of 2D matrix elements $Z_{ik}^{(j)}(m \times n)$ of BT consisted in the following sequence of actions:

- (i) the plane of BT histological sections ($\approx 10 \text{ mm} \times 20 \text{ mm}$) BT was scanned line by line by the laser beam with the radius $r = 1 \text{ mm}$ with the step of linear displacement $\Delta r = 2 \text{ mm}$;
- (ii) within each of 50 areas ($j = 1, 2, \dots, 50$) of illumination of the BT layer plane according to the algorithm (9) the local array ($m \times n = 800 \times 600$) of values of Mueller matrix elements $Z_{ik}^{(j)}(m \times n)$ was determined:

$$Z_{ik}^{(j)}(m \times n) = \begin{pmatrix} Z_{ik}^{11} & \dots & Z_{ik}^{1m} \\ \dots & \dots & \dots \\ Z_{ik}^{n1} & \dots & Z_{ik}^{nm} \end{pmatrix}_{j=1,2,\dots,50} \quad (10)$$

- (iii) for every local array $Z_{ik}^{(j)}(m \times n)$ statistic moments of the 3rd-4th $M^{(s=3,4)}$ orders were calculated;
- (iv) the histograms $N(M_{j=1,2,\dots,50}^{(s=3,4)})$ of the values of statistical moments of higher orders within the whole plane of the investigated BT histological sections were determined.

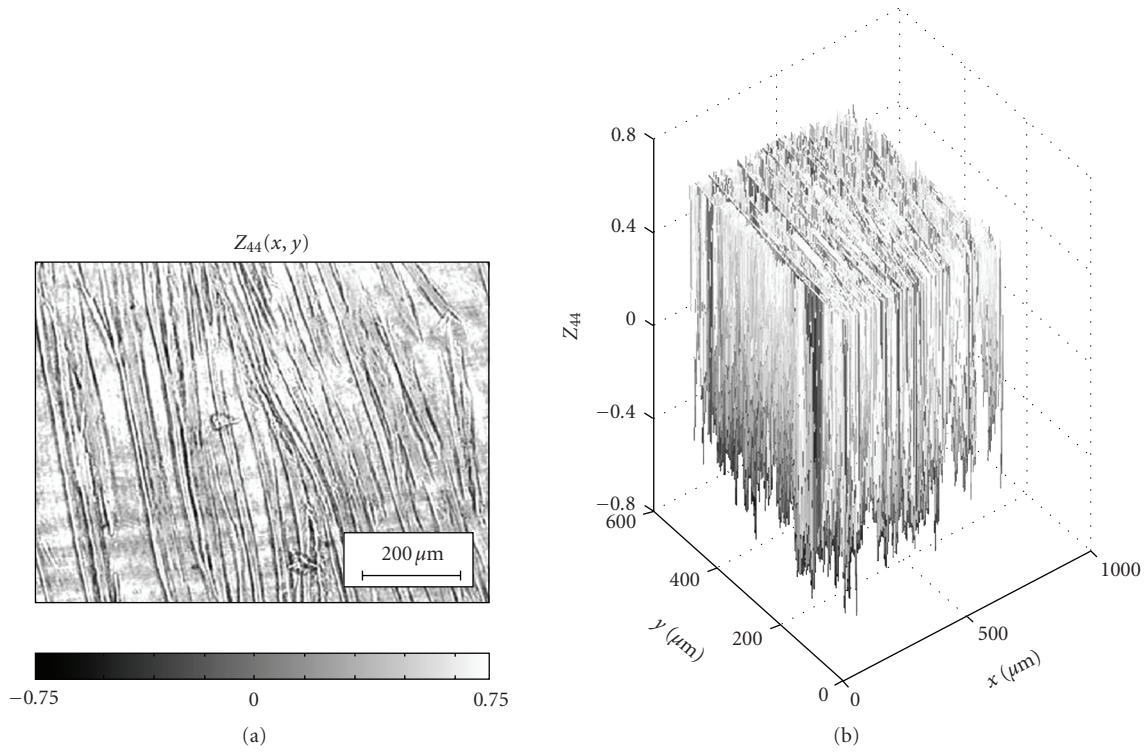


FIGURE 3: Coordinate and 3D distribution of the values of phase matrix element $Z_{44}(m, n)$ of histological section of optically thin ($\tau_1 = 0,08$) layer of the healthy rat's muscle tissue.

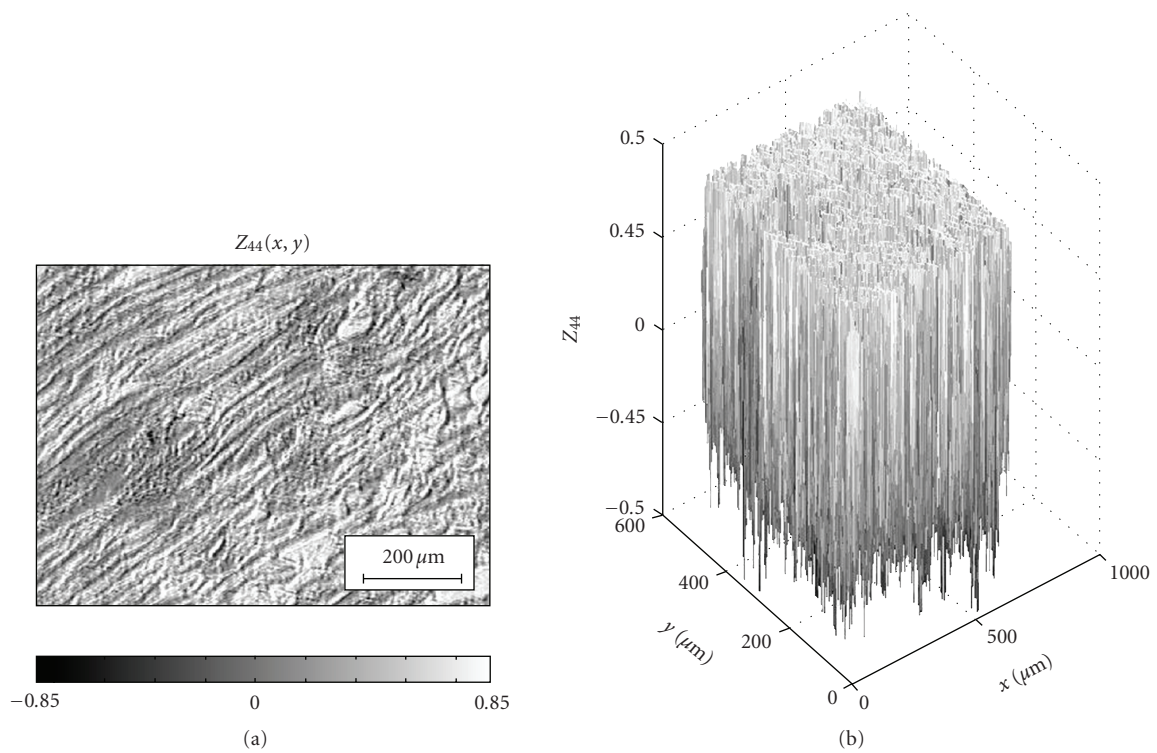


FIGURE 4: Coordinate and 3D distribution of the values of phase matrix element $Z_{44}(m, n)$ of histological section of optically thin ($\tau_1 = 0,08$) layer of the inflamed rat's muscle tissue.

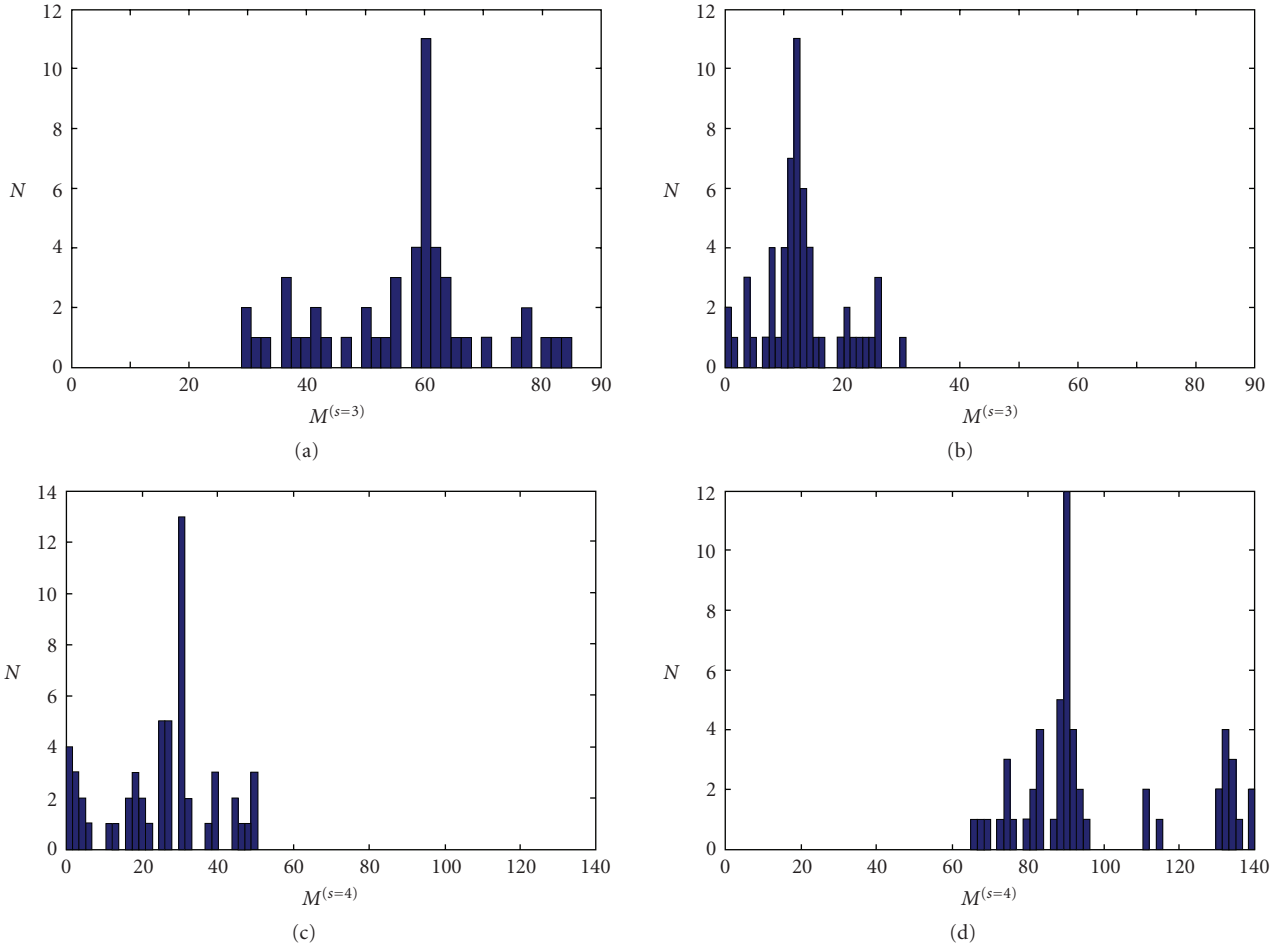


FIGURE 5: Histograms of the set of skewness $M^{(s=3)}$ values (a, b) and kurtosis $M^{(s=4)}$ (c, d) of coordinate distribution of the element $Z^{(j=1-50)}_{44}(m, n)$ of histological section of optically thin ($\tau_1 = 0,08$) layer of the healthy (a, c) and inflamed (b, d) rat’s skeletal tissue.

4. Investigation of Skewness and Kurtosis Distributions of 2D Phase Element of Mueller Matrix of the Samples of Skeletal Muscle Tissue

The following histological sections of different types of rat’s tissues were investigated—connection tissue, muscular tissue, epithelial tissue, and nervous tissue. All these tissues have common optical peculiarity—the presence of birefringent network of protein fibrils [1]. Therefore, in this work, without decrease of analysis completeness, we have concentrated on investigation of optical anisotropy of rat’s skeletal muscle tissue birefringent fibrils.

Distributions $N(M^{(s=3,4)})$ of the values of skewness $M^{(s=3)}$ and kurtosis $M^{(s=4)}$ of 2D phase (Z_{44}) element of Mueller matrix of rat’s skeletal muscle tissue were investigated. Histological sections of various optical thickness ($\tau_1 = 0,08$ and $\tau_2 = 1,47$) and physiological state were the object of investigation. Such choice of optical thickness of histological sections ($d_1 = 15 \mu\text{m}$; $d_2 = 50 \mu\text{m}$) allows us to investigate the influence of a single ($\tau_1 = 0,08$) and multiple ($\tau_2 = 1,47$) scattering on coordinate structure of Mueller matrix elements.

The choice of matrix element Z_{44} as an analytical parameter is explained by the fact that it is the most sensitive to the changes of birefringence of protein fibrils nets, connected with their pathological changes [1, 11]. The choice of a skeletal muscle tissue of a rat as the object of investigation is connected with the possibility of direct experimental formation of septic inflammation and monitoring the control of their optical manifestations under the condition of scattering of laser beam of various multiplication factor.

The series of Figures 3 and 4 presents the distributions of the element $Z_{44}(m, n)$ of optically thin histological sections of healthy (Figure 3) and inflamed (Figure 4) muscle tissue.

The following can be seen from the data obtained:

- (i) 2D distributions of matrix elements $Z_{44}(m, n)$ of both types of tissues are coordinately heterogeneous;
- (ii) for the sample of healthy muscle tissue (Figure 3) the lesser range of values change (from -0.7 to 0.7) of the matrix element $Z_{44}(m, n)$ is typical in comparison with the changes (from -0.85 to 0.85) of the analogous element of Mueller matrix of the inflamed tissue (Figure 4).

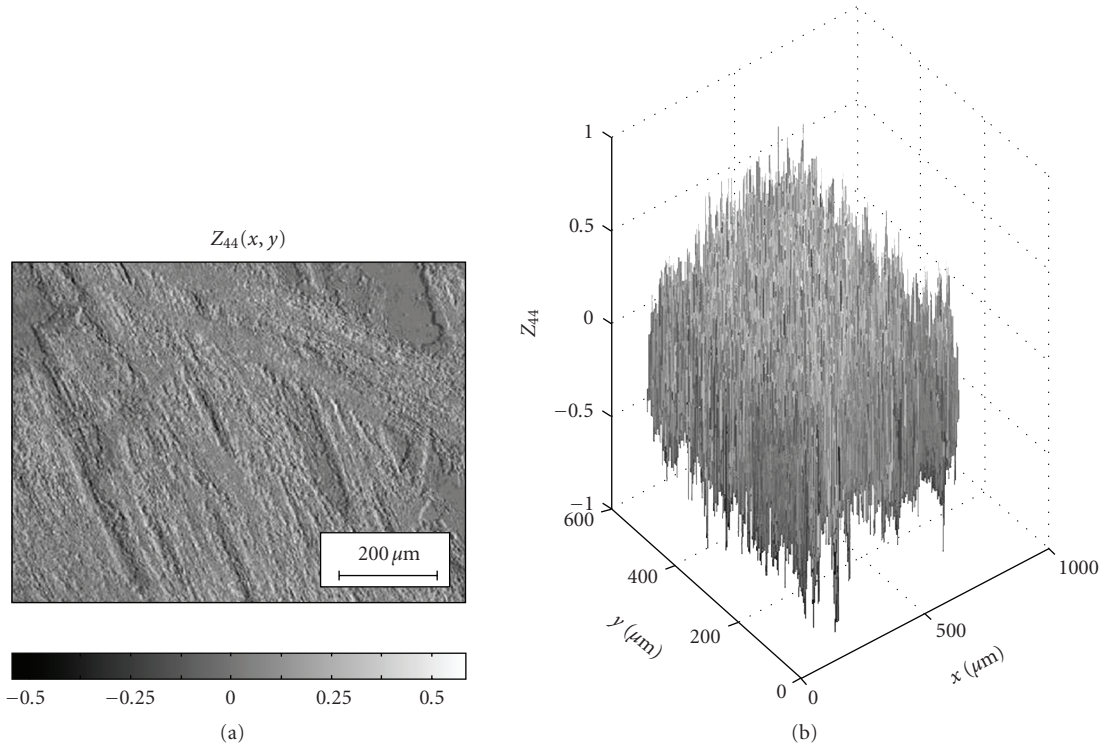


FIGURE 6: Coordinate and 3D distribution of the values of phase matrix element $Z_{44}(m, n)$ of histological section of optically thick ($\tau_1 = 1, 47$) layer of the healthy rat's muscle tissue.

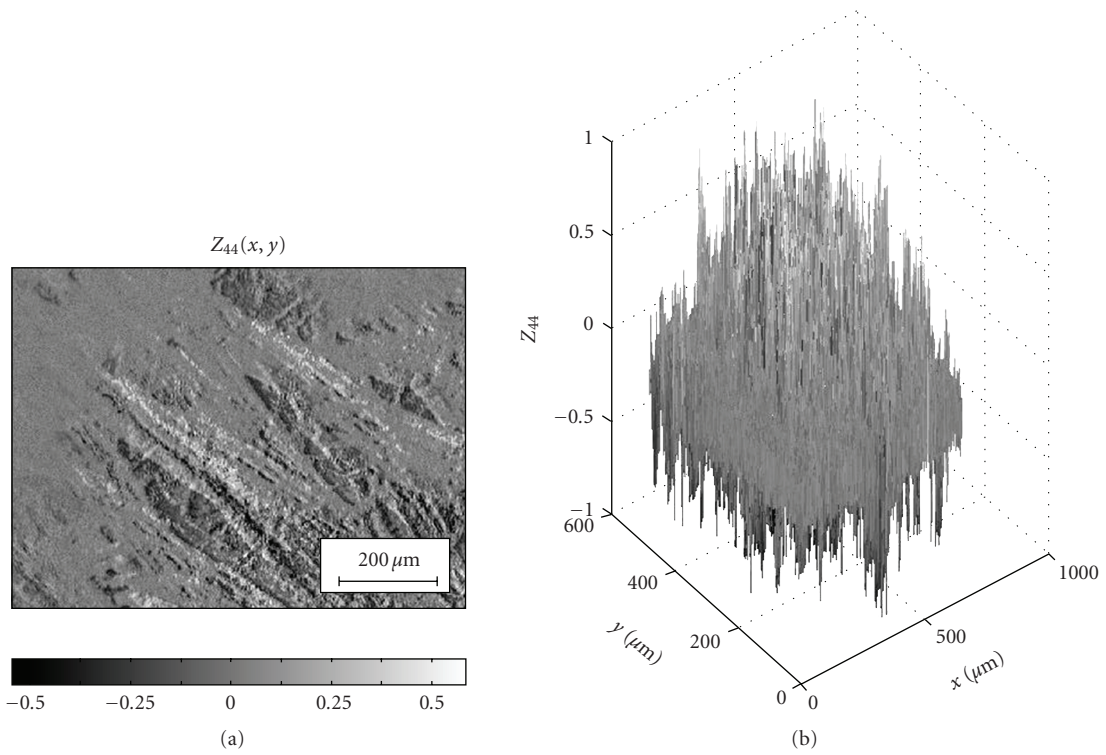


FIGURE 7: Coordinate and 3D distribution of the values of phase matrix element $Z_{44}(m, n)$ of histological section of optically thick ($\tau_1 = 1, 47$) layer of the inflamed rat's muscle tissue.

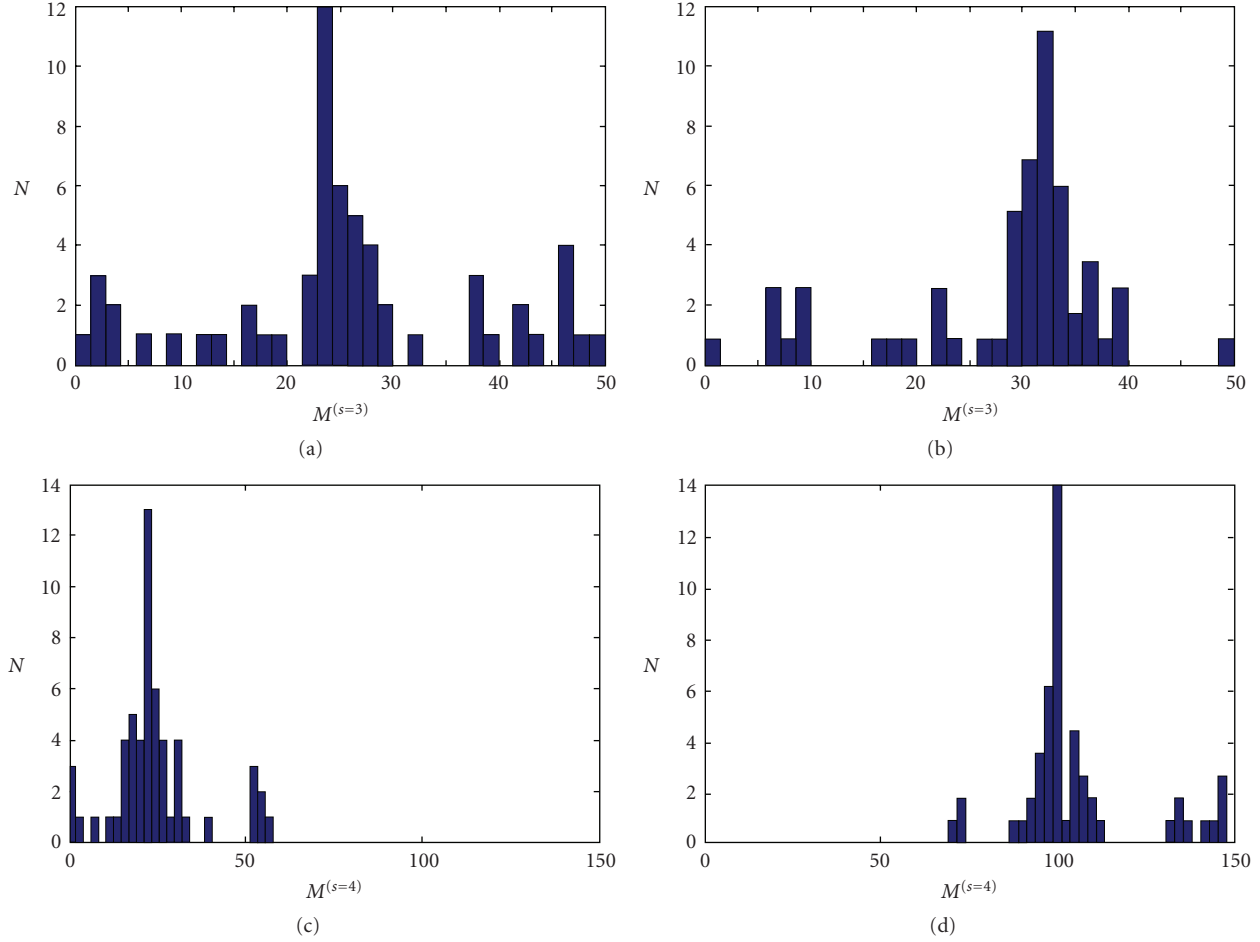


FIGURE 8: Histograms of the set of skewness $M^{(s=3)}$ values (a, b) and kurtosis $M^{(s=4)}$ (c, d) of coordinate distribution of the element $Z^{(j=1-50)}_{44}(m, n)$ of histological section of optically thick ($\tau_2 = 1, 17$) layer of the healthy (a, c) and inflamed (b, d) rat's skeletal tissue.

The structure of 2D distributions of elements $Z_{44}(m, n)$ can be connected with the following peculiarities of birefringent architectonics of the skeletal tissue samples. Firstly, while a laser wave (with the wave-length λ) propagates through the network of optically anisotropic (birefringence index $\Delta n = 1,5 \times 10^{-3}$ [7]) myosin fibrils, a wide range of values of phase shifts δ_k , proportional to their geometrical sizes d_k , is formed

$$\delta_k \sim \left(\frac{2\pi\Delta n}{\lambda} \right) \times \begin{cases} d_1 \\ \vdots \\ d_k. \end{cases} \quad (11)$$

Thus, phase elements $Z_{44}(m, n)$ distributions are coordinately heterogeneous and dependent on the peculiarities of morphological structure of extracellular matrix of muscle tissue samples.

Secondly, the inflammation process is accompanied by the increase of birefringence Δn due to formation of myosin fibrils edema [7]. Optically, it causes the increase of the range of phase shifts δ_k changes and the growth of fluctuations of the element $Z_{44}(m, n)$ connected with it (Figure 4).

The histograms of distribution $N(M^{(s=3,4)})$ of statistic moments of higher-orders $M^{(s=3,4)}$ of coordinate distributions $Z^{(j=1-50)}_{44}(m, n)$ of investigated samples of optically thin histological sections are presented in Figure 5.

The analysis of experimentally measured histograms $N(M^{(s=3,4)})$ proved the following:

- (i) the change ranges of the values of skewness $M^{(s=3)}$ and kurtosis $M^{(s=4)}$ of coordinate distributions $Z^{(j=1-50)}_{44}(m, n)$, measured for the healthy (a, c) and inflamed (b, d) muscle tissues, do not actually coincide;
- (ii) extreme values of skewness in the distribution $N(M^{(s=3)})$ for phase element Z_{44} of the healthy tissue are by 4–6 times higher than analogous values of the given statistic moment $M^{(s=3)}$ for the inflamed muscle tissue;
- (iii) extreme values of kurtosis in the distribution $N(M^{(s=4)})$ for the inflamed tissue are by 2–3 times higher than the values of the statistic moment $M^{(s=4)}$ for the healthy skeletal tissue.

Thus, it can be stated that for single differentiation of physiological state of optically thin layers of muscle tissue it is enough to measure the 2D phase matrix element $Z_{44}(m, n)$ in one domain (πr^2) of irradiation by the laser beam and to calculate the skewness and kurtosis of its values distribution.

The series of Figures 6 and 7 presents the results of experimental measurements of phase elements $Z_{44}(m, n)$ of Mueller matrix of optically thick ($\tau_2 = 1,47$) of the rat's muscle tissue layers.

It can be seen from the data obtained the following:

- (i) for the samples of the healthy and inflamed muscle tissue the same range of values change (from $-0,55$ to $0,55$) is typical in the distribution of matrix elements $Z_{44}(m, n)$;
- (ii) comparative visual analysis of coordinate distributions of matrix elements $Z_{44}(m, n)$ of histological sections of skeletal tissue of both types did not show any sufficient difference between them.

Similarity of the distribution structure $Z_{44}(m, n)$ of both types of rat's skeletal tissue samples can be explained by multiple light-scattering. As a result of every local (i th) act of interaction between laser radiation and separate fibril random value of phase shift $\delta^{(i)}$ is formed, which is multiplied ($\delta^* = \sum_{i=1}^R \delta_i$) in the process of propagation in the BT depth reaching equiprobable random values from 0 to $2k\pi$, $k = 1, 2, 3, \dots$

Figure 8 shows histograms $N(M^{(s=3,4)})$ of the set of values of statistic moments of skewness $M^{(s=3)}$ and kurtosis $M^{(s=4)}$ of distributions of the matrix element $Z^{(j=1-50)}_{44}(m, n)$ of optically thick samples of muscle tissue.

The analysis of experimental data showed the following:

- (i) the skewness $M^{(s=3)}$ values distribution of 2D phase $Z^{(j=1-50)}_{44}(m, n)$, and changes within the whole plane of samples of the layer of the healthy (a) and inflamed (b) muscle tissue practically coincide and cannot be used as an objective criterion for their optical properties differentiation;
- (ii) histograms $N(M^{(s=4)})$ of the values of the statistic moment $M^{(s=4)}$ of elements $Z^{(j=1-50)}_{44}(m, n)$ distribution possess individual structure that depends on physiological state of muscle tissue;
- (iii) extreme values of kurtosis $M^{(s=4)}$ in the histogram $N(M^{(s=4)})$ of the healthy tissue (c) are by 4-5 times less than analogous values of the given statistic moment of the inflamed rat's skeletal tissue (d).

5. Conclusion

Thus for realization of Mueller-matrix differentiation of optically thick BT layers at early stages of changing their physiological state the measurement of distributions of the kurtosis $N(M^{(s=4)})$ of the ensemble of phase elements $Z^{(j=1-50)}_{44}(m, n)$ is objective.

The Mueller-matrix approach in diagnostics and differentiation of the biological crystals networks appears to be effective for optically thick histological sections layers of human tissues (skin derma, tissues of women reproductive sphere, parenchymatous tissues) also.

References

- [1] A. G. Ushenko and V. P. Pishak, *Coherent-Domain Optical Methods. Biomedical Diagnostics, Environmental and Material Science*, Kluwer Academic Publishers, Dordrecht, The Netherlands, 2004.
- [2] J. F. de Boer and T. E. Milner, "Review of polarization sensitive optical coherence tomography and Stokes vector determination," *Journal of Biomedical Optics*, vol. 7, no. 3, pp. 359–371, 2002.
- [3] J. F. de Boer, T. E. Milner, and J. S. Nelson, *Trends in Optics and Photonics (TOPS): Advances in Optical Imaging and Photon Migration*, OSA, Washington, DC, USA, 1998.
- [4] M. J. Everett, K. Schoenenberger, B. W. Colston Jr., and L. B. Da Silva, "Birefringence characterization of biological tissue by use of optical coherence tomography," *Optics Letters*, vol. 23, no. 3, pp. 228–230, 1998.
- [5] S. Jiao, W. Yu, G. Stoica, and L. V. Wang, "Optical-fiber-based Mueller optical coherence tomography," *Optics Letters*, vol. 28, no. 14, pp. 1206–1208, 2003.
- [6] O. V. Angelsky, G. V. Demianovsky, A. G. Ushenko, D. N. Burkovets, and Yu. A. Ushenko, "Wavelet analysis of two-dimensional birefringence images of architectonics in biotissues for diagnosing pathological changes," *Journal of Biomedical Optics*, vol. 9, no. 4, pp. 679–690, 2004.
- [7] O. V. Angelsky, Yu. Ya. Tomka, A. G. Ushenko, Ye. G. Ushenko, S. B. Yermolenko, and Yu. A. Ushenko, "2-D tomography of biotissues images in pre-clinic diagnostics of their pre-cancer states," in *Advanced Topics in Optoelectronics, Microelectronics, and Nanotechnologies II*, Proceedings of the SPIE, 2004.
- [8] O. V. Angelsky, A. G. Ushenko, D. N. Burkovets, and Yu. A. Ushenko, "Polarization visualization and selection of biotissue image two-layer scattering medium," *Journal of Biomedical Optics*, vol. 10, no. 1, Article ID 014010, 2005.
- [9] O. V. Angelsky, Yu. Ya. Tomka, A. G. Ushenko, Ye. G. Ushenko, and Yu. A. Ushenko, "Investigation of 2D Mueller matrix structure of biological tissues for pre-clinical diagnostics of their pathological states," *Journal of Physics D*, vol. 38, no. 23, pp. 4227–4235, 2005.
- [10] Yu. A. Ushenko, "Statistical structure of polarization-inhomogeneous images of biotissues with different morphological structures," *Ukrainian Journal of Physical Optics*, vol. 6, pp. 63–70, 2005.
- [11] O. V. Angelsky, A. G. Ushenko, and Yu. A. Ushenko, "Polarization reconstruction of orientation structure of biological tissues birefringent architectonic nets by using their Mueller-matrix speckle-images," *Journal of Holography and Speckle*, vol. 2, pp. 72–79, 2005.
- [12] O. V. Angelsky, P. P. Maksimyak, V. V. Ryukhtin, and S. G. Hanson, "New feasibilities for characterizing rough surfaces by optical-correlation techniques," *Applied Optics*, vol. 40, no. 31, pp. 5693–5707, 2001.
- [13] O. V. Angelsky, P. P. Maksimyak, and T. O. Perun, "Optical correlation method for measuring spatial complexity in optical fields," *Optics Letters*, vol. 18, no. 2, pp. 90–92, 1993.

Research Article

On the Feasibilities of Using the Wavelet Analysis of Mueller Matrix Images of Biological Crystals

O. V. Dubolazov,¹ A. G. Ushenko,¹ V. T. Bachynsky,² A. P. Peresunko,² and O. Ya. Vanchulyak²

¹Optics and Spectroscopy Department, Chernivtsi National University, 2 Kotsyubinsky Str., 58012, Chernivtsi, Ukraine

²Department of Morbid Anatomy, Chernivtsi Medical University, 2 Theatral Sq, 58002, Chernivtsi, Ukraine

Correspondence should be addressed to A. G. Ushenko, yuriyu@gmail.com

Received 5 December 2009; Accepted 29 March 2010

Academic Editor: Oleg V. Angelsky

Copyright © 2010 O. V. Dubolazov et al. This is an open access article distributed under the Creative Commons Attribution License, which permits unrestricted use, distribution, and reproduction in any medium, provided the original work is properly cited.

The efficiency of using the statistical and fractal analyses for distributions of wavelet coefficients for Mueller matrix images of biological crystal networks inherent to human tissues is theoretically grounded in this work. The authors found interrelations between statistical moments and power spectra for distributions of wavelet coefficients as well as orientation-phase changes in networks of biological crystals. Also determined are the criteria for statistical and fractal diagnostics of changes in the birefringent structure of biological crystal network, which corresponds to pathological changes in tissues.

1. Introduction

In recent years, laser diagnostics aimed at the structure of biological tissues efficiently use the model approach [1], in accordance with the tissues that are considered as two components: amorphous $\{A\}$ and optically anisotropic $\{F\}$ ones. Each of these components is characterized by intrinsic matrix operators

$$\{A\} = \begin{pmatrix} 1 & 0 & 0 & 0 \\ 0 & 1 & 0 & 0 \\ 0 & 0 & 1 & 0 \\ 0 & 0 & 0 & 1 \end{pmatrix} \cdot e^{-\tau l}, \quad (1)$$

where τ is the extinction coefficient inherent to the layer of biological tissue with the geometric thickness l

$$\{F\} = \begin{pmatrix} 1 & 0 & 0 & 0 \\ 0 & f_{22} & f_{23} & f_{24} \\ 0 & f_{32} & f_{33} & f_{34} \\ 0 & f_{42} & f_{43} & f_{44} \end{pmatrix}$$

$$= \begin{pmatrix} 1 & 0 & 0 & 0 \\ 0 & \cos^2 2\rho + \sin^2 2\rho \cdot \cos \delta & \cos 2\rho \sin 2\rho (1 - \cos \delta) & \sin 2\rho \sin \delta \\ 0 & \cos 2\rho \sin 2\rho (1 - \cos \delta) & \sin^2 2\rho + \cos^2 2\rho \cos \delta & \cos 2\rho \sin \delta \\ 0 & -\sin 2\rho \sin \delta & -\cos 2\rho \sin \delta & \cos \delta \end{pmatrix} \quad (2)$$

Here, ρ is the orientation of a protein fibril in the architectonic network, the matter of which introduces the phase shift δ between orthogonal components of the laser wave amplitudes.

Topicality of this modeling is related with the possibility to apply the all-purpose Mueller matrix analysis to changes of polarization properties, which are caused by transformation of optical and geometric constitution of the anisotropic component (architectonic network of fibrils) in these biological objects [2–8]. Based on this model, there is the developed method for polarization differentiation of optical properties inherent to physiologically normal as well as pathologically changed biological tissues by using the wavelet analysis of local features observed in coordinate distributions of intensities in their coherent images.

This trend in polarization diagnostics got its development in investigations of a statistical and self-similar structure of Mueller-matrix images (MMIs) that are two-dimensional distributions $f_{ik}(x, y)$ [9, 10] describing biological tissues. So, in the approximation of single light

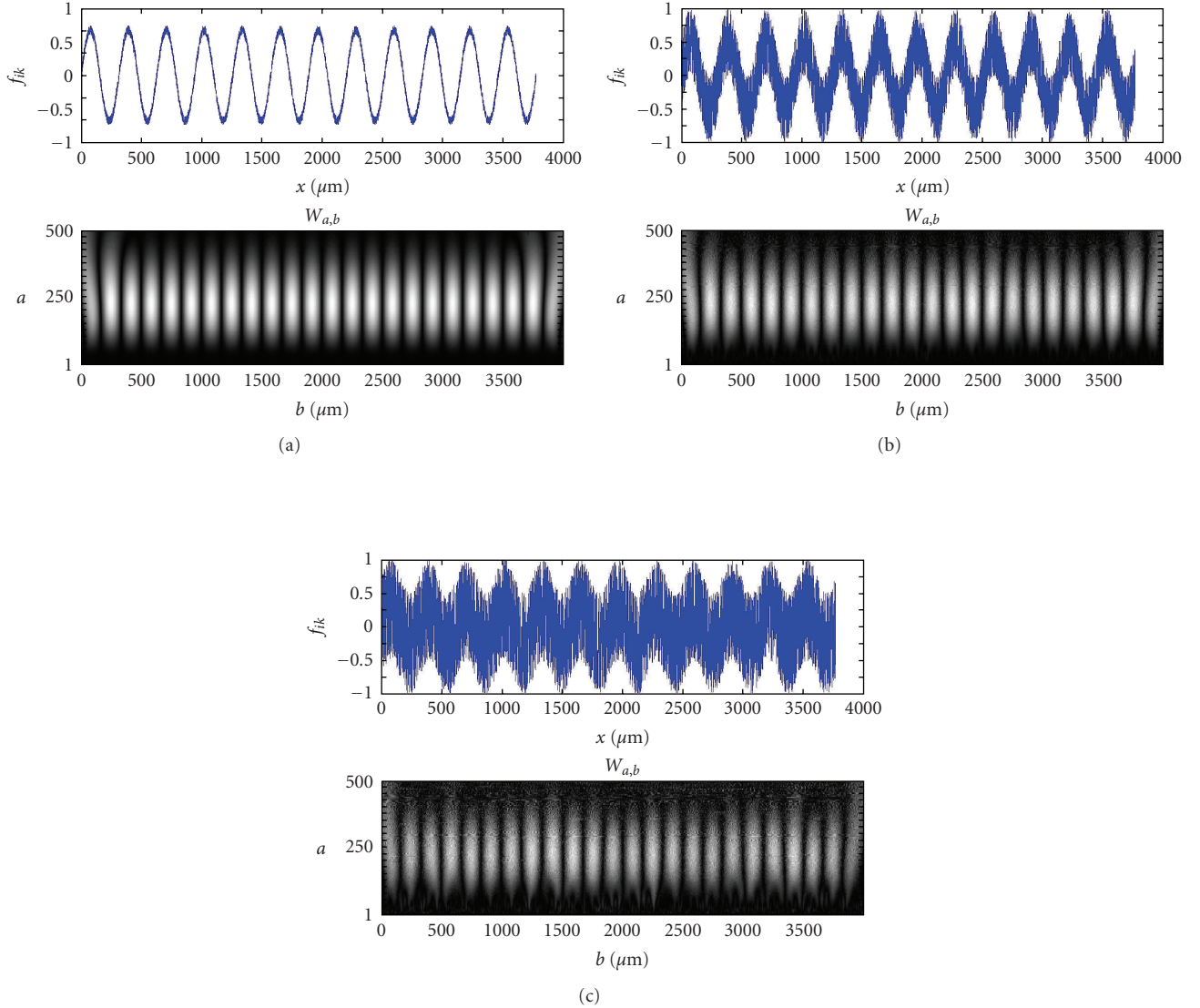


FIGURE 1: Wavelet coefficients $W_{a,b}$ of statistical and stochastic distributions for the matrix element $f_{ik}(x \equiv b)$. Commentaries are in the text.

scattering, there was found the interrelation between a set of statistical moments of the first to fourth orders $Z^{(j=1,2,3,4)}$ that characterize orientation (ρ) and phase (δ) structures of birefringent architectonics inherent to biological tissues as well as a set of respective statistical moments for MMI [10–14]. It is ascertained that the coordinate distributions of matrix elements $f_{ik}(x, y)$ describing physiologically normal biological tissue possess a self-similar, fractal structure. MMIs of physiologically changed biological tissues are stochastic or statistical [11].

This work is aimed at studying the efficiency of the wavelet analysis in application to the local structure of MMI inherent to biological tissues with using statistical and fractal analyses of the obtained wavelet coefficient distributions for diagnostics of local changes in orientation-phase structure of their architectonic networks.

2. Wavelet Analysis of Mueller-Matrix Images of Biological Tissues

Wavelet transformation of MMI consisted of its expansion within a basis of definite scale changes and transfers of the soliton-like function (wavelet) [6]. The distribution of values for f_{ik} elements of the Mueller matrix can be represented in the following form:

$$f_{ik}(x) = \sum_{j,l=-\infty}^{\infty} q_{jl} v_{jl}(x). \quad (3)$$

Here, $f_{ik}(x)$ distribution belongs to the space $L^2(\mathbb{R})$ created by wavelets v_{jl} . The basis of this functional space can be constructed using scale transformations and transfers of

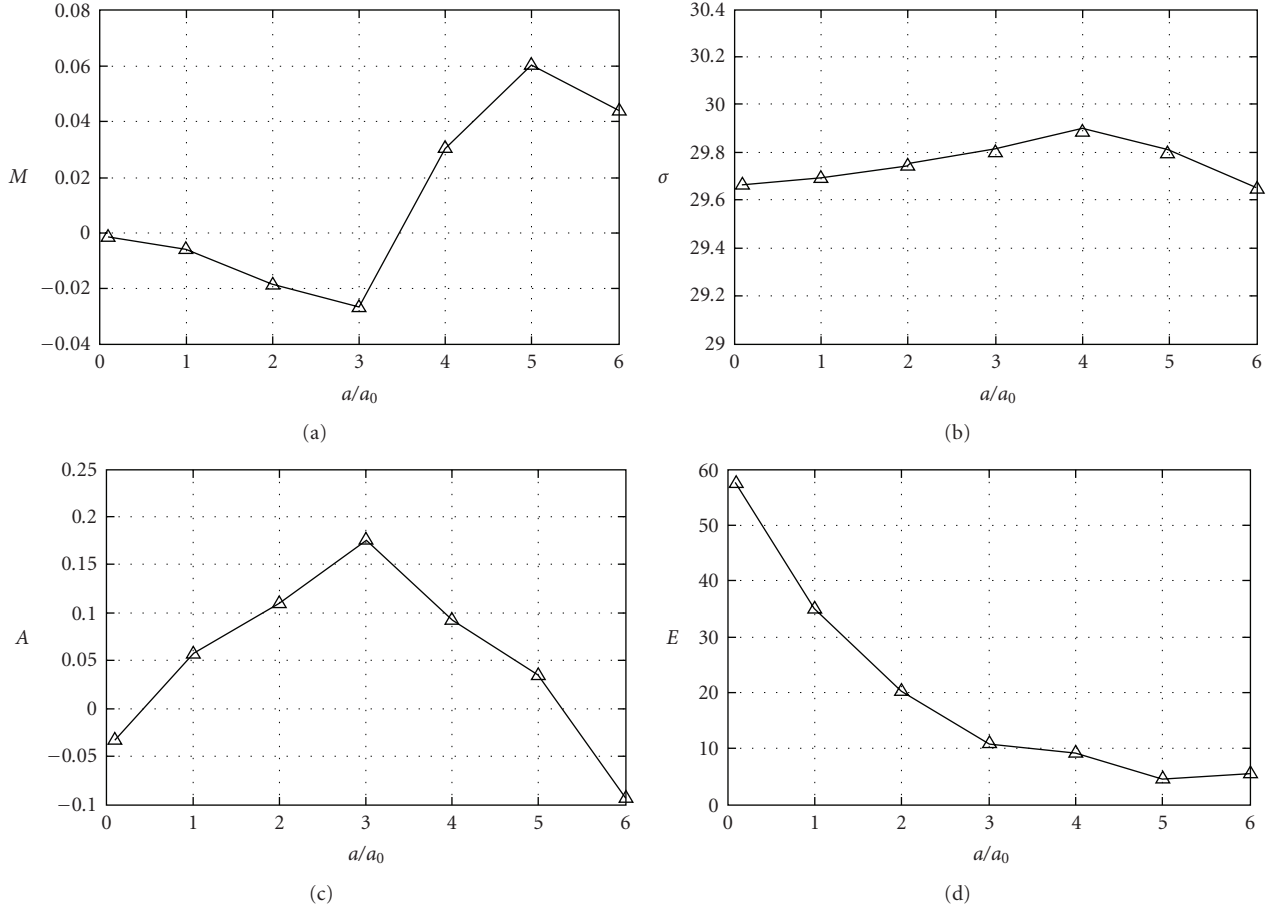


FIGURE 2: Mean value (a), dispersion (b), the skewness (c), and the kurtosis (d) of distributions inherent to wavelet coefficients $W_{a,b}(f_{ik})$. Commentaries are in the text.

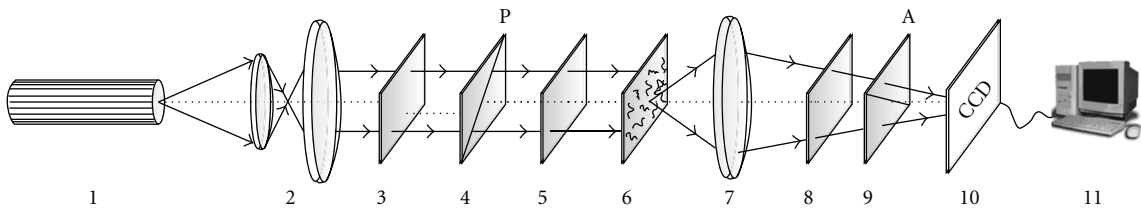


FIGURE 3: Optical scheme of polarimeter 1:He-Ne laser; 2:collimator; 3:stationary quarter-wave plates; 5, 8:mechanically movable quarter-wave plates; 4, 9:polarizer and analyzer correspondingly; 6:object of investigation; 7:micro-objective; 10:CCD camera; 11:personal computer.

the wavelet $v_{jl}(x)$ with arbitrary values of basic parameters—the scaling coefficient a and shift parameter b

$$v_{ab}(x) = |a^{-1/2}| \xi \left(\frac{x-b}{a} \right); \quad a, b \in R; \xi \in L^2(R). \quad (4)$$

Being based on it, the integral wavelet transformation takes a look at

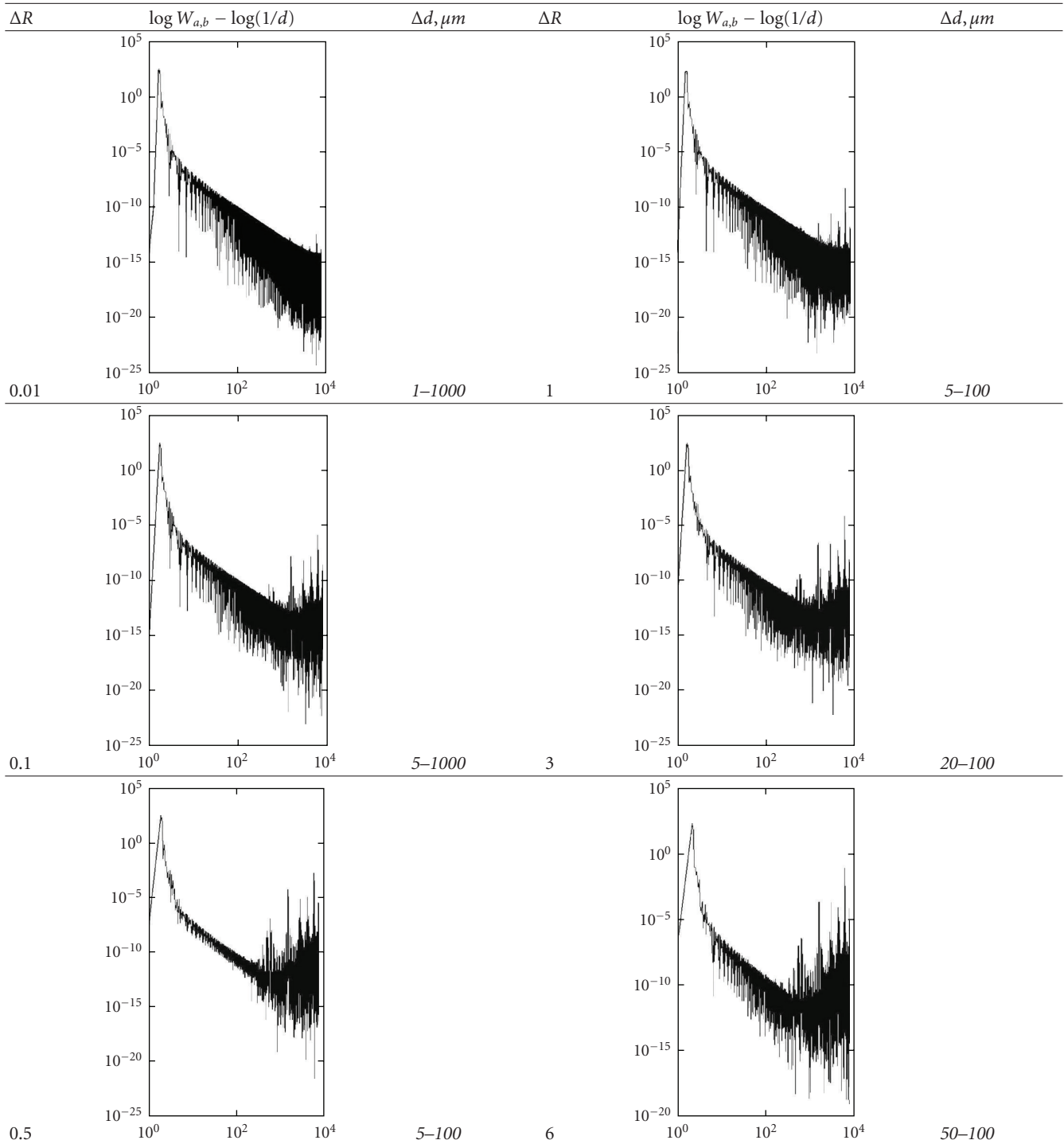
$$\begin{aligned} [W_v f_{ik}](a, b) &= |a|^{-1/2} \int_{-\infty}^{\infty} f_{ik}(x) v^* \left(\frac{x-b}{a} \right) dx \\ &= \int_{-\infty}^{\infty} f_{ik}(x) v_{ab}^*(x) dx. \end{aligned} \quad (5)$$

Coefficients $q_{jl} = \langle f_{ik}, v_{jl} \rangle$ of the expansion (3) for the function f_{ik} by wavelets can be defined via the following integral wavelet transformation:

$$q_{jl} = [W_v f_{ik}] \left(\frac{1}{2^j}, \frac{l}{2^j} \right). \quad (6)$$

In our work, to analyze MMI we used the most widely spread soliton-like function MHAT (“Mexican hat”, [6]) as a wavelet function. Such a function was effectively used in [15–19] for analysis of multiscale laser images of rough surfaces and histological sections of biological tissues. This case provides the possibility of comparative analysis of this

TABLE 1: Log-log dependences of power spectra for the wavelet coefficients $W_{a,b}$ of statistical-stochastic distributions for f_{ik} elements of the Mueller matrix describing single-axis biological crystals.



work with previous research of polarization inhomogeneous images of phase inhomogeneous layers. on the other hand, the task of selection of the most diagnostic appropriate function remains topical. However, this important task we consider as individual and it deserves the special research, which is not provided in our work.

3. Computer Modeling the Efficiency of the Wavelet Analysis to Differentiate MMI of Birefringent Fibrils

Birefringent architectonic networks of BT consist of a set of coaxial cylinder protein fibrils with a statistical distribution

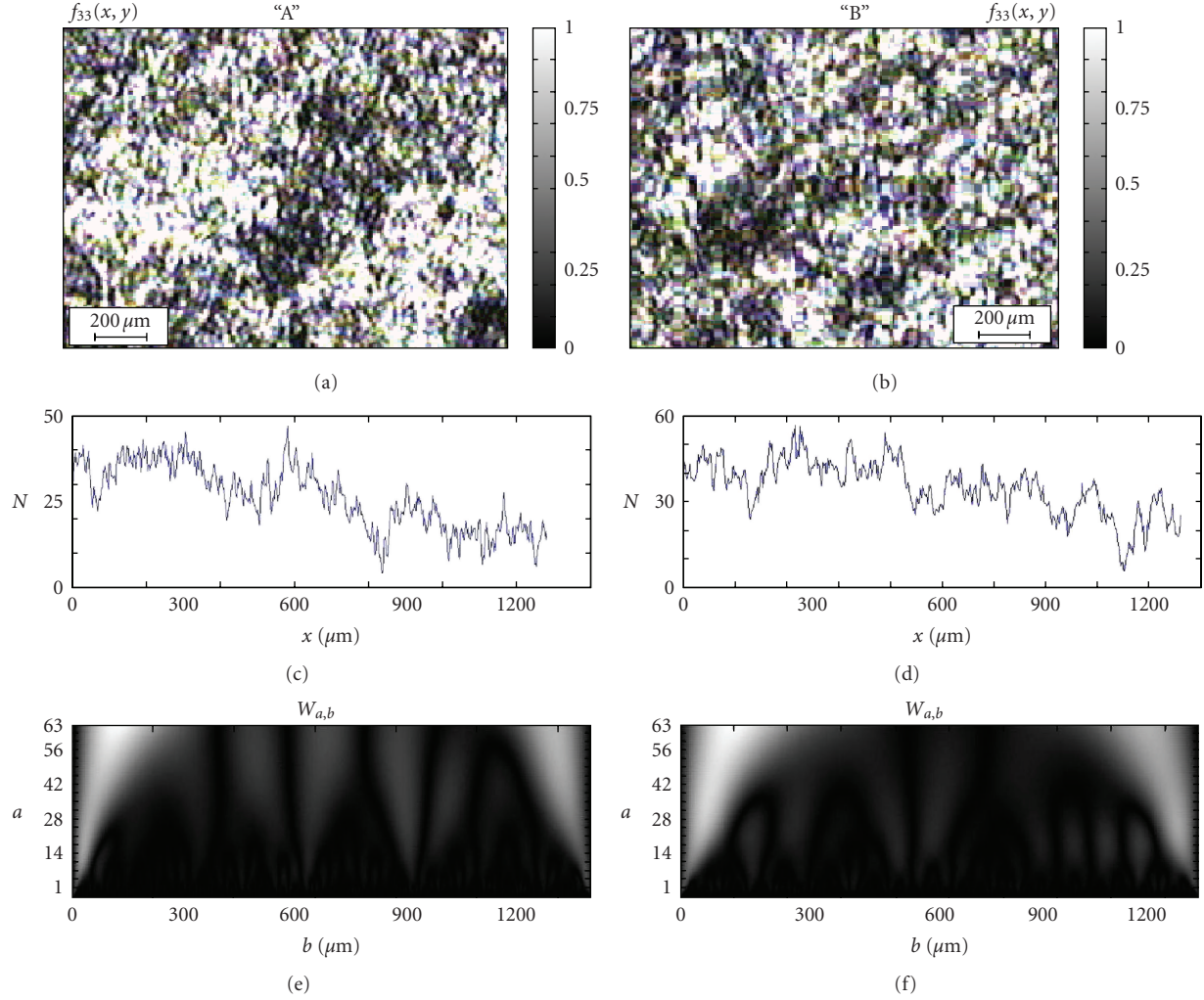


FIGURE 4: MMI of the f_{33} element and coordinate structure (a), (b), (c) and (d) as well as coefficients of wavelet expansion $W_{a,b}$ (e), (f) for the f_{33} element of A and B type connective tissues.

of optical axis orientations ρ and values of phase shifts δ [2–8]. We considered the most spread case of pathological changes in BT architectonics—formation of directions for pathological growth or excrescence of a tumor. Within mathematical frames, this case was modeled as a superposition of statistical (equiprobable) and stochastic (quasiregular) components in distributions of orientations ρ of birefringent fibrils as well as phase shifts δ that are caused by them

$$\begin{aligned} Q_1(\rho) &\approx R(\rho) + A \sin \frac{2\pi}{D} \rho, \\ Q_2(\delta) &\approx R(\delta) + B \sin \frac{2\pi}{D} \delta, \end{aligned} \quad (7)$$

where $Q_{i=1,2}$ are the functions of distributions for ρ and δ values; R is random (equiprobable) distribution of ρ and δ ; A, B are amplitudes of the stochastic component; D is mean statistical size of co-axial fibrils.

The analysis of (3) shows the set of Mueller matrix elements presented by combinations “ $\cos \times \sin$ ”; “ $\cos^2 + \sin^2 \times \cos$ ”; “ $\sin^2 + \cos^2 \times \cos$ ”, which depend on ρ and δ .

That is why, one can assume that coordinate distributions f_{ik} , which characterize the real architectonics networks of biological tissues, are also presented by superposition of statistic and stochastic components.

For simplicity we consider one-dimensional coordinate distribution in the following form:

$$f_{ik}(x) = R(x) + C \sin \frac{2\pi}{D} x. \quad (8)$$

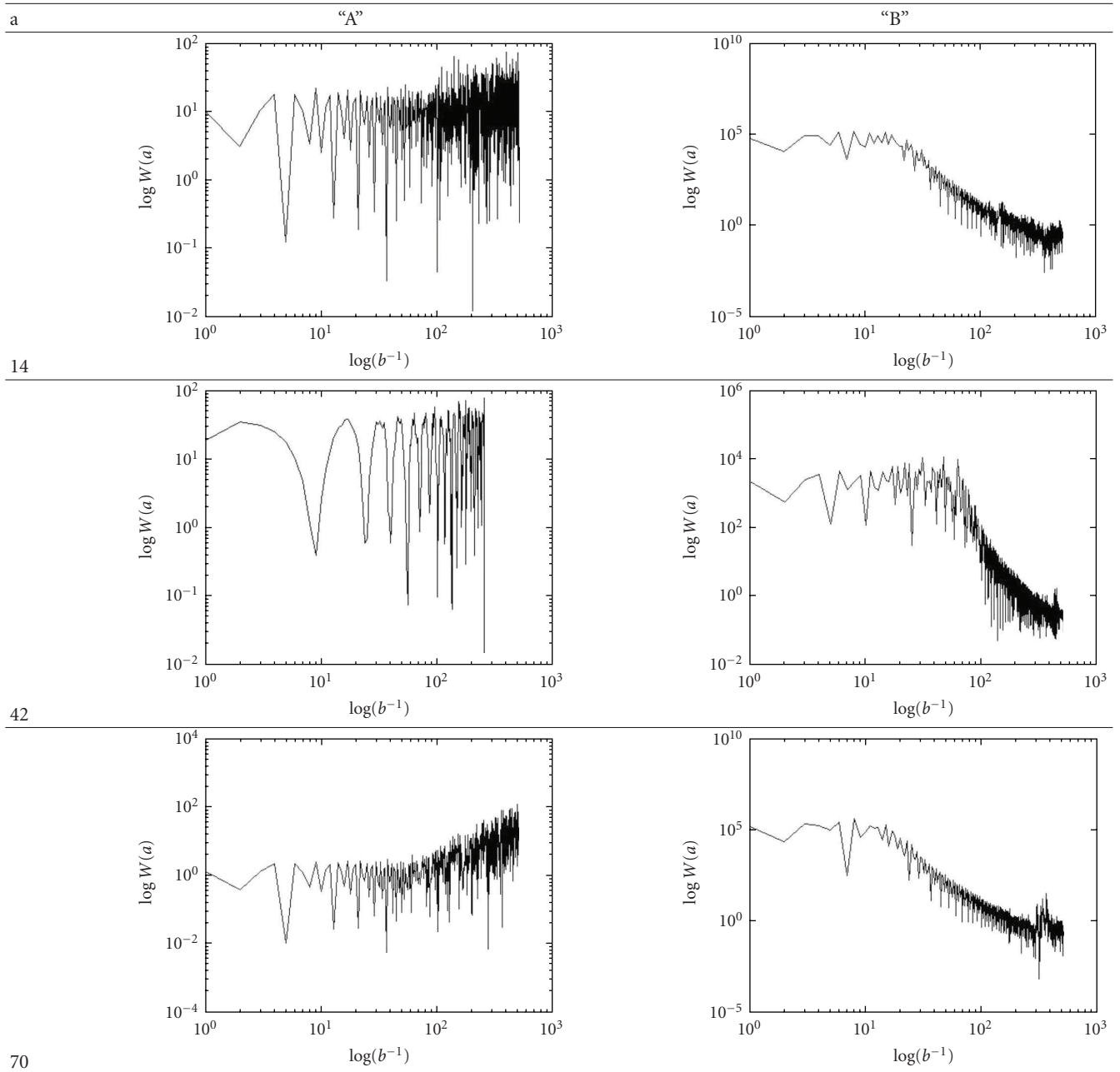
Here, C is the amplitude of a stochastic component.

We modeled a superposition of a “background” $R(x)$ and informative signal $C \sin 2\pi/Dx$ for the following relations between their amplitudes $R(x) = 0.01 \cdot C \sin(2\pi/D)x \div 6 \cdot C \sin(2\pi/D)x$.

Figure 1 shows wavelet coefficients $W_{a,b}$ for the respective distributions $f_{ik}(x)$.

As seen from the data obtained, the distributions of values for wavelet coefficients $W_{a,b}$ of all the types of signals $f_{ik}(x)$ behave like quasiharmonic structures. Even in the case

TABLE 2: Log-log dependences of power spectra for the wavelet coefficients $W_{a,b}$ of statistical-stochastic distributions for the f_{33} element of A and B type connective tissues.



of significant (six-fold) dominance of the statistical component amplitude (Figure 1(c)), the quasiregular structure of coordinate distribution for wavelet coefficients $W_{a,b}$ is preserved in full. This fact confirms a high efficiency of the wavelet analysis in separation of the harmonic component in the distribution of $f_{ik}(x)$ elements of the Mueller matrix.

To make diagnostic possibilities of the wavelet analysis more objective, we calculated statistical moments of the first to fourth orders (M, σ, A, E), which characterize distributions of the wavelet coefficients $W_{a,b}(f_{ik})$ for various ratios $0.01 \leq A_0/A \leq 6$ (Figure 2), and found their Log-log dependences of power spectra (Table 1):

$$\begin{aligned}
 M &= \frac{1}{m \times n} \sum_{i=1}^{m \times n} |W_{a,b}(f_{ik})|, \\
 \sigma &= \sqrt{\frac{1}{m \times n} \sum_{i=1}^{m \times n} [W_{a,b}(f_{ik})]^2}, \\
 A &= \frac{1}{\sigma_2^3} \frac{1}{m \times n} \sum_{i=1}^{m \times n} [W_{a,b}(f_{ik})]^3, \\
 E &= \frac{1}{\sigma_2^4} \frac{1}{m \times n} \sum_{i=1}^{m \times n} [W_{a,b}(f_{ik})]^4.
 \end{aligned} \tag{9}$$

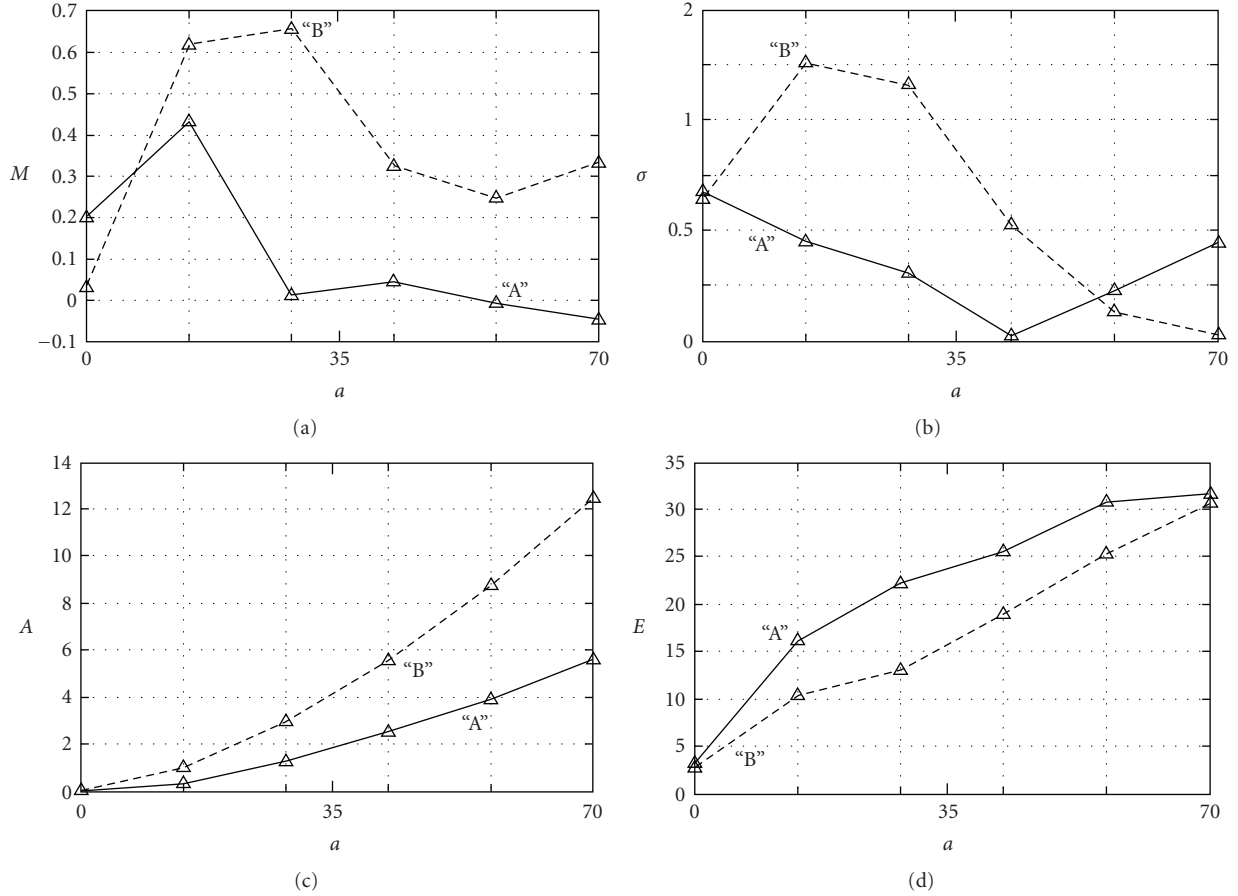


FIGURE 5: Dependences of statistical moments of the 1st to 4th orders on the scale of the wavelet function μ for connective tissue of A and B types.

Our analysis of the obtained data revealed that the change of the fourth statistical moment for the distribution of wavelet coefficients $W_{a,b}$ is the most dynamical from the above viewpoint, as the value of this moment changes within the range of one order in dependency of ratios $0.01 \leq A_0/A \leq 6$.

Our investigation of log-log dependences for power spectra of distributions describing the wavelet coefficients $W_{a,b}$ of matrix elements $f_{ik}(x)$ allowed revealing the following regularities:

- (i) all the dependences $\log W_{a,b} - \log(1/d)$ calculated for various relations between amplitudes of random and quasi-regular components of distributions characteristic for the Mueller matrix elements $f_{ik}(x)$ consist of two parts, namely, the fractal one (with one slope of the approximating curve within a definite range Δd for sizes of birefringent fibrils) and the statistical one (when a stable value for the slope angle of the approximating curve does not take place);
- (ii) when the amplitude of the statistical component in the $f_{ik}(x)$ distribution grows, the range Δd of a linear part in dependences $\log W_{a,b} - \log(1/d)$ is decreased;

- (iii) fractal component of log-log dependences for the power spectra of wavelet coefficients $W_{a,b}$ is preserved even for significant (six-fold) dominance of the noise amplitude and comprises the size range $\Delta d = 50\text{--}100 \mu\text{m}$.

Thus, the performed computer modeling indicates the diagnostic efficiency of the wavelet analysis when detecting local changes in birefringency (δ) of ordered biological crystals.

Besides, using the statistical and correlation analysis of wavelet coefficients $W_{a,b}$ in the expansion of the Mueller matrix elements, we have demonstrated the possibility to reveal the quasiharmonic component in distributions of orientation (ρ) and phase (δ) parameters in complex (statistical) architectonic networks.

4. Scheme and Methods of Experimental Investigations

Figure 3 shows traditional optical scheme of polarimeter for measuring due to technique provided in [14] of the Mueller matrix elements of BT histological sections.

The parallel ($\varnothing = 10^4 \mu\text{m}$) beam of He-Ne laser ($\lambda = 0.6328 \mu\text{m}$, $W = 5.0 \mu\text{W}$) was used as an illuminator.

Polarization illuminator consists of quarter-wave plates 3, 5 and polarizer 4, and it sequentially forms a series of linearly polarized ($I_0, I_{45}, I_{90}, I_{135}$) with azimuths $0^\circ, 90^\circ, 45^\circ, 135^\circ$, and right-hand (I_{\oplus}) and left-hand (I_{\ominus}) circularly polarized probing BT laser beams. The BT images made by microobjective ($4\times$) 7 were projected into the plane of a light-sensitive plate ($m \times n = 800 \times 600$ pixels) of CCD-camera 10. Polarization analysis of the BT images was performed by means of polarizer 9 and quarter-wave plate 8.

The optical thin (the absorption coefficient $\tau < 0,1$) BT histological sections were used as the objects of investigation. In this situation one has a single scattering regime of laser radiation scattered by BT network and the narrow-band scattering indicatrix is formed (95% of energy is concentrated within the angle cone $\Delta\Omega \leq 15^\circ$). Therefore, the speckle background formation in the BT histological section image due to scattering on optical elements is insignificant.

The technique of obtaining such objects is convenient: biological tissue is freezing to nitrogen temperature with the following obtaining, by means of medical microtome, the histological sections (from $10\ \mu\text{m}$ to $100\ \mu\text{m}$). Such a technique allows preserving the optical properties of biological tissues over a period of 24 hours.

5. The Diagnostics of Local Changes in the Optical and Geometrical Structure of Architectonic Networks Inherent to Real Biological Tissues

We performed comparative investigations of two types of mounts from connective tissue of a woman matrix:

- (i) healthy tissue (type A)—the set of chaotically oriented collagen fibrils;
- (ii) tissue in the state of dysplasia (precancer state (type B))—the set of chaotically oriented collagen fibrils with local quasiordered parts.

From the optical viewpoint, polarization properties of these tissues (types A and B) are similar to some extent. For instance, the coordinate distribution of random values inherent to phase shifts $\delta(x, y)$, which is related with the range of changes in geometric sizes of collagen fibrils, is close in both cases. The main differences in composition of the set of biological crystals lie in presence of local parts with quasi-ordered directions of optical axes in the tissue of the type B. Being based on this fact, one can assume that the coordinate distribution of the Mueller matrix element (Mueller-matrix images)—(MMIs) values for the type A tissue $f_{ik}(\rho, \delta)$ approaches the statistical one. The coordinate distribution $f_{ik}(\rho, \delta)$ for the type B tissue can be represented by a superposition of the random and quasi-regular components (8).

As a main element of the Mueller matrix for biological tissue of a given type, we chose the “orientation” matrix element f_{33} . It is known that the statistical and correlation

analysis of coordinate distributions for this element is considered as efficient in differentiation of optical properties characterizing collagen networks in healthy and pathologically changed skin [12].

Shown in Figure 4 are MMIs for the element f_{33} (fragment (a): type A, fragment (b): type B) and the respective, wavelet expansions (fragments (e) and (f) for the linear cross-section of $f_{33}(x, y)$, fragments (c) and (d) for healthy and pathologically changed connective tissue of the uterus neck).

Our comparative analysis of the obtained data shows a complex statistical structure of two-dimensional distributions for the matrix element $f_{33}(x, y)$ (see fragments (a) and (b)) as well as its linear cross-sections (fragments (c) and (d)) for MMI of biological tissues for their both types. The same can be stated for the distributions of wavelet coefficients $W_{a,b}$ (fragments (e) and (f)).

With account of the above observations, it seems actual to verify the efficiency of statistical (the set of the first to fourth moments for $W_{a,b}$ distributions) and correlation (features of the power spectra for wavelet coefficients of $W_{a,b}$) methods of analysis for diagnostics of formation of local parts containing quasi-ordered ($\rho(x, y) \approx \text{const}$) birefringent fibrils.

With this aim, we performed step-by-step “screening” of the pictures for wavelet coefficients $W_{a,b}$ (Figures 4(e) and 4(f)) using the scale change for the wavelet function $\mu = 0.5$. For each value of the wavelet function a_i , we found the dependences $W(b, a = a_i)$ and calculated the log-log dependences for the scale of their power spectra. As a result of this linear scanning, we obtained the array of data $\{\log W(a_i) - \log(b)\} \div \{\log W(a_j) - \log(b)\}$ summarized in Table 2.

Coordinate distributions for the matrix element f_{33} corresponding to a mount of the sample of healthy connective tissue (Table 2) are characterized by statistical distributions for the wavelet coefficients $W_{a,b}$ in all the range of scale a changes of the wavelet function μ . It is confirmed by the absence of any stable slope of the approximating curve for the considered set of dependences $\log W_{a,b}(1 \leq a \leq 5b) - \log(b^{-1})$.

Another picture can be observed for the sample of changed connective tissue (Figure 4). If the scale coefficient a of the wavelet function μ possesses some definite dimension, then there exists a linear part in the respective log-log dependence of the power spectrum characterizing the distribution of wavelet coefficients $W_{a,b}(a_i)$. In accordance with performed computer modeling, this fact indicates the availability of a quasi-harmonic component in $W_{a,b}(a_i)$ distributions, which is caused by respective geometry of biological crystals.

In our case, for the mean statistical size of a pathological creation $a = 28\ \mu\text{m}$ one can observe a quasi-ordered part of collagen fibrils with sizes lying within the range 10 to $50\ \mu\text{m}$.

Thus, one can state that the correlation approach, in the analysis of $W_{a,b}$ coefficients valid for the wavelet distribution in MMI of “orientation” element f_{33} for connective tissue of the uterus neck, is rather efficient for differentiation of its healthy and pathologically changed samples.

Some additional information for differentiation of these objects was obtained using the statistical analysis of coordinate distributions $W_{a,b}(a_i)$.

Shown in Figure 5 are the dependences of statistical moments of the first to fourth orders for coordinate distributions of wavelet coefficients $W_{a,b}$ in MMI of f_{33} , which correspond to different scales of the wavelet function μ .

The obtained data show that

- (i) statistical moments of the 1st and 4th orders for distributions of wavelet coefficients $W_{a,b}$, like of the case of computer modeling (Figure 2) the f_{33} element describing the samples of myometrium of both types, suffer insignificant changes (0 to 0.2) within the whole range of scales a_i for the wavelet function μ (Figure 5),
- (ii) the range of changes in values of skewness (A) and kurtosis (E) for $W_{a,b}$ distributions lies within the range of two orders (Figure 5),
- (iii) main differences between connective tissues of A and B types are found in the vicinity of the scale $a = 28\mu\text{m}$ where dependences between $A(a)$ and $E(a)$ reach two- or three-fold level.

Thus, we found that the differences between values of statistical moments of higher orders for a definite range of scales a of the wavelet function μ_a can be also used to differentiate local changes in orientation changes of optical axes inherent to territorial matrix crystals.

References

- [1] S. C. Cowin, "How is a tissue built?" *Journal of Biomechanical Engineering*, vol. 122, no. 6, pp. 553–569, 2000.
- [2] O. V. Angelsky, A. G. Ushenko, Yu. A. Ushenko, Ye. G. Ushenko, Yu. Ya. Tomka, and V. P. Pishak, "Polarization-correlation mapping of biological tissue coherent images," *Journal of Biomedical Optics*, vol. 10, no. 6, Article ID 064025, 2005.
- [3] J. F. de Boer and T. E. Milner, "Review of polarization sensitive optical coherence tomography and Stokes vector determination," *Journal of Biomedical Optics*, vol. 7, no. 3, pp. 359–371, 2002.
- [4] J. F. de Boer, T. E. Milner, and J. S. Nelson, "Two dimensional birefringence imaging in biological tissue using phase and polarization sensitive optical coherence tomography," in *Trends in Optics and Photonics (TOPS): Advances in Optical Imaging and Photon Migration*, OSA, Washington, DC, USA, 1998.
- [5] M. J. Everett, K. Schoenenberger, B. W. Colston, and L. B. Da Silva, "Birefringence characterization of biological tissue by use of optical coherence tomography," *Optics Letters*, vol. 23, no. 3, pp. 228–230, 1998.
- [6] O. V. Angelsky, G. V. Demianovsky, A. G. Ushenko, D. N. Burkovets, and Yu. A. Ushenko, "Wavelet analysis of two-dimensional birefringence images of architectonics in biotissues for diagnosing pathological changes," *Journal of Biomedical Optics*, vol. 9, no. 4, pp. 679–690, 2004.
- [7] O. V. Angelsky, Yu. Ya. Tomka, A. G. Ushenko, Ye. G. Ushenko, S. B. Yermolenko, and Yu. A. Ushenko, "2-D tomography of biotissues images in pre-clinic diagnostics of their pre-cancer states," in *Advanced Topics in Optoelectronics, Microelectronics, and Nanotechnologies II*, vol. 5972 of *Proceedings of the SPIE*, pp. 158–162, 2004.
- [8] O. V. Angelsky, A. G. Ushenko, D. N. Burkovets, and Yu. A. Ushenko, "Polarization visualization and selection of biotissue image two-layer scattering medium," *Journal of Biomedical Optics*, vol. 10, no. 1, Article ID 014010, 2005.
- [9] O. V. Angelsky, Yu. Ya. Tomka, A. G. Ushenko, Ye. G. Ushenko, and Yu. A. Ushenko, "Investigation of 2D Mueller matrix structure of biological tissues for pre-clinical diagnostics of their pathological states," *Journal of Physics D*, vol. 38, no. 23, pp. 4227–4235, 2005.
- [10] S. Jiao, W. Yu, G. Stoica, and L. V. Wang, "Optical-fiber-based Mueller optical coherence tomography," *Optics Letters*, vol. 28, no. 14, pp. 1206–1208, 2003.
- [11] Yu. A. Ushenko, "Statistical structure of polarization-inhomogeneous images of biotissues with different morphological structures," *Ukrainian Journal of Physical Optics*, vol. 6, pp. 63–70, 2005.
- [12] O. V. Angelsky, A. G. Ushenko, Yu. A. Ushenko, Ye. G. Ushenko, Yu. Ya. Tomka, and V. P. Pishak, "Polarization-correlation mapping of biological tissue coherent images," *Journal of Biomedical Optics*, vol. 10, no. 6, Article ID 064025, 2005.
- [13] O. V. Angelsky, A. G. Ushenko, and Yu. A. Ushenko, "Polarization reconstruction of orientation structure of biological tissues birefringent architectonic nets by using their Mueller-matrix speckle-images," *Journal of Holography and Speckle*, vol. 2, pp. 72–79, 2005.
- [14] A. G. Ushenko and V. P. Pishak, "Laser polarimetry of biological tissue. Principles and applications," in *Coherent-Domain Optical Methods. Biomedical Diagnostics, Environmental and Material Science*, V. Tuchin, Ed., pp. 67–93, Kluwer Academic Publishers, Dordrecht, The Netherlands, 2004.
- [15] O. V. Angelsky, A. G. Ushenko, D. M. Burkovets, V. P. Pishak, and O. V. Pishak, "Laser polarimetry of pathological changes in biotissues," in *The 7th International Symposium on Laser Metrology Applied to Science, Industry, and Everyday Life*, vol. 4900 of *Proceedings of the SPIE*, pp. 1045–1049, 2002.
- [16] O. V. Angelsky, D. N. Burkovets, A. V. Kovalchuk, and S. G. Hanson, "Fractal description of rough surfaces," *Applied Optics*, vol. 41, no. 22, pp. 4620–4629, 2002.
- [17] O. V. Angelsky, P. P. Maksimyak, and T. O. Perun, "Optical correlation method for measuring spatial complexity in optical fields," *Optics Letters*, vol. 18, no. 2, pp. 90–92, 1993.
- [18] O. V. Angelsky, D. N. Burkovets, P. P. Maksimyak, and S. G. Hanson, "Applicability of the singular-optics concept for diagnostics of random and fractal rough surfaces," *Applied Optics*, vol. 42, no. 22, pp. 4529–4540, 2003.
- [19] O. V. Angelsky, P. P. Maksimyak, and T. O. Perun, "Dimensionality in optical fields and signals," *Applied Optics*, vol. 32, no. 30, pp. 6066–6071, 1993.